Final Report

Regional Transport Aircraft with Regenerative Propulsion

Design Synthesis Exercise Spring 2022

Group 7

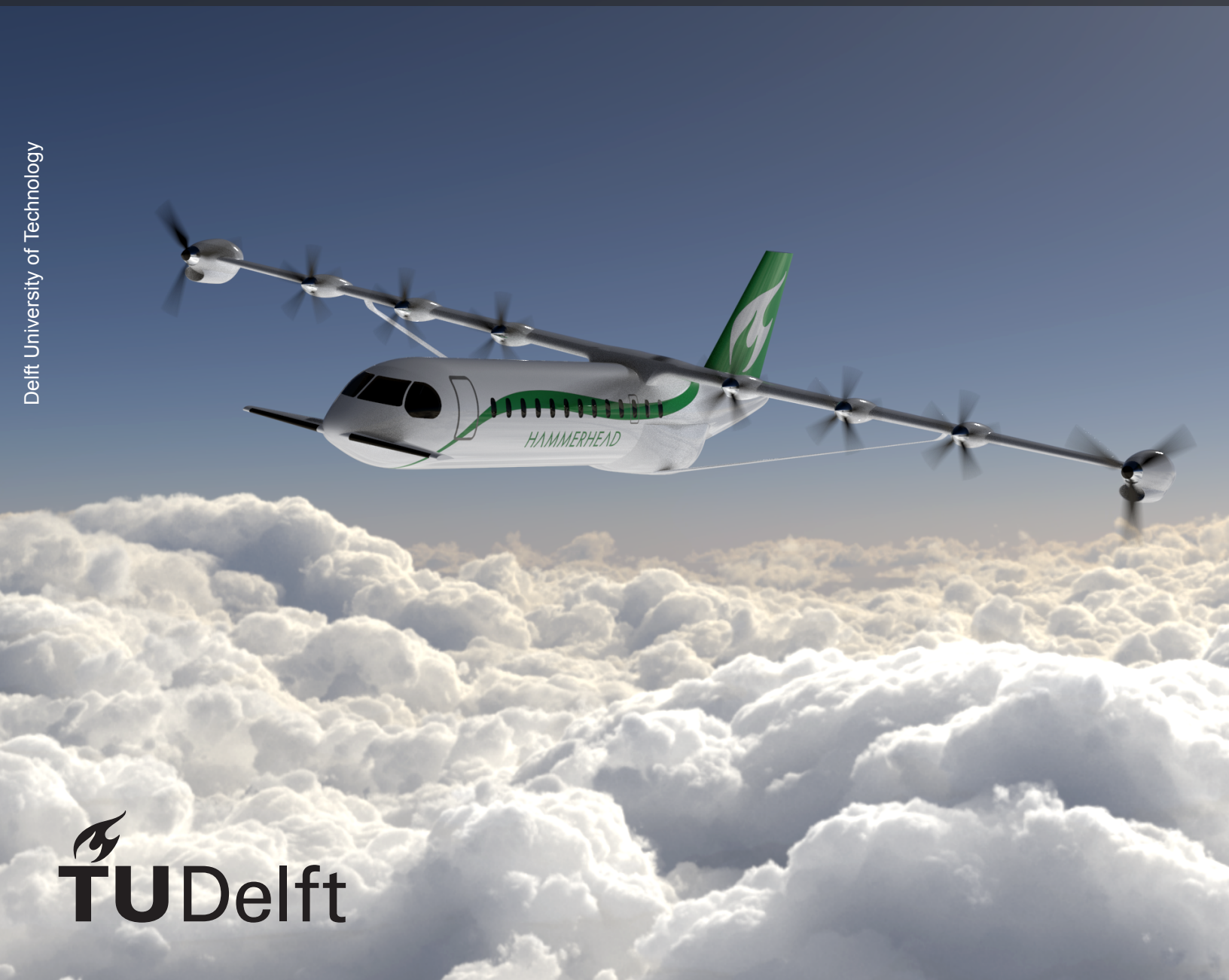

Delft University of Technology

TU Delft

Final Report

Regional Transport Aircraft with Regenerative Propulsion

by

Group 7

Student Name	Student Number
Sander Althuis	4884523
Arjen Boerdijk	4430654
Evan Emberger	5067677
David Gerts	5076927
Floris Gunter	4877764
Pablo Koop	4781163
Lennard Mascini	5017971
Oscar Rots	5063345
Pieter van de Ven	4661052
Eric van Pijlen	4783549

Tutors:	Dr.ir. M.F.M. Hoogreef, Dr.ir. T. Sinnige and ir. J. Goyal
Project Duration:	April, 2022 - June, 2022
Institution:	Delft University of Technology
Faculty:	Faculty of Aerospace Engineering

Cover:	Render of Hammerhead (own work)
Style:	TU Delft Report Style, with modifications by Daan Zwaneveld

TU Delft

Preface

This report was written by ten students from the faculty of Aerospace Engineering at the Delft University of Technology. It is the final report in a series of deliverables, all part of the concluding Design Synthesis Exercise for the Bachelor degree programme in Aerospace Engineering. Over the course of ten weeks, a conceptual design for a regional transport aircraft was created. The design is innovative in its use of a hybrid hydrogen-electric powertrain, distributed propulsion, and regenerative capabilities during descent.

The target audience for this report is defined as the fictional client that asked this team to perform the conceptual design of this aircraft. It is assumed that the reader has a basic knowledge of engineering and aircraft, but the nomenclature is included to introduce the used variables and symbols.

We would like to thank our supervisors Dr. ir. M.F.M. Hoogreef, Dr. ir. T. Sinnige, and ir. J. Goyal for their help during the project. They provided very useful advice on a technical level, but even more importantly, challenged us to make the most out of this project. We are convinced this project helped us become better engineers and taught us to work in a team better. We improved on being critical on previous and our own work, and have continuously been working on the completeness and soundness of our reasoning.

Group 7
Delft, June 2022

Executive Summary

To provide a clear mission and objective to the design of the aircraft, the mission need statement and project objective statement were set up. These two statements form a basis for the project throughout the design phases.

Mission Need Statement
"To provide a regional commuter aircraft to transport at least 50 passengers including luggage, which is financially competitive to the ATR 42-600 and comparable to ground transport for direct operating cost (DOC). Further, it needs to reduce the CO_2 and NO_X emissions compared to the ATR 42-600 by 75% and 90% respectively, to have a sustainable end-of-life solution, and have a design payload of at least 5300 $[kg]$ and operate at DOC range of at least 400 $[km]$ including reserves."

Project Objective Statement
"To design a regional aircraft leveraging distributed (hybrid)-electric propulsion and regenerative capability, with improved sustainability compared to an ATR 42-600 and driven by requirements from the EU-funded FutPrInt50 project, by ten students in ten weeks."

Trade-off
These statements were first analysed economically, and it was found that there is economic potential for this aircraft. The aviation market is growing by 2.7% annually, and the market for regional transportation tickets is expected to grow from 20,000 to 70,000 billion passenger-kilometres yearly. After analysing the functions and corresponding requirements of the aircraft, six design concepts were set up. These varied in overall aircraft configuration and powertrain concept. After performing a trade-off based on weight, mission energy, emissions, direct operating costs, technology readiness level, and passenger comfort, a single concept was chosen to be worked out in more detail. This concept featured a truss-braced high-wing configuration with a canard, leveraging a hybrid hydrogen-electric powertrain system. The most important final aircraft parameters are listed below in Table 1, and a render of the conceptual aircraft design is shown in Figure 1. The design of the aircraft is briefly substantiated in the continuation of the summary.

Table 1: Important aircraft parameters

Parameter	Value	Unit
MTOM	23314	kg
OEM	17867	kg
Span	31.4	m
Wing surface	62.2	m^2
Fuselage length	22.7	m
Cruise speed	0.45	M
Cruise altitude	170	FL
Pax	50	$-$
Design payload	5300	kg
Max payload	5800	kg
Design range	400	km
Harmonic range	800	km
TO field length (MTOM, SL, ISA)	1000	m

Table 1: Important aircraft parameters

Parameter	Value	Unit
Landing field length	379	m
Service ceiling	7620	m
CO_2 emissions	0	$kg/(pax \cdot 100km)$
NO_X emissions	0	$kg/(pax \cdot 100km)$
DOC	5.15	€$/km$

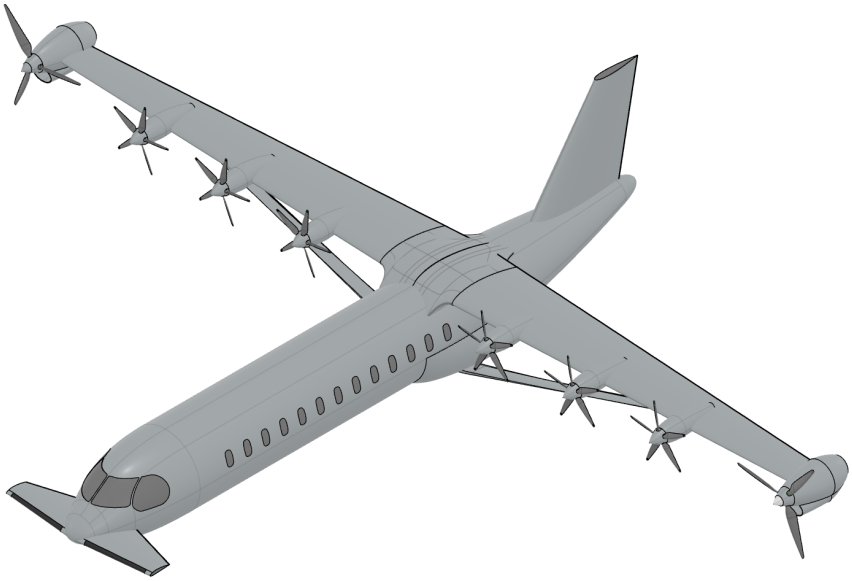

Figure 1: Isometric view of final design, ”Hammerhead”

Initial Sizing

Through an iteration between a class-I and a class-II weight estimation a final MTOW of $23314\ [kg]$ was found, with a final OEW of $17867\ [kg]$. In order to perform the class-II weight estimation, initial sizing was performed for all aircraft systems. This resulted in a wing surface area of $62.2\ [m^2]$. The fuselage was sized using the top-level requirements, resulting in a 2x2 seats abreast configuration, and a fuselage length of $22.7\ [m]$.

Wing Design

The wing has a span of $31.41\ [m]$ and is unswept with a taper ratio of 0.4. With the initial sizing done, a wing airfoil could be selected. The NACA 4415 airfoil was chosen, based on its low drag at and around the design lift coefficient as well as a $C_{l_{max}}$ of 1.908. For landing and take-off conditions a higher C_L was required, thus it was chosen to implement plain flaps. The induced angle of attack and acceleration of the flow provided by the distributed propulsion significantly increase the lift coefficient, meaning a $C_{L_{max}}$ of 3.39 can be achieved. The aerodynamics of the canard were also analysed. The canard uses a NACA 6412 airfoil and has a $C_{L_{max_h}}$ of 2.448 with a fully deflected elevator in landing conditions. The contributions to the drag of the non-lifting aircraft components were also analysed, which led to a total $\frac{C_L}{C_D}$ in cruise of 16.45.

Powertrain Design

An electric powertrain consisting of liquid hydrogen and batteries as energy sources was sized in more detail in this report. Liquid hydrogen is used as a primary energy source due to its low weight, with the hydrogen

converted into electricity in fuel cells.The batteries are used to provide additional power during take-off and cruise, and to store regenerated energy during descent. A powertrain weight of $1666\ [kg]$, battery weight of $4514\ [kg]$, and hydrogen fuel weight of $301\ [kg]$ were calculated. Next to this, a bus voltage of around $1200\ [V]$ was found together with a powertrain efficiency during cruise of 43.2%. Lastly, the general operation of the powertrain was validated and all components were integrated such that they fit into the other aircraft systems.

Propulsion System Design
The propulsion system design had two main design objectives: first of all, maximising propeller efficiency, and second of all, to leverage distributed propulsion to reduce the wing size. With the second objective in mind it was decided to place the propulsors on the main wing only. This also negated the potential interference of propeller wakes with downstream propellers, which would have reduced their efficiency. The propulsors are placed on the leading edge, in a 'tractor configuration', since this allows for a large lift increase and does not interfere with control surfaces or high lift devices. During cruise, only the wingtip propellers are used, and the inboard array propeller blades are folded back to reduce drag. The wingtip propellers were therefore sized for cruise efficiency, and the inboard array of propellers was sized for take-off power. Different combinations were traded-off based on efficiency, mass, and lift enhancement potential. This led to wingtip propellers with 3 blades and a cruise efficiency of 0.890, as well as 6 smaller propellers distributed over the wing span contributing to 60% of the take-off power. The wingtip propellers will be used for regenerating energy during descent, as maintaining the lift enhancement of the wing was deemed superior to the additional drag associated with the propeller-wing interaction in energy-harvesting condition.

Tail Design, Wing Positioning and Undercarriage Design
The canard was sized by combining requirements following from stability, controllability, and centre of gravity excursion. The resulting canard area S_h was computed to be $10.9\ [m^2]$. This also resulted in a longitudinal wing position of $\hat{X}_{LEMAC}$ of $14.6\ [m]$ from the fuselage nose. The vertical tail was sized for directional stability as the distributed propulsion can counteract the moments in case of OEI or crosswind. The resulting vertical tail area S_v was computed to be $13.9\ [m^2]$. The undercarriage design resulted in a landing gear at a longitudinal position of $14.28\ [m]$ and $4.55\ [m]$ for the main and nose landing gear respectively. The lateral position of the main landing gear would be at $1.89\ [m]$ from centre line of the fuselage, resulting in a fuselage podded landing gear. Lastly, the length of both landing gears would be $1.41\ [m]$ including tires.

Structural Design
The structural design of the aircraft was worked out on a conceptual level, mainly focusing on the truss supporting the wing. By attaching it at a spanwise location of $9.5\ [m]$ on the underside of the wing, the wing root bending moment was reduced by 45%, and the maximum shear force was reduced by 23%. This allows for an expected wing weight reduction of 30% compared to a conventional cantilever wing. Furthermore, the materials used for the cabin interior will be 100% bio-degradable woven flax fabric, and in the wing box, extensive use of carbon fibre reinforced plastics (CFRP) is expected.

Performance Analysis
The performance of the aircraft was analysed for supplied mission energy, regeneration performance, climb performance, take-off and landing field length, and reliability. The total supplied DOC mission energy was found to be $12521\ [MJ]$, excluding loiter and diversion. Similarly, the total harmonic range mission energy was found to be $39330\ [MJ]$. For the regenerative braking feature of the Hammerhead, the following performance characteristics where found. When the propeller is optimised for power, a maximum of $178\ [MJ]$ can be regenerated. Optimising the propeller for thrust results in worse performance for energy regeneration, but saves the most mission time for the DOC range, namely 4.57 minutes (-5.3%). In any case, the total supplied mission energy increases when regenerative braking is increased, and increases most when the aircraft is optimised for thrust, namely with $1080[MJ]$ ($+8.6\%$). To test for passenger comfort, the flight path angle during regeneration was investigated, and was only found to increase with $1.55\ [deg]$, which is still below $5\ [deg]$, and therefore deemed insignificant. Subsequently, for climb performance, values for the rate of climb of 1850, 1664, 1548 and $1221\ [ft/min]$ were for found for sea-level, $FL170$, $FL250$ and OEI at $4000\ [m]$, respectively, which all comply with the top-level requirements [1]. For the take-off field lengths, $970\ [m]$ and $781\ [m]$ were found for the maximum take-off weight, and STOL (no payload) cases. For landing

$871\ [m]$ was found. Lastly, a reliability analysis was performed for the battery system, hydrogen fuel-cell system, and the propulsion system. For these three systems, reliabilities of 0.994343, 0.98670, $0.\overline{9}$ were found, respectively, resulting in a resultant reliability of 0.99992 for the entire aircraft.

Requirement Compliance
For almost all requirements compliance could be proven. However, it could not be confirmed at this stage that the design will adhere to all requirement certification regulations, which corresponds to requirement REQ-TOP-SAF-05. This requirement should be reviewed after a more detailed design of the aircraft has been completed in a further design stage.

Outlook
As this project only lasted for 10 weeks, resources were limited and there is abundant room left for more work. The design of the aircraft needs to be further specified by analysing all systems in more detail, and checking compliance with system- and subsystem requirements. After this is finished, a test and certification process can be initiated, and an assembly line needs to be set up before production can be started.

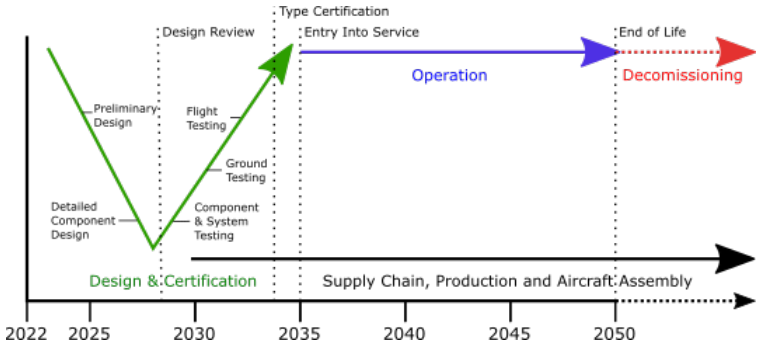

Figure 2: The program timeline and aircraft lifetime after the conceptual design phase.

Ground Operations
To accommodate the aircraft on ground and meet the requirement to have a turnaround time of less than 30 $[min]$ all the operations and the infrastructure were discussed. For hydrogen, a bowser system has been deemed most logical for refuelling. For the refuelling, a strict procedure would be required. This involves that first the fuelling system is connected, purged, chilled-down, refuelled, purged again, and then disconnected [2]. Here, it should be taken into account that during (dis-)connecting and refuelling a safety zone of 20 and 8 $[m]$ would be required. This imposes that certain ground activities, such as connecting/disconnecting the refueling hose and loading the cargo, can not be performed in parallel. Furthermore, the charging is done by two MCS chargers that both can deliver a power of 3.6 $[MW]$, which would lead to a charging time of 11.5 $[min]$[1]. Other operations would involve the pre-flight maintenance check, cargo (un-)loading, (dis-)embarking of passengers, and cleaning and resupplying of the aircraft cabin. This resulted in a turnaround time of 29.5 $[min]$. Lastly, taxiing is performed by a nose wheel-driven system reaching a taxiing speed between 16 and 19 $[kts]$ [3], [4].

Financial Analysis
A financial analysis was carried out, calculating economic relevance from 3 perspectives. Firstly, from the manufacturer's perspective, a total program cost of $4.565\ [billion\ €]$ is expected. Combined with a selling price of $14\ [M€]$ and expected sales of 400 aircraft over 20 years, results in a break-even point (BEP) in 2042. Secondly, from the perspective of an airline, the DOC is calculated to be $5.15\ [€/km]$ or $1461\ [€/hr]$, and these are barely influenced by regenerating energy during descent. The ROI after 10 years is 154% and grows to 308% in 20 years. Thirdly, from the consumer perspective, a ticket price of $80\ [€]$ results in a cost per kilometre of $0.2\ [€/km]$, which is slightly higher than that of train travel.

[1] https://www.charin.global/technology/mcs/, last consulted June 3, 2022

Nomenclature

Abbreviations

Abbreviation	Definition	Abbreviation	Definition
AC	Aerodynamic Centre	HLD	High-Lift Device
BAT	Battery	IN	Inverter
BEM	Blade Element Momentum	ISA	International Standard Atmosphere
BEP	Break Even Point	LT	Low Temperature
BMS	Battery Management System	LH2	Liquid Hydrogen
BOP	Balance-Of-Plant	MTOW	Maximum Take-off Weight
CG	Center of Gravity	OEI	One Engine Inoperative
CON	Converter	OEW	Operational Empty Weight
COM	Compressor	PEM	Proton-Exchange Membrane
DOC	Direct Operating Costs	PM	Power Management
DP	Distributed Propulsion	RPM	Rotations Per Minute
EM	Electric Motor	ROC	Rate Of Climb
EOL	End-of-Life	ROI	Return on Investment
FCS	Fuel Cell System	SAF	Sustainable Aviation Fuel
GB	Gearbox	SH	Shaft
GED	Gravimetric Energy Density	SHAPR	Shaft Power Ratio
GPD	Gravimetric Power Density	SOC	State Of Charge
GSD	Gravimetric Storage Density	SUPPR	Supplied Power Ratio
HEFA	Hydroprocessed Esters and Fatty Acids	TLR	Top Level Requirement
HEP	Hybrid-Electric Powertrain	TP	Turboprop
HEX	Heat Exchanger	TRL	Technology Readiness Level
HT	High Temperature	VLM	Voretx Lattice Method
HFC	Hydrogen Fuel Cell		

Symbols

Symbol	Definition	Unit	Symbol	Definition	Unit
A_x	Aspect ratio [x = plane]	$[-]$	D	Drag force	$[N]$
a	Axial induction factor	$[-]$	l_v	Distance between quarter-chords vertical tail and wing	m
a'	Rotational induction factor	$[-]$	m	Aircraft mass	$[kg]$
b_x	Span [x = plane]	$[m]$	m_x	Component mass [x = component]	
b_y	Span [x = reference/structural]	$[m]$	M	Mach number	$[-]$
b_f	Fuselage width	$[m]$	M_{dd}	Drag-divergence Mach number	$[-]$
b_{fl}	Width of Flaps (One wing)	$[m]$	M_x	Moment around the x-axis	$[Nm]$
b_n	Engine width	$[m]$	N_{props}	Number of propellers	$[-]$

Symbol	Definition	Unit	Symbol	Definition	Unit
h_f	Fuselage height	$[m]$	$\mathbf{n_j}$	Unit normal vector to panel j	$[-]$
B	Number of propeller blades	$[-]$	n_x	Ultimate load factor [x = limit/load]	$[-]$
C	Cost	[€]	n_x	Number of [x = object]	$[-]$
c_{x_y}	Chord length [x = plane] [y = position]	$[m]$	OC_y	Yearly Operating Costs	[€$/year$]
c_j	Chord length of panel j	$[m]$	P_x	Power [x = phase]	$[W]$
$c_{l_{lin,j}}$	Linear lift coefficient of panel j	$[-]$	P_c	Power coefficient = $\frac{2P}{\rho V_\infty^3 \pi r_{tip}^2}$	$[-]$
$c_{l_{visc,j}}$	Viscous lift coefficient of panel j	$[-]$			
C_D	Drag coefficient	$[-]$	OEW	Operation empty weight	$[kg]$
C_d	Airfoil drag coefficient	$[-]$	P	Purchasing price	[€]
C_{d_f}	Airfoil skin friction drag coefficient	$[-]$	$p_{s,f}$	parameter p at the inboard end of flaps	$[m]$
C_{d_p}	Airfoil pressure drag coefficient	$[-]$	q_∞	Dynamic pressure	$[Pa]$
C_{D_0}	Zero lift drag coefficient	$[-]$	R	Range	$[km]$
C_{L_x}	Lift coefficient [x = phase]	$[-]$	R_y	Yearly Operating Revenue	[€$/year$]
C_{L_h}	Lift coefficient horizontal tail in landing configuration	$[-]$	ROC	Rate of climb	$[m/s]$
$C_{L_{A-h}}$	Lift coefficient tailless aircraft in landing configuration	$[-]$	r	Radius from propeller centre	$[-]$
C_{L_0}	Lift coefficient wing at zero-lift angle of attack	$[-]$	r_{hub}	Hub radius of the propeller	$[m]$
C_{L_α}	Lift curve slope	$[1/rad]$	$r_{p_{m,i}}$	Spanwise distance from centre of a propeller to a wing section	$[m]$
$C_{L_{\alpha_h}}$	Lift curve slope canard	$[1/rad]$	r_{tip}	Tip radius of a propeller	$[m]$
$C_{L_{\alpha w}}$	Lift curve slope wing	$[1/rad]$	SM	Static margin	$[-]$
$C_{L_{\alpha_{A-h}}}$	Lift curve slope tailless aircraft	$[1/rad]$	S_{wet}	Wetted area	$[m^2]$
$C_{L_{des}}$	Design lift coefficient	$[-]$	S_{wf}	Flaps wetted area	$[m^2]$
C_l	Sectional lift coefficient	$[-]$	S_{ref}	Wing surface area reference aircraft	$[m^2]$
$C_{l_{M=0}}$	Sectional lift coefficient at zero Mach number	$[-]$	S_x	Surface area [x = lifting surface area of interest]	$[m^2]$
C_m	Moment coefficient	$[-]$	s_x	Distance [x = distance of interest]	$[m]$
$C_{m_{ac}}$	Moment coefficient at aerodynamic centre	$[-]$	SF_j	Speed factor at panel j	$[-]$
C_{m_0}	Moment coefficient wing at zero-lift angle of attack	$[-]$	T	Thrust	$[N]$
C_{n_β}	Directional-stability coefficient	$[-]$	T_c	Thrust coefficient = $\frac{2T}{\rho V_\infty^2 \pi r_{tip}^2}$	$[-]$
$C_{Y_{\alpha_v}}$	Lift gradient vertical tail	$[-]$	TOP	Take off parameter	$[ft \cdot /s]$
c_r	Root thickness	$[m]$	t	Time	$[s]$
c	Chord length	$[m]$	$\frac{t}{c}$	Thickness to chord ratio	$[-]$
$\bar{c}$	Mean aerodynamic chord length	$[m]$	t_r	Root thickness	$[m]$

Symbol	Definition	Unit	Symbol	Definition	Unit
c_g	Mean geometric chord length	$[m]$	U	Energy density	$[J]$
c'	Extended chord length with deflected flaps	$[m]$	V_∞	Free stream velocity	$[m/s]$
c_f	length of flap chord	$[m]$	V_{eff}	Effective velocity	$[m/s]$
dA_j	Area of panel j	$[m^2]$	$V_{u,p,j}$	Velocity induced in u-direction by all propellers on panel j	$[m/s]$
d_x	Diameter [x = diameter of component at interest] $[m]$	$[m^2]$			
D_p	Propeller diameter	$[m]$	$V_{u,p_{m\to i}}$	Velocity induced in u-direction by propeller m on section i	$[m/s]$
E	Energy	$[J]$	$V_{u,j}$	Velocity in u-direction over panel j	$[m/s]$
e	Oswald efficiency factor	$[-]$	$V_{u,eff,j}$	Effective velocity in u-direction over panel j	$[m/s]$
FC	Fuel consumption	$[kg/km]$	V_∞	Free stream velocity	$[m/s]$
g	Gravitational constant	$[m/s^2]$	V_h	Velocity at canard	$[m/s]$
i	Wing section numbering	$[-]$	W_x	Weight [x= component]	$[kg]$
k_x	Component constant [x = component]	$[-]$	W/S	Wing Loading	$[N/m^2]$
LF	landing factor	$[s^2/m]$	$\hat{\imath}$	Unit vector in x-direction	$[-]$
l_n	Distance tip of engine to LEMAC	m	$\bar{X}_{x1}$	Absolute distance from the nose of the aircraft [x1 = component of the aircraft]	$[m]$
l_h	Distance between quarter-chords canard and wing	m	$\hat{X}_{x1}$	Absolute distance from the LEMAC of the wing [x1 = component of the aircraft]	$[m]$
α	Angle of attack	$[^\circ]$	κ	Technology factor	$[-]$
α_{0L}	Zero lift angle of attack	$[^\circ]$	Λ_x	Sweep angle [x = position of sweep]	$[deg]$
$\alpha_{eff,j}$	Effective angle of attack at panel j	$[rad]$	λ	Taper ratio	$[-]$
$\alpha_{ind,j}$	Induced angle of attack at panel j	$[rad]$	μ_{PG}	Prantl-Glauert compressibility correction	$[-]$
$\alpha_{loc,j}$	Local angle of attack at panel j	$[rad]$	μ	Empirical flap pitching moment coefficient	$[-]$
$\alpha_{vlm,j}$	VLM angle of attack at panel j	$[rad]$	Φ	Ratio of battery output over total energy	$[-]$
β	Ratio of jet velocity to free stream velocity	$[-]$	ϕ_j	Quarter chord sweep of panel j	$[rad]$
β	Twist angle	$[rad]$	ρ_x	Density [x = phase]	$[kg/m^3]$
Γ_k	Circulation of horseshoe vortex k	$[m^2/s]$	φ	Ratio of secondary shaft power over total power	$[-]$
η_x	Efficiency [x = component]	$[-]$	φ	Propeller flow angle	$[rad]$
ϵ	Downwash angle	$[^\circ]$	χ	Power fraction by wingtip propellers	$[-]$
θ	Pitch angle	$[^\circ]$	ψ	Lateral tip-over limit	$[^\circ]$
θ	As subscript: in rotational direction	$[-]$	Ω	Rotational velocity	$[rad/s]$

Contents

Part I

Problem Context

1 Introduction

In the past few decades, there has been a large increase in aviation emissions due to the large growth of the aviation industry[1]. CO_2, NO_x, and sulphate emissions have contributed largely to climate change, in the form of radiative forcing, and air pollution in the form of contrails, cloud-forming, and aerosols [5]. The only way to reduce these emissions is to start operating aircraft that emit less or no greenhouse gasses, and the reduction in these emissions will have to be greater than the growth of the market[2]. In order to reach lower emissions, new energy sources have to be explored, which also heavily influence the design methods and operation of aircraft. Distributed propulsion is one of the design options that is opened up by integrating (hybrid)-electric powertrains, and it can enhance the airflow over the wing allowing the wing to be downsized [6]. This illustrates the need for new aircraft. To make this goal possible, this document continues to build on the mission need statement and the project objective statement for the design synthesis exercises, which were stated in the Project Plan report [7].

Mission Need Statement
"To provide a regional commuter aircraft to transport at least 50 passengers including luggage, which is financially competitive to the ATR 42-600 and comparable to ground transport for direct operating cost. Further, it needs to reduce the CO_2 and NO_X emissions compared to the ATR 42-600 by 75% and 90% respectively, to have a sustainable end-of-life solution, have a design payload of at least 5300 $[kg]$ and operate at DOC range of at least 400 $[km]$ including reserves."

Project Objective Statement
"To design a regional aircraft leveraging distributed (hybrid)-electric propulsion and regenerative capability, with improved sustainability compared to an ATR 42-600 and driven by requirements from the EU-funded FutPrInt50 project, by ten students in ten weeks."

Electric powertrains enable the use of distributed propulsion as mentioned in the project objective statement, which in turn widens the design space of the aircraft. The placement of the propulsion system can be used to influence the direct local aerodynamics, stability and control parameters, and weight distribution. Furthermore, the use of electric propulsion opens up the possibility to regenerate energy during descent, by using the electric motors as generators and essentially reversing the current flow in the powertrain system to recharge the power storage [8].

To analyse the climate impact of the designed aircraft, the ATR 42-600 aircraft, which entered service in 2012, is used as a benchmark. Specific requirements have been set up regarding the reduction in emissions compared to the benchmark, which covers both in-flight emissions and ground operation emissions.

This report aims to provide the final progress of the project. It is delivered after nine weeks of work and shows the stakeholders the complete design process. The contents of this report were orally presented in the Final Review, scheduled on Monday, June 20th, 2022.

[1] https://www.eesi.org/papers/view/fact-sheet-the-growth-in-greenhouse-gas-emissions-from-commercial-aviation, last consulted June 21, 2022

[2] https://ec.europa.eu/clima/eu-action/transport-emissions/reducing-emissions-aviation_en, last consulted June 21, 2022

The report is divided into three parts, namely Problem Context, Aircraft Design, and Entering Into Service. In the first part, multiple aspects of the design problem are analysed and reported. The market analysis is presented in Chapter 2, a functional analysis and requirements are presented in Chapter 3, and a risk analysis is presented in Chapter 4. Finally, a summary of the concept generation and trade-off that was performed previously is given in Chapter 5.

The second part, called Aircraft Design, presents all technical design work that has been performed on the chosen aircraft concept. The first chapter, Chapter 6, presents all preliminary sizing procedures and the design iteration process. After that, the remaining chapters are categorised per aircraft system, starting with the wing design and powertrain design in Chapter 7 and Chapter 8. Thereafter, the propulsion system design is presented in Chapter 9. The longitudinal placement of the wing and the canard sizing are discussed in Chapter 10. The last chapter on aircraft design, Chapter 11, presents some limited structural considerations, including wing truss placement and material selection. The second part is concluded with two chapters which are more analysis based rather than design-based, Chapter 12 and Chapter 13. They discuss several performance parameters and compliance with the requirements, respectively.

The third part gathers all work that has been done regarding the future of this aircraft. It starts by giving a global timeline towards the detailed design, certification, and a production plan in Chapter 14. Afterwards, the sustainable development of the aircraft is discussed in Chapter 15, and a detailed plan for ground operations is presented in Chapter 16. The last chapter of this report, Chapter 17, presents a financial analysis that was performed, containing calculations on the manufacturer's break-even point and the airline's return on investment. To close off this document, a conclusion and recommendations are included in Chapter 18 and Chapter 19.

2
Market Analysis

Before embarking on the technical design of the project, its relevance to the market was analysed, both on a sustainable and economic level. Two different markets were identified; the first and most straightforward market the aircraft must compete in is the regional transport aircraft market, where airlines buy regional aircraft from aircraft manufacturers. The analysis of this market is presented in Section 2.1. The second market to consider is the regional transportation market, presented in Section 2.2. This is the market where end-consumers buy services allowing them to travel over regional distances. Finally, an economic SWOT analysis was performed, which is shown in Section 2.3.

2.1. Regional Transport Aircraft Market

The regional transport aircraft market is defined as the market where airlines buy regional aircraft from the manufacturer. In this market both turboprops and regional jets form the products, and the customer can buy the product to either operate point-to-point or in a hub-and-spoke model.

Common passenger amounts for these aircraft range from 20 to 100 people. At the start of 2020, regional aircraft accounted for 12% of all available seat kilometres, and about 9300 regional aircraft were in operation. Next to this, the regional transport aircraft market is unique in the sense that it allows connecting smaller hubs to the world's aviation network. Regional aircraft require shorter airstrips, less infrastructure and are therefore able to serve more regional airports - a significant amount of 36% of all airports rely solely on turboprop aircraft.[1]

Research by Oliver Wyman[2] indicates that the compound annual growth rate for this market between 2020 and 2032 is equivalent to 2.7% for all classes of aircraft and 0.8% for turboprop aircraft. Thus, it can be concluded that indeed for both, significant annual growth can be expected. Additionally, the interest in turboprop aircraft in the future can be confirmed as well by the number of deliveries of turboprop aircraft by ATR as ATR has a large share in the turboprop aircraft market[3]. ATR had 75% of the turboprop aircraft orders between 2010 and 2017[4]. Furthermore, it is of great importance to recognize the technical development in terms of sustainability of aviation in the future as sustainability becomes increasingly urgent in aviation[5]. This confirms the relevance of developing new aircraft for any market.

For the analysis of the competition, current and future regional jets and turboprops must be considered. For the current regional jets, the top five (by number in service and orders placed) regional jets and turboprops with similar capacity are tabulated in Table 2.1. Future promising regional aircraft of which at least two parameters are known are tabulated in Table 2.2. Relevant parameters include the number of seats, range, take-off length and cost per hour. Cost per hour includes fixed costs and variable costs. These values are based on 450 hours of operation annually.

[1] https://www.clean-aviation.eu/clean-sky-2/programme-overview-and-structure/clean-sky-2-structure/regional-aircraft, last consulted April 26, 2022

[2] https://www.oliverwyman.com/our-expertise/insights/2022/feb/global-fleet-and-mro-market-forecast-2022-2032.html, last consulted April 26, 2022

[3] http://www.atr-aircraft.com/wp-content/uploads/2020/09/2018-MarketForecast__Digital.pdf, last consulted April 26, 2022

[4] https://www.atr-aircraft.com/wp-content/uploads/2020/07/2018_06_atr_42_marketing_booklet_152.pdf, last consulted April 26, 2022

[5] https://www.destination2050.eu/wp-content/uploads/2021/03/Destination2050_Report.pdf, last consulted April 26, 2022

Table 2.1: Current regional transport aircraft

Model	**Seats**	**Range** $[km]$	**Take-off Length** $[m]$	**Cost per hour** $[\$/h]$
ATR 42	30-50	1326	1165[6]	2976.27
ATR 72	72	1404	1383[7]	2902.71[8]
Bombardier CRJ Series	50-104	2593-3148	1605-2030	3891.32[9]
Embraer ERJ Family	37-50	3060-3700	1760-2270	4120.77[10]
Saab 340	34	870	1285	2242.04[11]

Table 2.1 shows that most current regional aircraft are designed for more than 50 pax and a larger range than 800 $[km]$, which is what the to-be-designed aircraft will be sized for (see Chapter 3). This indicates market potential; it means that the new aircraft will be able to perform this shorter mission more efficiently than most existing aircraft. It will also open up the possibility to fly at more airfields because of its short take-off and landing length, and make flying cheaper because of its lower expected fuel costs.

Table 2.2: Future regional transport aircraft

Model	**Seats**	**Range** $[km]$	**Take-off Length** $[m]$
Heart Aerospace ES-19	19	400	750
Embraer E50-H2GT	35-50	826	NA
Eviation Alice	9	815	792
Airbus Hydrogen Turboprop[12]	<100	>1852	NA

Table 2.2 shows that the Embraer E50-H2GT is the most similar aircraft as for range and capacity. However, this aircraft will enter into service in 2040 instead of 2035. The Airbus Hydrogen Turboprop does have a planned entry into service in 2035, but its range is more than double the harmonic range of the aircraft of this project. Also, no information on operating cost is known for any of the aircraft. Therefore, no real conclusions could be drawn from this information.

2.2. Regional Transportation Market

The regional transportation market is defined as the market where end consumers buy services allowing them to travel over regional distances. The products sold in this market are therefore the tickets, which can be for multiple modes of transport. The modes of transport analysed in this case include aircraft, trains, cars, buses, and boats. From research by ATR[13] it follows that a significant increase in regional travel is expected, with numbers up to a 47% growth between 2017 and 2037 in China. This data does need to be interpreted with caution, as it is provided by a commercial and non-objective party.

The market size is measured in passenger kilometres and is found to be as large as 20,000 billion passenger-kilometres in 2020. It is expected to grow to 70,000 billion by 2030, and 100,000 billion in 2050, both for the most conservative estimates made by the International Transport Forum in 2021 [9].

To examine the different regional transportation methods, an example is used to clarify the different modes of transportation. For this analysis of different transport modes, the journey from Amsterdam to London was reviewed. For this comparison, the sample date was chosen as July 9, 2022, for travel, and the corresponding prices were examined on April 28, 2022. The cost in euros is the price a traveller would pay for the

[6] https://www.atr-aircraft.com/wp-content/uploads/2020/07/2018_06_atr_42_marketing_booklet_152.pdf, last consulted April 28, 2022

[7] https://customer.janes.com/Janes/Display/JAWA0440-JAWA#ATR%2072-600, last consulted April 28, 2022

[8] https://www.aircraftcostcalculator.com/AircraftOperatingCosts/477/ATR+72-600, last consulted April 28, 2022

[9] https://www.aircraftcostcalculator.com/AircraftOperatingCosts/467/Bombardier+CRJ200+ER, last consulted April 28, 2022

[10] https://www.aircraftcostcalculator.com/AircraftOperatingCosts/178/Embraer+ERJ-145ER, last consulted April 28, 2022

[11] https://www.aircraftcostcalculator.com/AircraftOperatingCosts/60/Saab+SF+340, last consulted April 28, 2022

[12] https://www.airbus.com/en/innovation/zero-emission/hydrogen/zeroe

[13] https://www.atr-aircraft.com/wp-content/uploads/2020/09/2018-MarketForecast_Digital.pdf, last consulted April 29, 2022

journey, obtained from Omio[14]. Furthermore, the amount of CO_2 emitted in kilograms per passenger was estimated using EcoTree[15]. For the boat, a different route was examined, as it is not possible to get from Amsterdam to London solely by boat. Instead, the trip from Hoek van Holland to Harwich was reviewed[16].

Table 2.3: Regional transport modes comparison

Transportion mode	**Distance** $[km]$	**Travel time** $[hr]$	**Cost** $[€/km]$	**Emission CO_2** $[kg/km]$
Car (1 pers.)	540	7	0.156	0.167
Car (4 pers.)	540	7	0.039	0.042
Boat	240	6.5	0.25	0.111[17]
Aircraft	372	1.08	0.124	0.161
Train	355	4.25	0.183	0.002
Bus	540	10.5	0.076	0.111

As shown in Table 2.3 the emission for the train is much lower than for any of the other transport methods. However, the cost is much higher. Furthermore, the cost is the lowest for a shared car. In order to be time-efficient, travelling per aircraft would be the most attractive. Considering that if an aircraft would be less or even not emitting, travelling by aircraft would be the most attractive option by far, especially if the cost would not be much higher than it currently is.

2.3. SWOT Analysis

Finally, a SWOT analysis for the regional transport aircraft with regenerative propulsion is presented in Figure 2.1. This SWOT analysis is about the strengths, weaknesses, opportunities, and threats regarding the aircraft and incorporates its relevance to both the regional transport aircraft market and the regional transportation market.

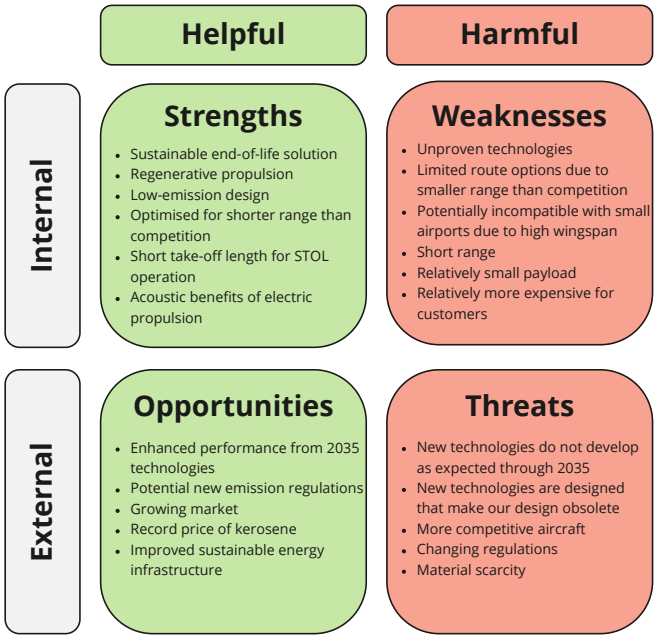

Figure 2.1: Market-oriented SWOT analysis of to-be-designed aircraft

[14]https://www.omio.com/search-frontend/results/L65A18BA51DE14AA893D8DDA11140C386/train?locale=en, last consulted April 28th, 2022

[15]https://ecotree.green/en/calculate-car-co2#result, https://calculator.carbonfootprint.com/calculator.aspx?tab=4, last consulted April 28, 2022

[16]shorturl.at/fjstI, last consulted April 28, 2022

3

Functional Analysis & Requirements

After the economic relevance of the to-be-designed aircraft was proven in Chapter 2, its intended use was further investigated. A mission was defined for which the aircraft would be optimised, following the top-level requirements. By analysing the mission profile, see Section 3.1, a list of functions was set up, containing everything the aircraft has to be able to do. Section 3.2 elaborates on the regenerative strategy and a full overview of the functional analysis is presented in Section 3.3. These functions were expanded into a list of requirements, which is shown in Section 3.4.

3.1. Mission Description

In order to obtain the optimal design solution for a mission, the mission profile must be defined and analysed. The mission profile affects multiple design and performance aspects of the aircraft, such as its sizing, energy consumption, emissions and operating cost. Moreover, a mission definition is necessary for defining a regenerative braking strategy.

The mission profile for this aircraft follows mainly from the top-level requirements [1] and can be divided into flight phases. Namely taxi, take-off, climb, cruise, descent, landing, loiter and diversion. The top-level requirements state that the aircraft must be able to fly a harmonic range of $800\ [km]$ with an additional $185\ [km]$ of diversion distance and $45\ [min]$ of loiter time [1]. This mission is visualised in Figure 3.1. Furthermore, the aircraft must be optimised for a DOC mission with a range of $400\ [km]$, where loiter and diversion are not included. This mission is visualised in Figure 3.2.

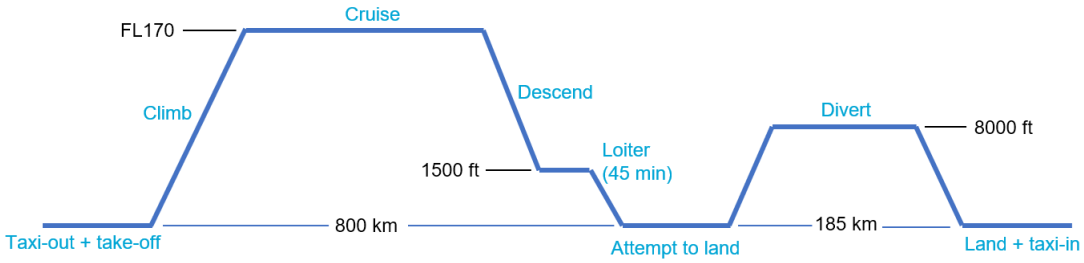

Figure 3.1: The mission profile for harmonic range.

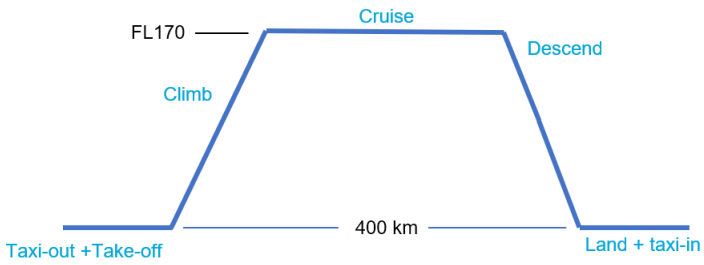

Figure 3.2: The mission profile for DOC range.

3.2. Regenerative Braking Strategy

At this stage, it was important to set up objectives for the use of regenerative braking. While the exact regeneration performance was not known yet, some general considerations must be taken into account in the design process. As the use of regenerative braking during descent increases the aircraft drag, the descent rate increases and the flight path becomes steeper. In order to still travel the same distance, the cruise phase would have to be extended. This fundamental principle of regenerative braking indicates that saving mission energy is not a viable objective. The most efficient descent is gliding, using zero power during descent. These effects are analysed and shown in Chapter 12.

An exception to this is when a certain approach angle to an airfield requires the aircraft to fly past the airfield first, after which it turns around and lands on the airstrip. In this case, being able to descend quicker might enable to reduce the length of the downwind leg, since a steeper descent requires a shorter horizontal distance flown past the airfield, potentially reducing mission energy.

However, there is still potential to explore regenerative braking. The increased descent angle can be used to fly a more preferable mission profile; it could save mission time, as the high cruise speed is extended, and it could be used to limit fly-over noise, by passing over a populated area at a higher altitude. Next to this, although the overall mission energy increases slightly by regenerating, it does allow the aircraft to land with energy left in the battery, as during the cruise phase the aircraft is powered entirely by liquid hydrogen. This could be used to taxi emission-free, or reduce turnaround time.

In further parts of the report, the usefulness of regenerative braking will be examined. Section 9.3 explains on a propeller level how a negative thrust is generated and Section 12.2 examines the regeneration performance itself. Also, the influence of regeneration on the direct operating costs was analysed, which is shown in Section 17.3.

3.3. Functional Analysis

After having analysed the mission profile, all functions that the aircraft has to perform could be derived. A Functional Flow Diagram is a flowchart indicating these functions for a design mission, ordered sequentially. Arrows indicate a dependency; the block following after an arrow can only be started after the previous block was completed. Logical *AND*/*OR* symbols are used to indicate parallel functions which are either required or optional. The Functional Flow Diagram created for this mission is presented in Figure 3.3.

The functions set up in the Functional Flow Diagram can also be categorized by their respective system, allowing for the removal of duplicate functions and therefore effective derivation of requirements. In this project, the categories distinguished are globally split up into the ground operations phase and the flight phase. The ground operations phase branch is split up into a stationary and dynamic branch, i.e. stationary ground operations and ground manoeuvring. The flight phase is further split up into take-off, climb-out, cruise, descent, and landing. The Functional Breakdown Diagram is presented in Figure 3.4.

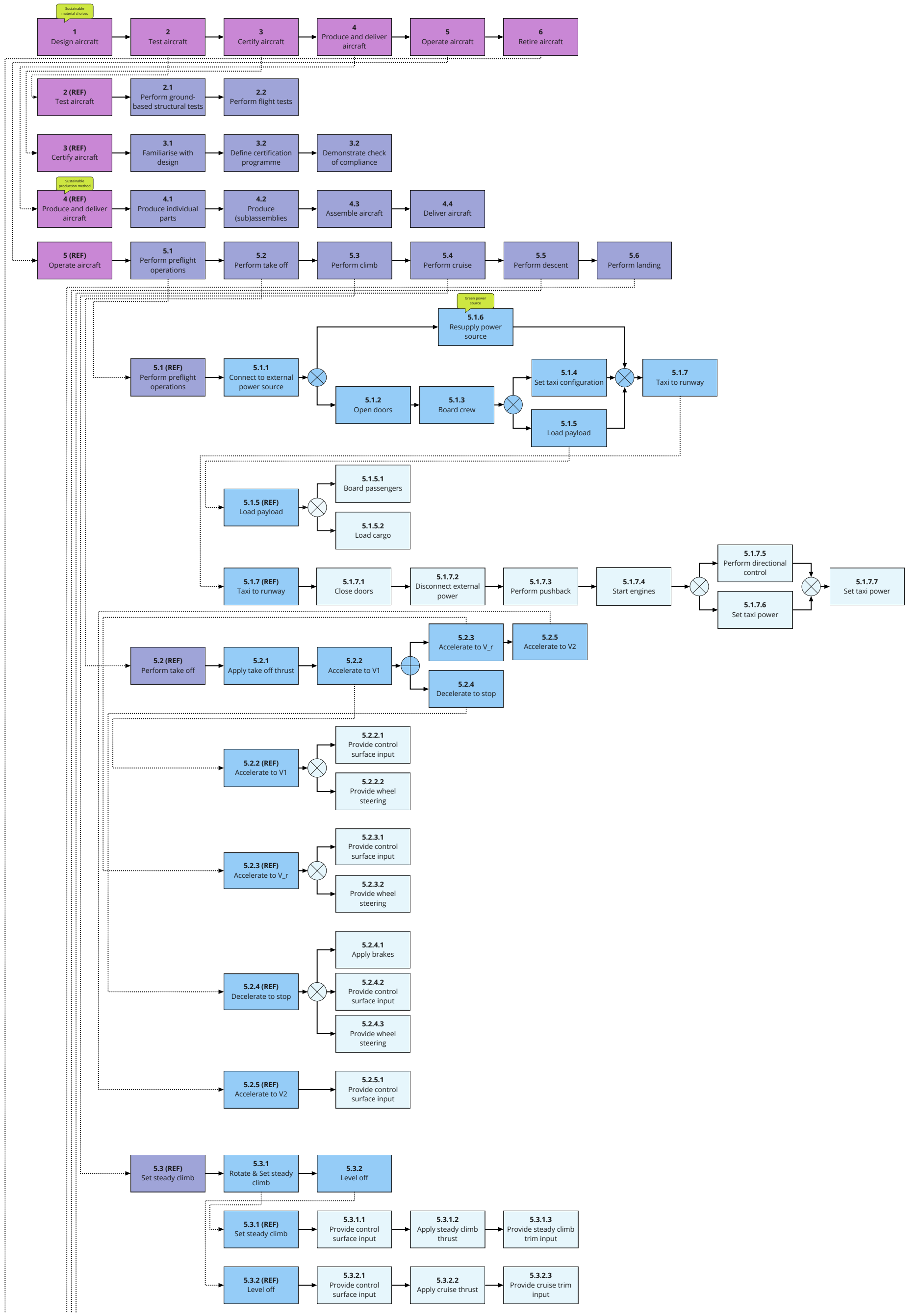
Sustainable material choices
1 Design aircraft
2 Test aircraft
3 Certify aircraft
4 Produce and deliver aircraft
5 Operate aircraft
6 Retire aircraft
2 (REF) Test aircraft
2.1 Perform ground-based structural tests
2.2 Perform flight tests
3 (REF) Certify aircraft
3.1 Familiarise with design
3.2 Define certification programme
3.2 Demonstrate check of compliance
Sustainable production method
4 (REF) Produce and deliver aircraft
4.1 Produce individual parts
4.2 Produce (sub)assemblies
4.3 Assemble aircraft
4.4 Deliver aircraft
5 (REF) Operate aircraft
5.1 Perform preflight operations
5.2 Perform take off
5.3 Perform climb
5.4 Perform cruise
5.5 Perform descent
5.6 Perform landing
Green power source
5.1.6 Resupply power source
5.1 (REF) Perform preflight operations
5.1.1 Connect to external power source
5.1.2 Open doors
5.1.3 Board crew
5.1.4 Set taxi configuration
5.1.5 Load payload
5.1.7 Taxi to runway
5.1.5 (REF) Load payload
5.1.5.1 Board passengers
5.1.5.2 Load cargo
5.1.7 (REF) Taxi to runway
5.1.7.1 Close doors
5.1.7.2 Disconnect external power
5.1.7.3 Perform pushback
5.1.7.4 Start engines
5.1.7.5 Perform directional control
5.1.7.6 Set taxi power
5.1.7.7 Set taxi power
5.2 (REF) Perform take off
5.2.1 Apply take off thrust
5.2.2 Accelerate to V1
5.2.3 Accelerate to V_r
5.2.5 Accelerate to V2
5.2.4 Decelerate to stop
5.2.2 (REF) Accelerate to V1
5.2.2.1 Provide control surface input
5.2.2.2 Provide wheel steering
5.2.3 (REF) Accelerate to V_r
5.2.3.1 Provide control surface input
5.2.3.2 Provide wheel steering
5.2.4 (REF) Decelerate to stop
5.2.4.1 Apply brakes
5.2.4.2 Provide control surface input
5.2.4.3 Provide wheel steering
5.2.5 (REF) Accelerate to V2
5.2.5.1 Provide control surface input
5.3 (REF) Set steady climb
5.3.1 Rotate & Set steady climb
5.3.2 Level off
5.3.1 (REF) Set steady climb
5.3.1.1 Provide control surface input
5.3.1.2 Apply steady climb thrust
5.3.1.3 Provide steady climb trim input
5.3.2 (REF) Level off
5.3.2.1 Provide control surface input
5.3.2.2 Apply cruise thrust
5.3.2.3 Provide cruise trim input

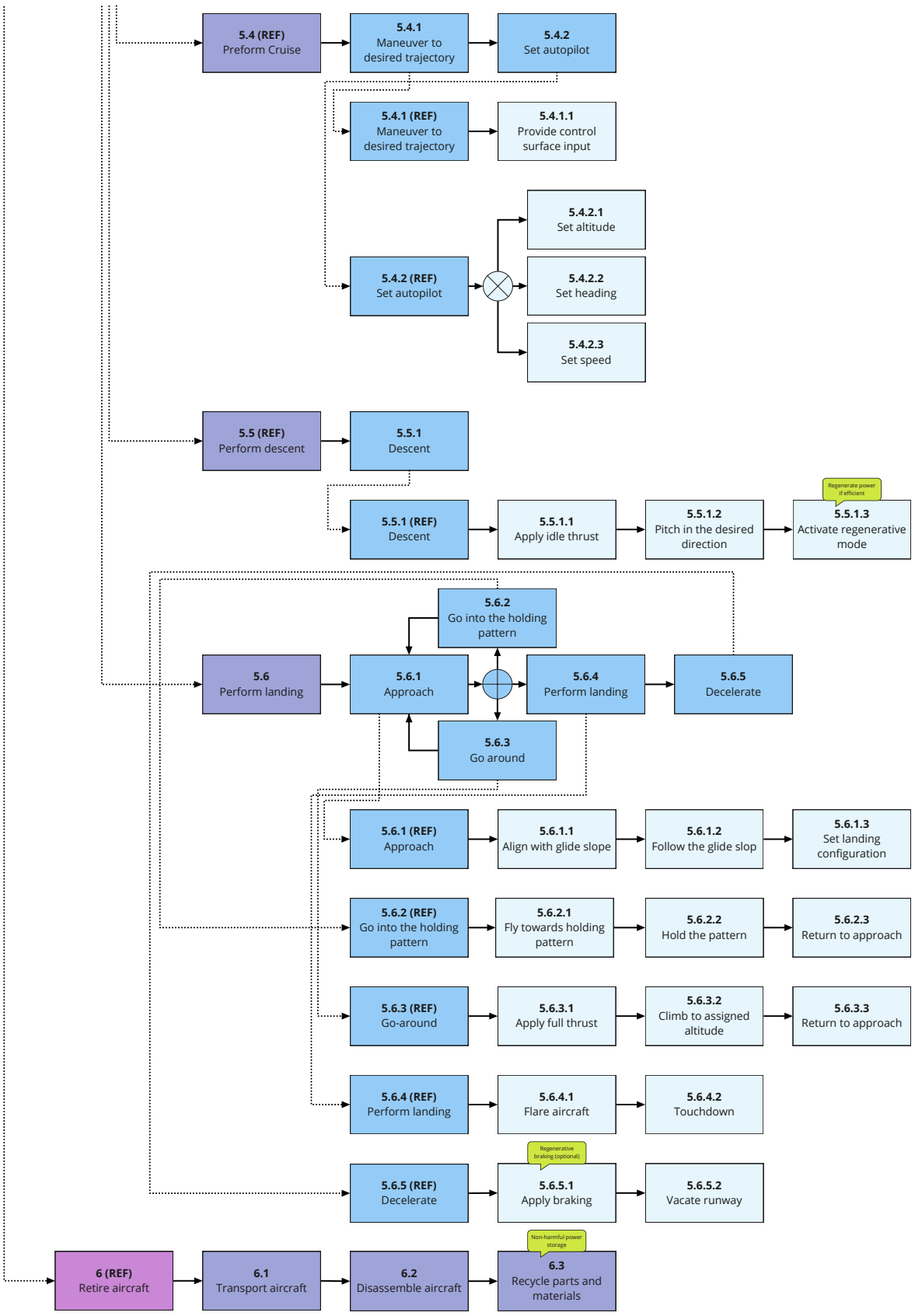

Figure 3.3: The functional flow diagram contains the functions the aircraft has to perform, ordered chronologically over a design mission profile.

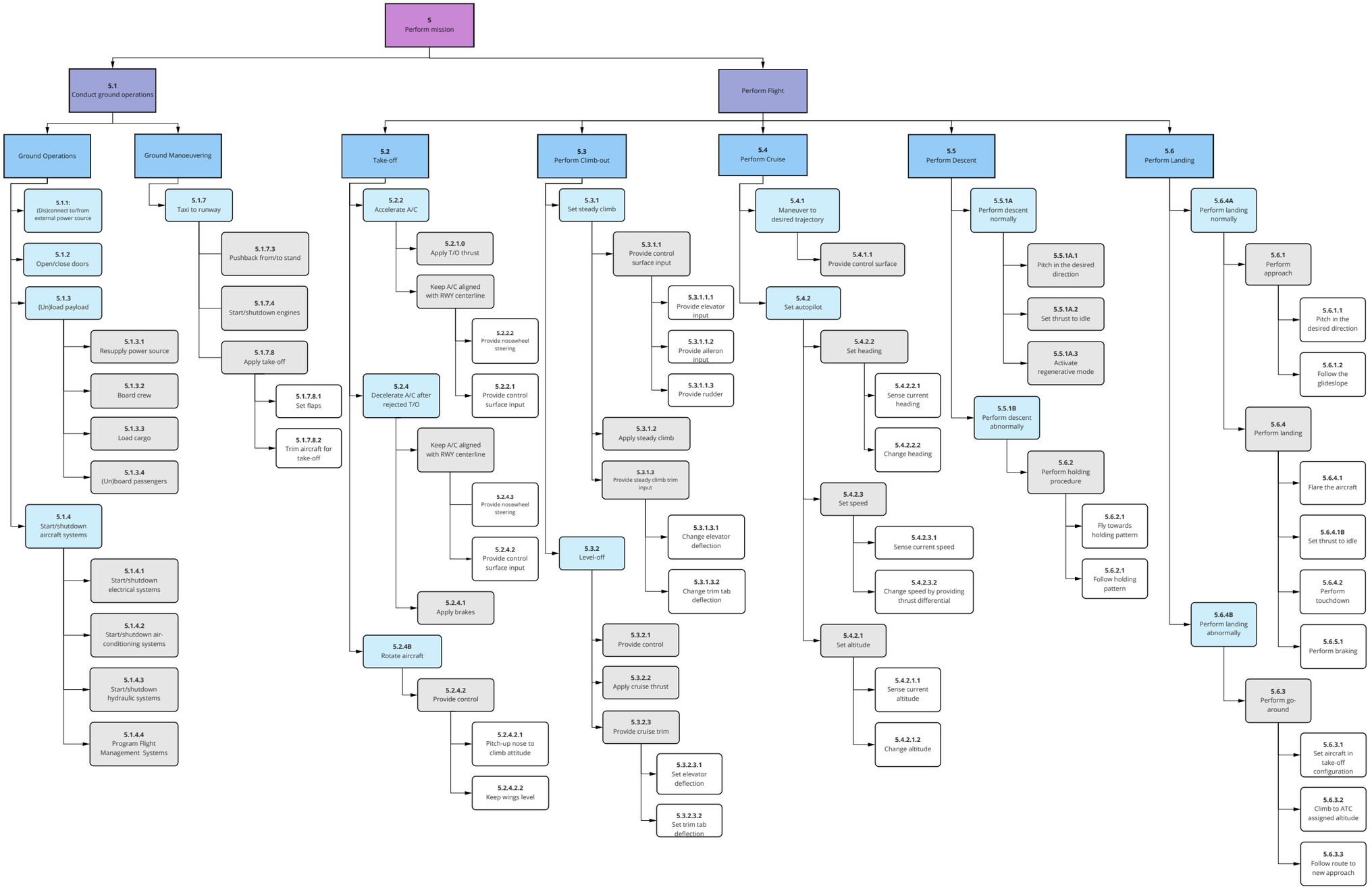

Figure 3.4: The functional breakdown diagram, containing the functions the aircraft has to perform, is categorised to eliminate double functions as much as possible.

3.4. Requirements

In order to set specific and measurable design targets, an extensive list of requirements was set up. The top-level requirements follow from the stakeholders, and more specific system and subsystem requirements were derived from the functional analysis presented above. Figure 3.5 presents the top-level requirements driving the design. An overview of the compliance of the aircraft to all of these requirements is given in Chapter 13.

Identifier	Description
Performance	
REQ-TOP-PER-01	The aircraft's design cruise speed shall be at least 450 km/h
REQ-TOP-PER-02	The aircraft's design cruise speed shall be at most 550 km/h
REQ-TOP-PER-03	The aircraft's design cruise speed shall be at least Mach 0.4
REQ-TOP-PER-04	The aircraft's design cruise speed shall be at most Mach 0.48
REQ-TOP-PER-05	The aircraft's design cruise altitude shall be FL170
REQ-TOP-PER-06	The aircraft's design payload shall be at least 5300 kg
REQ-TOP-PER-07	The aircraft shall be able to carry 50 passengers (at 95 kg per passenger)
REQ-TOP-PER-08	The aircraft shall be able to carry at least 500 kg of other payload when carrying 50 passengers
REQ-TOP-PER-09	The aircraft shall be able to carry a payload of at least 5800 kg
REQ-TOP-PER-10	The range at which Direct Operating Costs are evaluated shall be at least 400 km at cruise speed with design payload and reserve fuel
REQ-TOP-PER-11	The aircraft shall have a harmonic range of at least 800 km at cruise speed with design payload and reserve fuel
REQ-TOP-PER-12	The aircraft shall be able to carry the reserve fuel necessary to fly 185 km and stay in a 45 min holding pattern
REQ-TOP-PER-13	The aircraft shall have a range of 450 km with design payload when taking off from Denver International Airport
REQ-TOP-PER-14	The aircraft shall have a take-off field length of at most 1000 m at maximum take-off mass, sea level, from a paved runway, assuming international standard atmosphere
REQ-TOP-PER-15	The aircraft shall have a take-off field length of at most 800 m at sea level, from a paved runway, assuming international standard atmosphere, for short take-off and landing operation
REQ-TOP-PER-16	The aircraft's landing field length shall not be longer than the take-off field length
REQ-TOP-PER-17	The aircraft shall be able to attain a rate of climb of 1850 ft/min at maximum take-off mass, sea level, assuming international standard atmosphere
REQ-TOP-PER-18	The aircraft shall be able to attain a rate of climb of 300 ft/min at top of climb
REQ-TOP-PER-19	The aircraft shall be able to climb to cruise altitude within 12.7 min
REQ-TOP-PER-20	The aircraft shall be able to operate up to an altitude of 7620 m
REQ-TOP-PER-21	The aircraft shall have a wingspan of at most 36 m
REQ-TOP-PER-22	The aircraft shall have at least 1 lavatory
REQ-TOP-PER-23	The aircraft shall have at least 1 galley
REQ-TOP-PER-24	The flight shall be comfortable for all passengers and crew during nominal flight operations
Safety & Reliability	
REQ-TOP-SAF-01	The aircraft's one engine inoperative (or equivalent) service ceiling shall be higher than 4000 meters, at 95% of maximum take-off weight and ISA+10 conditions.
REQ-TOP-SAF-02	The aircraft's cabin altitude shall be lower than 2000 meters.
REQ-TOP-SAF-03	The aircraft's reliability shall be higher than 98%.
REQ-TOP-SAF-04	The aircraft shall be able to operate in all weather conditions.
REQ-TOP-SAF-05	The aircraft shall adhere to relevant certification standards and regulations.
REQ-TOP-SAF-06	The aircraft shall safely transport all passengers during all phases of flight and ground operations.
Sustainability	
REQ-TOP-SUS-01	The aircraft shall have a reduction in CO2 emmisions during operation of 75 % compared to an ATR 42-600 built in 2035.
REQ-TOP-SUS-02	The aircraft shall have a reduction in NOx emmisions during operation of 90 % compared to an ATR 42-600 built in 2035.
REQ-TOP-SUS-03	The aircraft shall emit no CO2 or NOx during ground operations.
REQ-TOP-SUS-04	The aircraft shall have a sustainable end-of-life solution.
REQ-TOP-SUS-05	The aircraft shall emit less noise than an ATR 42-600 built in 2035.
Financial	
REQ-TOP-FIN-01	The aircraft's direct operating cost (DOC) shall be competitive with ground transport.
REQ-TOP-FIN-02	The aircraft's production cost shall be mimimised by choosing materials and manufacturing methods appropriate for the annual production rate supported by the aircraft's potential market size
REQ-TOP-FIN-03	The aircraft shall have have turn-around time of less than 30 minutes after flying DOC range

Figure 3.5: Top Level Requirements

4

Technical Risk Assessment

In this chapter, the technical risks in this project are analysed. Executing a technical risk assessment is critical as not adequately mitigating risks will have large consequences for the project. This chapter covers the technical risks involved in the aircraft design and their mitigation strategies.

Table 4.1 lists the identified risks involved in the aircraft design. Each risk is labelled with a unique ID for ease of reference. Furthermore, each risk is assessed based on both its likelihood of occurrence and level of impact. The likelihood of occurrence is categorised into one of the following five categories: *very low (1)*, *low (2)*, *medium (3)*, *high (4)*, or *very high (5)*. The level of impact is categorised into one of the following five categories, from low to high: *trivial (1)*, *marginal (2)*, *serious (3)*, *critical (4)*, or *fatal (5)*.

Table 4.1: Risks associated with the aircraft design and their mitigation strategies. Abbreviations: GT = General Technical, PR = Propulsion, AE = Aerodynamics, PT = Powertrain, ST = Structures, FP = Flight Performance, ES = Electrical System, SC = Stability & Control, GO = Ground Operations, DS = Design Specific, Lik. = Likelihood, and Imp. = Impact.

ID	Risk Event	Consequence	Lik. (old)	Imp. (old)	Mitigation Strategy	Lik. (new)	Imp. (new)
GT-01	Key requirement not met	Failure to deliver a satisfactory product to the customer	2	5	Compliance with key requirements is checked at every design decision and after every design calculation, and adjustments to the design are made if necessary	1	5
GT-02	Other requirement not met	Failure to deliver a good product to the customer	3	4	Compliance with other requirements is monitored daily per department, and adjustments to the design are made if necessary	1	4
GT-03	Killer requirement not identified	Impossible to make consistent design	2	5	Killer requirements were discussed with the whole group, and comparisons were drawn to competitors	1	5
GT-04	Overrun of sustainability budgets	Failure to meet sustainability goals	4	4	Compliance with sustainability budgets is checked often & sustainability manager checks in with departments regularly about their compliance	2	4
GT-05	Underestimation of task duration	Having to work outside planned hours	5	2	Consistent check-ins about progress & adaptation of the Gantt chart, as well as adding time for overrunning tasks	3	1
GT-06	Selected technologies don't progress as expected for 2035	Product doesn't work as designed & year of service will be delayed	4	4	Confidence in technological progress will be taken into account when selecting design options & worst-case scenarios will be assessed	2	4
GT-07	New technologies developed that were not considered in the design	Design becomes obsolete before planned entry into operation	3	3	All technologies will be considered in every design stage when making design choices	2	3
GT-08	Airworthiness or environmental regulation changes	Aircraft fails certification	2	4	Aircraft will not simply be designed to the limits of airworthiness regulations, but slightly overdesigned for these requirements, and due to the customer's sustainability requirements, new environmental regulations are not an issue	1	3
GT-09	Increasing prices or material scarcity	Increase in prices or inability to use certain materials	3	4	Material cost (current + projected) and material scarcity are taken into account when choosing materials	1	4

PR-01	Bird strike	Possible failure of propulsion system	2	2	No mitigation necessary	2	2
PR-02	Propeller pitch controller fails	Reduced range and diversion needed	2	3	Redundancy built into controller system	1	2
PR-03	Propulsion vibrations cause resonance	Greatly increased loads on the aircraft	2	4	Vibrations from propulsion system qualitatively taken into account and safety margins will be used for load calculations	1	3
AE-01	Aerodynamic simulation software malfunction	Delays due to finding new software	3	2	Research all available aerodynamic simulation software beforehand, read about possible flaws and choose software based on this	2	2
AE-02	Excessive high stall speed	Cannot meet take-off and landing distance	3	4	Stall speed will be tracked in detail and a maximum allowable stall speed will be set	1	4
AE-04	Ice formation on the wing	Reduced aerodynamic performance	3	2	Install anti-icing system on wings	1	2
AE-05	Aerodynamic simulation software error	Incorrect aerodynamic data and reprogramming required	2	4	Verify and validate aerodynamic model	1	4
PT-01	Recharge / refuel failure	Aircraft cannot take-off on time	3	3	Add a back-up refuel system	2	2
PT-02	Energy storage system catches fire	Fire on board aircraft	3	4	Add extinguisher system, equip the aircraft with firewalls, and monitor important parameters	2	3
PT-03	Energy storage system explodes	Terminal aircraft failure	2	5	Include redundancy in the system and monitor critical parameters	1	4
PT-04	Regenerative mechanism fails	Aircraft not able to regenerate energy and mission time will increase	3	3	Redundancy will be built into the system and the regenerative propellers will run in parallel so that a failure of one does not constitute a failure of the whole system	2	2
PT-05	Engine failure	Forced emergency landing	2	4	Design for OEI	2	2
ST-01	Cabin pressure drops	Aircraft forced to significantly reduce altitude and divert	3	3	Add redundancy in the fuselage design	2	3
ST-02	Fatigue failure	Terminal aircraft failure	3	5	Perform fatigue analysis and prevent crack propagation	2	3

ST-03	Unexpected stress concentrations	Terminal aircraft failure	2	5	Apply safety factors to structure	2	3
ST-04	Excessive wing flexing	Higher structural loads in the wing	3	4	Pass wing bending test	1	4
FP-01	Unclearable obstacle after take-off	Terminal aircraft failure	3	5	Assure climb-out performance is sufficient to clear any obstacles that are allowed to be present	1	5
FP-02	Aborted landing	Time loss and higher energy usage	3	2	Assure sufficient take-off and climb-out performance in landing configuration to safely abort the landing and ensure sufficient endurance	3	1
FP-03	Aborted take-off	Time loss, potential replacement of brakes or tyres in case of very late abortion	3	2	Assure a low take-off speed to abort more easily, and assure sufficient braking performance that tyres and breaks will not need to be replaced after a late abortion	3	1
ES-01	Wire break	System failure	4	3	Apply wiring harnessing	1	3
ES-02	Faulty connector	System failure	3	3	Seal connectors against moisture	1	3
SC-01	Instability due to wrong loading	Terminal aircraft failure	3	5	Loading limits with a margin are specified, this means that even in the unlikely event of the loading exceeding the specified margins it will not immediately lead to an unstable aircraft	1	3
SC-02	Unstable eigenmotions	Controllability issues	3	3	Considerations are given to all eigenmotions, and it will be assessed whether they are unstable, the spiral is allowed to be slightly unstable, but will be assessed to see if it is easily correctable by the pilot	1	2
SC-03	Airleron reversal	Local angle of attack decrease, making it very difficult for the pilot to perform turns	4	4	Consideration will be given to the loads created by the ailerons and the wing will be designed such that twist is not severe enough for this phenomenon to occur	1	2
SC-04	Uncontrollable aircraft due to wrong loading	Unable to take-off	3	3	Loading limits with a margin are specified, thus even in the event that the loading exceeds the specified margins it will not immediately lead to an uncontrollable aircraft	1	2
GO-01	Electricity/fuel shortage	Aircraft temporarily unable to fly	4	4	Build fuel reserve and set up back up power supply system	2	2

GO-02	Aircraft lands at runway from which it can not take of	Aircraft has to be transported by truck or rail to another airport	1	4	Inform pilots about diverting options	1	1
GO-03	Inability to recharge / refuel with standard airport equipment	Unable to land at or divert to airports that do not have the necessary specialised equipment	4	4	Take into account recharge / refuel capabilities with standard airport equipment when designing energy storage system and if necessary restrict aircraft use to routes where suitable airports can be used for diversions or add an emergency energy storage system that can be recharged / refuelled with standard airport equipment	2	3
GO-04	Canard interfering with ground equipment such as jet bridge and ground vehicles	Canard becomes damaged	2	4	Possible mitigation strategies for preventing canard damage during ground operations include adding lights to the canard and giving extra training to ground staff	1	4
DS-01	Hydrogen tank leakage	Hydrogen leaks into aircraft and possible inflammation fire risk	2	4	Detailed tank pressure calculations to ensure correct and strong enough valves are used	1	4
DS-02	Battery thermal runaway	Battery overheats and possibly catches fire and explodes	3	4	Update battery certification for use in passenger flight & testing and analysing that no cell-to-cell propagation occurs	2	4
DS-03	Excessive unforeseen battery degradation	Rapid battery drainage, possibly making it impossible to fly	2	3	Careful battery capacity monitoring	1	3
DS-04	Canard deep stall	Aircraft's AOA continues to increase until canard also stalls, leading to a uncontrolled aircraft	3	5	Design the canard to stall before the main wing	1	5
DS-05	Clearance problems with wingtip mounted propellers	Increased risk of the propellers to be hit by debris or ground objects	3	3	Increased landing gear height	2	3
DS-06	Canard downwash	Wing experiences air at a lower angle of attack	4	1	Ensure a sufficient horizontal distance between the wing and the canard	2	1

5

Conceptual Design & Trade-off

This chapter gives a summary of the design choices that have been made up until the Midterm Report [10]. This first phase consisted of analyzing the design problem, listing design options for all subsystems, and combining these into a final concept. Section 5.1 presents the design options and how these are combined into complete concepts. After the concepts have been configured, a trade-off was performed, which is presented in Section 5.2. In Section 5.3 the limitations of the trade-off will be discussed.

5.1. Concept Generation

To arrive at complete aircraft concepts, a design option tree was set up to explore all possible options per subsystem of the aircraft. Many of these were incompatible with each other, but sixteen combinations were deemed feasible concepts. In order to reduce the number of concepts being considered, ten of these were discarded because it was evident that they would perform worse than a similar concept. This left six design concepts, shown in Table 5.1, which entered a more extensive trade-off.

Table 5.1: Morphological overview of remaining design concepts.

Aircraft Config.	Energy Storage	Energy Integration	Propulsion	Empennage Config.	Wing config.	ID
Conventional	Battery, HFC	Inside Wing (BAT), Under Wing (HFC)	EM	T-tail	High	CO-03
Tailless	Battery, HFC	Inside Wing (BAT), Aft Fuselage (HFC)	EM	Canard	Low	CO-09
Truss-braced	Battery	Inside Wing	EM	T-tail	High	CO-11
	Battery, HFC	Inside Wing (BAT), Aft Fuselage (HFC)	EM	T-tail	High	CO-14
			EM	Canard	High	CO-15
	Battery, SAF	Inside Wing (BAT), Inside Wing (SAF)	EM, TP	T-tail	High	CO-16

5.2. Concept Selection

The remaining concepts were analysed for the criteria shown in Table 5.2. For the mission energy and weight computations, an iterative script was set up, since these two criteria are dependent on each other. The emissions were calculated using emission factors per unit of mission energy used. These three calculations were all validated by running the scripts for a reference aircraft, the ATR 42-600, and comparing the results to public manufacturer data.

The four other criteria were included to ensure a fair trade-off since they were deemed to have a significant impact on the quality of a concept. They could only be analysed qualitatively, and rated on a scale of four categories, to prevent introducing a false feeling of accuracy. The four ratings used were *good*, *acceptable*, *poor*, and *unacceptable*.

[0]https://www.thrustcarbon.com/insights/how-to-calculate-emissions-from-a-ferry-journey, last consulted April 28, 2022

Table 5.2: Trade-off criteria and weights

Criteria	Method	Weight
Mission Energy	Calculation	4
Emissions	Calculation	4
Weight	Class I estimate	3
DOC	Estimation	3
TRL	Estimation	3
Ground operation	Estimation	2
Passenger comfort	Estimation	2

Table 5.3 shows the results of the trade-off. It was concluded that CO-09 and CO-15 scored equally well, but it was also found that the results of the trade-off were generally very similar, and might lacked detail. Therefore, the remaining two designs were assessed for feasibility, and based on that criterion CO-15 was chosen as a final concept. Section 5.3 discusses and verifies the trade-off result and method.

Table 5.3: Trade-off table of the selected concepts: green cells represent performance that meets requirements, blue represents correctable deficiencies, yellow represents risky but correctable deficiencies and red represents unacceptable performance. Pass. stands for passengers and Ops. for operations

Criteria / Concept	Mission Energy $[kWh]$	Emissions $[kg/pass. \cdot 100km]$	Weight $[kg]$	DOC $[€/hr]$	TRL	Ground Ops.	Pass. Comfort
CO-03 Conv, H2	10963	0	20772	2259.23	Acceptable	Acceptable	Acceptable
CO-09 Tailless, H2	10963	0	20772	2259.23	Acceptable	Acceptable	Good
CO-11 Truss, BAT	9148	0	35184	1542.62	Good	Poor	Acceptable
CO-14 Truss, H2	9378	0	19719	2012.48	Acceptable	Acceptable	Acceptable
CO-15 Truss, H2 C	9378	0	19719	2012.48	Acceptable	Acceptable	Good
CO-16 Truss, SAF	9071	0.439 CO_2 4.28E-4 NO_X	33030	1637.97	Good	Poor	Poor

5.3. Limitations of Trade-off

As mentioned in Section 5.2, the trade-off results turned out to be relatively similar between the different concepts. This was due to the lack of differentiation applied between the concepts. For example, some concepts used the same components, but with a different placement. This made it difficult to distinguish the concepts in weight and drag when evaluated at this conceptual level. This also followed from the sensitivity analysis, shown in Figure 5.1 and Figure 5.2.

Figure 5.1 shows the statistical distribution of the results when the weights of the criteria are increased or decreased by 1, and Figure 5.2 shows the distribution when the applied rating for the qualitative criteria is increased or decreased by one level. Both plots show similar results, with a concentrated distribution and similar rankings, indicating a relatively robust trade-off method. Lastly, a sensitivity analysis was performed without incorporating the qualitative criteria, to ensure that these 'subjective' criteria don't sway the result in a certain direction. The ranking was the same for the full trade-off as for only the quantitative trade-off, confirming the fairness of the trade-off.

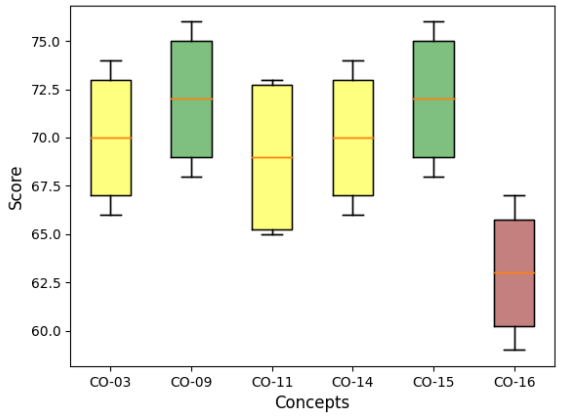

Figure 5.1: Box plot of the resulting scores of each concept from the weight sensitivity analysis

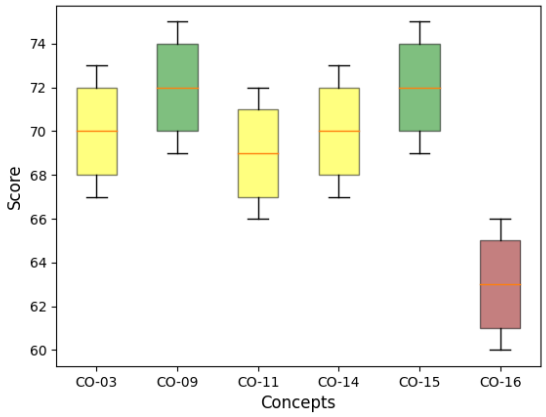

Figure 5.2: Box plot of the resulting scores of each concept from the qualitative score sensitivity analysis

Part II

Aircraft Design

6

Preliminary Design

Aircraft design is a highly interconnected design exercise, and one can wonder where to start. A common approach is to use empirical relations to estimate an initial weight and do a preliminary sizing of large aircraft systems. An iteration can be set up between this first estimation and a more detailed approach, which should converge to a final design. This is described in Section 6.1. In Section 6.2 the design point in the power loading diagram is determined and in Section 6.3 the wing is sized. The fuselage and the empennage are sized in Section 6.4 and Section 6.5 chapter describes this design process and the initial sizing steps.

6.1. Design Process

In order to achieve a well-assessed and converged design, the design process must be properly structured. This section explains the process that was used to arrive at the final design.

6.1.1. Design Process Overview

The basic design process is shown in Figure 6.1. As can be seen in the blue box, the first step was to determine the initial input variables. These either came directly from the requirements or were estimated. In the second step, depicted by the purple box, the input variables were used for preliminary sizing. The outputs of the preliminary sizing codes, were used as an input for the automated class-I/class-II estimation iteration, which is depicted by the yellow circle. Subsection 6.1.2 elaborates further on the relation between the detailed design calculations and the class-I/class-II iteration. The iteration outputs new variables - such as the mission energy - and updates some of the originally assumed input variables to newly calculated values. These are then used for the detailed designs such as sizing the tail for stability and control. The resulting design parameters now form the final design.

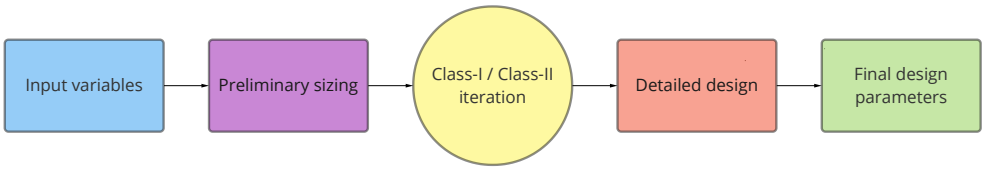

Figure 6.1: Overview of the design and sizing process.

However, in order to achieve a converged overall design, the results from the detailed design calculations should be fed back into the class-I/class-II iteration. The reasoning behind this is that there is a high interdependence between the different scripts and the effect they have on sizing. For example, the detailed propulsion system weight calculated in Subsection 9.2.3 obviously differs from the initially estimated propulsion system weight in Section 6.7, which was used for the OEW estimation. This means that the sum of the individual weight components does not add up to the OEW. In order to update the initially calculated OEW, the results from the detailed design calculations should be fed back into the class-I/class-II iteration. A schematic representation of this process is shown in Figure 6.2. Unfortunately, due to time constraints, this feedback loop from the detailed design to the class-I/class-II iteration was not implemented in this report.

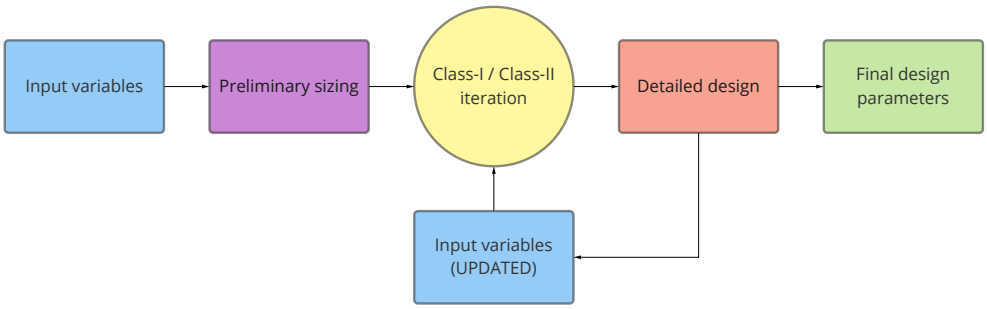

Figure 6.2: New iteration process based on Figure 6.1

6.1.2. Class-I/Class-II Iteration

The automated class-I/class-II iteration code as well as its relation with the preliminary sizing calculations mentioned above, are expanded into more detail in Figure 6.3 as a N2 chart. The yellow boxes on the diagonal are functions that were involved in the iteration process. Furthermore, the purple boxes above the N2 chart are the preliminary sizing calculations.

The goal of the iteration was to obtain a converged OEW and MTOW, in combination with corresponding sizing values. It was decided that, for a converged design, a maximum difference of 1% between the current and last estimations of both OEW and MTOW was required. The OEW and MTOW at each iteration are shown in Figure 6.4. It can be observed that the iteration converges after one iteration, where the errors for both OEW and MTOW are below 1%.

After convergence, weights and new dimensions for the aircraft components were obtained. These new values were used to perform detailed design calculations, which give the final weights and dimensions.

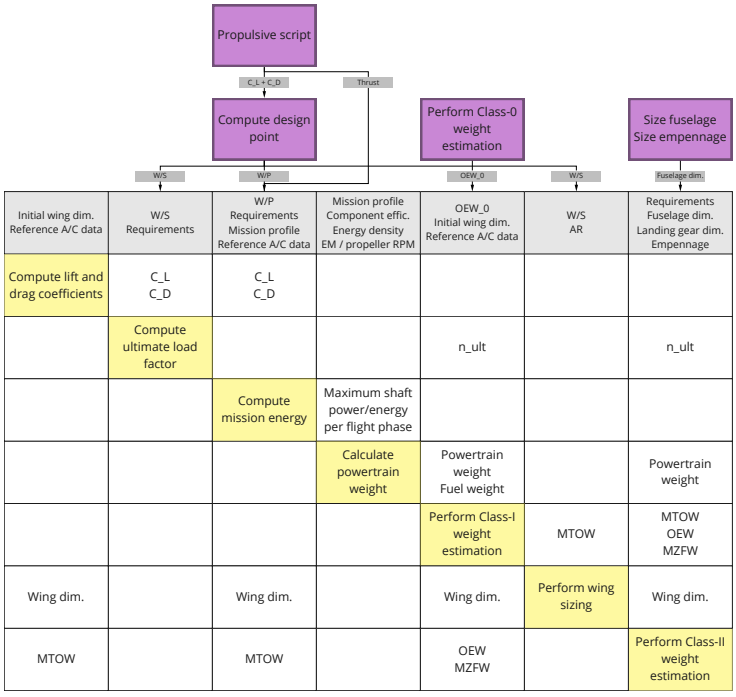

Figure 6.3: N2 chart of the iteration process. The purple boxes and the yellow boxes correspond to the detailed design calculations and functions involved in the class-I/class-II iteration respectively, as shown in Figure 6.1.

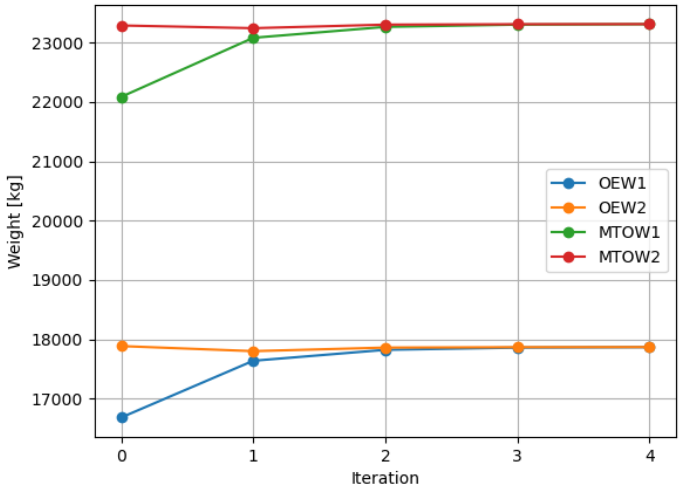

Figure 6.4: Convergence of the OEW and MTOW after one iteration. The suffixes 1 and 2 represent the class-I and class-II estimations of the OEW and MTOW respectively.

6.2. Power Loading & Wing Loading

As said in Section 6.1 one of the input computations is the design point. It determines the wing loading (W/S) and the power loading (W/P) of the aircraft for different moments in the mission profile. The determination of the design point is done using six different requirements. These requirements restricted the design space obtaining a maximum power loading and wing loading per flight phase. All of the equations derived in this chapter are based on Raymer [11].

Firstly, the aircraft has to be sized for stall speed. This is done using Equation 6.1 This sizing will constrain the design point on the wing loading value.

$$\frac{W}{S} = \frac{C_{Lmax} \cdot \rho \cdot \frac{s_{land}}{0.594008}}{2 \cdot LF} \tag{6.1}$$

Here, S_{land} comes from the requirements given, $C_{l_{max}}$ is approximated and the landing factor (LF) comes from Equation 6.2, with the input values from the ATR 42.

$$LF = \frac{s_{land_{ATR}}}{V^2_{land_{ATR}}} \tag{6.2}$$

Then the loading's need to be sized for take off. Which is done using Equation 6.3.

$$\frac{W}{P_{TO}} = \frac{TOP \cdot \eta_{prop_{TO}}}{\frac{W}{S}} \cdot C_{L_{TO}} \tag{6.3}$$

In this equation, TOP is the take-off parameter and can be determined using the Raymer method using the required take-off distance [11]. $\eta_{prop_{TO}}$ is the propulsive efficiency which was approximated together with the $C_{L_{TO}}$. What should be noted is that this was initially done using imperial units and afterwards converted to SI units.

The design point needed to be determined for the required cruise speed as well and was computed using Equation 6.4.

$$\frac{W}{P_{cr}} = 0.9 \cdot \eta_{prop_{cruise}} \cdot (\frac{C_{D_0} \cdot 0.5 \cdot \rho_{cr} \cdot V_{cr}^3}{\frac{W}{S}} + \frac{\frac{W}{S}}{\pi \cdot A \cdot e \cdot 0.5 \cdot \rho \cdot V_{cr}}) \tag{6.4}$$

The value 0.9 comes from the power setting, $\eta_{prop_{cruise}}$ is the propeller efficiency during cruise, the zero-lift drag, C_{D_0}, is approximated and the cruise velocity, and V_{cruise}, comes from the requirements. Furthermore, A is chosen and e is estimated.

The climb rate restriction follows the cruise restriction. For the climb rate, there were two requirements to be met. Namely the rate of climb at sea level and the rate of climb at cruise altitude. The restrictions of these two requirements were determined using Equation 6.5. For each requirement a different air density and rate of climb were implemented.

$$\frac{W}{P_{climb}} = \frac{\eta_{prop_{climb}}}{ROC + \frac{\sqrt{\frac{W \cdot 2}{S \cdot \rho}}}{1.345 \cdot \frac{(A \cdot e)^{3/4}}{C_{D_0}^{1/4}}}} \tag{6.5}$$

Where $\eta_{prop_{climb}}$ is the propulsive efficiency during climb and ROC is the required rate of climb. Subsequently, the restrictions were determined for the manoeuvring limits. This was done using Equation 6.6

$$\frac{W}{P_{manoeuvring}} = \frac{\eta_{prop_{cruise}}}{\frac{C_{D_0} \cdot 0.5 \cdot \rho_{cruise} \cdot V_{cruise}^3}{\frac{W}{S}} + \frac{\frac{W}{S} \cdot n_{lim}^2}{\pi \cdot A \cdot e \cdot 0.5 \cdot \rho_{cruise} \cdot V_{cruise}}} \tag{6.6}$$

Here, n_{lim} is the restrictive variable limit loading resulting from the maneuvering diagram. Finally, the restriction of the climb gradient requirement is computed, using Equation 6.7.

$$\frac{W}{P_{climbgrad}} = \frac{\eta_{P_{climb}}}{\sqrt{\frac{W}{S}}(\frac{c}{V} + \frac{C_D}{C_L})\sqrt{\frac{2}{\rho \cdot C_L}}} \tag{6.7}$$

In this equation, $\frac{c}{V}$ is the required climb gradient. Combining these restrictions Figure 6.5 can be set up. From this figure, it can be seen that the take-off and landing requirement are the most limiting restrictions. This gives the design point as shown by the grey point in the figure. The power loading and wing loading have the values 0.035197 $[N/W]$ and 3710 $[N/m^2]$ respectively, for which the to-be-designed aircraft will be sized.

Table 6.1: Power loading & wing loading parameters

Parameter	Values	Unit	Parameter	Values	Unit
A	16	$[-]$	TOP	330	$[\frac{bf^2}{ft^2 shp}]$
C_{D_0}	0.021	$[-]$	V_{cruise}	143.9	$[m/s]$
$C_{L_{max}}$	3.6	$[-]$	$\eta_{prop_{climb}}$	0.8	$[-]$
$C_{L_{TO}}$	1.74	$[-]$	$\eta_{prop_{cruise}}$	0.88	$[-]$
e	0.85	$[-]$	$\eta_{prop_{TO}}$	0.8	$[-]$
LF	0.594	$[s^2/m]$	ρ	1.225	$[kg/m^3]$
n_{lim}	3	$[-]$	ρ_{cruise}	0.72	$[kg/m^3]$
S_{land}	1000	$[m]$			

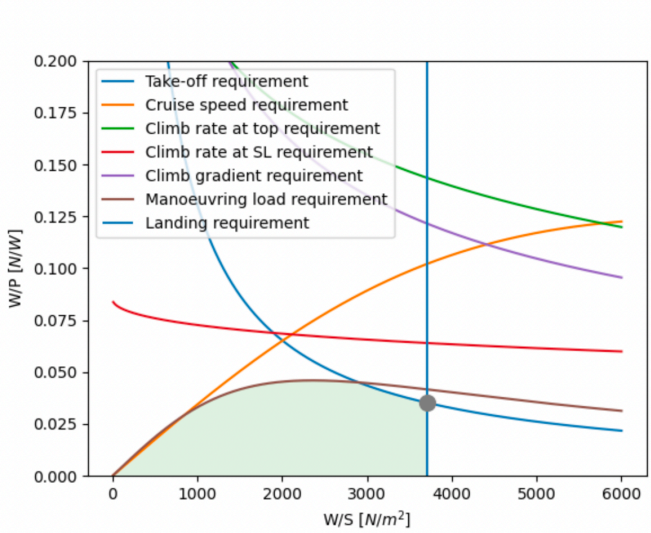

Figure 6.5: The power loading diagram.

6.3. Wing Sizing

The first step in the design of the wing was to size the wing planform, which could be performed using the wing loading discussed in Section 6.2 and the following initial values. As the cruise Mach number is not in the trans-sonic region, a quarter chord sweep angle of 0°and the optimal taper ratio associated with this sweep angle of 0.4 were chosen for the main wing [11]. The optimal taper ratio is chosen to create a quasi-elliptical lift distribution, however, for the designed aircraft the lift distribution will be affected by distributed propulsion. It was decided to keep a taper ratio which is optimal for non-distributed propulsion, as during the longest flight phase, cruise, the distributed propulsors would not be engaged, and thus the effect on the lift distribution from these propulsors is not present. The effect of the wingtip propellers on the lift distribution is neglected in this phase. From the sweep and taper ratio, as well as the wing loading computed and the aspect ratio assumed in the performance diagram, the rest of the geometry of the wing planform could be computed. This was done using the equations presented by Raymer [11], shown in Equation 6.8 to Equation 6.14. The results from this are provided in Table 6.2.

$$S_{wing} = \frac{MTOW}{W/S} \tag{6.8}$$

$$b = \sqrt{S_{wing} \cdot A} \tag{6.9}$$

$$c_r = \frac{2S_{wing}}{(1+\lambda)\,b} \tag{6.10}$$

$$c_t = \lambda c_r \tag{6.11}$$

$$\bar{c} = \frac{2c_r\left(1+\lambda+\lambda^2\right)}{3\,(1+\lambda)} \tag{6.12}$$

$$y_{\bar{c}} = \frac{b\,(1+2\lambda)}{6\,(1+\lambda)} \tag{6.13}$$

$$\text{`}\Lambda_{LE} = \Lambda_{0.25c} - \arctan\left(\frac{-0.25\,(c_r - c_t)}{\frac{b}{2}}\right) \tag{6.14}$$

Table 6.2: Wing sizing parameters

Parameter	Values	Unit
$MTOW$	228710	$[N]$

Table 6.2: Wing sizing parameters

Parameter	Values	Unit
W/S	3710	$[N/m^2]$
A	16	$[-]$
λ	0.4	$[-]$
$\Lambda_{0.25c}$	0	$[rad]$

Table 6.3: Wing sizing results

Parameter	Values	Unit
S_{wing}	61.63	$[m^2]$
b	31.41	$[m]$
c_{root}	2.62	$[m]$
c_{tip}	1.05	$[m]$
$\bar{c}$	2.04	$[m]$
$y_{\bar{c}}$	6.98	$[m]$
Λ_{LE}	0.021	$[rad]$

6.4. Fuselage Sizing

In this section, the sizing of the fuselage of the aircraft is performed. First, the cabin cross-section is created in Subsection 6.4.1. Second, the fuselage top and side view are presented in Subsection 6.4.2 to ensure sufficient cabin space and pilot visibility.

6.4.1. Cabin Cross-section

Sizing the cross-sectional area of the fuselage is performed by fitting all the necessary components into the smallest fuselage diameter. Minimising the circumference of the fuselage minimises the drag during flight [12]. The diameter of the fuselage is greatly influenced by the number of seats abreast, calculated in Equation 6.15. The outcome of 3.18 seats abreast was rounded up to four, since margins for storing batteries in the fuselage bottom were taken into account. Also, the placement of the hydrogen tanks in the fuselage will result in an elongated fuselage. Therefore, opting for a wider fuselage diameter is balanced by this effect [12].

$$n_{sa} = 0.45\sqrt{n_{pax}} \tag{6.15}$$

Four seats abreast resulted in a single-aisle configuration, which was sized at the minimum required width [13]. To ensure passenger comfort the height of the aisle was set to $1.8\ [m]$ [14]. Since the aircraft is designed for a short-range mission the seat width and pitch were sized to meet the minimal requirements [12]. Based on sitting postures the shoulder height was set to $0.95\ [m]$ and the head height to $1.5\ [m]$ [14]. By sketching this cross-sectional profile the smallest possible fuselage diameter of $2.726\ [m]$ was selected. For the outer diameter, $100\ [mm]$ was added to fit structural components [12], and the floor thickness was

set to $100\ [mm]$. The cabin will be pressurised at a height of $2000\ [m]$. Finally, the cargo compartments and overhead luggage compartments were sized in the available space leftover, resulting in an storage area of $1.1532\ [m^2]$. After sizing other subsystems the total amount of cargo that can be carried by the aircraft is $1056.4\ [kg]$. The cargo bay will be located in the forward section of the fuselage, in front of the battery pack.

6.4.2. Fuselage Top and Side View

The length of the cabin is constructed using Equation 6.16, in which the factor k_{cabin} is an empirical sizing factor [12]. The size of the flight deck is required to be at least $2.5\ [m]$ [14]. For the total cockpit length, an additional $1.5\ [m]$ was added for the implementation of the nosecone and rear fire door [12]. Based on the sizing of the hydrogen tank $2.2\ [m]$ of length should be added to the fuselage length. Finally, the length of the tail is estimated by an empirical relationship with the fuselage's outer diameter [12]. This estimation is scaled down due to the canard configuration, resulting in a tail length of $3\ [m]$. Adding all these lengths together results in a fuselage length of $26.17\ [m]$. The nosecone length coefficient was selected to be 1.5 [12] to match the size of the cockpit to provide sufficient cabin space. The tailcone length coefficient of 2.4 was selected [12]. To ensure sufficient cargo and luggage storage, the volume of the compartments is checked by using the length of the cylindrical part of the fuselage. The top view of the aircraft is depicted in Figure 6.6.

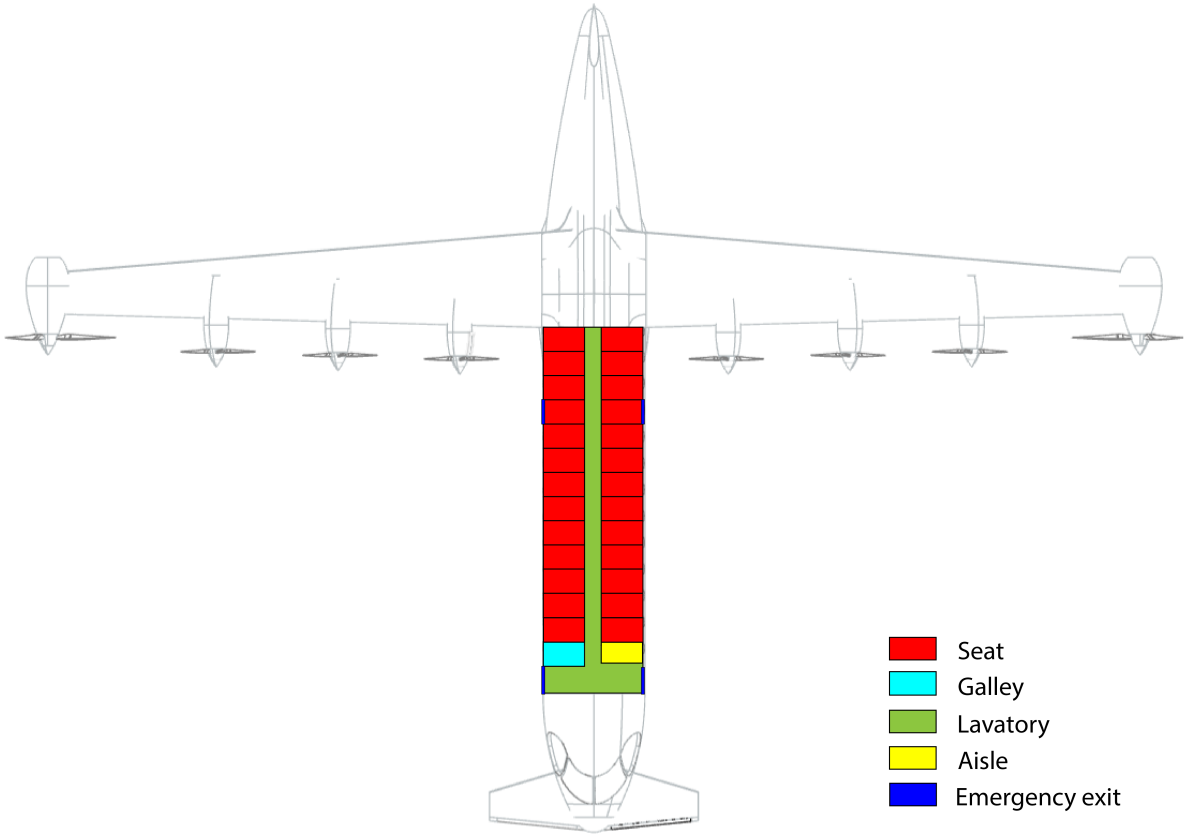

Figure 6.6: Top view of the aircraft including the seating plan

$$l_{cabin} = \frac{n_{pax}}{n_{sa} \cdot k_{cabin}} \tag{6.16}$$

To ensure the visibility for the pilot, an over-nose angle of $20\ ^\circ$, a grazing angle of $35\ ^\circ$, and an upward-view angle of $20\ ^\circ$ were selected. Furthermore, an over-side angle of $35\ ^\circ$ was ensured [12]. In order to ensure a sufficient rotation angle, the aircraft was designed with a scrape angle of $20\ ^\circ$. The tail was shaped to

reduce the drag coefficient as much as possible resulting in the side view depicted in Figure 6.7. The most important parameters are presented in Table 6.4.

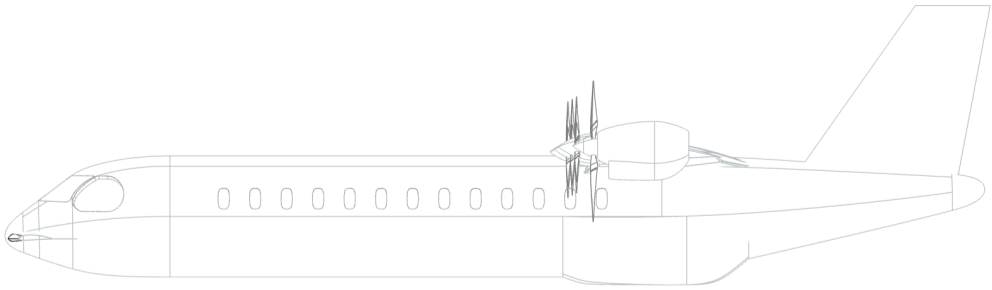

Figure 6.7: Side view of the aircraft

Table 6.4: Fuselage sizing parameters

Parameter	Value	Unit
k_{cabin}	1.08	$[-]$
n_{sa}	4	$[-]$
n_{pax}	50	$[-]$

Table 6.5: Fuselage sizing results

Parameter	Value	Unit
$l_{fuselage}$	22.7	$[m]$
l_{cabin}	13.5	$[m]$
$d_{f_{outer}}$	2.83	$[m]$
V_{total}	11.75	$[m^3]$

6.5. Horizontal and Vertical Tail Sizing

After performing the fuselage sizing it was possible to perform the sizing for the empennage. Usually, the horizontal and vertical tail areas are estimated using statistics on the horizontal and vertical tail volume coefficients, respectively. However, since the aircraft features a canard this is difficult in practice as there is little information available on volume coefficients of similar aircraft featuring a canard. Therefore a different method was conceived to estimate the horizontal and vertical tail area. It comprises of estimating the horizontal and vertical tail area by looking at similar aircraft and then updating these areas with the updated tail area computed in Chapter 10 and iterating until these tail areas are sufficiently close. Using the horizontal and vertical tail area, the dimensions of the tail surfaces were subsequently computed using Section 6.3. With the initial, assumed horizontal tail area $S_h = 8.2\ [m^2]$ and vertical tail area $S_v = 14.0\ [m^2]$ this yielded the following tail sizing parameters in Table 6.6. A detailed empennage analysis including the generation of the scissor plot will be described in Chapter 10.

Table 6.6: Tail sizing results

Parameter	Value	Unit	Parameter	Value	Unit
S_h	8.2	$[m^2]$	S_v	14.0	$[m^2]$
b_h	5.7	$[m]$	b_v	4.6	$[m]$
c_h	1.5	$[m]$	c_v	3.4	$[m]$
$c_{h_{root}}$	2.0	$[m]$	$c_{v_{root}}$	4.4	$[m]$
$c_{h_{tip}}$	0.8	$[m]$	$c_{v_{tip}}$	1.7	$[m]$

6.6. Class-I Weight Estimation

For the class-I weight estimation, an adaptation of the De Vries method was to account for the design of a hybrid-electric aircraft with distributed propulsion [15]. At the start of the process a so-called ”class-I empirical weight estimation” was performed. The class-I empirical weight estimation consists of historical data of comparable aircraft, from which an empirical relation between OEW and MTOW was set up. Out of the class-I empirical weight estimation an initial OEW was obtained. To adjust for the fact that the aircraft to be designed would be a hybrid-electric aircraft with distributed propulsion the powertrain weight (W_{pt}) and wing weight (W_{wing}) were subtracted. As shown in Equation 6.17.

$$OEW_{empirical} = OEW - W_{wing} - W_{pt} \tag{6.17}$$

Afterwards, an approximation of the to-be-designed aircraft the wing weight and powertrain weight was calculated and added as described in Chapter 7 and Chapter 8. By adding the payload and fuel weight the MZFW and MTOW were calculated. The values MZFW, MTOW, and OEW were further used in the iteration.

6.7. Class-II Weight Estimation

In this section, the class-II weight estimation are explained. All formulas used in this chapter compute the weights in $[kg]$ for consistency with Torenbeek’s method [14].

6.7.1. Weight Categories

To estimate the aircraft’s OEW, the weight estimation equations of Torenbeek were used [14]. This method divides the OEW up in component weights. The aeroplane’s OEW can be divided into the three main categories shown in Equation 6.18.

$$OEW = W_{structure} + W_{propulsion} + W_{equipment}, \tag{6.18}$$

where $W_{structure}$ is the total structural weight, $W_{propulsion}$ is the propulsion group weight, and $W_{equipment}$ is the weight of the airframe services and equipment. Due to the use of a HEP, the powertrain weight was not determined by the use of statistical relations, but by sizing the powertrain with the required power as explained in Chapter 8. Therefore, it is not discussed in this chapter. Next to that, $W_{structure}$ can be split up into the components shown in Equation 6.19.

$$W_{structure} = W_{wing} + W_{emp} + W_{fus} + W_{uc} + W_{sc} \tag{6.19}$$

Here, W_{wing} is the wing weight, W_{emp} the empennage weight, W_{fus} the fuselage weight, W_{uc} the undercarriage weight, and W_{cs} the control surface weight. Next to that, $W_{equipment}$ can be computed using Equation 6.20,

$$W_{equipment} = W_{inst} + W_{furn} + W_{ac}, \tag{6.20}$$

where W_{inst} is the instruments and electronics weight, W_{furn} is the furnishing weight, and W_{ac} is the air-conditioning and anti-ice system weight.

6.7.2. Structural Weight

Wing Weight

Torenbeek's equation for estimating the wing weight is shown in Equation 6.21.

$$W_{wing} = k_w \cdot W_G \cdot b_s^{0.75} \cdot \left(1 + \sqrt{\frac{b_{ref}}{b_s}}\right) \cdot n_{ult}^{0.55} \cdot \left(\frac{b_s/t_r}{W_G/S}\right)^{0.30} \tag{6.21}$$

For this equation, $k_w = 6.67 \cdot 10^{-3}$ for transport aircraft, W_G is the aircraft gross weight, $b_{ref} = 1.905$ is the reference span, $b_s = b/cos(\Lambda_{\frac{1}{2}})$ is the structural span, n_{ult} is the ultimate load factor, t_r is the absolute maximum thickness of the root chord, and S is the wing surface area [14]. As the designed aircraft has no sweep, as explained in Section 6.3, $b_s = b/cos(\Lambda_{\frac{1}{2}}) = b$. The term W_G/S can be rewritten as follows:

$$\frac{W_G}{S} = \frac{MZFW}{S} = \frac{OEW + W_{PL}}{S}, \tag{6.22}$$

Here, $W_G = MZFW$ for transport aircraft above 5670 $[kg]$ according to Torenbeek [14]. Here OEW and S were updated in the class-I and class-II iterations until convergence was achieved.

Since Equation 6.21 is an empirical relation based on aircraft without wingtip propellers it does not take the effect it has on the structural weight into account. Having a large propeller on the wingtip creates a large bending moment at the wing root, which is beneficial during flight as it then relieves the bending moment produced by the lift force. However, during ground operations, this larger weight and the corresponding wing root bending moment need to be supported. A study has shown the effect of shaft power ratio - defined as the shaft power of the secondary electric wingtip mounted propellers over the total shaft power - on the total wing weight [16]. A higher shaft power ratio implies larger, more powerful, and heavier wingtip-mounted electric propellers. The study shows that an increase from 0.1 to 0.35 in shaft power ratio results in a wing weight reduction of hardly 2%. Therefore, the effect of the wingtip-mounted propellers on the wing weight is thus assumed negligible and Equation 6.21 was not adjusted for having a wingtip-mounted propeller.

Torenbeek mentions some adaptations for Equation 6.21. A total reduction of 30% relative to Equation 6.21 can be expected when making use of trusses to support the wings [14]. Next to that, for wing-mounted engines, a weight reduction of between 5% and 10% can be expected. To be conservative, a reduction of 5% was chosen. Lastly, if the undercarriage is mounted on the fuselage, the wing weight should be reduced by 5%. Taking these adaptations into account together with the earlier stated simplifications results in Equation 6.23.

$$\begin{aligned} W_{wing} &= 0.7 \cdot 0.95 \cdot 0.95 \cdot 6.67 \cdot 10^{-3} \cdot MZFW \cdot b^{0.75} \cdot \left(1 + \sqrt{\frac{1.905}{b}}\right) \cdot n_{ult}^{0.55} \cdot \left(\frac{b/t_r}{(OEW + W_{PL})/S}\right)^{0.30} \\ &= 4.214 \cdot 10^{-3} \cdot MZFW \cdot b^{0.75} \cdot \left(1 + \sqrt{\frac{1.905}{b}}\right) \cdot n_{ult}^{0.55} \cdot \left(\frac{b/t_r}{(OEW + W_{PL})/S}\right)^{0.30} \end{aligned} \tag{6.23}$$

Empennage Weight

The empennage consists of both the horizontal and vertical stabilisers. The total empennage weight can then be defined as the sum of Equation 6.24 and Equation 6.25.

$$W_h = K_h \cdot S_h \cdot \left(\frac{3.81}{1000} \cdot \frac{S_h^{0.2} \cdot V_D}{\sqrt{cos(\Lambda_{1/2_h})}} - 0.287 \right) \tag{6.24}$$

$$W_v = K_h \cdot S_v \cdot \left(\frac{3.81}{1000} \cdot \frac{S_v^{0.2} \cdot V_D}{\sqrt{cos(\Lambda_{1/2_v})}} - 0.287 \right) \tag{6.25}$$

In these equations, subscripts h and v indicate the horizontal or vertical stabiliser, $W_{h/v}$ is the stabiliser weight, $S_{h/v}$ is the stabiliser surface area, and $K_{h/v}$ is a factor for the type of stabiliser, which is 1 in the case of a fixed incidence/fuselage-mounted stabiliser. Furthermore, V_D is the design dive speed and $\Lambda_{h/v}$ is the stabiliser sweep angle at 50% chord.

Fuselage weight
For the fuselage group weight, Equation 6.26 can be used. The factors 1.08 and 1.07 are applied to account for having a pressurized cabin and a fuselage stored landing gear respectively. Furthermore, k_{wf} is a constant with a value of 0.23, l_t is defined as the distance between the quarter-chord points of the local wing chord and the horizontal tailplane, b_f is the width of the fuselage, h_f is the height of the fuselage, and S_G the gross shell area of the fuselage.

$$W_{fus} = 1.08 \cdot 1.07 \cdot k_{wf} \cdot \sqrt{V_D \frac{l_t}{b_f + h_f}} \cdot S_G^{1.2}, \tag{6.26}$$

Undercarriage Weight
To determine the undercarriage weight, Equation 6.27 was used for both the main landing gear and the nose gear. k_{uc} is a constant with a value of 1 since the undercarriage is stored in the fuselage. A, B, C and D, are based on statistics and have a value of 18.1, 0.131, 0.19 and $2.23 \cdot 10^{-5}$ respectively for the main landing gear. For the nose landing gear, they have a value of 9.1, 0.082, 0 and 2.97 respectively.

$$W_{uc} = k_{uc} \cdot (A + B \cdot MTOW^{0.75} + C \cdot MTOW + D \cdot MTOW^{1.5}), \tag{6.27}$$

Control Surface Weight
Note that Torenbeek [14] uses the term 'surface control weight' for this weight component. For the control surface weight, empirical Equation 6.28 was used, where k_sc is a constant with a value of 0.64.

$$W_{sc} = 0.768 \cdot k_{sc} \cdot MTOW^{2/3} \tag{6.28}$$

6.7.3. Airframe Services & Equipment Weight

Instruments, navigational equipment, and electronics group
For subsonic transporters, the weight of the instruments, navigational equipment, and electronics group was estimated using Equation 6.29, where k_{ieg} = 0.347 is a constant and W_{DE} is the delivery empty weight. For simplicity the OEW was used. Furthermore R_D is the maximum range.

$$W_{inst} = k_{ieg} \cdot W_{DE}^{5/9} \cdot R_D^{1/4} \tag{6.29}$$

Furnishing and equipment group
For passenger transport, a rough approximation is obtained with the statistical expression from Equation 6.30, where $MZFW$ is the maximum zero-fuel weight.

$$W_{furn} = 0.196 \cdot MZFW^{0.91}, \tag{6.30}$$

Air-conditioning and anti-icing group
For pressurised transports, the air-conditioning and anti-icing group weight can be approximated using Equation 6.31, where l_{cabin} is the cabin length.

$$W_{ac} = 14 \cdot l_{cabin}^{1.28}, \tag{6.31}$$

6.7.4. Parameters & Class-II Weight Estimation Results

After convergence between the class-I and class-II weight estimation iteration was reached, the weights of the structural components mentioned in this chapter were known. The values of the parameters used in Equation 6.21 to Equation 6.31 are shown in Table 6.7. The final component weights are shown in Table 6.8.

Table 6.7: Class-II weight estimation parameters

Parameter	Value	Unit	Parameter	Value	Unit
b	31.4	$[m]$	S	61.62	$[m^2]$
b_f	2.82	$[m]$	S_G	201.5	$[m^2]$
h_f	2.82	$[m]$	S_h	8.2	$[m^2]$
l_{cabin}	13.5	$[m]$	S_v	14.0	$[m^2]$
l_t	3	$[m]$	t_r	0.25	$[m]$
$MTOW$	23314	$[kg]$	V_D	179.9	$[m/s]$
$MZFW$	23117	$[kg]$	W_{pl}	5300	$[kg]$
n_{ult}	4.5	$[-]$	$\Lambda_{h1/2}$	-6.1	$[deg]$
OEW	17867	$[kg]$	$\Lambda_{v1/2}$	-15.9	$[deg]$
R_D	985	$[km]$			

Table 6.8: Class-II weight estimation results

Parameter	Value	Unit
W_{ac}	392	$[kg]$
W_{furn}	1834	$[kg]$
W_{fus}	3148	$[kg]$
W_h	439	$[kg]$
W_{inst}	425	$[kg]$
W_{sc}	401	$[kg]$
W_{uc}	1039	$[kg]$
W_v	855	$[kg]$
W_{wing}	2654	$[kg]$

7

Aerodynamic Design

This chapter describes the design of the aerodynamics of the aircraft including the aerodynamics of the wing and canard, as well as the interactions with other subsystems such as the effect of the propulsion system on the aerodynamics. In Section 7.1, an airfoil for the main wing is selected. Next, the manner of analysing the aerodynamics is explained and the interaction between the distributed propulsion and the wing aerodynamics is explored in Section 7.2. Furthermore, in Section 7.3, the choice of high-lift devices (HLDs) is discussed. Subsequently, the aerodynamics of the canard are analysed in Section 7.4. Finally, in Section 7.5, the drag contributions of non-lifting aircraft components are estimated and the final results of the aerodynamic analysis are presented.

7.1. Airfoil Selection

Once the conceptual sizing of the aircraft had been completed, an airfoil should be selected. As cruise is the largest flight phase in terms of time and energy, the airfoil was primarily optimised for cruise, but other considerations were also incorporated. First, the design lift coefficient was determined. Second, airfoils were found that have their minimum drag approximately at the design lift coefficient. Third, the drag of these airfoils at the design lift coefficient was determined. Finally, the airfoils which had a similar level of drag at the design lift coefficient were analysed in terms of the size of their drag bucket and their $C_{L_{max}}$.

The design lift coefficient could be determined from the values obtained from the class-I weight estimation, described in Section 6.6, and the performance diagram, presented in Section 6.2, using Equation 7.1 [17]. The result of this calculation was that a $C_{l_{des}}$ of approximately 0.5 was needed.

$$C_{l_{des}} \approx \frac{2W/S}{\rho_{cr} \cdot V_{cr}^2} \tag{7.1}$$

It was decided to limit the scope of the airfoil search to only NACA airfoils, due to the large amount of verified wind tunnel data available. In addition, the search was restricted to airfoils with a thickness to chord ratio of between 0.12 and 0.2. This was because this is a common range for subsonic civil transport aircraft [18]. A variable airfoil was also deemed outside the scope of the research. This left 26 airfoils for which drag had to be determined using XFOIL[1].

The best drag for a C_l of approximately 0.5 was exhibited by the NACA 4415 airfoil, which had a C_D of 0.00527 at a C_l of 0.5454. This was the result of an angle of attack of 0. Airfoils with a C_D of at most 10% greater (0.00580) were also selected for the next step in the analysis. They are shown in Table 7.1.

[1] https://web.mit.edu/drela/Public/web/xfoil/, last consulted June 14, 2022

Table 7.1: List of airfoils considered in the final airfoil choice step.

Airfoil Name	C_d **at** $C_{l_{des}}$	$C_{l_{max}}$
NACA 4418	0.00560	1.9075
NACA 4415	0.00527	1.9954
NACA 2418	0.00571	1.1969
NACA 2415	0.00548	1.9797
NACA 2414	0.00540	1.9677

As can be seen, the NACA 4415 airfoil, which had the lowest C_D at $C_{l_{des}}$, also had the highest $C_{l_{max}}$. However, the NACA 2415 and NACA 2414 had very similar performance. However, in the end, the NACA 4415 was chosen, not only because of its low C_D at $C_{L_{des}}$ and high $C_{l_{max}}$ but also because of its ability to generate significant lift while limiting drag. While keeping drag under 1.5 times minimum C_D at $C_{L_{des}}$, the NACA 4415 airfoil is capable of producing a lift coefficient of 1.3215, while the NACA 2415 and NACA 2414 airfoils are only capable of producing a C_L of 1.1563 and 1.1685 respectively. The C_m of this airfoil at an angle of attack of $0°$ is -0.1047.

7.2. Aero-propulsive Interaction

As this aircraft uses distributed propulsion, the effect of the propeller wake on the wing aerodynamics cannot be neglected. The propeller induces an acceleration on the flow, which is determined through the axial induction factor, as well as an induced angle of attack, due to the angular velocity of the rotating propeller. In order to model this, the Blade Element Momentum (BEM) theory is combined with an extension of the Vortex Lattice Method (VLM), presented by Bohari et al. [19]. All further equations in this section are from this research unless otherwise indicated. The set of panels is set up using the location of several wing sections in spanwise direction. The 41 sections are distributed using Equation 7.2, and each panel in chordwise direction contains 5 wing sections, of which 2 are the spanwise boundaries of the panel. In chordwise direction, there are 4 rows of panels. All positions are relative to the reference frame centred on the quarter chord point on the plane of symmetry of the wing, in line with the chord, with the x direction being in the direction of the LE of the wing, and z direction pointing perpendicular to the plane of the wing, in upwards direction.

$$y_i = \frac{b}{2} \cdot \cos\left(\frac{(i-1)\cdot\pi}{n}\right) \tag{7.2}$$

The axial velocity induced by the propeller on each section is calculated using Equation 7.3, and the induced rotational velocity is calculated using Equation 7.4. It is assumed that the propeller-induced velocities act only upon sections which lie directly behind the propeller [19].

$$V_{x,p_{m\to i}} = a \cdot V_\infty \tag{7.3}$$

$$V_{\theta,p_{m\to i}} = \left(1 - \sqrt{1 - 4\cdot\frac{V_{x,p_{m\to i}}}{V_\infty}\cdot\left(1+\frac{V_{x,p_{m\to i}}}{V_\infty}\right)\cdot\left(\frac{V_\infty}{\Omega_{p_m}\cdot r_{p_{m,i}}}\right)^2}\right)\cdot\Omega_{p_m}\cdot r_{p_{m,i}} \tag{7.4}$$

From the rotational velocity, using Equation 7.5, the induced velocity in x and y direction can be computed.

$$V_{x,p_{m\to i}} = V_{\theta,p_{m\to i}} \cdot \frac{r_{p_{m\to i}}}{r_{tip}}$$
$$V_{y,p_{m\to i}} = V_{\theta,p_{m\to i}} \cdot \frac{\sqrt{r_{tip}^2 - r_{p_{m\to i}}^2}}{r_{tip}} \tag{7.5}$$

A weighted average of the relevant sectional induced velocities can be used for the induced velocities on each panel. From there, the velocity vector forms the basis of the right-hand side of the VLM equation. The flow acting on each panel in the x-z plane can be further characterised by an angle of attack and a magnitude of the flow, calculated using Equation 7.7 and Equation 7.8.

$$\mathbf{V_j} = \begin{pmatrix} V_{x,j} \\ V_{y,j} \\ V_{z,j} \end{pmatrix} = \begin{pmatrix} V_\infty \cdot \cos(\alpha_{loc,j}) \cdot \cos(\beta - \phi_j) + V_{x,p,j} \\ -V_\infty \cdot \sin(\beta - \phi_j) + V_{y,p,j} \\ V_\infty \cdot \sin(\alpha_{loc,j}) \cdot \cos(\beta - \phi_j) + V_{z,p,j} \end{pmatrix} \tag{7.6}$$

$$\alpha_{vlm,j} = \arctan\left(\frac{V_{z,j}}{V_{x,j}}\right) \tag{7.7}$$

$$|V_{xz,j}| = \sqrt{V_{x,j}^2 + V_{z,j}^2} \tag{7.8}$$

The circulation of the horseshoe vortex located at the quart-chord of each panel can be found using Equation 7.9, where $A_{j,k}$ is computed using Equation 7.10 [20].

$$A_{j,k}\Gamma_k = -\mathbf{V_j} \cdot \mathbf{n_j} \tag{7.9}$$

$$A_{j,k} = \frac{1}{4\pi}\left[\frac{\mathbf{a}\times\mathbf{b}}{|\mathbf{a}||\mathbf{b}| + \mathbf{a}\cdot\mathbf{b}}\left(\frac{1}{|\mathbf{a}|} + \frac{1}{|\mathbf{b}|}\right) + \frac{\mathbf{a}\times\mathbf{x}}{|\mathbf{a}| - \mathbf{a}\cdot\mathbf{x}}\left(\frac{1}{|\mathbf{a}|}\right) - \frac{\mathbf{b}\times\mathbf{x}}{|\mathbf{b}| - \mathbf{b}\cdot\mathbf{x}}\left(\frac{1}{|\mathbf{b}|}\right)\right] \cdot \mathbf{n_j} \tag{7.10}$$

Here, **a** and **b** are defined using Figure 7.1. Point **r** is the collocation point of each panel, and thus at the centre of the three-quarter chord line of the panel [20]. The linear prediction of the lift coefficient can then be found using the Kutta-Joukowski Theorem and the lift coefficient formula, as shown in Equation 7.11 [21].

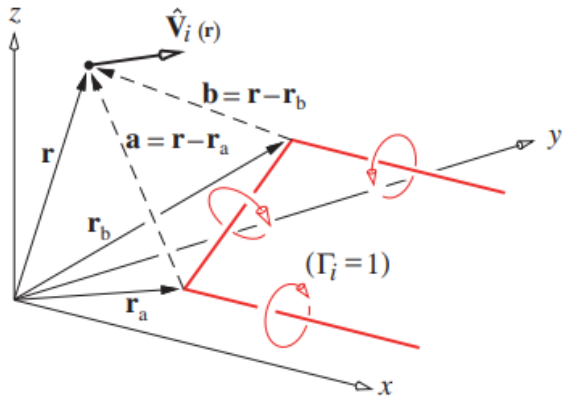

Figure 7.1: Definition of vectors for calculation of $A_{j,k}$ and $C_{j,k}$ [20]

$$c_{l_{lin,j}} = \frac{2L'}{\rho_\infty \cdot |V_{xz,j}|^2 \cdot c_j} = \frac{2\Gamma_k}{|V_{xz,j}| \cdot c_j} \tag{7.11}$$

However, this circulation will also induce velocity, which will then be taken into account in the viscous lift calculation. The induced velocities can be calculated using Equation 7.12 [20] and Equation 7.13 [20], where $\mathbf{a}'$ and $\mathbf{b}'$ are defined similarly to $\mathbf{a}$ and $\mathbf{b}$, except instead of $\mathbf{r}$ being the collocation point, it is the midpoint of the bound vortex, and thus at the midpoint of the quarter chord line of each panel [20].

$$V_{eff,j} = \Gamma_k C_{j,k} \tag{7.12}$$

$$C_{j,k} = \frac{1}{4\pi}\left[\frac{\mathbf{a}\times\mathbf{k}}{|\mathbf{a}| - \mathbf{a}\cdot\mathbf{k}}\left(\frac{1}{|\mathbf{a}|}\right) - \frac{\mathbf{b}\times\mathbf{k}}{|\mathbf{b}| - \mathbf{b}\cdot\mathbf{k}}\left(\frac{1}{|\mathbf{b}|}\right)\right] \tag{7.13}$$

An angle of attack of this effective flow can be calculated in the same way as $\alpha_{vlm,j}$, and this is then input into XFOIL[1] to calculate $c_{l_{visc,j}}$, which is done using a viscous calculation at the appropriate Mach and Reynolds number for the particular altitude, $|V_{xz,j}|$, and chord length. The difference between the viscous calculation and the linear prediction of the lift coefficient is then used to iterate, with the process repeated from Equation 7.9. The updated values and errors are calculated using Equation 7.14.

$$\Delta\alpha_j = \frac{c_{l_{visc,j}} - c_{l_{lin,j}}}{2\pi} \tag{7.14}$$

$$\alpha^{k+1}_{vlm,j} = \alpha^{k}_{vlm,j} + \Delta\alpha_j \tag{7.15}$$

$$V^{k+1}_{x,j} = |V_{xz,j}| \cos\left(\alpha^{k+1}_{vlm,j}\right) \tag{7.16}$$

$$V^{k+1}_{z,j} = |V_{xz,j}| \sin\left(\alpha^{k+1}_{vlm,j}\right) \tag{7.17}$$

$$\varepsilon^k = 2\pi\left(|\Delta\alpha_j|\right)_{max} \tag{7.18}$$

The procedure is considered converged when $\varepsilon^k < 10^{-3}$. At this point, the coefficients of the full wing can be computed, using the speed factor and the induced angle of attack, presented in Equation 7.19 and Equation 7.20.

$$SF_j = \frac{V^2_{x,eff,j} + V^2_{z,eff,j}}{V^2_\infty} \tag{7.19}$$

$$\alpha_{ind,j} = \alpha_{vlm,j} - \alpha_{eff,j} \tag{7.20}$$

The aerodynamic coefficients are then computed as shown in Equation 7.21. Results from this can then be combined with the aerodynamics of other aircraft components as shown in Section 7.5, and full results will be presented there.

$$\begin{aligned} C_L &= \frac{\sum_j \left(c_{l_{visc,j}} \cdot dA_j \cdot SF_j \cdot \cos\alpha_{ind,j} - c_{dp,j} \cdot dA_j \cdot SF_j \cdot \sin\alpha_{ind,j}\right)}{\sum_j dA_j} \\ C_D &= \frac{\sum_j \left(\sin\alpha_{ind,j} \cdot c_{l_{visc,j}} \cdot dA_j \cdot SF_j + c_{d,j} \cdot dA_j \cdot SF_j \cdot \cos\alpha_{ind,j}\right)}{\sum_j dA_j} \end{aligned} \tag{7.21}$$

7.3. High-Lift Devices

HLDs are commonly used in civil transport aircraft to postpone stall or increase the maximum lift coefficient [11]. However, the usage of trailing edge HLDs also cause a significant negative moment about the aerodynamic center of the wing [22]. For a canard configuration, this creates significant issues with controllability [23]. Furthermore, the implementation of leading edge HLDs is made impossible by the distributed propulsion. However, to reach the necessary $C_{L_{max}}$ for take-off and landing, it was necessary to implement simple trailing edge HLDs. To minimise the impact on C_m, it was chosen to use plain flaps and limit the length of the

flaps to a quarter of the chord, as they correspond to a lower $\Delta C_{l_{max}}$ and lower empirical coefficients than more advanced types of HLDs [23]. The HLDs can be sized using the method presented in Equation 7.22 through Equation 7.25. The $\Delta C_{l_{max}}$ of the flaps is taken from [24] and modified using [25]. The HLDs are not included within the VLM, as the complex geometry used cannot be adequately modeled in the model with its current coarse mesh. Della Vecchia et al. specify that distributed propulsion increases the lift production by 60-80% in flapped configuration, and to have a conservative estimation, a 60% increase is applied to the $\Delta C_{l_{max}}$. The parameters and results of the HLD sizing are presented in Table 7.2 and Table 7.3, with the wing planform geometry being sourced from Section 6.3.

$$\frac{c'}{c} = 1 + \frac{\Delta c}{c_f} \cdot \frac{c_f}{c} \tag{7.22}$$

$$\frac{S_{wf}}{S} = \frac{C_{L_{max}} - C_{L_{max,clean}}}{0.9 \Delta C_{l_{max}}} \tag{7.23}$$

$$b_{fl} = \frac{-\left(\frac{c_{s,f}+c_r}{2} + \frac{(\lambda-1)\cdot c_r \cdot y_{s,f}}{b_w}\right) + \sqrt{\left(\frac{c_{s,f}+c_r}{2} + \frac{(\lambda-1)\cdot c_r \cdot y_{s,f}}{b_w}\right)^2 + 4\left(\frac{(\lambda-1)c_r \cdot S_w f}{b_w}\right)}}{\frac{2c_r(\lambda-1)}{b_w}} \tag{7.24}$$

$$\Delta C_{m_{ac}} = \mu_2 \left(-\mu_1 \cdot \Delta C_{l_{max}} \cdot \frac{c'}{c} - \left(C_{L_{max,clean}} + \Delta C_{l_{max}} \left(1 - \frac{S_{wf}}{S}\right)\right) \frac{1}{8} \frac{c'}{c} \left(\frac{c'}{c} - 1\right)\right) \tag{7.25}$$

Table 7.2: HLD design parameters

Parameter	Value	Unit
$\frac{\Delta c}{c_f}$	0.4	$[-]$
$\frac{c_f}{c}$	0.25	$[-]$
$C_{L_{max}}$	3.2	$[-]$
$C_{L_{max,clean}}$	2.5	$[-]$
$\Delta C_{l_{max}}$	1.4	$[-]$
$c_{s,f}$	2.60	$[m]$
$y_{s,f}$	1.91	$[m]$
μ_1	0.155	$[-]$
μ_2	0.7	$[-]$

Table 7.3: HLD design results

Parameter	Value	Unit
$\frac{c'}{c}$	1.1	$[-]$
$S_w f$	33.28	$[m^2]$
b_{fl}	8.14	$[m]$
$\Delta C_{m_{ac}}$	-0.202	$[-]$

7.4. Canard Aerodynamics

In a canard configuration, the horizontal stabiliser also provides lift, and thus this was also designed. The planform was designed in Section 10.4, and in this section an airfoil will be selected and the aerodynamics will be analysed.

The selection criteria for the airfoil of the canard were different from that of the main wing. For the canard, the most important factor is a high maximum angle of attack. Furthermore, with a canard it is desirable to stall the canard earlier than the main wing, thus a low stall angle of attack was also considered. Apart from the different selection criteria, the process of airfoil selection was the same as in Section 7.1. In the end, the NACA 6412 airfoil was selected, as due to its high camber it has a very low $\alpha_{L=0}$ which leads to a low α_{stall} but a high $C_{L_{max}}$.

The lift slope, maximum lift coefficient, and stall angle of attack can be computed using the DATCOM method [24], these use Equation 7.26 through Equation 7.28. The necessary parameters and results are shown in Table 7.4 and Table 7.5.

$$C_{L_\alpha} = \frac{2\pi A}{2 + \sqrt{4 + \left(\frac{A\sqrt{1-M_\infty^2}}{\eta}\right)^2 \cdot \left(1 + \frac{\tan^2 \Lambda_{0.5c}}{1-M_\infty^2}\right)}} \tag{7.26}$$

$$C_{L_{max}} = \left(\frac{C_{L_{max}}}{C_{l_{max}}}\right) C_{l_{max}} + \Delta C_{L_{max}} \tag{7.27}$$

$$\alpha_{stall_{canard}} = \frac{C_{L_{max}}}{C_{L_\alpha}} + \alpha_{0L} + \Delta\alpha_{C_{L_{max}}} \tag{7.28}$$

Table 7.4: Parameters and Results of Canard Aerodynamic Analysis

Parameter	Value (cruise)	Value (landing)	Unit
A	2	2	$[-]$
η	0.95	0.95	$[-]$
M_∞	0.12	0.45	$[-]$
$\Lambda_{0.5c}$	0	0	$[deg]$
$\frac{C_{L_{max}}}{C_{l_{max}}}$	0.9	0.9	$[-]$
$C_{l_{max}}$	1.83	1.84	$[-]$
$\Delta C_{L_{max}}$	-0.35	0	$[-]$
α_{0L}	-6.0	-6.0	$[deg]$
$\Delta\alpha_{C_{L_{max}}}$	1.2	0	$[deg]$

Table 7.5: Parameters and Results of Canard Aerodynamic Analysis

Parameter	Value (cruise)	Value (landing)	Unit
$C_{L_{\alpha_h}}$	2.008	1.894	$[rad^-1]$
$C_{L_{max_h}}$	1.297	1.656	$[-]$
α_{stall_h}	31.01	44.10	$[deg]$

The $C_{L_{max_h}}$ presented in the table is without elevator deflection. The elevator will not be designed in this project, but a $\Delta C_{L_{max}}$ that can be achieved with a simple elevator can be assumed to be 0.9 [24], leading to an overall $C_{L_{max_{h,deflected}}}$ of 2.448 in landing conditions. Usually, it is preferable to stall the canard before the main wing, however, due to the extreme difference in aspect ratio between the two surface, this is impossible. Thus, stall must be managed by a digital flight control system. The $C_{L_{max_{A-h}}}$ in landing is 3.24, as derived from the results in Section 7.5.

7.5. Drag Analysis of other Components and Final Results

Finally, with the 2 main lifting surfaces taken into account, the drag of the fuselage, nacelles, vertical tail, and truss can be taken into account. For each component, the ΔC_{D_0} is estimated using Equation 7.29 [24].

$$\Delta C_{D_{0,c}} = 1.15 \cdot \frac{S_{wet,c}}{S_{ref}} \cdot C_{D_c} \tag{7.29}$$

The C_{D_c} and wetted areas, as well as the resulting $\Delta C_{D_{0,c}}$ of each component are shown in Table 7.6, with the areas being sourced from their . The final results of the aerodynamic analysis are shown in Table 7.7.

Table 7.6: Parameters and Results of Canard Aerodynamic Analysis

Parameter	**Value** $[unit]$
$C_{D_{fus}}$	0.080
$C_{D_{nac}}$	0.060
$C_{D_{vtail}}$	0.008
$C_{D_{truss}}$	0.007
$S_{wet_{fus}}$	$25.16\ [m^2]$
$S_{wet_{nac}}$	$4.22\ [m^2]$
$S_{wet_{vtail}}$	$15.10\ [m^2]$
$S_{wet_{truss}}$	$4.94\ [m^2]$
S_{ref}	$61.63\ [m^2]$
$C_{D_{0_{fus}}}$	0.038
$C_{D_{0_{nac}}}$	0.005
$C_{D_{0_{vtail}}}$	0.002
$C_{D_{0_{truss}}}$	0.001

Table 7.7: Parameters and Results of Aerodynamic Analysis of full Aircraft

Parameter	Take-off	Ground Run	Climb	Cruise	Descent	Landing
$C_{L_{max}}$	2.83 [–]	N/A	2.67 [–]	1.2 [–]	2.67 [–]	3.39 [–]
$C_{L_{opt}}$	2.36 [–]	1.21 [–]	2.23 [–]	0.51 [–]	2.23 [–]	2.01 [–]
C_D	0.173 [–]	0.064 [–]	0.155 [–]	0.031 [–]	0.155 [–]	0.134 [–]
α	7.75 [°]	0.00 [°]	9.50 [°]	0.00 [°]	9.50 [°]	3.75 [°]
α_{stall}	10.75 [°]	N/A	12.25 [°]	6.25 [°]	12.25 [°]	12.5 [°]

As can be seen, the initially assumed C_L of 3.6 is not attained, but it should be noted that the results from the Vortex Lattice Method are sometimes unreliable around stall angles of attack. This might also explain the very low stall angles of attack. More verification and validation is necessary to understand the source of these potential inaccuracies, but the method has been verified and validated for lower angles of attack, where the method gives comparable results to methods such as the DATCOM method [26] without propulsion and a similar increase to other studies when comparing the increase [25].

8

Powertrain Design

This chapter describes the design and integration of the powertrain. In Section 8.1, the architecture of the aircraft's powertrain is outlined, together with the main principles of its operation. Subsequently, in Section 8.2, the individual powertrain components are sized. Finally, the integration of the powertrain with the other aircraft systems is portrayed in Section 8.3.

8.1. Powertrain Architecture

The purpose of the powertrain is to safely store the energy sources used for the aircraft's propulsion and to convert the energy efficiently into rotational motion of the propeller shaft, which is used to generate thrust. The scope of the powertrain thus includes all components between and including the energy sources and the shaft used to drive the propellers. As explained in Chapter 5, the aircraft leverages an all-electric powertrain, using both hydrogen and batteries to store energy. Furthermore, two different engines are specified that correspond to two different types of propulsors used in the aircraft; wing tip propulsors capable of regeneration (2), and smaller propellers used to enhance lift during take-off (1). The arrows indicate the flow direction of power with a double arrow indicating the regenerative capabilities of the powertrain. The architecture of the powertrain is displayed in Figure 8.1.

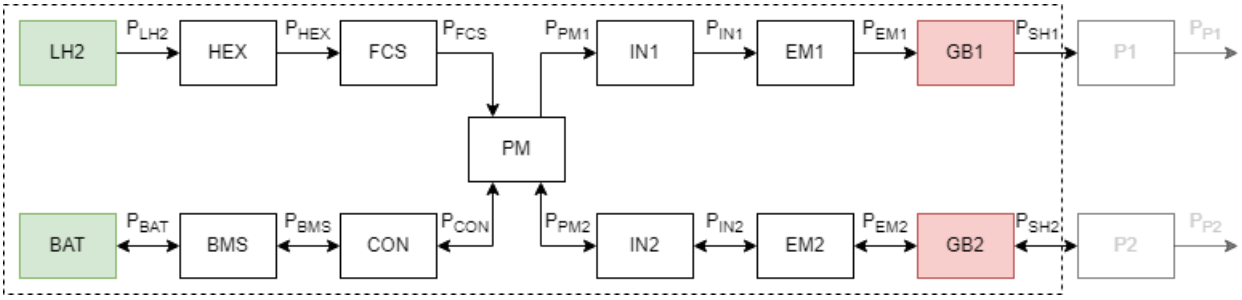

Figure 8.1: Diagram of the powertrain architecture, based on the method by De Vries [6].

In order to provide power for the rotation of the shaft, the following energy conversion sequence takes place. Liquid hydrogen (LH2) boils off, is heated up in a heat exchanger (HEX), and is converted into electricity by a fuel cell system (FCS). Concurrently, battery power can be provided when required, which passes through a battery management system (BMS) and a converter (CON) that makes sure the battery voltage matches the fuel cell voltage. Subsequently, a power management unit divides the battery power over the two different drivetrains. Engine 1 corresponds to the smaller engines used for lift enhancement, while engine 2 corresponds to wing-tip engines capable of regeneration. The electricity is inverted (IN) to AC for the electric motors (EM), which convert the electric power into rotation of the shaft. Lastly, a gearbox (GB) makes sure the shaft rotational speed is reduced to a desired rotational speed for the propellers.

To size the powertrain, a method by de Vries is used [6]. For each component, the output power can be computed using a matrix of 14 equations. The first 11 can be calculated by deriving the power flow through each component.

$$\sum P_{out} = \eta \sum P_{in} \tag{8.1}$$

Here η is the efficiency of each component. The remaining three equations can be calculated by specifying the supplied power ratio, shaft power ratio and the required shaft and compressor powers. The supplied power ratio is defined in Equation 8.2 as the ratio of the battery output power over the total energy source output power. Similarly, the shaft power ratio is defined in Equation 8.3 as the ratio of the secondary shaft power over the total shaft power.

$$\Phi = \frac{P_{bat}}{P_{bat} + P_{LH2}} \tag{8.2}$$

$$\varphi = \frac{P_{sh2}}{P_{sh2} + P_{sh1}} \tag{8.3}$$

Thus, by combining these equations, the matrix shown below can be found. When regeneration is used, this matrix is altered to account for the reverse flow of power to the batteries. The efficiencies presented in this matrix are derived from literature and shown in Table 8.1 [6].

$$\begin{bmatrix}
-\eta_{hex} & 1 & 0 & 0 & 0 & 0 & 0 & 0 & 0 & 0 & 0 & 0 & 0 & 0 \\
0 & -\eta_{fcs} & 1 & 0 & 0 & 0 & 0 & 0 & 0 & 0 & 0 & 0 & 0 & 0 \\
0 & 0 & -\eta_{pm} & 0 & 0 & -\eta_{pm} & 1 & 1 & 0 & 0 & 0 & 0 & 0 & 0 \\
0 & 0 & 0 & -\eta_{bms} & 1 & 0 & 0 & 0 & 0 & 0 & 0 & 0 & 0 & 0 \\
0 & 0 & 0 & 0 & -\eta_{con} & 1 & 0 & 0 & 0 & 0 & 0 & 0 & 0 & 0 \\
0 & 0 & 0 & 0 & 0 & -\eta_{in1} & 0 & 1 & 0 & 0 & 0 & 0 & 0 & 0 \\
0 & 0 & 0 & 0 & 0 & 0 & -\eta_{in2} & 0 & 1 & 0 & 0 & 0 & 0 & 0 \\
0 & 0 & 0 & 0 & 0 & 0 & 0 & -\eta_{em1} & 0 & 1 & 0 & 0 & 0 & 0 \\
0 & 0 & 0 & 0 & 0 & 0 & 0 & 0 & -\eta_{em2} & 0 & 1 & 0 & 0 & 0 \\
0 & 0 & 0 & 0 & 0 & 0 & 0 & 0 & 0 & -\eta_{gb1} & 0 & 1 & 0 & 0 \\
0 & 0 & 0 & 0 & 0 & 0 & 0 & 0 & 0 & 0 & -\eta_{gb2} & 0 & 1 & 0 \\
0 & 0 & \Phi & 0 & 0 & \Phi - 1 & 0 & 0 & 0 & 0 & 0 & 0 & 0 & 0 \\
0 & 0 & 0 & 0 & 0 & 0 & \phi & \phi - 1 & 0 & 0 & 0 & 0 & 0 & 0 \\
0 & 0 & 0 & 0 & 0 & 0 & 0 & 0 & 0 & 0 & 0 & 0 & 1 & 1
\end{bmatrix}$$

Table 8.1: Supplied power and shaft power ratios per phase.

Efficiency	Value	Efficiency	Value
η_{hex}	0.90[1]	η_{pm}	0.99
η_{fcs}	0.51[2]	$\eta_{in1,in2}$	0.99
η_{bms}	0.95	$\eta_{em1,em2}$	0.97
η_{con}	0.99	$\eta_{gb1,gb2}$	0.96

[1] Derived in Subsection 8.2.2
[2] Derived in Subsection 8.2.1

The supplied power ratio is defined per phase and chosen such that the fuel cell power is constant throughout the flight. This prevents the fuel cell from being oversized and simplifies the design of the hydrogen subsystem because the hydrogen mass flow will be constant. Next to this, batteries will be used to taxi the aircraft and store regenerated energy during descent. The final supplied power and shaft power ratios are presented in Table 8.2, with the divergence climb, cruise and descent equal to their nominal mission counterparts. It is noted that during descent, the fuel cells might struggle to provide enough power in the case of an aborted landing. However, as will be explained in Subsection 8.2.4, the batteries are capable of quickly providing enough power until the fuel cells take over again.

Table 8.2: Supplied power (Φ) and shaft power (φ) ratios per phase.

Ratio	Taxi	Take-off	Climb	Cruise	Descent	Loiter
Φ	1	0.62	0.44	0	1	0
φ	-	0.62	0.44	0	1	0

Lastly, the total shaft power is the sum of the primary and secondary shaft power. Most powertrain components are sized by dividing their maximum output powers resulting from this method by specific powers derived from literature. However, the liquid hydrogen tank, heat exchanger, fuel cell, compressor, batteries and gearbox are sized in more detail as explained in Section 8.2.

In order to size the powertrain, several assumptions have to be made. Current powertrains in electric vehicles employ powertrains around a voltage of $1000[V]$ [27]. Due to technological advancements in 2030, it is assumed that the actual powertrain voltage can be slightly higher, up to around $1200[V]$. This value will be important in determining the amount of fuel cell stacks and battery modules connected in series. Next to this, it is noted that with an increase in altitude, the compressor will require more power to pressurise the air to the desired level. To account for this effect, the compressor and fuel cell will be sized for the worst-case condition with the lowest ambient pressure, which is cruise.

8.2. Component Trade-off and Design

The fuel cell is seen as the heart of the powertrain, and will therefore be sized first. Afterwards, the balance of plant will be sized, along with the hydrogen storage system, batteries and other powertrain components.

8.2.1. Fuel Cell

Fuel cells convert chemical energy from hydrogen into electricity. At the anode side of the fuel cell, a catalyst separates the hydrogen into protons and electrons. The protons migrate through an electrolyte to combine with oxygen to form water, while the electrons go through an external circuit, creating electricity. A fuel cell thus requires air and hydrogen and only produces heat and water as by-products [27].

There are many different types of fuel cells depending on the kind of electrolyte they employ. In general, polymer electrolyte membrane (PEM) fuel cells are considered for mobility due to their high power density, low weight and low volume, and are therefore the only type of fuel cell considered in this report[3]. A distinction can also be made between different types of PEM fuel cells depending on their operating temperature. Near-term, low-temperature PEM (LTPEM) fuel cells offer the most feasible solution to aviation[4]. However, thermal management of LTPEM fuel cells is challenging. Therefore, novel high-temperature PEM (HTPEM) technology is under development that would reduce the complexity and weight of the thermal management system of a fuel cell, as the greater operating heat allows for a greater heat rejection[4]. In Table 8.3, the fuel cell types are compared to decide which is most suitable to be used for an aircraft in 2035. The specific power of the stack and the balance of plant, the operating temperature, the technology readiness level (TRL), and the resilience of the fuel cells against impurities and balance of plant failures are considered.

[3]https://www.energy.gov/eere/fuelcells/types-fuel-cells, last consulted June 3rd, 2022

[4]https://www.ati.org.uk/wp-content/uploads/2022/03/FZO-PPN-COM-0033-Fuel-Cells-Roadmap-Report.pdf, last consulted June 3rd, 2022

Table 8.3: Comparison between LTPEM and HTPEM fuel cell types.

Fuel cell type	Specific power $[kW/kg]$	Operating temperature $[^\circ C]$	TRL	Resilience
LTPEM	2.5	80	8	Poor
HTPEM	3.0	180	6	Good

Due to their higher operating temperature of $180\ [^\circ C]$, HTPEM fuel cell system architectures are less complex and therefore more lightweight[4]. Furthermore, HTPEM fuel cells use a hydrocarbon electrolyte that is more resistant to carbon oxide impurities in the hydrogen than the fluorocarbon electrolyte used in LTPEM [28]. Moreover, LTPEM fuel cells require a mechanism that regulates the humidification of the incoming air and hydrogen [28]. A failure of this system can result in the failure of the entire fuel cell. HTPEM fuel cells don't require humidification. The resilience of HTPEM fuel cells is thus rated as good, compared to a poor rating of LTPEM fuel cells. On the other hand, LTPEM fuel cell technology is more mature with a TRL of 8 in 2030 compared to a TRL of 6 for HTPEM fuel cells[4]. It is argued from these considerations that HTPEM fuel cell technology is preferred due to its low weight, simpler design and better resilience.

In order to size the fuel cell in more detail, the voltage and current density design point needs to be determined using a polarisation curve. The following equations are used to model the open circuit and cell voltage, which are used to obtain the polarisation curve [29].

$$V_{oc} = 1.18 - 0.0023 \cdot \frac{(T_{fc} - 298) + R \cdot T_{fc}}{4 \cdot F} \cdot \ln\left(p_{h2} + 0.5 p_{o2}\right) \tag{8.4}$$

$$V_{cell} = V_{oc} - \frac{R}{2 \cdot \alpha \cdot F} \cdot \ln\left(\frac{i_{cell} + i_{leak}}{i_0}\right) - r \cdot i_{cell} - c \cdot \ln\left(\frac{i_{lim}}{i_{lim} - i_{cell} - i_{leak}}\right) \tag{8.5}$$

In these equations, V_{oc} is the open-circuit voltage, which is calculated using fuel cell temperature T_{fc}, gas constant R, Faraday constant F and the partial pressures of hydrogen and oxygen in the fuel cell, p_{h2} and p_{o2}. Subsequently, the cell voltage is computed by subtracting the activation, ohmic and mass transport losses from the open-circuit voltage. The cathode transfer coefficient α, limit current density i_{lim}, leak current density i_{leak}, exchange current density i_0, area-specific resistance r, and mass transport loss constant c are used as set parameters. The values of the parameters used in these equations are displayed in Table 8.4 and are taken from LTPEM literature, changed slightly where applicable to match experimental results from existing HTPEM fuel cell technology[5] [27]. An array of cell current densities i_{cell} is passed through this equation to derive the polarisation curve.

Table 8.4: Fuel cell parameters used in fuel cell sizing.

$T_{fc}\ [K]$	$p_{h2}\ [bar]$	$p_{o2}\ [bar]$	$\alpha\ [-]$	$i_{leak}\ [A/m^2]$	$i_0\ [A/m^2]$	$i_{lim}\ [A/m^2]$	$r\ [\omega/m^2]$	$c\ [V]$
433	2.0	1.0	0.5	100	10^{-5}	20000	10^{-6}	0.5

[5]https://docsend.com/view/t9aw2mk, last consulted June 8th, 2022

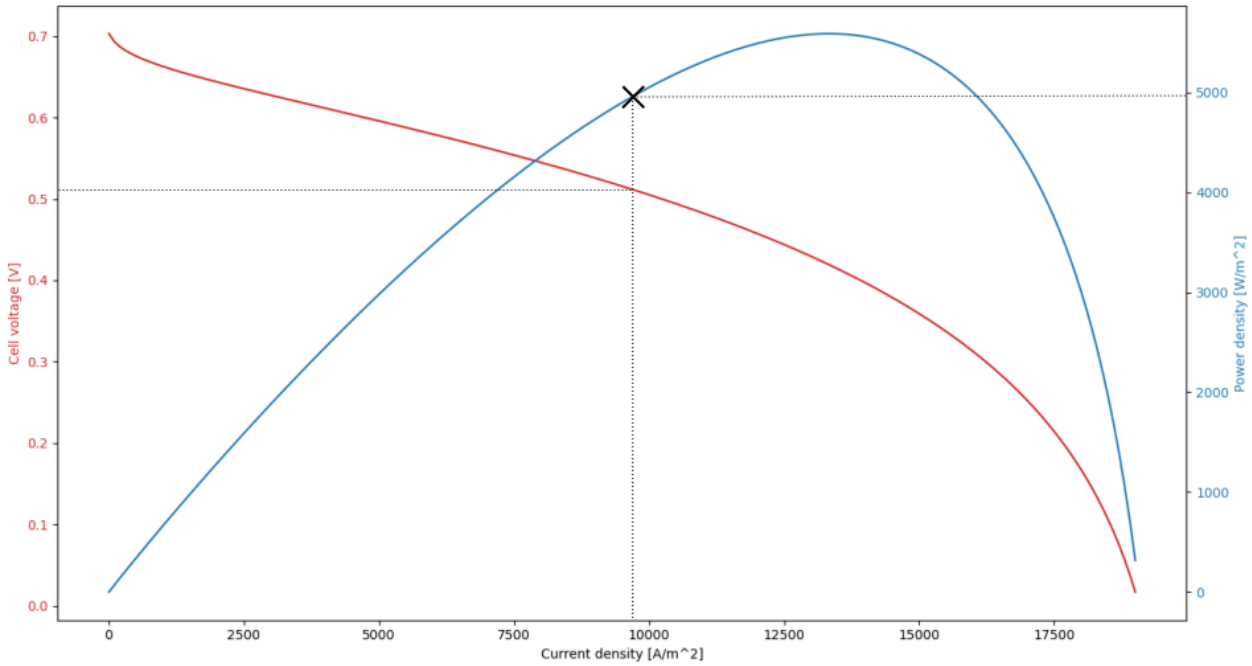

Figure 8.2: Polarisation curve of the fuel cell, with the design point marked with a cross.

From Figure 8.2, the design point can be located at a voltage of $0.51\ [V]$ and a current density of $9100\ [W/m^2]$. This point was determined by expressing the voltage and power density as ratios of their maximum values, and by optimising for the maximum of the summation of those values. Even though it would be tempting to choose the voltage at which maximum power density is achieved, it is preferred to choose a point with a higher efficiency. Because the fuel cell provides a continuous amount of power throughout the whole mission, the total required fuel cell area can be calculated by dividing the fuel cell cruise power by the current density, as can be seen in Equation 8.6. Subsequently, in Equation 8.7, the number of cells required can be found by dividing the total required cell area by an assumed single cell area of $0.096\ m^2$, which is a reasonable estimate for a PEM fuel cell [30]. Finally, the number of fuel cell stacks is determined using Equation 8.8.

$$A_{cell,total} = \frac{P_{cr}}{i_{design}} \quad (8.6) \qquad N_{cell} = \frac{A_{cell,total}}{A_{cell}} \quad (8.7) \qquad N_{stack} = \frac{V_{pow}}{V_{cell} \cdot N_{cell}} \quad (8.8)$$

It follows that two fuel cell stacks will be used, consisting of 1168 cells connected in series to obtain a voltage of $1191\ [V]$. The fuel cell stack shape is derived from HyPoint's design[5]. Here, a compressor is placed in the centre of the fuel cell stack. The compressor blows pressurised air through the fuel cell modules' built-in radial direction around the compressor. This allows for the fuel cell stack to obtain a cylindrical shape, which is aerodynamically advantageous. The size of fuel cell stacks is computed by assuming that 10 modules of cells can be placed around the compressor[5], and by assuming that the thickness of the fuel cells is $2\ [mm]$ [31]. A picture of the HyPoint fuel cell and the corresponding design for this project are shown in Figure 8.3a and Figure 8.3b.

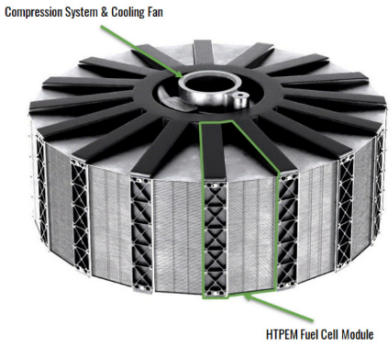

(a) Render of the HyPoint fuel cell[5].

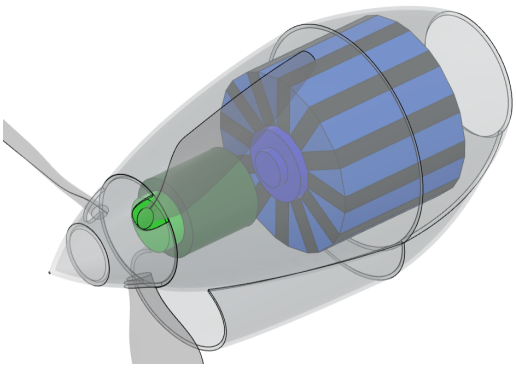

(b) Render of the wing-tip engine and fuel cell (in black and blue) sized in this project.

Figure 8.3: Renders of the chosen fuel cell architecture.

The final fuel cell sizing parameters are presented in Table 8.5. The weight is calculated using the de Vries method, and the stack surface area is derived using 3D modelling software. It should be noted that the weight, current, power, and surface area are given for a single stack.

Table 8.5: Final fuel cell parameters for one fuel cell stack.

Parameter	Value	Parameter	Value
n_{cells}	1168 $[-]$	V_{stack}	1191 $[V]$
$n_{modules}$	10 $[-]$	I_{stack}	874 $[A]$
h_{module}	0.295 $[m]$	P_{stack}	1041 $[kW]$
l_{module}	0.800 $[m]$	W_{stack}	413 $[kg]$
w_{module}	0.120 $[m]$	S_{stack}	3.72 $[m^2]$
n_{stacks}	2 $[-]$	η_{stack}	0.58 $[-]$

8.2.2. Balance of Plant

The purpose of the balance of plant is to cater for the operation of the fuel cell. More specifically, it should condition the air before it enters the cathode, the hydrogen before it enters the anode, and handle the exhaust water and heat. As explained before in Subsection 8.2.1, HTPEM fuel cells don't require extensive cathode conditioning, except for a compressor that pressurises the incoming air to improve the efficiency of the fuel cell.

Compressor

A compressor is used that pressurises the incoming air to improve the efficiency of the fuel cell. Next to this, the compressor is used to blow air through the fuel cell stack to cool it. The compressor can thus be sized by analysing the required mass flow of air for both the cooling and the cathode reaction. First, the generated heat of the fuel cell is calculated using Equation 8.9 [29]. Subsequently, the heat dissipation due to natural convection is calculated in Equation 8.10 [29]. These values can be used to calculate the required heat dissipation from the fan airflow in Equation 8.11. Lastly, the mass flow of air is calculated in Equation 8.12 [29].

$$\dot{Q}_{gen} = (V_{oc} - V_{cell}) I_{cell} n_{cell} \quad (8.9) \qquad \dot{Q}_{con} = \alpha_{air} S_{stack} (T_{fc} - T_{amb}) \quad (8.10)$$

$$\dot{Q}_{fan} = \dot{Q}_{gen} - \dot{Q}_{con} \quad (8.11) \qquad \dot{m}_{fan} = \frac{\dot{Q}_{fan}}{c_{p,air}(T_{fc} - T_{amb})} \quad (8.12)$$

In these equations, α_{air} is a convection constant, $c_{p,air}$ is the isobaric specific heat, S_{stack} is the surface area of the stack, and T_{amb} and T_{fc} are the ambient and fuel cell temperatures, respectively. The values of these parameters are presented in Table 8.6

Table 8.6: Parameters used in the fuel cell cooling computations.

α_{air} $[W/[m^2K]$	$c_{p,air}$ $[kJ/(kgK)]$	T_{amb} $[K]$
25[6]	1.006[7]	253[8]

Next to the cooling mass flow, the mass flow required for the cathode reaction needs to be calculated. The maximum between these values is used to size the compressor. The cathode reaction mass flow can be computed using Equation 8.13 [27].

$$\dot{m}_{cath} = \frac{M_{air} P_{stack} \lambda}{0.21 V_{cell} F} \quad (8.13) \qquad P_{com} = max(\dot{m}_{cath}, \dot{m}_{fan})(h_1 - h_3) \quad (8.14)$$

In this equation, M_{air} is the molar mass of air which equals 28.97 $[g/mol]$, and λ is the stoichiometric coefficient of the fuel cell, for which a value of 2 can be chosen [27]. Finally, the compressor power can be calculated using Equation 8.14, where h_1 and h_3 are the compressor enthalpies and are computed to be 307 $[kJ/kg]$ and 253 $[kJ/kg]$ respectively. The total efficiency of the fuel cell system, including the compressor, can thus be calculated utilising Equation 8.15, resulting in a fuel cell system efficiency of 51%.

$$\eta_{fc,system} = \frac{P_{stack}}{P_{stack} + \dot{Q}_{gen} + P_{com}} \quad (8.15)$$

Heat Exchanger

Before it is possible to use liquid hydrogen for energy generation, it should be vaporised and heated to room temperature[9]. The vaporisation is achieved by heating the liquid hydrogen after extracting it from the tank. Liquid hydrogen transfer lines should be vacuum insulated to prevent the forming of liquid air around it[9]. Therefore, it is desired to perform the initial vaporisation immediately after extraction from the tank. During this process the gaseous hydrogen will be heated such that liquid air forming is prevented.

The hydrogen that boils-off needs to be heated before it can be used in the fuel cell[9]. The hydrogen is first heated from around -253.15 $[°C]$ to -110.00 $[°C]$, to prevent dangerous formation of liquid oxygen around the hydrogen piping. Afterwards, the cold hydrogen gas can be used to cool down the electric components of the aircraft, including the batteries, electric motors, and power converters.

The first heat exchanger uses electrical tape to heat up the hydrogen to the required temperature. The power required for this heat exchange can be estimated using Equation 8.16 and Equation 8.17.

[6] https://www.engineeringtoolbox.com/overall-heat-transfer-coefficient-d_434.html, last consulted June 9th, 2022
[7] https://www.engineeringtoolbox.com/air-specific-heat-capacity-d_705.html, last consulted June 9th, 2022
[8] https://www.digitaldutch.com/atmoscalc/, last consulted June 9th, 2022
[9] https://www.airproducts.com/-/media/airproducts/files/en/900/900-13-082-us-liquid-hydrogen-safetygram-9.pdf, last consulted June 1, 2022

$$\dot{Q} = \dot{m}_{h2} c_{h2} (T_{out} - T_{in}) \tag{8.16}$$

$$\dot{m}_{h2} = 1.05 \cdot 10^{-8} \frac{P_{stack} \cdot n_{stack}}{V_{design}} \tag{8.17}$$ [10]

Table 8.7: Parameters used in the liquid hydrogen heating computations.

$c_{p,h2}$ $[kJ/(kgK)]$	T_{out} $[K]$	T_{in} [K]
14.304[11]	-253.15	-80.00

It follows that a power of 105 $[kW]$ is needed per fuel cell, which corresponds to a power of 210 $[kW]$ for both fuel cells. Incidentally, this is around 10% of the fuel cell power delivered during cruise. To take this power into account, the efficiency of the heating tape heat exchanger is taken to be 90%. The tube heat exchangers are discussed in more detail in Subsection 8.3.1. The final balance of plant sizing parameters can be found in Table 8.8.

Table 8.8: Final fuel cell parameters for one fuel cell stack

Parameter	Value	Parameter	Value
$\dot{Q}_{gen}$	747 $[kW]$	P_{comp}	221 $[kW]$
$\dot{Q}_{con}$	16.6 $[kW]$	$\dot{Q}_{hex}$	1191 $[kW]$
$\dot{Q}_{fan}$	730 $[kW]$	$\dot{m}_{h2}$	0.043 $[kg/s]$
$\dot{m}_{fan}$	4.09 $[kg/s]$	η_{hex}	0.90 $[-]$
$\dot{m}_{cath}$	3.50 $[kg/s]$	$\eta_{fc,system}$	0.51 $[-]$

8.2.3. Hydrogen Storage

With a gravimetric energy density of 120 $[MJ/kg]$, hydrogen is one of the lightest energy carriers. However, due to the low volumetric energy density of hydrogen, it cannot be stored under standard conditions for mobility applications [32]. Therefore, hydrogen is either pressurised to 350 or 700 $[bar]$, liquified by cooling it to cryogenic temperatures, or stored in a material-based fashion[12]. In this project, liquid hydrogen is argued to be the most feasible technology due to its high gravimetric and volumetric energy densities, low tank weight, and favourable tank shape which make it easier to integrate into aircraft compared to gaseous hydrogen storage [32].

At -252.87 $[°C]$, hydrogen liquefies[12]. Due to this low temperature, liquid hydrogen tanks need to be insulated to prevent excessive vaporisation, or boil-off, of the liquid hydrogen. The ideal insulation material will have low thermal conductivity and diffusivity, and a low mass density. Two insulation methods possess these properties; single-walled tanks with an additional insulation layer of aerogels or polymer foams, and double-walled tanks with a vacuum between the inner and outer tank wall, accompanied by multi-layer insulation (MLI) [33].

Aerogels have lower thermal conductivity than polymer foams, but are fragile and brittle due to their high porosity [33]. Polymer foams have a very low density and are easily applicable to complex shapes, but suffer from higher thermal conductivity compared to aerogel and vacuum insulation [33]. Finally, vacuum insulation has the lowest thermal conductivity. However, to maintain the vacuum, a more complex and heavier system is compared to the other insulation methods [33]. Considering these properties, it was decided to design the hydrogen tank using vacuum insulation. Due to the low thermal conductivity of this type of tank, the boil-off

[10] https://onlinelibrary.wiley.com/doi/pdf/10.1002/9781118878330.app2, last consulted June 13th, 2022
[11] https://www.engineeringtoolbox.com/hydrogen-d_976.html, last consulted June 14th, 2022
[12] https://www.energy.gov/eere/fuelcells/hydrogen-storage, last consulted June 9th, 2022

mass flow can be matched to the hydrogen consumption of the fuel cell. This prevents dangerous build-up of pressure in the tank or the venting of hydrogen into the atmosphere, which is a greenhouse gas in itself and thus incompatible with the project's top-level requirements[13].

A double-walled storage vessel has two concentric tank shells, with a layer of vacuum in between. The only significant heat transfer into the tank comes from the conduction of heat of the support structure used to connect the inner and outer tank, the conduction through the piping used to fill and extract the hydrogen, and radiation [15]. MLI can be used to significantly reduce the heat transfer through radiation, such that conduction through the tank connections becomes the main source of heat. Therefore, the shape and size of the tank do not drive the sizing of the liquid hydrogen tank, but rather the structural design and material choice of the tank connections [15]. A detailed structural design of a liquid hydrogen tank falls outside the scope of this project. Thus, a general sizing of the hydrogen storage system is provided, including an estimation of its weight, size and shape.

The weight of the hydrogen fuel is calculated by computing the sum of the liquid hydrogen energy needed per phase, and dividing it by the lower heating value of hydrogen, which is $120\ [J/kg]$[14]. To compute the tank weight, the fuel weight is divided by a gravimetric efficiency, as per Equation 8.19. The gravimetric efficiency of a double-walled vacuum insulated liquid hydrogen tank for a regional turboprop aircraft is estimated to be 0.61[15] in 2030. This value includes both the tank and the heat exchanger used to condition the hydrogen to be used in the fuel cell.

$$W_{fuel} = \frac{E_{LH2}}{LHV_{LH2}} \tag{8.18}$$

$$W_{tank} = \frac{W_{fuel}}{GE} - W_{fuel} \tag{8.19}$$

Due to the concentric shelves, the shape of the tank will be a capsule. The tank is sized by dividing the fuel weight by the density of liquid hydrogen to obtain the required volume of hydrogen. A filling ratio of 0.9 is applied as a safety factor to account for boil-off during operation, as can be seen in Equation 8.20. This additional amount of space will prevent the need for immediate venting if a small amount of hydrogen boils off. Next, the length of the tank can be calculated using Equation 8.21 and by assuming an inner tank radius of $1.00\ [m]$, which leaves ample space for the vacuum insulation layer and a piping system between the outer tank and fuselage wall. Finally, a vacuum layer thickness of $0.10\ [m]$ is assumed to arrive at a final tank radius of $1.20\ [m]$ and a length of $2.28\ [m]$. A summary of the hydrogen tank parameters can be seen in Table 8.9.

$$V_{tank} = \frac{W_{fuel}}{\rho_{LH2} FR} \tag{8.20}$$

$$l_{tank} = \frac{V_{tank}}{\pi r_{tank}^2} + \frac{2}{3} r_{tank} \tag{8.21}$$

Table 8.9: Final liquid hydrogen tank parameters.

Parameter	Value	Parameter	Value
E_{LH2}	10030 $[kWh]$	r_{inner}	1.00 $[m]$
W_{fuel}	301 $[kg]$	l_{inner}	2.17 $[m]$
FR	0.90 $[-]$	r_{outer}	1.20 $[m]$
V_{tank}	4.72 $[m^3]$	l_{outer}	2.37 $[m]$
W_{tank}	192 $[kg]$	$W_{LH2,system}$	493 $[kg]$

[13]https://assets.publishing.service.gov.uk/government/uploads/system/uploads/attachment_data/file/1067144/atmospheric-implications-of-increased-hydrogen-use.pdf, last consulted June 9th, 2022

[14]https://h2tools.org/hyarc/calculator-tools/lower-and-higher-heating-values-fuels, last consulted June 14th, 2022

[15]https://www.ati.org.uk/wp-content/uploads/2022/03/FZO-PPN-COM-0027-Cryogenic-Hydrogen-Fuel-System-and-Storage-Roadmap-Report.pdf, last consulted June 9th, 2022

8.2.4. Battery Storage

Batteries are used to power the aircraft during taxiing, provide additional power during take-off and climb, and to harvest energy during regenerative descent. To size the batteries, they need to be sized for both power and energy. Equation 8.23 and Equation 8.24 describe the equations used to size the batteries. Next to this, the degradation of the battery is reduced by never discharging the battery beyond a depth of discharge (DOD) of 80%, and never charging beyond a DOD of 10%. Furthermore, the battery is sized for an end-of-life condition where only 85% of its capacity is usable, as per Equation 8.22.

$$E_{bat,EOL} = \frac{E_{bat,req}}{\eta_{EOL}(DOD_{dis} - DOD_{cha})} \tag{8.22}$$

Using the method described in Section 8.1, a maximum battery power of $3457\ [kW]$ was calculated, and a total required energy of $1335\ [kWh]$. Furthermore, on a cell level, a gravimetric power density of $1.0\ [kW/kg]$ and a gravimetric energy density of $0.5\ [kWh/kg]$ are assumed [34] [6].

$$W_{bat,cell} = \frac{P_{bat,req}}{GPD_{bat}} \tag{8.23}$$

$$W_{bat,cell} = \frac{E_{bat,EOL}}{GED_{bat}} \tag{8.24}$$

The total cell weight is thus the maximum value between the power and the energy-sized battery, and equals $4514\ [kg]$. To design the battery in more detail the physical dimensions of the battery cell and the cell packing need to be considered. There are ample methods by which battery cells can be manufactured. For example, Tesla used cylindrical cells for their cars, while other automotive companies such as BMW and Chevrolet use prismatic and pouch cells, respectively [35]. Cylindrical cells have the advantage of being small, safe and comparably cheap [35]. On the other hand, prismatic cells are considerably larger and have a larger cell capacity [35]. Pouch cells are also characterised by higher cell capacity, but due to their low internal resistance also poses a safety hazard [35]. Due to the relatively low cost compared to prismatic cells, and lower safety hazard compared to pouch cells, a cylindrical cell architecture was chosen for this design.

The cylindrical cell design will be based on the Panasonic 4680 Li-ion battery[16]. The battery is divided into 105 modules connected in parallel. The modules consist of 8 layers of cells stacked on top of each other and connected in series, with an average of 37 cells per layer, which are also connected in series. This configuration makes sure that both batteries can provide the required power and energy, and that they roughly match the voltage of the fuel cell. The final battery parameters are shown in Table 8.10.

Table 8.10: Final fuel cell parameters for one fuel cell stack

Parameter	Value	Parameter	Value
$E_{bat,EOL}$	1335 $[kWh]$	$n_{cells,lay}$	37.125 (avg.) $[-]$
$P_{bat,req}$	3457 $[kW]$	V_{cell}	3.7 $[V]$
$W_{bat,pack}$	4514 $[kg]$	V_{bat}	1099 $[V]$
$n_{modules}$	105 $[-]$	r_{cell}	0.046 $[m]$
n_{layers}	8 $[-]$	h_{cell}	0.080 $[m]$

[16] https://somanytech.com/what-is-tesla-4680-battery-specs-detail-specification, last consulted June 10th, 2022

8.2.5. Electrical Powertrain Components & Gearbox

The battery management system, DC-DC converter, power management unit, inverter, and electric motor are sized according to the method by de Vries [6]. Their weights can be estimated by using the maximum power calculated for these components over the entire mission profile and dividing it by the specific power, as seen in Equation 8.25. The specific powers of these components are derived from literature and summarised in Table 8.11[17]. The gearbox weight is empirically established using equation Equation 8.26 [36].

$$W_{comp} = \frac{P_{comp,max}}{SP_{comp}} \tag{8.25}$$

$$W_{gb} = k \cdot (1.34 \cdot P_{gb}^{0.76}) \frac{\omega_{em}^{0.13}}{\omega_p^{0.89}} \tag{8.26}$$

The gearbox weight is thus computed using the maximum gearbox power P_{gb}, electric motor speed ω_{em} and propeller speed ω_p, and a fudge factor k to take into account future improvements in gearbox design. The electric motor speed is assumed to be $10,000\ [RPM]$[18], while the propeller speed is defined in Chapter 9. For k, a value of 26 is used [37]. The final gearbox weights are displayed in Table 8.11.

Table 8.11: Maximum powers, specific powers and weights of electrical components in the powertrain per engine, and total powertrain weights.

Component	**Max power** $[kW]$	**Specific power** $[kW/kg]$	**Weight** $[kg]$
BMS	3440	40	86
DC-DC converter	3405	40	85
Power management	5477	40	137
Inverter 1	400	40	10
Electric motor 1	393	23	17
Gearbox 1	377	-	9
Inverter 2	1730	40	43
Electric motor 2	1695	23	74
Gearbox 2	1627	-	38
Total engine 1	2262	10.5	216
Total engine 2	3254	10.5	310
Total battery system	3405	0.7	4685
Total hydrogen system	2755	2.1	1319
Total powertrain	5217	0.8	6530

[17] https://www.ati.org.uk/wp-content/uploads/2022/03/FZO-PPN-COM-0030-Electrical-Propulsion-Systems-Roadmap-Report.pdf, last consulted June 10th, 2022

[18] https://www.h3x.tech/#motor, last consulted June 10th, 2022

8.3. Powertrain Integration

With the powertrain components sized, the integration of these components with each other and with the rest of the aircraft can be considered. First, the thermal management and performance of the powertrain are discussed. Afterwards, the physical integration of the powertrain is presented, along with the final detailed architecture.

8.3.1. Thermal Management

Sufficient cooling should be provided to prevent the battery pack from overheating and other electric components. However, the cooling of the battery packs cannot be achieved by an air-cooling system because of the low thermal conductivity of polymers [38]. A liquid cooling system will be installed in the aircraft, since this method of cooling has good thermal management performance and is commonly used in other industries [39].

Since both a heating system for the liquid hydrogen and a cooling system for the battery pack is required, it is desired to combine the thermal flows into a heat exchange system. For this design a counterflow heat exchanger is selected, since the performance of this type is superior compared to other types [40]. During the sizing process 3M Novec 7200 Engineering Fluid was taken as cooling fluid, because of its desired boiling and freezing point[19].

For the sizing of the heat exchanger, the assumption was made that heat is only transferred between fluids and gasses and heat is not transferred between the heat exchanger and the surroundings. Therefore, the energy input is equal to the energy output resulting in Equation 8.27. In this formula $\dot{m}$ is the mass flow, c_p is the specific heat constant, T is the temperature, U is the convection heat transfer coefficient, and A the contact area. The subscript h represents the hot gas, c the cold gas, i the incoming flow and o the outgoing flow [40].

$$\dot{m}_h c_{ph}(T_{hi} - T_{ho}) = \dot{m}_c c_{pc}(T_{co} - T_{ci}) = UA\Delta T_{mean} = Q \tag{8.27}$$

From the input and output temperatures and the mass flow of the gaseous hydrogen, the mass flow of the coolant can be determined. An important parameter in Equation 8.27 is the convection heat transfer coefficient U. This parameter is dependent on the type and state of the used substances within the heat exchanger and represents the ability to transfer heat to another substance. The heat transfer between two substances in a thin-walled tube can be estimated by combining the individual coefficients as shown in Equation 8.28. Since limited data on the heat transfer coefficient is available an estimation was made. Due to the fact the substances are flowing through tubes, forced convection was assumed. It was concluded that gasses have a much lower coefficient value compared to liquids[20]. Therefore, the coefficient of the gaseous hydrogen was set to $20\ [W/(m^2K)]$ and the coefficient of the coolant was set to $1200\ [W/(m^2K)]$.

$$\frac{1}{U} = \frac{1}{h_h} + \frac{1}{h_c} \tag{8.28}$$

The mean temperature difference ΔT_{mean} can be computed with the input and output temperatures of the fluids/gasses as shown in Equation 8.29 and is dependent on the type of heat exchanger used [40]. From this, the contact area for the heat exchanger can be calculated, resulting in a contact area of $1.748\ [m^2]$.

$$\Delta T_{mean} = \frac{(T_{hi} - T_{co})(T_{ho} - T_{ci})}{\ln\left(\frac{T_{hi} - T_{co}}{T_{ho} - T_{ci}}\right)} \tag{8.29}$$

Difficulties with this system arise when the batteries are either not active or being recharged. Both of these scenarios would result into insufficient cooling capabilities with this heat exchanger only. Recharging will be performed during ground operations and descent when recharging the batteries. During ground operations,

[19] https://multimedia.3m.com/mws/media/199819O/3m-novec-7200-engineered-fluid-en.pdf, last consulted 3 June, 2022
[20] https://www.thermopedia.com/content/841/, last consulted 3 June, 2022

the fuel cells are turned off and no hydrogen flow is present. Furthermore, the fuel cell system is sized for the cruise phase, resulting in no heat flow from the batteries since these are turned off. To solve these issues, a connection to the battery cooling line is integrated into the design, ensuring cooling can be provided from the ground during the recharging procedure. Since the hydrogen has to be preheated before it can enter the heat exchanger, this system will be designed to be capable of heating the hydrogen to $20°C$. Therefore, part of the hydrogen heating system will be switched off when the heat exchanger is active.

8.3.2. Physical Integration

Finally, the electric components, thermal management system, and reactant systems need to be physically integrated into the aircraft. An overview of the detailed powertrain architecture is provided in Figure 8.5. The battery and DC-DC converters are integrated into the fuselage, visible as the right box in Figure 8.4b. In each engine nacelle, the inverters, electric motors and gearboxes are located. The gearbox is coloured light green in Figure 8.3b, and the inverter and electric motor combination is shown in darker green. Additionally, the compressors and fuel cells are incorporated into the wing tip engines, in order to accommodate for air cooling of the fuel cells, and to relieve the bending load of the wings during landing. They are depicted in dark blue and lighter blue combined with black, respectively.

As presented in Figure 8.4b, the liquid hydrogen tank and tape heat exchanger are fitted in the tailcone, behind the pressure bulkhead. The tube heat exchangers are inside the wing, such that the size of the electric component cooling system can be minimised, as can be seen in Figure 8.4a. Due to the aft position of the wings, hydrogen can easily flow to the fuel cells at the tip of the wing, further away from the passenger cabin than in a conventional wing position. This prevents any direct danger to passengers due to hydrogen leakage. However, to prevent hydrogen from building up and potentially catching fire or exploding during a leak, leakage sensors will be placed along the span of the wing. A safety protocol will have to be devised that can take adequate measures during a leak, such as preventing hydrogen from flowing to the leak by closing certain valves. Moreover, during the event of a leak, the affected area needs to be ventilated. However, the detailed design of such a safety system falls outside the scope of this conceptual design, and therefore has to be considered for further development of the aircraft.

Lastly, the battery pack fits into the same cross-sectional area as the cargo compartment, as per Figure 8.4b. Even though the batteries could fit into the wing, their placement in the fuselage was necessary due to lateral tip-over stability considerations explained in Subsection 10.6.2. An overview of the final powertrain architecture can be found in Figure 8.5.

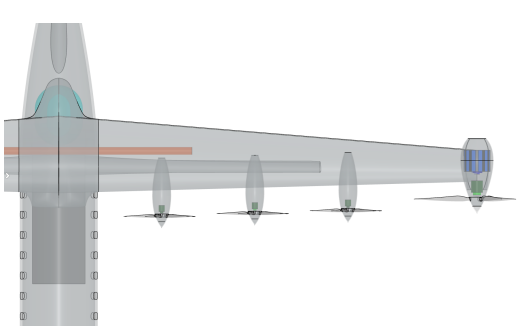

(a) Top view of the powertrain components in the wing and fuselage.

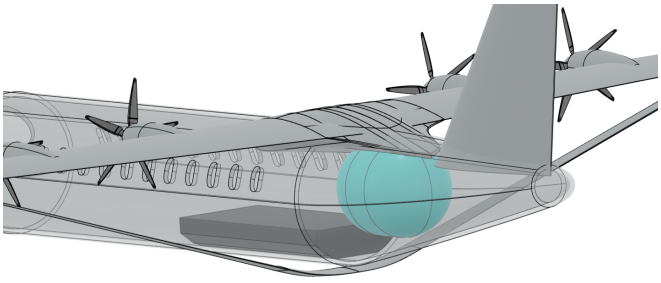

(b) Isometric view of the powertrain components in the fuselage, with the batteries displayed in black, and the liquid hydrogen tank in light blue.

Figure 8.4: Renders of the physical integration of the powertrain components into the aircraft

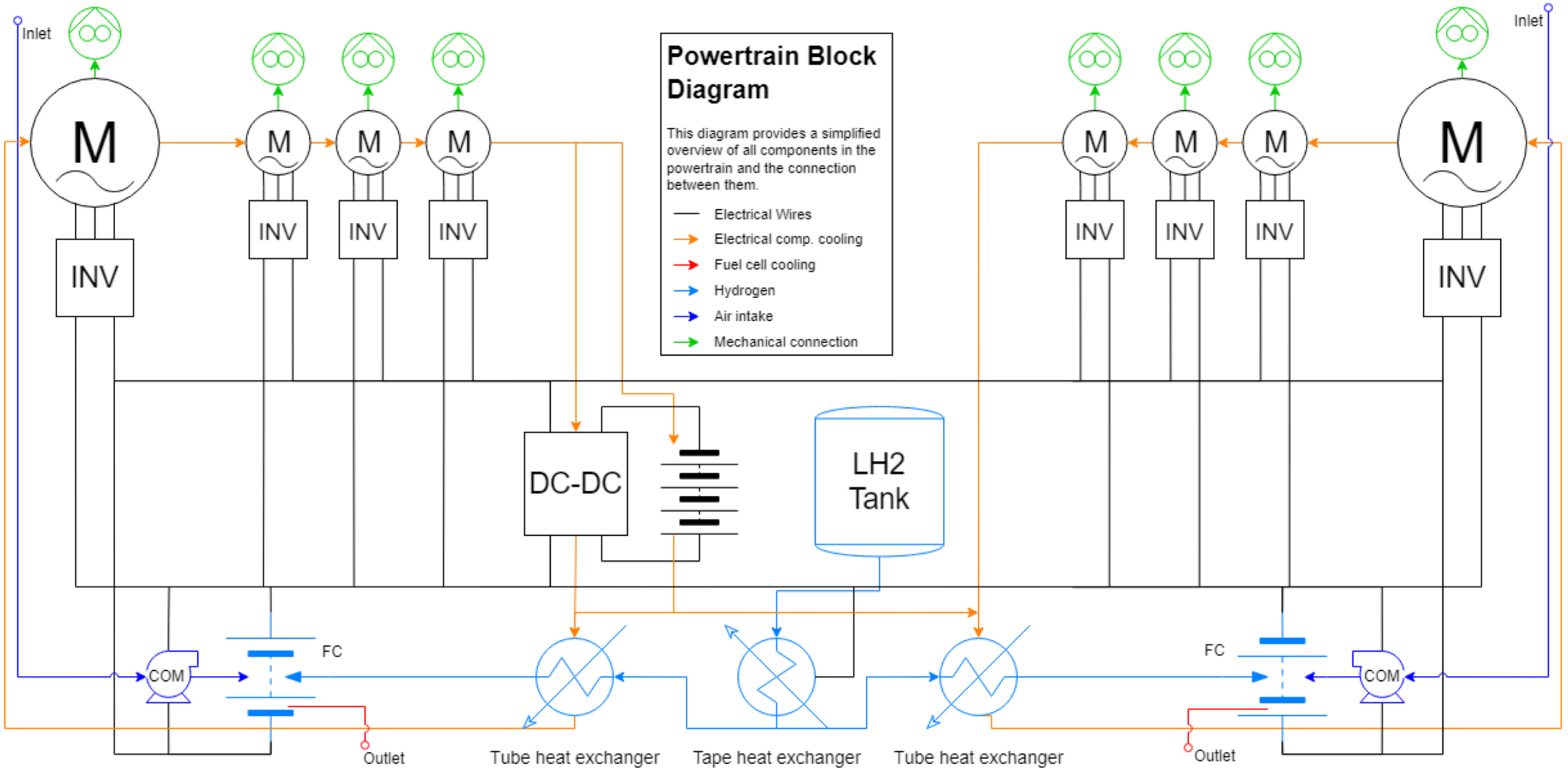

Figure 8.5: Block diagram of the powertrain components and their connections.

9

Propulsion Design

The lack of weight- and efficiency penalties when scaling down electric motors allows for the strategic placement of multiple smaller electric motors over an airframe [41]. This opens up the possibility to enhance aerodynamic performance by optimising aero-propulsive interaction, as well as allowing potential control force augmentation, and boundary layer ingestion. Apart from these advantages of distributed propulsion effects, electric powertrains also allow for energy regeneration when decelerating, similarly to regenerative braking in an electric car. This chapter presents the design of the distributed propulsion system of this aircraft, which leverages regenerative capabilities. Section 9.1 shows how the propulsors were distributed over the airframe, and Section 9.2 explains how the propellers themselves were designed. The regenerative performance of the obtained propellers will be discussed in Section 9.3. Finally, the accuracy and limitations of the methods used will be treated in Section 9.4.

9.1. Amount of Propulsors and their Placement

This section will present how the propulsors have been placed over the airframe. It starts by introducing the objectives of using distributed propulsion (DP), and continues by concluding on a general system concept.

Placement of propellers near a lifting surface can be used to enhance the lift of this surface, because the incoming flow is energized by the propeller. Because weight reduction is one of the main goals of the design, a propeller array on the main wing was used to enhance lift performance, and therefore allow for a smaller wing.

Apart from increasing the lift of the main wing, propellers can also be used to reduce lift-induced drag, arriving at a higher lift over drag ratio. Propeller placement at the wingtips is most often used to reduce drag, by counteracting the wingtip vortex and therefore reducing the lift induced drag. Research has shown that a reduction of 15% in induced drag can be achieved for certain thrust settings [42]. Placing a propeller at the wingtip could impose problems due to the increased wing root bending moment it causes during ground operations, but as the concept considered in this study involves a truss, this is deemed acceptable. During flight, the wing root bending moment is reduced by placing a weight far outboard on the wing.

With the need for a combination of a lift enhancing propeller array and a drag reducing wingtip propeller clear, the concept could be detailed further. A trade-off between tractor and pusher configurations was performed, taking the following points into account:

- Both configurations increase effective span efficiency when the propeller is placed at the wingtip [43].
- The power consumption of a pusher configuration was found to be up to 9% lower than that of a tractor configuration [43][8].
- The pusher configuration shows better potential for energy harvesting in negative thrust setting, because in case of a tractor configuration, the sectional lift behind an energy harvesting propeller would be decreased drastically [43].
- The pusher configuration is generally noisier [44].
- The tractor configuration allows for a larger lift increase [43].
- The pusher configuration might interfere with control surfaces and high lift devices placed on the trailing edge of a wing.

Because of the noise penalty and the interference with control surfaces like ailerons, the pusher configuration was discarded for the wing array. Over-the-wing placement was considered as well, since it has less negative impact on the lift distribution and therefore lift-induced drag, but due to its complexity and lower absolute lift increase, it was discarded in favour of leading edge placement for the wing array [6].

For the wingtip propeller, both pusher and tractor configurations would perform well. The interference with control surfaces or high lift devices of pusher configurations is not applicable at the wingtip, and in previous research the pusher configuration showed a lower power consumption for a given lift and thrust force coefficient [43]. However, a tractor configuration was chosen because of the high noise penalty that a pusher propeller incurs. If this noise penalty can be overcome, implementing a method to analyse a pusher configuration for the wingtip propellers would be a fruitful area for further research.

The number of distributed propulsors was fixed before starting the propeller design process as an optimal value could be determined by inspecting constraints and objectives of the propulsion system. Indeed, accelerating the airflow only over some sections of the wing would lead to a less uniform wing lift distribution compared to accelerating it over a larger fraction of the span of the wing. This would lead to a reduction of the Oswald efficiency factor of the wing, effectively increasing its induced drag. The goal was thus to choose a number of propellers that would allow to span the whole wing, while taking into account the preliminary dimensions of the wingtip propellers based on the ATR 42-600's propellers[1] as well as a margin of 1 meter from the fuselage and margins of 5% of the propeller diameter between each propeller to avoid possible dangerous collisions between blades. It was found that two distributed propellers per side of the aircraft would require a diameter that would likely interfere with the aircraft lateral clearances limits to provide accelerated flow over the whole wing.

On the other hand, increasing the number of array propellers to four per side of the aircraft would constrain their diameter to be 25% less than when using three propulsors, to fit on the half-span of the wing. As the thrust and power both scale with the square of a propeller's diameter, this 25% diameter reduction would lead to a power reduction of 43.75% per propeller, assuming the blade number and geometry are kept the same. Thus, with four propulsors instead of three, a total power reduction of 25% can be expected if the chord and blade number were kept the same. This means that the distributed propeller's blade chord would have to be larger to produce the same combined power as a 3 propulsors combination, reducing the aspect ratio of the blades and reducing the propeller efficiency. Alternatively, the blade number could be increased, inducing weight penalties. Furthermore, studies by de Vries have shown that increasing the number of distributed propulsors from three to four present marginal increase in wing aerodynamic performance [6]. It was thus decided to set the number of distributed propulsors to three per aircraft side.

9.2. Propeller Design

With the placement and main functions of the propulsors derived from literature, the design can be extended to a propeller level. This is done using a method incorporating blade element momentum (BEM) theory. Subsection 9.2.1 describes the choice of airfoil used while Subsection 9.2.2 investigates the propellers sizing in more detail. Results are presented in Subsection 9.2.3.

9.2.1. Airfoil selection

In order to reduce complexity and computational cost of the propeller design, the number of design variables was reduced by choosing a constant propeller airfoil. It is both constant between all propellers (wingtip and array) as well as along the blade span of every single propeller. In reality, thicker airfoils would have to be used near the root to provide enough structural strength during operation. However, some thicker airfoils (such as the MH112-il airfoil[2]) achieve similar lift over drag ratio as airfoils used for more outboard sections of propellers. Additionally, the section near the hub of the propellers has a low contribution to the total thrust and torque. Thus, the inaccuracies induced by this assumption are deemed acceptable.

Research by Teeuwen [45] confirmed that evaluating only the camber and thickness to chord ratio (t/c) of an airfoil gives for a sufficient level of comparison to choose an airfoil in conceptual design stages. Apart

[1] https://www.atr-aircraft.com/our-aircraft/atr-42-600/, last consulted June 21, 2022
[2] http://airfoiltools.com/airfoil/details?airfoil=mh112-il

from these two airfoil parameters, availability of verifiable performance data was also deemed an important factor in the airfoil choice.

In general, cambered airfoils have a higher lift over drag ratio than symmetric airfoils [45]. A lower t/c increases the critical Mach number and therefore postpones the occurrence of drag divergence on the airfoil [46]. Together with the need for availability of performance data, this limited the search for an airfoil. Two options that were considered were the HAM-STD HS1-606 airfoil[3] and the Gilbert Morris GM15 F1C airfoil[4]. Based on research from Wisniewski et al. [47], the GM15 airfoil was chosen because of its favourable lift over drag ratio, without a penalty in aerodynamic efficiency or noise production.

9.2.2. Design Procedure

As will be investigated in more detail in Section 12.1, the highest amount of energy is consumed during cruise for both DOC and harmonic ranges. As the aircraft is optimised for DOC range, the parameters of this mission profile, namely mission energy, will be used to perform the propeller design and optimisation. Thus, the wing tip propellers were sized for cruise efficiency, limiting emissions and costs linked to energy usage. As the array propellers are mainly present for lift enhancement, these will not be powered during cruise, and folded backward to reduce drag. This also allows the distributed propellers to be fixed-pitch since they do not have to operate at a large free stream velocity range, unlike the wingtip propellers. The complexity and the mass of the distributed propulsors will thus be decreased due to this. The wingtip propellers should then be able to power the aircraft during cruise by themselves. They will also be used during all other flight phases which meant that a pitch variation system was necessary to maintain optimal efficiency throughout the whole flight.

As mentioned in Section 9.1, the number of distributed propulsors have been fixed which constrains their size and maximum power output. Thus, the efficiency and mass are influenced negatively when too much power is required. For this reason, propeller combinations where wingtip propellers are also designed for high take-off power in addition to cruise efficiency will be investigated as well.

Next to providing accelerated flow for the main wing, the goal of the propulsion design is to minimise the overall energy consumption of the aircraft. Feasible propeller combinations will thus be assessed based on their efficiencies weighted by a preliminary estimate of the output energy required at each flight phase of the DOC mission, accordingly to Equation 9.1, where χ is the fraction of power delivered by the wingtip propellers during a particular flight phase. These energies were computed using the procedure described in Section 12.1 by assuming propeller efficiencies of 1. Some considerations will also be given for system mass and lift enhancement potential.

$$\eta_{tot} = \frac{1}{E_{tot}}[\eta_{WT_{cr}} E_{cr} + (\eta_{AR_{TO}}(1-\chi_{TO}) + \eta_{WT_{TO}}\chi_{TO})E_{TO} + (\eta_{AR_{climb}}(1-\chi_{climb}) + \eta_{WT_{climb}}\chi_{climb})E_{climb}] \tag{9.1}$$

Blade Element Momentum Theory

The blade element momentum (BEM) theory combines blade element theory and momentum theory to determine the performance of a propeller. This theory is used throughout the design procedure of the propulsion subsystem for optimising the propeller blade's planform and computing the propeller's performance under different operating conditions.

Blade element theory allows to compute forces on each section that a propeller blade has been divided into. The propeller blades are first divided into small radial sections of radius dr, from the propeller hub until the blades' tip as shown in Figure 9.1. As a first estimate, hub to blade diameter ratio of 0.25 and 0.3 are considered for sizing wingtip propellers and distributed propellers, respectively [48]. This accounts for space to fit a pitch variation system of wingtip propellers and the folding mechanism of the distributed propellers. The number of blade sections were then considered. The mesh was refined until the results converged, which occured when blade elements of 3% of the tip radius were used. This led to 25 sections of equal size,

[3] http://airfoiltools.com/airfoil/details?airfoil=hs1606-il
[4] http://airfoiltools.com/airfoil/details?airfoil=gm15sm-il

from $r = 0.25$ (or $r = 0.30$, for distributed propellers) to $r = 0.99$, which is comparable and even slightly greater than the amount of sections used in previous research [49].

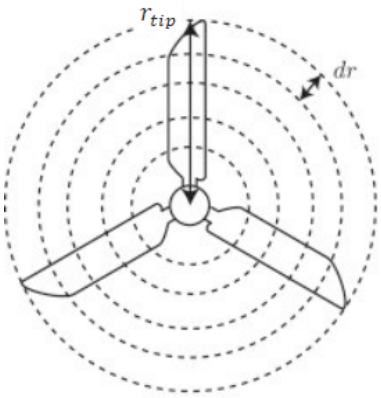

Figure 9.1: Decomposition of propeller blades into radial sections [50].

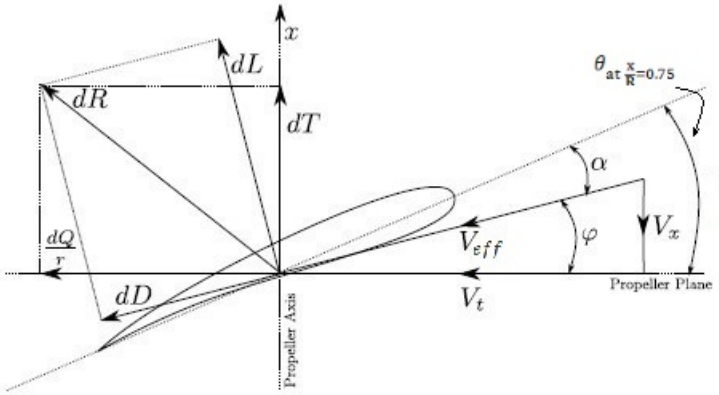

Figure 9.2: Flow and force elements around a propeller blade element [51].

For each blade element obtained, a top view is obtained and shown in Figure 9.2. An incoming air flow of axial velocity V_x impinges on the propeller airfoil, which rotates at an angular velocity Ω, which in turn generates a tangential flow component V_t. This rotational components adds to the axial flow velocity, leading to an effective flow vector V_{eff} angled at an angle of attack α with respect to the airfoil's chord line. Given the blade element chord as well as air density and temperature, the Reynolds number can be computed.

Using XFOIL[5], the lift and drag coefficients of the selected airfoil are obtained for various Reynolds numbers at zero Mach number. For each blade element, the corresponding flow Reynolds number and angle of attack are linearly interpolated to obtain the corresponding lift and drag coefficient. These coefficients are then corrected for compressibility by applying the Prandtl-Glauert correction factor shown in Equation 9.2 and Equation 9.3 [52].

$$C_l = \frac{C_{l_{M=0}}}{\sqrt{1-M^2}} \tag{9.2}$$

$$C_d = C_{d_f} + \frac{C_{d_{p_{M=0}}}}{\sqrt{1-M^2}} \tag{9.3}$$

The Prandtl-Glauert correction becomes increasingly inaccurate as the Mach number increases, especially when the drag divergence Mach number (M_{dd}) is approached. The drag divergence Mach number can be estimated using the Korn relation, shown in Equation 9.4 [53].

$$M_{dd} = \kappa - \frac{c_{l_{M=0}}}{10} - \frac{t}{c} \tag{9.4}$$

As the GM15 airfoil has been designed for transonic performance similarly to the NACA 16-series, it was assumed to have the same technology factor of $\kappa = 0.87$ [53], leading to a drag divergence Mach number of 0.74. When designing propellers, flows up to Mach 0.9 can be encountered at the blade tip[6]. For this reason, when the flow surpasses the drag divergence Mach number, it was decided to correct the lift and drag coefficients using the Kaplan relation shown in Equation 9.5 and Equation 9.6 as used by Teeuwen [53], since such correction is best fitted for transonic regimes.

$$C_l = C_{l_{M=0}} \mu_k \frac{1-M^2}{1-M_{dd}^2} \tag{9.5}$$

$$C_d = C_{d_{M=0}} + (\frac{M-M_{dd}}{1-M_{dd}})^3 \tag{9.6}$$

[5]https://web.mit.edu/drela/Public/web/xfoil/, last consulted June 12, 2022
[6]https://www.kitplanes.com/wind-tunnel-52/#, last consulted June 11, 2022

$$\mu_k = \mu_{PG} + \frac{\frac{t}{c}}{1+\frac{t}{c}}[\mu_{PG}(\mu_{PG}-1) + \frac{1}{4}(\gamma+1)(\mu_{PG}^2-1)^2] \tag{9.7}$$

where μ_{PG} is the Prandtl-Glauert correction factor mentioned in Equation 9.2.

Once the lift and drag coefficients have been corrected, by summing all blade elements, the thrust and shaft power needed are computed in Equation 9.8 and Equation 9.9.

$$T = \frac{B}{2}\int_{r_{hub}}^{r_{tip}} \rho V_{eff}^2 c(C_l \cos\varphi - C_d \sin\varphi)dr \tag{9.8}$$

$$P = \Omega\frac{B}{2}\int_{r_{hub}}^{r_{tip}} \rho V_{eff}^2 c(C_l \sin\varphi + C_d \cos\varphi)rdr \tag{9.9}$$

The incoming axial flow is altered by the thrust produced by the propeller and thus differs from the free stream velocity by a so-called axial induction factor, a, such that $V_x = V_\infty(1+a)$. The same applies for the rotational component of the flow which is impacted by the rotation of the propeller by a so-called rotational induction factor a' when it reaches the blade. This effectively reduces the tangential velocity to $V_t = \Omega r(1-a')$. When computing blade element theory, these factors are not known in advance. A way to obtain the axial and rotational induction factors is to use momentum theory which states that the thrust produced at a radial section r should be equal to the change in momentum of the flow. Similar theory applies for the torque produced and change in angular momentum of the flow which should be equal. Initial values of 0 are used for both a and a' and are iterated over, based on the thrust and torque produced by each blade element until their errors are within reasonable bounds (<0.01% difference) [54]. To facilitate the convergence of this process, a relaxation factor of 0.2 was used.

Similar to an aircraft wing, a propeller blade is finite and its analysis differs from the approach taken for an airfoil. Indeed, airflow near the tip tends to flow from the pressure side to the suction side of the blade, effectively reducing the forces produced. This is accounted for by using the Prandtl tip- and hub loss correction factors shown in Equation 9.10 and Equation 9.11 [55]. These are included when computing the axial and rotational induction factors by reducing the thrust and torque contributions to the conservation of momentum equations.

$$F = \frac{2}{\pi}\arccos e^{-f} \tag{9.10}$$

$$\begin{aligned} f_{tip} &= \frac{B}{2}\frac{r_{tip}-r}{r\sin\varphi} \\ f_{hub} &= \frac{B}{2}\frac{r-r_{hub}}{r\sin\varphi} \end{aligned} \tag{9.11}$$

After convergence of the induction factors, the efficiency of the propeller can be computed with equation Equation 9.12.

$$\eta_{prop} = \frac{TV_\infty}{P} \tag{9.12}$$

Application to wingtip and array propeller design

The wingtip propellers are sized using the method proposed by Liebeck et al. [54], which makes use of the BEM theory while adding several modifications to make it suitable for the design of optimum propellers. At each radial section, the angle of the blade element is computed as the sum of the flow angle and the required angle of attack as shown in Figure 9.2. The angle of attack is chosen such that it leads to the lowest drag-to-lift ratio, which helps minimising viscous and momentum losses [54]. To do this, a database containing aerodynamic coefficients of the selected GM15 airfoil for several Reynolds number ranging from 250 000 to 2 000 000 and angles of attack going from -9 degrees to 10 degrees with increments of 0.1 degrees was used. For a given Reynolds number and Mach number at a blade section, the angle of attack that led to the highest lift-over-drag was automatically chosen, after applying the compressibility corrections discussed in Equation 9.2.2. This angle ranged from 3.2 to 5.6 degrees, allowing each blade to be designed with lift-over-drag ratios of up to more than 110 in cruise condition. The rest of the procedure relies on

generating a circulation distribution along the propeller blades that minimizes the induced drag. At a certain blade element with given aerodynamic coefficients, the chord is computed such that it allows the section to produce the thrust necessary to obtain an optimal loading distribution. The thrust, power and efficiency are then computed using the standard approach in Equation 9.8, Equation 9.9 and Equation 9.12. It should be noted that each of the wingtip and array propellers are designed as if they were isolated and positioned parallel to the incoming free stream. This will be developed in more detail in Subsection 9.4.2.

As mentioned earlier, to keep the array propellers within reasonable sizes and efficiencies, the wingtip propellers can be sized in a particular way, allowing them to produce more power during take-off. This was done by reducing the maximum Mach number achieved on the blade tip of the wingtip propellers during cruise to 0.7 instead of the 0.8 or 0.9[7] commonly achieved. By doing so while keeping their diameter constant, the Liebeck method will still allow to compute a blade geometry for the wingtip propellers that satisfies the cruise power specified. However, because the speed of the flow is now constrained to lower values than normally achieved when using a tip Mach number limit of 0.8 or 0.9, the chord of the blade will have to be larger to produce the same loading. The propeller is then still designed with optimal thrust distribution during cruise but now has a higher total blade surface compared to if the propeller was designed with a Mach number constraint of 0.8 or 0.9.

Sizing with Mach number limit of 0.7 leaves room to increase the RPM of the propeller such that the tip Mach number reaches 0.9. Compared to a propeller which was designed with a cruise Mach number limit of 0.9, both options now rotate at the same speed. However, due to the higher blade surface of the wingtip propeller sized with tip Mach constraint of 0.7, more thrust will be produced. This increase in RPM may be used during take-off to reduce the contribution of the distributed propellers to the total thrust needed, allowing their blades to be more slender. This will increase their efficiency as well as providing weight reductions. The drawback of this modification is that the efficiency of the wingtip propeller will be slightly decreased since a larger chord for the same diameter reduces the aspect ratio and increases induced drag.

A total of over 4500 different wingtip propeller combinations varying in tip Mach number limit, blade number, radius and rotational speed were investigated. Table 9.1 shows the ranges of parameters considered. A preliminary estimate from Raymer for the propeller diameter, as a function of the maximum power delivered, (shown in Equation 9.13) was used to orient the range of radii investigated [11]. Inputting a cruise power of $2030[W]$ as computed in Subsection 12.1.9 leads to a radius of $1.55[m]$. Since higher radii allow to size with higher efficiency, the range of radii was extended to higher values. Based on the maximum tip Mach number limit, ranges of rotational speeds were then obtained.

$$D_p = 0.55 \cdot \sqrt[4]{\frac{P_{max}}{1000 N_{props}}} \tag{9.13}$$

Table 9.1: Ranges of tip Mach numbers, blade numbers, radii, and RPM investigated for the design of the wingtip propellers

Parameter	Lower bound	Upper bound	Increment
Tip Mach number constraint [-]	0.7	0.9	0.1
Blade number [-]	3	8	1
Radius [m]	1.3	2.2	0.1
RPM [-]	600	2000	50

Due to the enormous amount of alternatives to investigate, it was decided to make a preliminary round of eliminations such as to arrive at three options with tip Mach number 0.7, 0.8 and 0.9, respectively. That way, the choice of sizing the wingtip propeller for more take-off power could be compared to a designed fully

[7] https://www.kitplanes.com/wind-tunnel-52/#, last consulted June 12, 2022

optimised for cruise efficiency (tip Mach number limit of 0.9 during cruise) and an in-between design with a tip Mach number constraint of 0.8. To select each of the three options, the chord of the blades were first investigated. Indeed, in order to withstand thrust, torque and centrifugal forces, the propeller's blade chord should have a minimum length near the hub. Thus, wingtip propeller combinations whose chord-to-radius ratio was smaller than 0.06 until 50% $\frac{r}{r_{tip}}$ were eliminated. Within the remaining combinations for each tip Mach number limit, the one with the highest cruise efficiency was selected to move to the final trade-off.

The next step was to design an optimal array of propellers to match each combination of wingtip propellers. This required computing the power provided by the latter during take-off which varies significantly from cruise due to differences in free stream velocity and air density. The variation of operational condition also means that the pitch and rotational speed of the propeller had to be changed to avoid stalling the blades. As the method from Liebeck is valid for a single operational condition, a more general BEM approach had to be taken to compute the wingtip propeller performance under take-off conditions. The steps taken in this method follow directly from the theory mentioned earlier in this section. RPM combinations between 1000 and 1300 were used, depending on the wingtip propeller option considered, such as to reach a tip Mach number of 0.9 to provide maximum power. The pitches were defined such that they allowed each wingtip propeller combination to either produce the maximum amount of power with an efficiency superior or equal to 0.8 or to produce power with the maximum efficiency, if no value above 0.8 could be achieved.

Once the wingtip propeller take-off power was obtained, the propeller array was sized for optimal efficiency in take-off conditions, again using the procedure by Liebeck. Table 9.2 displays the ranges of parameters used to create all combinations investigated. Just as for wingtip propellers, these were generated by considering Equation 9.13 as a preliminary indication for the radii. Due to the folding mechanism already adding complexity to the distributed propellers, the number of blades investigated was limited to 6.

Table 9.2: Ranges of blade numbers, radii, and RPM investigated for the design of the distributed propellers

Parameter	Lower bound	Upper bound	Increment
Blade number [-]	3	6	1
Radius [m]	0.75	1.45	0.05
RPM [-]	2000	3500	50

For each of the three wingtip propeller option, the combination of array propellers with the highest take-off efficiency was selected, after eliminating alternatives whose chord-to-radius did not meet the 6% constraint defined previously.

Propeller weight estimation

To improve the accuracy of the weight estimation, the mass of the propellers was estimated. To stay consistent with the rest of the weight estimation approaches used for the Hammerhead design, a method by Torenbeek, modified by Teeuwen to account for more recent propeller applications, was used [56]. Such estimation is shown in Equation 9.14.

$$m_{prop} = 1.1 \cdot \left(D_p \cdot P_{max} \cdot \sqrt{B} \right)^{0.52} \tag{9.14}$$

9.2.3. Results

The three feasible propeller options having been obtained, these are compared in Table 9.3 to decide on the final propulsion system design. Option 1, 2 and 3 use a tip Mach number constraint on the wingtip propellers of 0.7, 0.8 and 0.9, respectively. The selected design combination is highlighted in green. Sizing wingtip propellers for very high take-off power contribution (>60%) was not investigated as such system would have to operate in sub-optimal regime during cruise, impacting its efficiency on the flight phase that contributes to more than two thirds of the total DOC mission energy as will be detailed in Subsection 12.1.9.

In order to achieve high cruise efficiency while providing sufficient power, wingtip propellers require a high blade radius since they provide a high aspect ratio, which limits induced drag. This will limit the loading per blade section compared to a smaller propeller. Increasing the number of blades over 5 further reduced this loading to levels which implied that the chord constraint could not be met. Thus, designs with 3 and 4 blades came out on top of the design options. Several benefits are associated with using few blades, such as mass reduction and simplifications of the hub. This will come at the cost of passenger comfort as higher sound-pressure levels will be produced, due to the high loading of each blade [49]. However, the large distance of the wingtip propellers to the cabin will help mitigating this effect.

Table 9.3: Propeller specifications of three feasible design options. Total efficiency was computed using Equation 9.1. The selected option is highlighted in green.

	Option 1	**Option 2**	**Option 3**
Wingtip propeller			
Cruise tip Mach number constraint	0.7	0.8	0.9
Number of blades [-]	3	3	4
Radius [m]	2.1	2.0	1.6
Array propeller			
Number of blades [-]	3	4	4
Radius [m]	1.25	1.25	1.3
Take-off power share [-] (Wingtip/Array)	50/50	40/60	35/65
Total efficiency [-]	0.875	0.876	0.869
Total mass [kg]	516	570	602
Take-off thrust coefficient [-]	0.58	0.68	0.68

The final propeller design was chosen based on total efficiency, mass and thrust coefficient as this parameter influences the induction factor and thus gives insight on the lift enhancement potential of a combination of distributed propellers. Due to the relatively low fidelity of the BEM model used, as will be discussed in Subsection 9.4.2, the small differences in total efficiency between the three options do not represent a distinguishing factor. Moreover, Options 2 and 3 present similar thrust coefficient, making them advantageous choices compared to Option 1 for downsizing the wing. This criterion was deemed more important than the mass of the propeller systems as Table 9.3 shows differences of at most $90[kg]$. Between Option 2 and 3, Option 2 was designed with lower take-off power contribution from the array propellers which proved to have a significant impact on the overall propulsion system mass. Option 2 was thus chosen due to its lower mass compared to Option 3 and its higher lift enhancement potential compared to Option 1. Figure 9.3 shows the obtained propulsion system integrated on the Hammerhead.

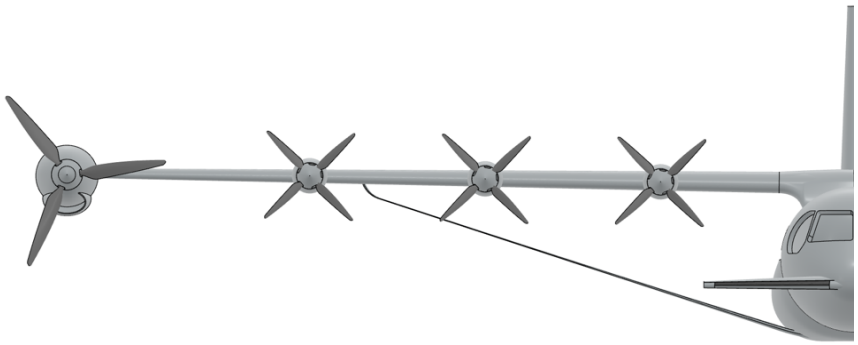

Figure 9.3: Front view of the Hammerhead, showing the half-span with the wingtip propeller and the array propellers

Blade geometries

The blade geometries of the wingtip propellers and distributed propellers of the selected option are shown in Figures 9.4-9.6. Some sections of the blade feature a constant chord section, due to the structural constraints imposed in the vicinity of the propeller hub. The wingtip propellers have blade angles at 75% radius of 51 degrees (where the twist angle is set to 0). This is due to the high free stream velocities during cruise, combined with the relatively low tip speed which cause a high advance ratio (around 2.15). Next, as the distributed propellers have been designed for take-off conditions, they present a much lower advance ratio (slightly above 0.6) which leads their blade to require smaller angles of 23 degrees at 75% radius. Bronz M. et al. mentions blade angles for reaching optimal propeller efficiency for different advance ratio which are in line with the Hammerhead propeller design despite the airfoils used being different [57].

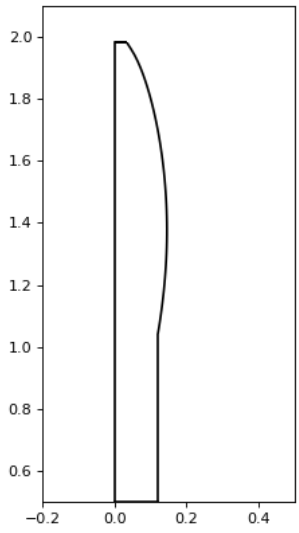

Figure 9.4: Wingtip propeller blade chord distribution as a function of the radial position from propeller axis.

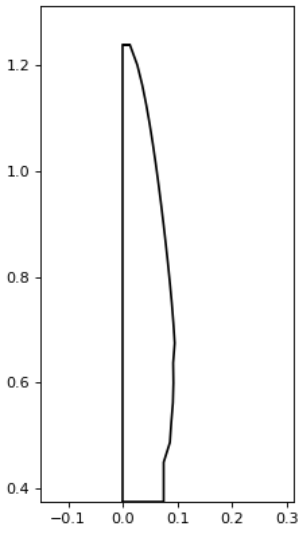

Figure 9.5: Array propeller blade chord distribution as a function of the radial position from propeller axis.

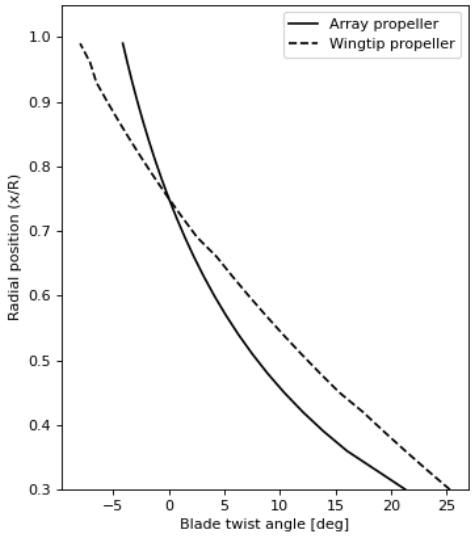

Figure 9.6: Blade twist angle distribution of the wingtip propeller.

It should be noted that the geometries shown do not present sweep. In reality, the propeller blades will be swept, especially near the tip, to reduce the effective Mach number such as to limit drag divergence phenomenons. However, such effect was not included in the performance analysis.

Each propeller type has been designed for different purposes. To assess the compliance with requirements

for which the propellers have not been directly designed for such as rate of climb or time to climb, the performance of this subsystem had to be evaluated under other operational conditions. For the wingtip propellers, one pitch setting was defined for each flight phase to not overload the pilot. These were computed such that they produce the required amount of power while keeping the highest possible efficiency. Values obtained are displayed in Table 9.4.

Table 9.4: wingtip and array propeller settings for different operational conditions

Operational condition	Pitch setting [°]	RPM setting	Efficiency
Wingtip propeller			
Cruise	51	1000	0.890
Take-off	24	1300	0.803
Climb	25	1250	0.775
Array propeller			
Take-off	23	2300	0.782
Climb	23	2200	0.826

The efficiency of the array propellers increases from take-off to climb, despite them being optimised for the former condition. The reason for this is that the thrust coefficient changes from 0.68 during take-off to 0.395 at $70[m/s]$, near the middle of the climb phase. This lower thrust coefficient reduces the axial induction factor, reducing losses from momentum theory and increasing the propeller efficiency [58].

9.3. Propeller Regenerative Braking

Where Section 3.2 discussed potential benefits of regeneration during descent, this section will explain how energy regeneration is achieved on a propeller level. Later in the report, in Section 12.2, the aircraft level influence of regeneration on mission energy and mission time will be discussed.

Energy regeneration using propellers is done by producing negative angles of attack over the blades, by either reducing their pitch (into the rotational plane) or by reducing the rotational speed of the propeller. This then produces a negative lift coefficient, which generates negative thrust. When further decreasing the angle of attack, the direction of the torque acting on the propeller inverts as well, effectively generating power. Such phenomenon is estimated using the BEM method introduced in Subsection 9.2.2 using the designed wingtip propeller blade planform.

For this research it was decided to regenerate using the wingtip propellers only. They have a variable pitch, which allows increasing the regenerative efficiency. Also, a downside of regenerating with the wing array, which is set up in a tractor configuration, is that the drag it produces reduces dynamic pressure over the wing and is expected to significantly reduce lift [43]. Since the regeneration is used during descent, with low speeds, this loss of lift is not desirable. Next to a reduction in lift, a limited airflow over control surfaces on the trailing edge of the wing is highly undesirable.

One big downside of regenerating with the wingtip propellers is the large increase in lift induced drag it causes, since the wingtip vortex is enhanced by the propeller. As the total aircraft drag during descent can be seen as a budget resource, it is desirable for the mission energy to have as little drag as possible induced by the airframe, and as much as possible coming from the regeneration. Regenerating at the wingtips is therefore probably not a good solution for saving mission energy. However, since the regeneration objectives for this project were mainly based on the steeper descent path, namely fly-over noise reduction and reducing mission time, increasing the drag is not seen as an unacceptable penalty.

As neither the wingtip vortex enhancement nor the loss of lift in regeneration by the array were quantified in this project, this is a fruitful area for further research. It might very well be that regenerating at the wingtips produces unacceptable amounts of drag, and that regenerating on the leading edge, potentially only with part of the propellers, is the better solution.

The propulsion system was designed for propulsive mode only, as this is the mode that is used for almost the whole flight. The regenerative capabilities are assessed only, and described further in Section 12.2.

9.3.1. Propeller regeneration analysis

The camber of the chosen GM15 airfoil used for all propeller's blades reduces the range of angles of attack which allow to produce a regenerative regime. Additionally, throughout the descent, air density and free stream velocity vary by 50% and 25%, respectively. Using a single pitch setting for this flight phase would lead to significant variations in performance, reducing the effectiveness of regeneration. Thus, the pitch of the wingtip propellers will be controlled automatically to provide best regeneration performance [59].

As described in Section 3.2, performing regeneration provides two benefits being the reduced mission time and the additional energy stored in the batteries after landing. In order to analyse the impact of regeneration on these parameters, the following three different regeneration strategies were defined at propeller level:

- **Maximising braking capabilities.** This was done by operating the wingtip propellers such that they produced the highest amount of negative thrust, regardless of the propeller efficiency attained. With this, the main objective was to investigate how effective regeneration was at reducing mission time.
- **Maximising propeller efficiency** during regeneration (defined according to Equation 9.15). In this strategy, the wingtip propellers were operated such that the absolute value of the airfoil lift-over-drag was maximum. This case was selected to investigate the relevance of minimising propeller losses on the regeneration performance.
- **Maximising regenerated power** by operating the wingtip propellers at particular combinations of pitches and RPM such that the product of the propeller efficiency and thrust generated was maximum. This case was chosen to estimate the maximum possible energy regenerated in the perspective of identifying its impact on ground operations.

$$\eta_{prop(regen)} = \frac{P}{T \cdot V_\infty} \tag{9.15}$$

In this section, only the impact of the different regeneration strategies on the propellers are investigated. Influence on mission energy, mission time and on-ground operations will be discussed in Section 12.2.

To compute regeneration performance, a time stepping approach was used to split the descent in multiple points. For each point, the operational conditions are defined as the local altitude and free stream velocity. From these, the wingtip propeller's thrust, power and efficiency were computed for multiple combinations of propeller rotational velocities and pitch settings using the BEM method. These ranged from 500 to 1000 RPM and from 15 degrees to 40 degrees, respectively. The best settings were then selected for each point of the descent, depending on the strategy investigated. Figure 9.7 and Figure 9.8 show the obtained efficiencies and powers regenerated as a function of the progression of the descent, for each of the strategies explored.

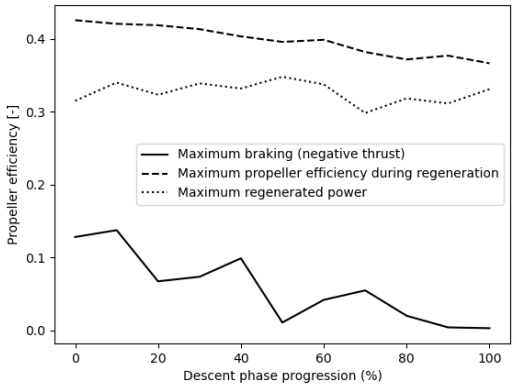

Figure 9.7: Wingtip propellers efficiencies in regenerative regime against descent progression for different regeneration strategies

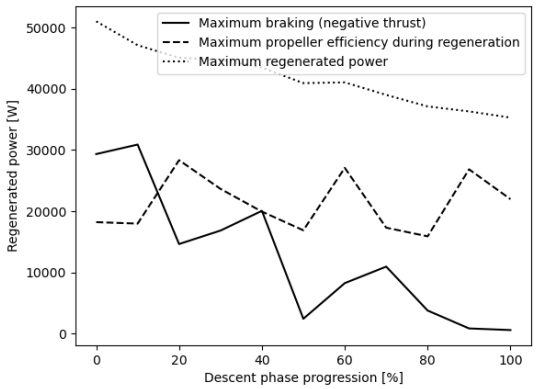

Figure 9.8: Power regenerated by wingtip propellers against descent progression for different regeneration strategies

It can be seen in Figure 9.7 that minimising mission duration through maximum braking leads to propeller efficiencies close to 3 times lower compared to the maximum power and maximum propeller efficiency strategies. This leads to the lowest power regeneration out of the three strategies as seen in Figure 9.8. Furthermore, the strategy in which power regenerated is maximised allows to produce about twice as much power than when optimising propeller efficiency. This means that while aiming for high efficiency might lead to potentially advantageous power generation for a certain breaking level, this strategy is clearly not optimal in term of absolute power regeneration.

9.4. Accuracy and Limitations

The models used throughout the propulsion system design are tools with finite accuracy and whose relevance depend on the desired level of detail to be investigated. In this section, the correct implementation of the sizing tools will be assessed through a validation process in Subsection 9.4.1. The limits of such methods will then be discussed along with their implications on the propeller design in Subsection 9.4.2.

9.4.1. Model Verification and Validation

The model used for the implementation of the propeller planform optimisation was validated with a reference design case that Liebeck uses to demonstrate the accuracy of his method [54]. The same input values were used: a 2 bladed propeller of $0.87\ [m]$ radius and $0.076\ [m]$ hub using a NACA4415 airfoil and rotating at $2400\ [RPM]$ in a $49\ [m/s]$ flow. Once the planform was obtained, the more general version of the BEM method was ran with the obtained geometry and same operational conditions to observe if the output efficiency and thrust were similar. The results are compared in Table 9.5.

Table 9.5: Comparison of the model used for the Hammerhead design and reference data from Liebeck [54].

	Reference data	Optimisation model used	BEM model used	Differences [%]
Efficiency [-]	0.8699	0.8638	0.8970	-0.74 / +3.0
Thrust [N]	929.6	903.7	982.5	-2.8 / +5.7
Torque [Nm]	209.1	203.8	214.2	-2.5 / +2.4

Concerning the planform optimisation model, results are nearly identical, meaning the method has been implemented correctly. The model used in the Hammerhead design includes hub losses which are not taken into account in the data from Liebeck and can explain the slightly lower thrust and efficiency of the Hammerhead model. Additionally, lift and drag coefficients have to be determined at each blade section based

on XFOIL data whose accuracy may differ depending on Reynolds number and angle of attack increments used.

When comparing the reference data to the BEM model uses, larger but still acceptable differences are observed. Indeed, the thrust and torque distributions slightly differ from the results of the optimisation model as seen in Figure 9.9.

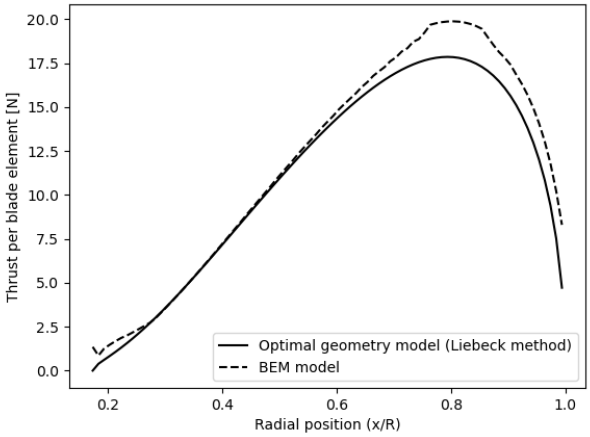

Figure 9.9: Thrust distributions of the Liebeck model and BEM model used, for the same operational condition. The blade was divided over 28 sections.

This likely comes from compressibility corrections used in the airfoil aerodynamic database that slightly overestimate the lift coefficient and therefore influence the thrust produced, also influencing the induction factors and the way thrust is distributed. It should thus be kept in mind that as the results from the BEM model do not give exact indication of the propeller performance under non-optimal operational conditions.

9.4.2. Model Limitations

The BEM theory used in the models for this report presents several limitations. The most important ones being that interactions between blades are not considered [45]. Given the low amount of blades of the obtained propellers, it is likely that the impact of this assumption will be small. Moreover, the BEM model has been proven to be inaccurate for evaluating regenerative capabilities. The absence of rotational effects in the polar data used is the main reason for this lack of fidelity [60]. Regeneration results are thus highly inaccurate and are used more as a conceptual indication of what could be achieved by making use of such principle.

Furthermore, additional limitations were created when implementing the BEM theory into a propeller design tool. Indeed, as mentioned earlier, the angles of attack considered throughout this chapter varied between -9 and 10 degrees. This range does not cover stall characteristics which means that such behaviour will be incorrectly predicted by the model even after implementing an aerodynamic penalty for extreme angles of attack. This is especially true when computing regeneration performance, where angles of attack easily reach the lower limit of the database used. Finally, the incoming flow was assumed to be parallel to the axis of rotation of the propeller. This means that the effects of flow coming under an angle (when the pitch of the aircraft changes for example) were not considered. In reality, the axial flow velocity component would be smaller, slightly reducing the propeller's thrust.

10

Wing Positioning, Tail Design, and Undercarriage Design

A detailed stability and control analysis is key to arrive at a stable aircraft design, both in the air and on the ground. This chapter presents design activities that were performed taking stability and controllability into account. Section 10.1 presents the loading diagrams that were generated, showing the centre of gravity excursion during loading of the aircraft. Subsequently, Section 10.2 presents the influence of wing position on the centre of gravity position, and Section 10.3 presents the scissor plot, graphing horizontal tail size against the centre of gravity position for stability and controllability requirements. In Section 10.4, the canard is sized in more detail, in conjunction with setting the longitudinal wing position. Afterwards, Section 10.5 presents the sizing of the vertical tail, and finally the undercarriage is sized in Section 10.6.

10.1. Loading Diagrams

Constructing the loading diagrams is the first step towards determining the canard area and the longitudinal wing position. It starts with determining the CG at OEW. Subsequently, cargo, passengers and fuel are added respectively, resulting in the final loading diagram. Some input parameters are used in multiple equations for the calculations in Subsection 10.1.1, Subsection 10.1.2, Subsection 10.1.3 and Subsection 10.1.4. These inputs are summarized in Table 10.1.

Table 10.1: General inputs for Section 10.1

Variable	Value	Rationale
l_f	22.7 $[m]$	Computed in Section 6.4
$\bar{c}$	2.0 $[m]$	Computed in Section 6.3
$\hat{x}_{LEMAC}$	0.643 $[-]$	Computed in Section 10.4

10.1.1. CG at OEW

The construction of the loading diagram starts with determining the CG at OEW. This requires the component weights from the class-II weight estimation to be known, as well as estimates of the position of these components from the sizing done in between the class-I and class-II weight estimation. To estimate the CG at OEW, the weight components were divided up into either belonging to the fuselage group or the wing group. Since one of the key objectives of this chapter is to determine the longitudinal wing position, all calculations are expressed in terms of this longitudinal wing position. This allows to parameterize all computations in terms of the longitudinal wing position and therefore to solve for it at a later stage. This is also the reason the distinction between the fuselage and wing group was made as the longitudinal wing position links these groups and determines the CG at OEW to a great extent. Given that the fuselage and wing group CG's are known, the absolute CG at OEW can be computed using the following equation. The procedure used to calculate the CG's of the fuselage and wing group is presented later in this section.

$$\hat{X}_{CG@OEW} = \frac{W_{FCG} \cdot \hat{x}_{FCG} \cdot l_f + W_{WCG} \cdot (\bar{x}_{WCG} \cdot \bar{c} + \hat{x}_{LEMAC} \cdot l_f)}{W_{FCG} + W_{WCG}} \tag{10.1}$$

The weight of the fuselage group, of which the components are given in Table 10.2, can be computed with the following equation:

$$W_{FCG} = \sum_{i \in FCG}^{n} W_i \tag{10.2}$$

The weight of the wing group, of which the components are given in Table 10.4, can be computed with the following equation, similar to the one for computing the fuselage group weight:

$$W_{WCG} = \sum_{i \in WCG}^{n} W_i \tag{10.3}$$

It is more convenient to work with relative figures rather than absolute figures which is why it is useful to convert this absolute CG to a relative CG position with respect to the wing longitudinal position and then normalize this figure by the MAC length. This can be done by applying the following equation.

$$\bar{x}_{CG@OEW} = \frac{\hat{X}_{CG@OEW} - \hat{x}_{LEMAC} \cdot l_f}{\bar{c}} \tag{10.4}$$

A large X signifies an absolute distance, whereas a small x indicates a relative, normalized distance. Furthermore, the bar or hat above a distance figure indicates the reference that is used. To exemplify, $\hat{x}$ indicates a relative, normalized distance with respect to the nose of the aircraft normalized by the fuselage length, $\hat{X}$ indicates an absolute distance measured with respect to the nose of the aircraft, $\bar{x}$ indicates a relative, normalized distance with respect to the leading edge of the MAC normalized by the MAC length and lastly, $\bar{X}$ indicates an absolute distance measured with respect to the leading edge of the MAC.

Fuselage Group

All weight components belonging to the fuselage group are tabulated in Table 10.2. In this table, the weights and moment arms with respect to the front of the nose are presented. The moment arms are expressed as a fraction of the fuselage length.

Table 10.2: Fuselage group components, their weights and their arms

Weight Name	**Weight** $[kg]$	**Arm Name**	**Arm** $[-]$	**Rationale**
$W_{horizontal}$	439	$\hat{x}_{horizontal}$	0.05	Horizontal tail weight assumed to be at 5% of fuselage length
$W_{vertical}$	855	$\hat{x}_{vertical}$	0.90	Vertical tail weight assumed to be at 90% of fuselage length
$W_{fuselage}$	3148	$\hat{x}_{fuselage}$	0.50	Fuselage weight assumed to be at 50% of fuselage length
W_{nlg}	188	$\hat{x}_{nlg}$	0.40	Nose landing gear weight assumed to be at 40% of fuselage length

Table 10.2: Fuselage group components, their weights and their arms

Weight Name	Weight $[kg]$	Arm Name	Arm $[-]$	Rationale
W_{mlg}	851	$\hat{x}_{mlg}$	0.70	Main landing gear weight assumed to be at 70% of fuselage length
$W_{instruments}$	425	$\hat{x}_{instruments}$	0.20	Instruments weight assumed to be at 20% of fuselage length
W_{furn}	1834	$\hat{x}_{furn}$	0.35	Furniture weight assumed to be at 35% of fuselage length
W_{aircon}	392	$\hat{x}_{aircon}$	0.50	Air conditioning weight assumed to be at 50% of fuselage length
$W_{battery}$	4515	$\hat{x}_{battery}$	0.70	Battery position assumed at 70% of fuselage length, behind the cargo hold

The CG of the fuselage group expressed as a fraction of fuselage length can then be computed using the following equation.

$$\hat{x}_{FCG} = \frac{\sum_{i \in FCG}^{n} \hat{x}_i \cdot W_i}{\sum_{i \in FCG}^{n} \cdot W_i} \tag{10.5}$$

Putting in the weights and their arms yields the following outputs for the fuselage group in Table 10.3.

Table 10.3: Fuselage group outputs

Variable	Value
W_{FCG}	12647 $[kg]$
$\hat{x}_{FCG}$	0.56 $[-]$

Wing Group

The same table showing the components that the wing group comprises is given in Table 10.4. In this table the weights and their arms with respect to the leading edge of the mean aerodynamic chord are presented. The arms are expressed as a fraction of the mean aerodynamic chord length.

Table 10.4: Wing group components, their weights and their arms

Weight Name	Weight $[kg]$	Arm Name	Arm $[-]$	Rationale
W_{wing}	2654	$\hat{x}_{wing}$	0.4	Wing weight assumed to be at 40% of MAC length
$W_{powertrain}$	1666	$\hat{x}_{powertrain}$	0.2	Powertrain weight assumed to be at 20% of MAC length

Table 10.4: Wing group components, their weights and their arms

Weight Name	Weight $[kg]$	Arm Name	Arm $[-]$	Rationale
$W_{controlsurfaces}$	401	$\hat{x}_{controlsurfaces}$	0.8	Control surfaces weight assumed to be at 80% of MAC length

Again, the CG of the wing group was then computed using the following equation.

$$\bar{x}_{WCG} = \frac{\sum_{i \in WCG}^{n} \bar{x}_i \cdot W_i}{\sum_{i \in WCG}^{n} \cdot W_i} \tag{10.6}$$

Putting in the weights and their arms yields the following values for the wing group in Table 10.5.

Table 10.5: Wing group outputs

Variable	Value
W_{WCG}	4721 $[kg]$
$\hat{x}_{WCG}$	0.36 $[-]$

Combining Wing and Fuselage Group
Combining the weights and CG positions computed for the wing group and the fuselage group yields the following outputs in Table 10.6.

Table 10.6: CG at OEW outputs

Variable	Value
$W_{CG@OEW}$	17368 $[kg]$
$\bar{x}_{CG@OEW}$	-0.56 $[-]$

10.1.2. Adding Cargo

The next step in constructing the loading diagram was adding cargo to the aircraft in order to assess the changes in CG location and weight. The cargo bay is continuous due to the high wing configuration not having to pass through it. Furthermore, for the stability and control analysis it was assumed that this cargo hold was loaded from the centre of the hold outwards. The new CG with the cargo added was then computed using the following equation.

$$\bar{x}_{CG@OEW+cargo} = \frac{\bar{x}_{CG@OEW} \cdot W_{OEW} + \bar{x}_{cargo} \cdot W_{cargo}}{W_{OEW} + W_{cargo}} \tag{10.7}$$

The longitudinal position of the cargo as a fraction of fuselage length, $\hat{x}_{cargo}$ must therefore be expressed as $\bar{x}_{cargo}$. This is done by applying the following equation.

$$\bar{x}_{cargo} = \frac{\hat{x}_{cargo} \cdot l_f - \hat{x}_{LEMAC} \cdot l_f}{\bar{c}} \tag{10.8}$$

The weights and arms in Table 10.7 were used when computing the weight and CG location after adding cargo.

Table 10.7: Weights and arms used to compute weight and CG location after adding cargo

Weight Name	**Weight** $[kg]$	**Arm Name**	**Arm** $[-]$	**Rationale**
W_{OEW}	17368	$\bar{x}_{CG@OEW}$	-0.56	W_{OEW} is the sum of the WCG and FCG components in Subsection 10.1.1, arm was computed in Subsection 10.1.1 as well
W_{cargo}	500	$\hat{x_{cargo}}$	0.5	Cargo weight stems from requirements, cargo hold centre assumed to be at 40% of fuselage length

The new weight and CG after adding cargo are tabulated in Table 10.8.

Table 10.8: Outputs after adding cargo

Variable	**Value**
$W_{CG@OEW+cargo}$	17868 $[kg]$
$\hat{x}_{CG@OEW+cargo}$	-0.59 $[-]$

10.1.3. Adding Passengers

After adding cargo, passengers are added. It is assumed this happens according to the window-seating rule. This rule states that first the seats at the window are filled either from front to back or from back to front after which the aisle seats are filled either from front to back or from back to front as well. To compute the CG after adding passengers to rows sequentially, the number of seat rows and seat pitch must be determined first. The number of seat rows is $n_{rows} = \lceil \frac{n_{pax}}{n_{sa}} \rceil = \lceil \frac{50}{4} \rceil = 13$. The seat pitch is $s_{pitch} = \frac{l_{cabin_{seats}}}{n_{rows}} = \frac{12.1}{13} = 0.93[m]$. Next, this calculation using Equation 10.9 was performed iteratively for every seat row i, first for the window seats, then for the aisle seats. The difference between loading passengers at the window seats and at the aisle seats is the initial start weight and the initial CG position. The 2 in front of every W_{pax} refers to the fact that 2 passengers are boarded for every row.

$$\bar{x}_{CG@OEW+cargo+pax_{i+1}} = \frac{\bar{x}_{CG@OEW+cargo+pax_i} \cdot W_{OEW+cargo+pax_i} + 2 \cdot \bar{x}_{pax} W_{pax}}{W_{CG@OEW+cargo+pax_i} + 2 \cdot W_{pax}} \tag{10.9}$$

The $\bar{x}_{pax}$ depends on the boarding procedure. This distance is more conveniently expressed as a fraction of fuselage length, therefore the following conversion was applied.

$$\bar{x}_{pax} = \frac{\hat{X}_{row} - \hat{x}_{LEMAC} \cdot l_f}{\bar{c}} \tag{10.10}$$

For boarding from back to front $X_{row} = l_{fwdcabin} + l_{cabin} - i \cdot s_{pitch}$ was used, for boarding front to back $X_{row} = l_{fwdcabin} + (i+1) \cdot s_{pitch}$. The $+1$ is required such that the seats align. For the calculations, $l_{fwdcabin} = 5.4[m]$ and $l_{cabin} = 12.1[m]$ were used. Table 10.9 lists the initial variables used in computing the new weights and CG locations after adding passengers.

Table 10.9: Weights and arms used to compute weight and CG location after adding window passengers as well

Weight Name	**Weight** $[kg]$	**Arm Name**	**Arm** $[-]$	**Rationale**
$W_{OEW+cargo}$	17868	$\bar{x}_{CG@OEW+cargo}$	-0.59	$W_{OEW+cargo}$ and $\bar{x}_{CG@OEW+cargo}$ have been computed in Subsection 10.1.2
W_{pax}	95	$\hat{x}_{pax}$	-	W_{pax} stems from requirements, arm varies for every row as explained above

The new weight and CG after adding window passengers are tabulated in Table 10.10.

Table 10.10: Outputs after adding window passengers

Variable	**Value**
$W_{CG@OEW+cargo+windowpax}$	20338 $[kg]$
$\hat{x}_{CG@OEW+cargo+windowpax}$	-0.68 $[-]$

The start values for computing the weight and CG after adding the aisle passengers are given as well in Table 10.11.

Table 10.11: Weights and arms used to compute weight and CG location after adding aisle passengers as well

Weight Name	**Weight** $[kg]$	**Arm Name**	**Arm** $[-]$	**Rationale**
$W_{OEW+cargo+windowpax}$	20338	$\bar{x}_{CG@OEW+cargo+windowpax}$	-0.68	Variables have been computed earlier in this section
W_{pax}	95	$\hat{x}_{pax}$	-	W_{pax} stems from requirements, arm varies for every row as explained above

The new weight and CG after adding all passengers, that is window and aisle passengers, are tabulated in Table 10.12.

Table 10.12: Outputs after adding all passengers

Variable	Value
$W_{CG@OEW+cargo+pax}$	22808 $[kg]$
$\hat{x}_{CG@OEW+cargo+pax}$	-0.75 $[-]$

10.1.4. Adding Fuel

After adding the cargo and the passengers, the fuel is added. The new CG after adding fuel can be computed using the following equation.

$$\bar{x}_{CG@OEW+cargo+pax+fuel} = \frac{\bar{x}_{CG@OEW+cargo+pax} \cdot W_{OEW+cargo+pax} + \bar{x}_{fuel} \cdot W_{fuel}}{W_{OEW+cargo+pax} + W_{fuel}} \tag{10.11}$$

Again, $\bar{x}_{fuel}$ must be expressed in terms of $\hat{x}_{fuel}$ since the fuel tank is located aft in the fuselage making it easier to use $\hat{x}_{fuel}$. The conversion is as follows.

$$\bar{x}_{fuel} = \frac{\hat{x}_{fuel} \cdot l_f - \hat{x_{LEMAC}} \cdot l_f}{\bar{c}} \tag{10.12}$$

The values used to compute the new weight and CG after adding fuel are given in Table 10.13

Table 10.13: Weights and arms used to compute weight and CG location after adding cargo and window passengers

Weight Name	Weight $[kg]$	Arm Name	Arm $[-]$	Rationale
$W_{OEW+cargo+pax}$	22808	$\bar{x}_{CG@OEW+cargo+pax}$	-0.75	$W_{OEW+cargo+pax}$ and $\bar{x}_{CG@OEW+cargo+pax}$ have been computed earlier in Subsection 10.1.3
W_{fuel}	197	$\hat{x}_{fuel}$	0.8	W_{fuel} was computed in Chapter 8, the fuel is assumed to be at 80% of the fuselage length

The new weight and CG after adding fuel is tabulated in Table 10.12.

Table 10.14: Outputs after adding all passengers

Variable	Value
$W_{CG@OEW+cargo+pax+fuel}$	23005 $[kg]$
$\hat{x}_{CG@OEW+cargo+pax+fuel}$	-0.73 $[-]$

10.1.5. Loading Diagram Result

The computational steps outlined in Subsection 10.1.1, Subsection 10.1.2, Subsection 10.1.3 and Subsection 10.1.4 were implemented in a Python script. It was implemented in such a way that allows to assess

the effect of longitudinal wing position on the loading diagram. The results of this analysis are shown in Figure 10.1.

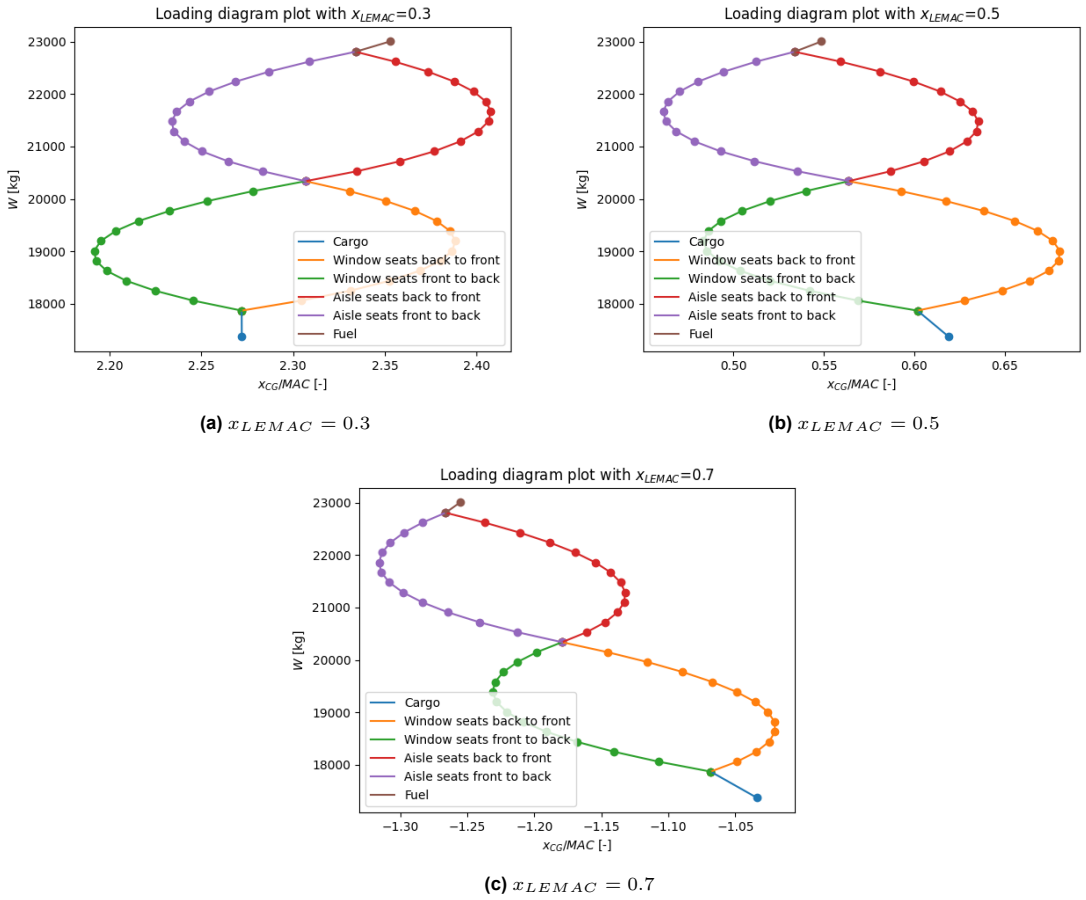

(a) $x_{LEMAC} = 0.3$

(b) $x_{LEMAC} = 0.5$

(c) $x_{LEMAC} = 0.7$

Figure 10.1: Loading diagrams for various longitudinal wing positions

Clearly, the longitudinal wing position has great influence on the CG variation of the aircraft. For more forward wing positions, such as at $x_{LEMAC} = 0.3$ in Figure 10.1a, the CG after loading the aircraft is significantly backwards with respect to the CG at OEW. For more backward wing positions, such as at $x_{LEMAC} = 0.5$ and $x_{LEMAC} = 0.7$ in Figure 10.1b and Figure 10.1c respectively, the CG does the opposite.

However, as already stated before, the optimal wing longitudinal position is $\hat{x}_{LEMAC} = 0.643[-]$. Therefore, Figure 10.2 shows the loading diagram for this final optimal wing longitudinal position.

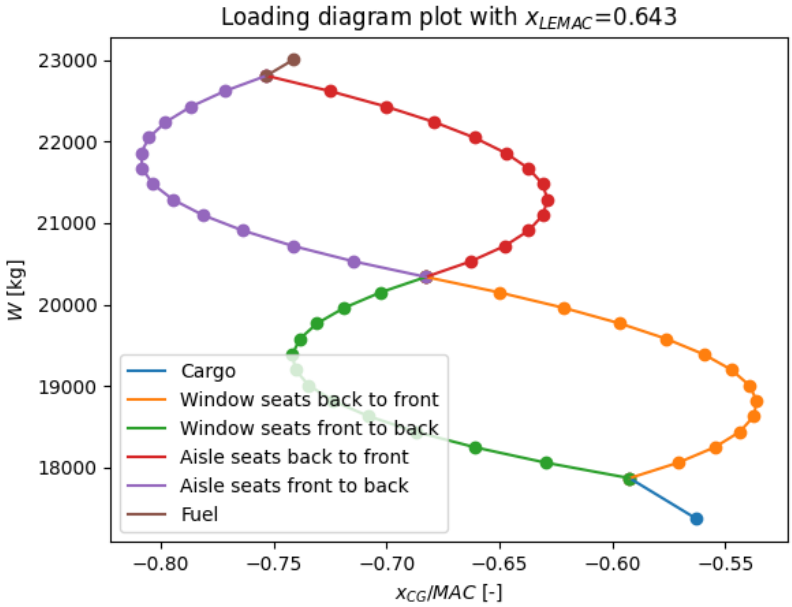

Figure 10.2: Loading diagram for $\hat{x}_{LEMAC} = 0.643$

From this loading diagram the most forward and most aft CG's can be derived. For these most extreme CG positions, 2% margins were added as to account for moving masses during flight. This yields the following extreme CG positions, tabulated in Table 10.15.

Table 10.15: Extreme CG positions for the optimal longitudinal wing position

Variable	Value
$\bar{x}_{cg,fwd}$	-0.82 [−]
$\bar{x}_{cg,aft}$	-0.53 [−]

10.2. CG Variation Plot

As discussed in Section 10.1, the loading diagram yields a most forward and most aft CG position as a function of the longitudinal wing position. Accordingly, a plot can also be constructed showing the most forward and most aft CG as a function of various longitudinal wing positions. This is what the CG variation plot shows in Figure 10.3.

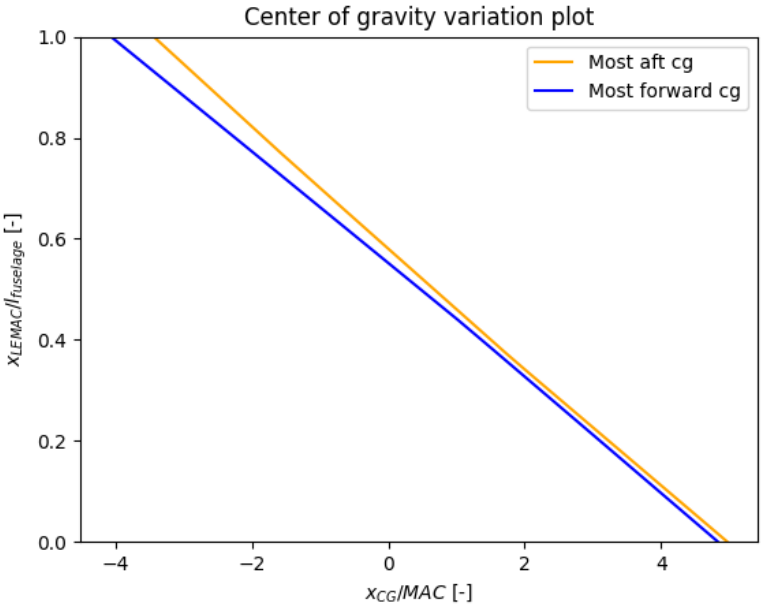

Figure 10.3: Variation of CG for various longitudinal wing positions

This plot essentially summarizes the analysis in Subsection 10.1.5. Two observations can be made from this plot. First, for extreme backward longitudinal wing positions, the CG range becomes larger. This is sensible as the weight arms of the fuel, passengers, and cargo become larger on average when the CG at OEW moves in front of the wing. To minimize CG variation, it is therefore desirable to have a wing positioned as forward as possible. Secondly, for aft x_{LEMAC} the CG's will move in front of the wing whereas for forward x_{LEMAC} the CG's will move behind the wing. The real power behind this graph is its synergy when combined with the scissor plot as that allows for deriving the optimal horizontal tail area and optimal longitudinal wing position. This is further outlined in Section 10.4.

10.3. Scissor Plot

The scissor plot comprises the controllability curve and the stability curve. It essentially shows what the required tail ratio needs to be for a given CG variation. The controllability and stability curves for the aircraft are derived in Subsection 10.3.1 and Subsection 10.3.2 respectively. The corresponding scissor plot is presented in Subsection 10.3.3. The following inputs stem from other sections of the report and are needed in Subsection 10.3.1, Subsection 10.3.2 and Subsection 10.3.3.

Table 10.16: Inputs for the controllability and stability curve

Variable	Value	Rationale
C_{L_h}	2.448 $[-]$	Canard lift coefficient in landing configuration, computed in Section 7.4
$C_{L_{A-h}}$	3.2 $[-]$	Tailless aircraft lift coefficient, can be assumed equal to the wing lift coefficient in landing configuration, computed in Section 7.5
$\bar{c}$	2.0 $[m]$	Computed in Section 6.3
$\hat{x}_h$	0.05 $[-]$	Assumed in Subsection 10.1.1
l_f	22.7 $[m]$	Computed in Section 6.4

Table 10.16: Inputs for the controllability and stability curve

Variable	Value	Rationale
$\bar{c}_h$	1.5 $[m]$	Computed in Section 6.5
$C_{m_{0_{airfoil}}}$	-0.1047 $[m]$	Computed in Section 7.1
C_{L_0}	0.4873 $[m]$	Computed in Section 7.1
A	16 $[-]$	Computed in Section 6.2
Λ	0 [rad]	Computed in Section 6.3
S	61.6 $[m^2]$	Computed in Section 6.3
b_f	2.8 $[m]$	Assumed equal to outer fuselage diameter, computed in Section 6.4
h_f	2.8 $[m]$	Assumed equal to outer fuselage diameter, computed in Section 6.4
$\Delta_{flaps} C_{m_{AC}}$	-0.18	Computed in Section 7.3
M	0.45	Computed in Subsection 12.1.4
η	0.95 $[-]$	Airfoil efficiency factor assumed equal to 0.95 [17]
c_r	2.6 $[m]$	Computed in Section 6.3
b	31.4 $[m]$	Computed in Section 6.3

10.3.1. Controllability Curve

The controllability curve of the aircraft can be described by the following equation.

$$\frac{S_h}{S} = \frac{1}{\frac{C_{L_h}}{C_{L_{A-h}}} \frac{l_h}{\bar{c}} \left(\frac{V_h}{V}\right)^2} \bar{x}_{CG} + \frac{\frac{C_{m_{AC}}}{C_{L_{A-h}}} - \bar{x}_{AC}}{\frac{C_{L_h}}{C_{L_{A-h}}} \frac{l_h}{\bar{c}} \left(\frac{V_h}{V}\right)^2} \tag{10.13}$$

Since this aircraft will feature a canard, one simplification can be made:

- The canard operates in an undisturbed flow field causing $\frac{V_h}{V}$ to be equal to 1, the reduced velocity effect of the canard on the main wing will be neglected

This reduces the controllability curve to the following equation.

$$\frac{S_h}{S} = \frac{1}{\frac{C_{L_h}}{C_{L_{A-h}}} \frac{l_h}{\bar{c}}} \bar{x}_{CG} + \frac{\frac{C_{m_{AC}}}{C_{L_{A-h}}} - \bar{x}_{AC}}{\frac{C_{L_h}}{C_{L_{A-h}}} \frac{l_h}{\bar{c}}} \tag{10.14}$$

The arm between the quarter-chords of the canard and the wing, l_h, can be determined using Equation 10.15. The scissor plot figure should be negative for aircraft featuring a canard. The aerodynamic centres for the horizontal tail, $\bar{x}_{AC_h}$, and the wing, $\bar{x}_{AC_w}$, were assumed to be at 25% of their MAC lengths.

$$l_h = \hat{x}_h l_f + \bar{x}_{AC_h} \bar{c}_h - x_{LEMAC} l_f - \bar{x}_{AC_w} \bar{c} \tag{10.15}$$

The pitching moment coefficient around the aerodynamic centre can be determined using the empirical method presented in Systems Engineering & Aerospace Design: Requirement Analysis and Design Principles for A/C Stability and Control (Part II) [23].

$$C_{m_{AC}} = C_{m_{AC_w}} + \Delta_{fus} C_{m_{AC}} + \Delta_{flaps} C_{m_{AC}} \tag{10.16}$$

$C_{m_{AC_w}}$ was computed as follows.

$$C_{m_{AC_w}} = C_{m_{0_{airfoil}}} \left(\frac{A \cos^2 \Lambda}{A + 2 \cos \Lambda} \right) \tag{10.17}$$

$\Delta_{fus} C_{m_{AC}}$ was computed with the following empirical relation. $C_{L_{\alpha_{A-h}}}$ was computed with the DATCOM method in Subsection 10.3.2.

$$\Delta_{fus} C_{m_{AC}} = -1.8 \left(1 - \frac{2.5 b_f}{l_f} \right) \frac{\pi b_f h_f l_f}{4 S \bar{c}} \frac{C_{L_0}}{C_{L_{\alpha_{A-h}}}} \tag{10.18}$$

The aerodynamic centre was determined as follows, presented in Systems Engineering & Aerospace Design: Requirement Analysis and Design Principles for A/C Stability and Control (Part I) [61].

$$\bar{x}_{AC} = \bar{x}_{AC_{wf}} + \bar{x}_{AC_{nac}} \tag{10.19}$$

Where $\bar{x}_{AC_{wf}}$ of the wing-fuselage was computed using Equation 10.20. Of the parameters in this equation that were not elaborated on before, the distance from the nose to the wing-fuselage intersection point l_{fn} was assumed equal to $\hat{x}_{LEMAC} l_f$ as the aircraft does not have sweep. Not having sweep also causes the third term to become 0 as this makes $\tan \Lambda_{0.25c} = 0$. Therefore, the fuselage has only a destabilizing effect on the aerodynamic centre as it makes the aerodynamic centre move forward.

$$\bar{x}_{AC_{wf}} = \bar{x}_{AC_w} - \frac{1.8}{C_{L_{\alpha_{A-h}}}} \frac{b_f h_f l_{fn}}{S \bar{c}} + \frac{0.273}{1 + \lambda} \frac{b_f c_g (b - b_f)}{\bar{c}^2 (b + 2.15 b_f)} \tan (\Lambda_{0.25c}) = \bar{x}_{AC_w} - \frac{1.8}{C_{L_{\alpha_{A-h}}}} \frac{b_f h_f l_{fn}}{S \bar{c}} \tag{10.20}$$

Further, $\bar{x}_{AC_{nac}}$ was computed on the wing with Equation 10.21. Of the parameters not discussed before, the engine width b_n and engine protruding distance from the leading edge l_n varies for the tip and inboard engines, this was measured from the 3D drawings of the aircraft. These were $b_{n_{in}} = 0.4[m]$ and $l_{n_{in}} = 1.2[m]$ for the inboard engines and $b_{n_{tip}} = 0.8[m]$ and $l_{n_{tip}} = 0.9[m]$ for the tip engines.

$$\bar{x}_{AC_{nac}} = \sum_{i}^{n_{eng}} k_n \frac{b_{n_i}^2 l_{n_i}}{S \bar{c} C_{L_{\alpha_{A-h}}}} \tag{10.21}$$

10.3.2. Stability Curve

The stability curve of the aircraft can be described by the following equation:

$$\frac{S_h}{S} = \frac{1}{\frac{C_{L_{\alpha_h}}}{C_{L_{\alpha_{A-h}}}} \left(1 - \frac{d\epsilon}{d\alpha}\right) \frac{l_h}{\bar{c}} \left(\frac{V_h}{V}\right)^2} \bar{x}_{cg} - \frac{\bar{x_{AC}} - SM}{\frac{C_{L_{\alpha_h}}}{C_{L_{\alpha_{A-h}}}} \left(1 - \frac{d\epsilon}{d\alpha}\right) \frac{l_h}{\bar{c}} \left(\frac{V_h}{V}\right)^2} \tag{10.22}$$

On top of the simplification given in Subsection 10.3.1, one additional simplification can be made because of the canard:

- There is no downwash effect on the canard because of the main wing causing $\frac{d\epsilon}{d\alpha}$ to be 0, the downwash effect of the canard on the main wing will be neglected

Applying these two simplifications further reduces the stability equation to the following form.

$$\frac{S_h}{S} = \frac{1}{\frac{C_{L_{\alpha_h}}}{C_{L_{\alpha_{A-h}}}} \frac{l_h}{\bar{c}}} \bar{x}_{cg} - \frac{x_{\bar{AC}} - SM}{\frac{C_{L_{\alpha_h}}}{C_{L_{\alpha_{A-h}}}} \frac{l_h}{\bar{c}}} \tag{10.23}$$

$SM = 0[-]$ was chosen because canard aircraft have limited CG range and reducing the SM to 0 allows for maximizing the allowed CG range. The lift gradients were determined using the DATCOM method [61] with $\beta = \sqrt{1 - M^2}$. As the aircraft does not feature sweep on either the horizontal tail or the wing, the $\tan^2 \Lambda_{0.5c}$ goes to 0 which causes the equation to further simplify.

$$C_{L_\alpha} = \frac{2\pi \cdot A}{2 + \sqrt{4 + \left(\frac{A \cdot \beta}{\eta}\right)^2 \left(1 + \frac{\tan^2 \Lambda_{0.5c}}{\beta^2}\right)}} = \frac{2\pi \cdot A}{2 + \sqrt{4 + \left(\frac{A \cdot \beta}{\eta}\right)^2}} \tag{10.24}$$

For $C_{L_{\alpha_h}}$, $AR_h = 4$ was computed in Section 6.5. However, to end up with a feasible design in Section 10.4, this aspect ratio had to be lowered to 2. The lift gradient of the tailless aircraft requires some modification to convert the lift gradient of the wing to the lift gradient of the tailless aircraft:

$$C_{L_{\alpha_{A-h}}} = C_{L_{\alpha_w}} \left(1 + 2.15 \frac{b_f}{b} \frac{S_{net}}{S}\right) + \frac{\pi}{2} \frac{b_f^2}{S} \tag{10.25}$$

S_{net} is the wing area minus the area where the wing intersects with the fuselage. This intersection was estimated by multiplying c_r with b_f.

10.3.3. Result

The scissor plot was then constructed by combining the stability and controllability curve. The resulting figure is shown in Figure 10.4. As was to be expected for a canard aircraft, the CG range allowed for certain tail ratios is rather limited.

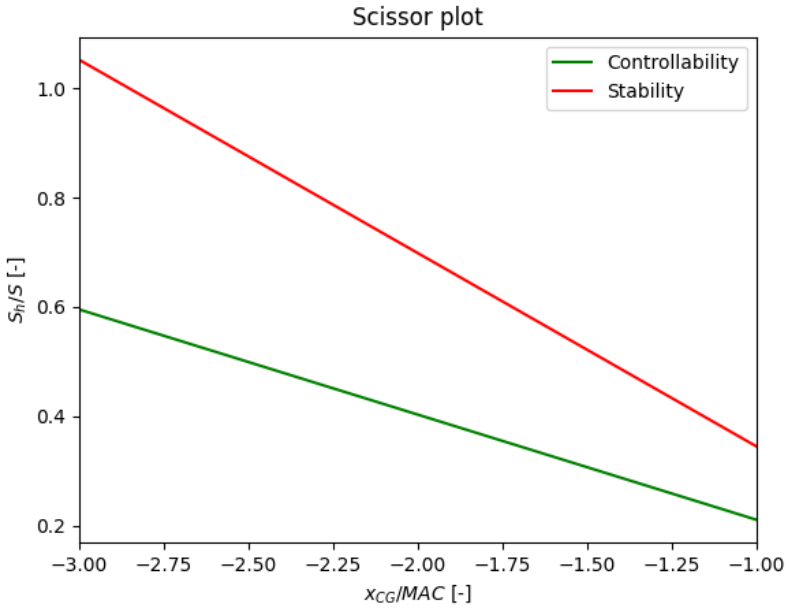

Figure 10.4: Variation of CG for various longitudinal wing positions

10.4. Canard Sizing and Wing Positioning

Determining the tail ratio $\frac{S_h}{S}$ and the longitudinal position of the leading edge of the mean aerodynamic chord of the wing $\bar{x}_{LEMAC}$ can be done by overlapping the CG variation plot and the scissor plot. An algorithm was written that can automatically generate the optimal $\frac{S_h}{S}$ and $\bar{x}_{LEMAC}$ values. It works as follows. For every possible $\bar{x}_{LEMAC}$ value, the corresponding most forward CG and most aft CG is extracted from the CG variation plot. This is then projected onto the scissor plot. By projection the most aft and most forward CG onto the scissor plot, two values for $\frac{S_h}{S}$ are obtained. Since the aircraft cannot have two different tail ratios, the objective is to minimize the difference between these two $\frac{S_h}{S}$ ratios such that they can be considered equal. This optimization is done using a brute-force approach, by trying various longitudinal wing positions. The $\bar{x}_{LEMAC}$ for which the difference between the two $\frac{S_h}{S}$ ratios is the smallest is the optimal solution. By decreasing the step size used to step over possible $\bar{x}_{LEMAC}$ values, it is ensured that the two $\frac{S_h}{S}$ values converge to the same $\frac{S_h}{S}$ value. This procedure can also be visualised, which is shown in Figure 10.5. As can be observed from the graph, the optimal $\bar{x}_{LEMAC}$ is close to 64% of the fuselage length. For longitudinal wing positions more forward of this position, the aircraft could become uncontrollable due to the CG variation going past the maximum allowed CG deviation. For longitudinal wing positions more aft, the aircraft remains stable and controllable at all times. However, the CG is even allowed to shift further back than it will ever attain during operation. Therefore, this is not an optimal wing position.

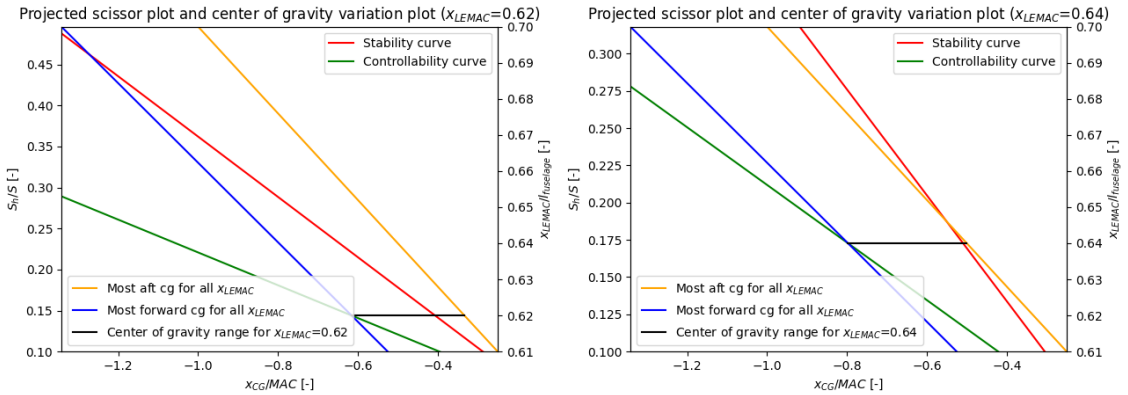

(a) $x_{LEMAC} = 0.62$ **(b)** $x_{LEMAC} = 0.64$

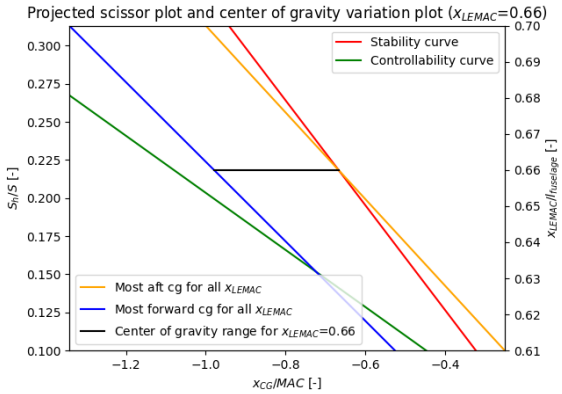

(c) $x_{LEMAC} = 0.66$

Figure 10.5: Matching the scissor plot and the CG variation plot

The final combined scissor plot and CG variation plot yielding an optimal combination between $\frac{S_h}{S}$ and $\bar{x}_{LEMAC}$ is shown in Figure 10.6. This figure was obtained in the same way, but with an increased resolution to get a better estimate of the optimal wing position.

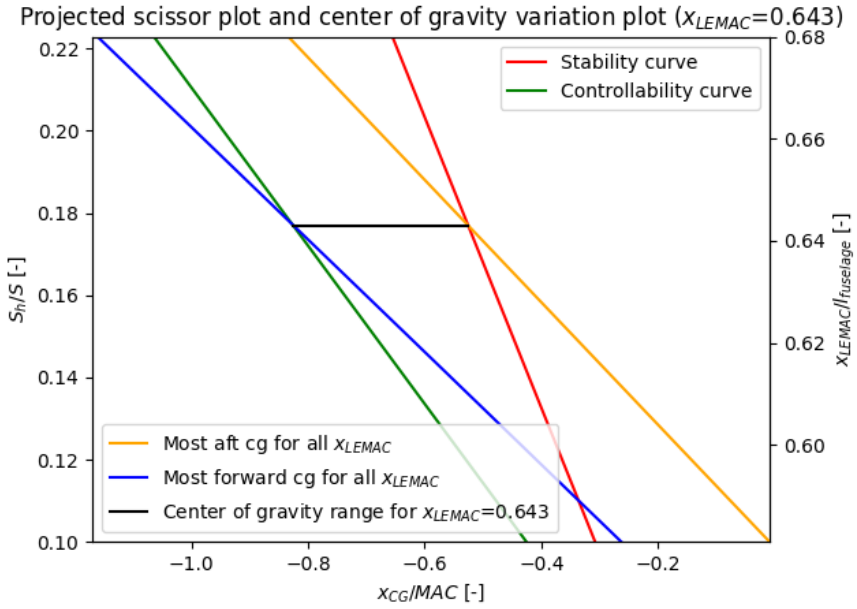

Figure 10.6: Projected scissor plot and CG variation plot

As can be observed from the plot, the optimal tail ratio is $\frac{S_h}{S} = 0.177$ and the optimal $\hat{x}_{LEMAC} = 0.643$. This translates to $\hat{X}_{LEMAC} = 14.6[m]$. Using the wing area of the aircraft, the canard area can be computed. The span of the canard, the root chord length, the tip chord length and the MAC of the canard can then be calculated as well using Equation 6.9, Equation 6.10, Equation 6.11 and Equation 6.12 respectively. The results for the canard are summarized in Table 10.17.

Table 10.17: Canard Sizing Parameters

Parameter	Value
S_h	10.9 $[m^2]$
b_h	4.7 $[m]$
$c_{h_{root}}$	3.3 $[m]$
$c_{h_{tip}}$	1.3 $[m]$
$\bar{c}_h$	2.5 $[m]$

10.5. Vertical Tail Sizing

Vertical tail sizing is sized by evaluating the required vertical tail size for the requirements governing them. For vertical tail sizing, the critical design case is usually the case in which one of the outermost engines fails [62]. Other design cases for the vertical tail sizing are requirements related to operating in crosswinds and having sufficient directional-stability. Since the aircraft features 8 engines distributed over the wing, it is assumed that, should one of the tip engines fail in an OEI condition, the other engines can counteract the resulting moment introduced by the thrust asymmetry and enough thrust remains to divert to an alternative airport. Furthermore, it is physically unpractical to size for OEI because the relatively small arm between the quarter-chords of the wing and of the vertical tail would require an enormous vertical tail that could not be fit

onto the aircraft. It is also assumed that in crosswind, the distributed propulsion can introduce the required moment to counteract crosswinds. Therefore, the vertical tail was only sized for directional-stability. The sizing for directional-stability was done using the following equation from Torenbeek [14].

$$S_v = \frac{S \cdot b}{l_v} \frac{C_{n_{\beta_{required}}} - C_{n_{\beta_{A-v}}}}{C_{Y_{\alpha_v}} \cdot \left(\frac{V_v}{V}\right)^2} \tag{10.26}$$

The following inputs stem from other sections of the report and are needed for the vertical tail sizing.

Table 10.18: Inputs for vertical tail sizing

Variable	Value	Rationale
S	61.6 $[m^2]$	Computed in Section 6.3
b	31.4 $[m]$	Computed in Section 6.3
$\bar{c}$	2 $[m]$	Computed in Section 6.3
$\bar{c}_v$	2.5 $[m]$	Computed in Section 6.5
l_f	22.7 $[m]$	Computed in Section 6.4
$\hat{x}_v$	0.9 $[-]$	Assumed in Subsection 10.1.1
$\hat{x}_{LEMAC}$	0.643 $[m]$	Computed in Section 10.4
$d_{f_{outer}}$	2.8 $[m]$	Computed in Section 6.4

$C_{n_{\beta_{required}}}$ was set at 0.03, which is a reasonable value for the directional-stability for transport aircraft according to Torenbeek. $C_{Y_{\alpha_v}}$ was taken as the lift gradient of the symmetrical NACA 0012 airfoil, which is equal to $5.3476[1/rad]$. Since no estimate on $\left(\frac{V_v}{V}\right)^2$ was available, it was set to 1. $\bar{x}_{ac_v}$ and $\bar{x}_{ac_w}$ were assumed to be at 25% of the MAC length. The arm between the quarter-chords of the wing and the vertical tail was computed with the following relation:

$$l_v = \hat{x}_v l_f + \bar{x}_{ac_v} \bar{c}_v - \hat{x}_{LEMAC} l_f - \bar{x}_{ac_w} \bar{c} \tag{10.27}$$

Where $C_{n_{\beta_{A-v}}}$ was computed using the following empirical relations from Torenbeek as well.

$$C_{n_{\beta_{A-v}}} = C_{n_{\beta_{fus}}} + C_{n_{\beta_{prop}}} + \Delta_i C_{n_\beta} \tag{10.28}$$

$\Delta_i C_{n_\beta}$ is -0.017 for a high-wing configuration. $C_{n_{\beta_{fus}}}$ is defined as follows:

$$C_{n_{\beta_{fus}}} = -k_\beta \frac{S_{fs} \cdot l_f}{S \cdot b} \left(\frac{h_{f1}}{h_{f2}}\right)^{\frac{1}{2}} \left(\frac{b_{f2}}{b_{f1}}\right)^{\frac{1}{3}} \tag{10.29}$$

S_{fs} was taken equal to the fuselage length l_f multiplied by the fuselage outer diameter $d_{f_{outer}}$. The width and height ratios $\frac{h_{f1}}{h_{f2}}$ and $\frac{b_{f2}}{b_{f1}}$ were assumed to equal 1, assuming the fuselage does not have any height and width variations. k_β is defined as follows. l_{cg} was taken as the CG position after loading cargo, passengers and fuel, which was retrieved from Section 10.1. $h_{f_{max}}$ was again taken as the fuselage outer diameter $d_{f_{outer}}$.

$$k_\beta = 0.3\frac{l_{cg}}{l_f} + 0.75\frac{h_{f_{max}}}{l_f} - 0.105 \tag{10.30}$$

$C_{n_{\beta_{prop}}}$ is defined as follows. The arm of each of the engines to the fuselage centerline l_p, the number of blades per propeller B_p and the disk diameter of each propeller D_p were determined in Chapter 9

$$C_{n_{\beta_{prop}}} = -0.053 \sum_{i}^{n_{eng}} \frac{l_{p_i} \cdot B_{p_i} \cdot D_{p_i}^2}{S \cdot b} \tag{10.31}$$

The vertical tail sizing parameters after having performed these calculations are presented in Section 10.5.

Table 10.19: Vertical Tail Sizing Parameters

Parameter	Value
S_v	13.9 $[m^2]$
b_v	4.4 $[m]$
$c_{v_{root}}$	4.5 $[m]$
$c_{v_{tip}}$	1.8 $[m]$
$\bar{c}_v$	3.3 $[m]$

10.6. Undercarriage Sizing and Integration

The integration of the landing gear was determined based on the centre of gravity excursion. The other geometrical characteristics of the aircraft that were required are the wing planform, fuselage aft shape, engine types and locations, and centre of gravity excursion. In order to size and integrate the landing gear the design has to fulfil certain requirements as will be discussed in Subsection 10.6.2 [63]. Before this is done, the design of the undercarriage itself must be examined. This is done in Subsection 10.6.1.

10.6.1. Undercarriage Design

The undercarriage has several functions to fulfil. These would be to absorb landing and taxiing shocks, manoeuver on ground, provide braking capability, tow the aircraft, and protect the ground surface. In order to design the undercarriage the design of the tires will be evaluated in Subsection 10.6.1.

Tire design

Firstly, the amount of wheels for both the main and nose gear have to be determined in order to size the undercarriage. This would be solely dependent on the MTOW. This resulted in 2 nose and 4 main landing gear wheels. Based on this the static load per wheel for both the main and nose gears can be calculated. This is determined by assuming that the main gear would carry 92% and the nose gear 8% of the weight of the aircraft. Further, the tire pressure would be determined by Equation 10.32.

$$p = 430\ln(LCN) - 680, 10 < LCN < 100 \tag{10.32}$$

Here, LCN is the load classification number. This value defines the runways the aircraft is allowed to land on. Therefore, the LCN value of the undercarriage is not allowed to exceed the lowest LCN value of the airfield it will operate [14]. Based on reference aircraft in Figure 10.7a a value of LCN was estimated. As the MTOW is equal to 23314 a LCN of 21 would be viable. With both the inflation pressure and static load per wheel evaluated the tire dimensions can be examined in Figure 10.7b.

AIRCRAFT TYPE	MTOW (LB)	TIRE PRESS. (PSI)	LCN
Fokker F-27 Mk 500	45,000	80	19
Fokker F-28 Mk 2000	65,000	100	27
McDonnell D. DC-9/10	90,700	129	39
Boeing 707/320	300,000	135	58
McDonnell D. DC-10/10	410,000	175	88

(a) LCN of several airliners - main landing gear [14]

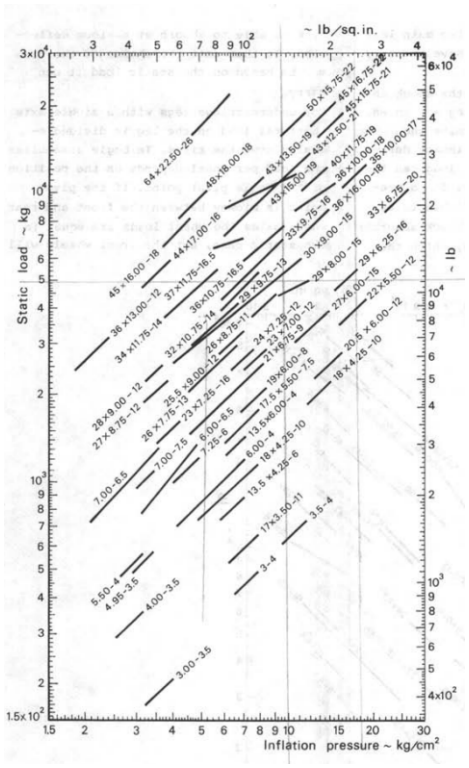

(b) Tire dimensions as function of static load and inflation pressure [14]

This resulted in tire design of 33, 9.75, and 16 $[inch]$ for the outer radius, the width, and inner radius of the tire for the main landing gear and 18, 4.25, and 10 $[inch]$ for the nose landing gear.

10.6.2. Undercarriage Integration

Before the design can be performed, there are several design requirements that will be set. The constraints that will be reviewed are the tire clearance limit, scrape angle, roll angle limit, lateral and longitudinal tip over angle, minimum and maximum nose load, and nose stowage [63].

Longitudinal design space limits

Firstly, to position the main landing gear in the longitudinal direction some aerodynamic performance parameters during take-off are required. Limit number 5 in Figure 10.8 is the longitudinal tip over limit, θ_{TO}. In order to determine this, the angle of attack at take-off was established in Equation 10.33 and adding 5° to guarantee no auto-rotation would occur [63].

$$\alpha_{TO} = \frac{C_{L_{TO,req}} - dC_{L,TO} - C_{L_{TO,\alpha=0}}}{\frac{dC_L}{d\alpha}} \tag{10.33}$$

$C_{L_{TO,req}}$ is calculated by evaluating the lift coefficient that would be required during take-off. Here, the weight would be the MTOW and the speed the take-off speed, which is 1.1 times the stall speed resulting in a value of 2.98. $dC_{L,TO}$ is the difference between the maximum lift coefficient during take-off and the maximum lift coefficient in clean configuration being equal to 3.6 and 2.96 respectively, and $C_{L_{TO,\alpha=0}}$ the lift coefficient at take-off for angle of attack of zero having a value of 1.2. Based on these values and the most aft centre of gravity from Section 10.4 the main landing gear can be positioned in the longitudinal direction [63].

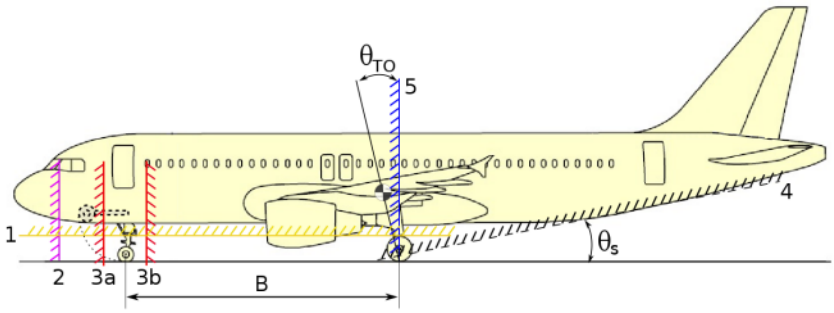

Figure 10.8: Landing gear design space limits in longitudinal direction [63]

Further, the integration of main landing gear would still have to comply with limit 1 and 4 in Figure 10.8. Limit 1 would be the tire clearance and limit 4 the scrape limit. The scrape limit defines the limit that for a flat tire that no part of the aircraft would touch the ground during rotation at take-off which is set at 15°. Then, these constraints including the longitudinal tip over limit can be expressed in Equation 10.34. Here, $z_{fus} = 1.81[m]$, $z_{tire,top} = 0.41[m]$, and $z_{cg} = 2.83[m]$ are the height of the fuselage, the flat tire, and centre of gravity respectively and the result of z_{MG} and x_{MG}, which are the height and longitudinal position of the main landing gear, are displayed in Table 10.20 as length of the main landing gear. When all these limits are met the longitudinal position is set. If this is not the case the design would have to be reiterated [63].

$$\begin{aligned} \text{Limit 1: } & z_{fus} - z_{tire,top} - 0.1524 \leq 0 \\ \text{Limit 4: } & \theta_{TO} - \tan^{-1}\left(\frac{z_{MG} - z_{fus}}{x_{fus} - x_{MG}}\right) \leq 0 \\ \text{Limit 5: } & \theta_{TO} - \tan^{-1}\left(\frac{x_{cg,aft} - x_{MG}}{z_{MG} - z_{cg}}\right) \leq 0 \end{aligned} \tag{10.34}$$

For the longitudinal position of the nose gear the limits 2, 3a, and 3b need to be reviewed, which are expressed in Equation 10.35. Here, $x_{cg,aft}$ and $x_{cg,fwd}$ are the longitudinal centre of gravity positions from Section 10.4. Limit 2 is the constraint regarding the stowing of the nose gear when retracted. Further, limit 3a and 3b are the limits regarding the longitudinal position of the nose gear. These are determined by the minimum and maximum nose load which are 8% and 15% of MTOW respectively. The resulting value of x_{NG} is then shown in Table 10.20.

$$\begin{aligned} \text{Limit 2: } & L_{NG,stowed} - x_{NG} + 0.2 \leq 0 \\ \text{Limit 3a: } & F_{n,min} = \frac{x_{cg,aft} - x_{MG}}{x_{NG} - x_{cg,aft}} \cdot F_{m,max} \\ \text{Limit 3b: } & F_{n,max} = \frac{x_{cg,fwd} - x_{MG}}{x_{NG} - x_{cg,fwd}} \cdot F_{m,min} \end{aligned} \tag{10.35}$$

Lateral design space limits

Additionally, the lateral position of the landing gear also had to be reviewed. The lateral design space limits are shown in Figure 10.9.

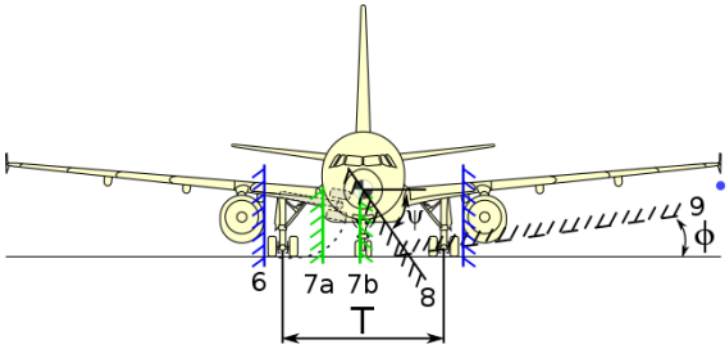

Figure 10.9: Landing gear design space limits in lateral direction[63]

The design limits 6 until and including 9 are the nacelle-strut interference, lateral main gear stowage (7a and 7b), lateral tip over limit, and roll limit respectively. The nacelle-strut interference is the limit regarding if the landing gear would interfere with the engine [63].

Limit 7a involves the stowage of the bogie when it is retracted and limit 7b involves if there is still clearance when both bogies are retracted [63]. Limit 7a would not be of importance as this limit considers the stowage of the bogie in the wing. As the aircraft has a high wing configuration this would not be a possibility. Here, $y_{wheel,bot}$ from limit 7b is the lateral position of the nose wheel which would be 0.11 $[m]$.

Further, a constraint is set on roll. The aircraft should be able to at least roll for $8°$ and have no interference with the ground. This might be imposed by the wing tip or the propellers [63]. As a larger propeller will be integrated at the wing tip, this will be the limiting factor.

Lastly, the lateral tip over limit needs to be reviewed. The limit upon this has been set that it should be lower than $55°$. This angle can be computed as follows, where the dimensions can be reviewed in Figure 10.10 [63]. The design space limits in lateral direction are then expressed in Equation 10.37. Here in α_{wb}, T and B are distance between the main landing gear bogies in lateral position and the distance between the main and nose landing gear in longitudinal direction respectively.

$$\psi = \tan^{-1}\left(\frac{H_{cg}}{l_n \cdot \sin\alpha_{wb}}\right), \qquad \alpha_{wb} = \tan^{-1}\left(\frac{0.5T}{B}\right) \tag{10.36}$$

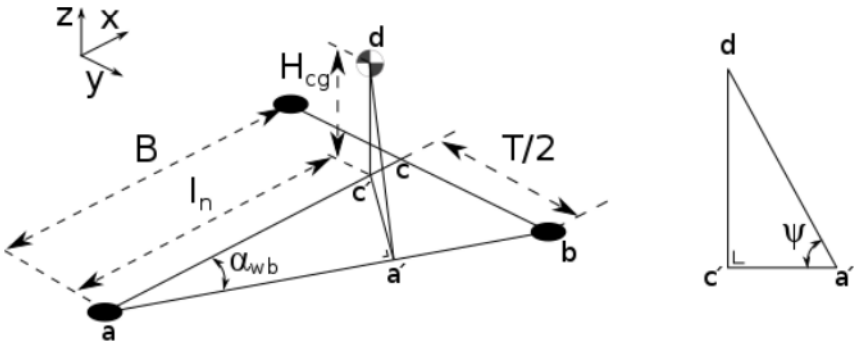

Figure 10.10: Lateral tip over limit[63]

$$\text{Limit 6: } y_{MG} - \left(y_{eng} - \frac{D_{eng}}{2}\right) \leq 0$$
$$\text{Limit 7b: } 0.05 - y_{wheel,bot} \leq 0, \tag{10.37}$$
$$\text{Limit 8: } \phi - \tan^{-1}\left(\frac{z_{eng} - z_{MG}}{y_{eng} - y_{MG}}\right) \leq 0, \quad \text{Limit 9: } \psi - 55 \leq 0$$

Considering both the longitudinal, lateral constraints, and the design of the tail and wing positioning lead to the results of undercarriage design shown in Table 10.20. Here, the reference position of the longitudinal and lateral position is the nose of the aircraft and middle of the fuselage respectively. The lateral tip over limit had shown to be the constraining limit and as already described in Subsection 8.3.2 the battery had to be stored in the fuselage instead of the wing to lower the centre of gravity height, z_{cg}, and the landing gear had to be put outside the fuselage resulting in a fuselage podded landing gear configuration.

Table 10.20: Undercarriage results

Parameter	**Main landing gear**	**Nose landing gear**
Longitudinal position $[m]$	14.28	4.55
Lateral position $[m]$	1.89	0
Length of landing gear $[m]$	1.41	1.41

11

Structural Design

While the fuselage sizing was performed and presented in Section 6.4, there is still abundant room left for more work on the structural design. This chapter describes the placement of the wingbox inside the wing, the material choice for the wing and cabin, and the structural design of the wing truss structure. These are presented in Section 11.1, Section 11.2 and Section 11.3 respectively.

11.1. Wingbox Lay-out

In order to place all of the necessary equipment inside the wing, the wingbox should provide sufficient space to accommodate this systems. The front spars of the wingbox are placed at 20% of the chord and the aft spars are placed at 75% of the chord. The spar locations are placed most forward and aft respectively [11]. This increases the moment of inertia of the wingbox and maximises the volume to store all the equipment.

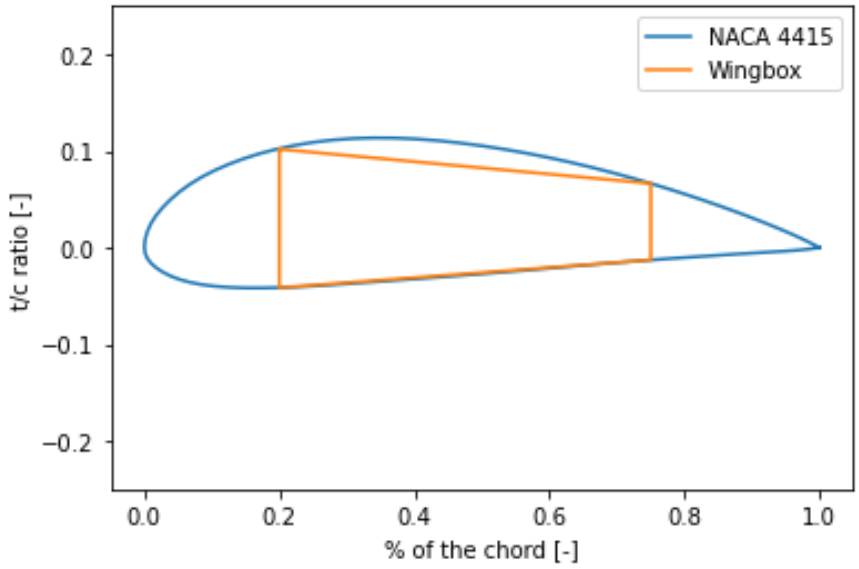

Figure 11.1: Wingbox placement in the airfoil

An estimation on the moment of inertia was made. Since a full wingbox design was out of the scope of this project, further structural analysis for a full wingbox design still has to be performed after this project is finished. For this estimation a plate thicknesses of 2 [mm], stringer dimensions of $15 \times 15 \times 1.5$ [mm], and a stringer configuration of 60 top stringers and 40 bottom stringers were assumed. With this estimation a bending moment and shear force analysis will be performed in Section 11.3. Important parameters of the wingbox are presented in Table 11.1. The distances to the center of gravity of the wingbox were taken with respect to the leading edge of the airfoil.

Table 11.1: Wingbox Parameters

Parameter	Value
$I_{wingbox}$	2.37 $[10^{-4}m^2]$
x_{centre}	0.07 $[m]$
y_{centre}	1.45 $[m]$

11.2. Material Choice

Selecting the materials for the main components of the aircraft allows for a a more detailed structural analysis of the aircraft due to it requiring inputs from material properties. In this section the materials for the cabin interior, fuselage, and wing box will be selected.

The interior of the cabin will be entirely made from natural composites. Woven flax fabric with a phenolic resin ended up being the material of choice. Both the fibers and the resin are 100% bio-degradable. The flax fibres have moderate fire resistance. Therefore, a fire resistant coating has to be applied before it is impregnated in the resin in order to meet the regulations [64]. The natural composites are readily available for production and do have a low cost. Furthermore, they have higher material properties than materials currently used for cabin design [64].

The wingbox should provide sufficient strength and stiffness for the wing, but should be kept a light as possible. Therefore, materials with a high specific strength and stiffness are desired. Carbon fiber reinforce plastics (CFRP) possess both of these aforementioned properties and can lead to a weight savings up to 25% [65]. Although CFRP's are less sustainable than natural composites their higher material properties are deemed to be more important due to the large aspect ratio wing, heavy battery equipment and better fire resistance [64]. Due to CFRP's requiring large amounts of energies to create, it was ensured that the selected fibers could be recycled in a sustainable matter with the use of peracetic acid (PAA) [66]. PAA is an organic substance, which is already commonly used for other applications and is not polluting for the environment[1]. The selected material for the construction of the wingbox is HexPly M21. This material was previously used in the wingbox design of the airbus A350 XWB[2]. Using a [0,+45,-45,90] degree lay-up an E-modulus of 102 [GPa], an ultimate tensile strength of 1142 [MPa], and an ultimate compression strength of 720 [MPa] were achieved. These values will be considered during the upcoming truss analysis in Section 11.3.

11.3. Truss Analysis

During the weight iterations a relaxation factor of 30% for the wing weight was assumed due to the fact that the main wing was supported by a truss [14]. The addition of the truss also resulted in an additional drag penalty. In order to verify these assumptions, an analysis of the wing bending moments and shear forces will be made to check if these assumptions were valid. First, the method to set the structural model up will be discussed in Subsection 11.3.1. After this, the location for the truss will be determined in Subsection 11.3.2.

11.3.1. Method of the Structural Model

To select the optimal attachment point for the truss, the internal shear forces, internal bending moments, and the deflections should be evaluated. For the analysis two load cases are considered. The first load case is derived from the maneuver loading diagram and corresponds a scenario where maximum lift is generated resulting in a load factor of $3g$. The second load case considered is based on the bottom line of the maneuvering diagram, where a negative load factor of $1g$ is experienced. The free-body diagrams for

[1] https://synergist.aiha.org/201612-peracetic-acid-uses-and-hazards, last consulted June 13, 2022

[2] https://www.reinforcedplastics.com/content/features/hexcel-s-composites-ready-to-fly-on-the-a350-xwb, last consulted on June 14, 2022

both load cases are displayed in Figure 11.2 and Figure 11.3. The carry-through structure of the aircraft will consist out of the connected struts at the bottom of the fuselage and the continuous wingbox at the top of the fuselage.

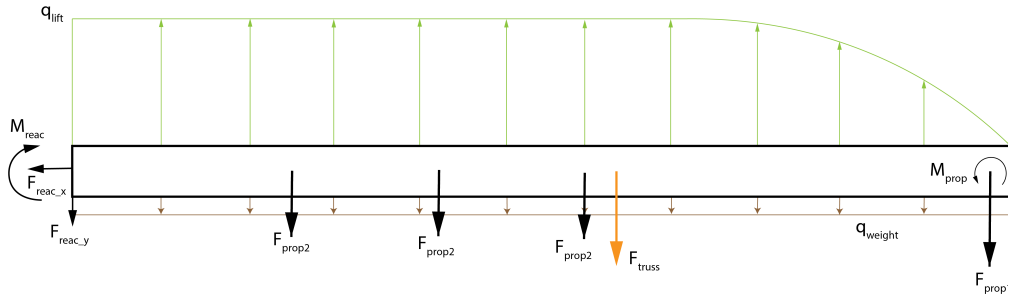

Figure 11.2: Free body diagram for the 3g maneuvering load case

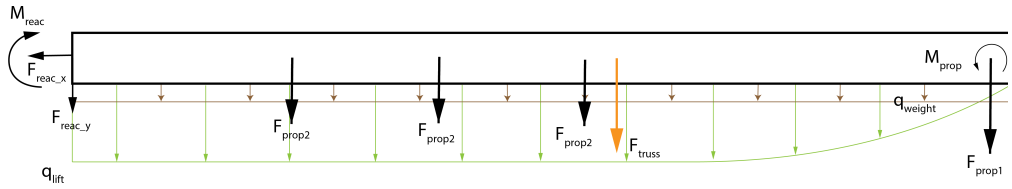

Figure 11.3: Free body diagram for the -1g maneuvering load case

Since both the wingbox and the truss structure are continuous, the system is statically indeterminate. Therefore, the deflections of the structure should be analysed to provide a sufficient amount of equations to determine all the loads. Since the strut will prevent the wing from deflecting at its attachment point, the deflection at this point was assumed to be zero. Further, the wing weight was modelled as a constant distributed load. The lift distribution was constructed using the method of superposition. Multiple distributed loads were added on top of each other, all starting at a different position from the tip and ending in the root. This way, every type of wing distribution could be accurately represented in the simulation. The weight of the engines and the force of the truss were introduced to the structure as point loads. For the engines also the torque exerted on the main wing was considered.

Since the wing is fastened at the point of attachment of the truss, the ability to deform at this point will be significantly lower than in the rest of the wing. Therefore, the deflection at this point was considered zero, yielding the vertical force of the truss exerted on the wing. Since the angle of the truss is known by choosing the location of the truss, the force in the horizontal direction can be computed as well.

Finally, the truss position was determined by analysing the bending stress diagram for every spanwise location the truss can be attached to. From this some of the attachment positions were deemed unfeasible due to the bending stresses exceeding the material limits. As the highest loads on the structure will be introduced by the first loadcase, the initial placement will be performed considering these loads. After, the loads for the second loadcase will be verified by inputting the obtained truss position from the first loadcase.

The model was verified by examining how the loads in the truss differ with a varying truss attachment point. It is observed that the further away from the center the wing is attached, the more the bending load in the wing is reduced and the larger the normal force in the truss. This behaviour of the model was expected due to the attachment point being constrained in deflection. Therefore, attaching the truss further away from the fuselage results in a larger deflection that has to be countered by the truss force.

11.3.2. Bending and Shear Load Model Including Truss Placement

To stay within the limits of allowable compressive stress of the material in the upper plate for the first loadcase the truss has to be attached at least $9.5\ [m]$ from the center of the wing. The bending stress was evaluated

with Equation 11.1 at the most critical point located in the upper left corner of the wingbox. Due to its position being the furthest away from the center of gravity, the largest compressive load is present for the first loadcase at this point. Due to the taper ratio the wingbox will become smaller across the wingspan. In both the the bending stress diagrams in Figure 11.4 and bending moment diagrams in Figure 11.5 it is clearly visible that the truss reduces the bending loads significantly. The quadratic scaling of the lift distribution with the spanwise position of the wing is clearly visible. The negative slope of the bending moment becomes positive after the attachment point, due to the counteracting force of the truss. Comparing the bending stress diagram of the truss attached at $9.5\ [m]$ from the wing center with a stress diagram of the wing without truss, a reduction in bending stress of 45% can be observed. Designing this wing without a truss would mean the moment of inertia of the wingbox would have to increase with a factor of 2, leading to a significant increase in the wing weight.

$$\sigma_{bending} = \frac{-M_x y}{I} \tag{11.1}$$

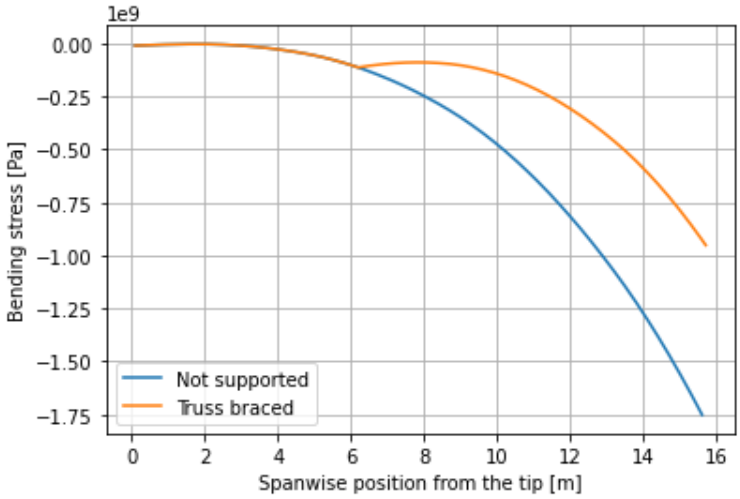

Figure 11.4: Comparison of the bending stress over the span of the wing between a truss braced wing and a non-supported wing.

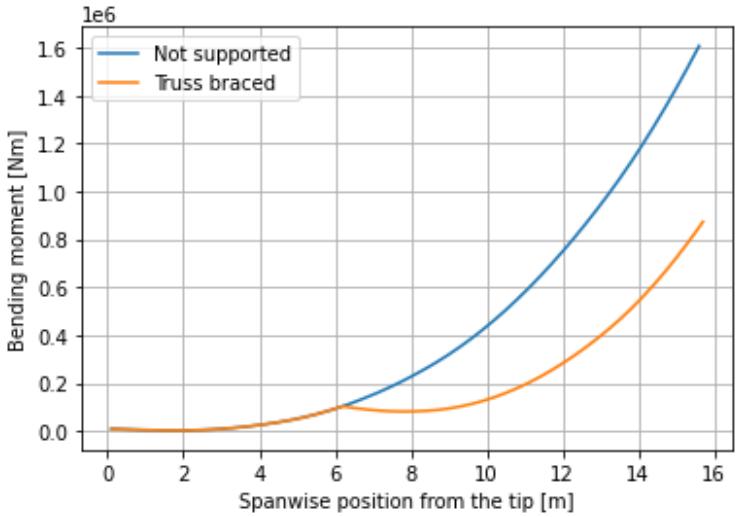

Figure 11.5: Comparison of the bending moment over the span of the wing between a truss braced wing and a non-supported wing.

Also, in the shear force diagram in Figure 11.6 the effect of the truss is clearly visible due to applying a vertical downwards load of 80.5 [kN] to the wing structure. Because of this the maximum shear force decreases by 23%. The truss itself will have to carry the compressive loads calculated from the deflection analysis performed on the wing and will be sized accordingly.

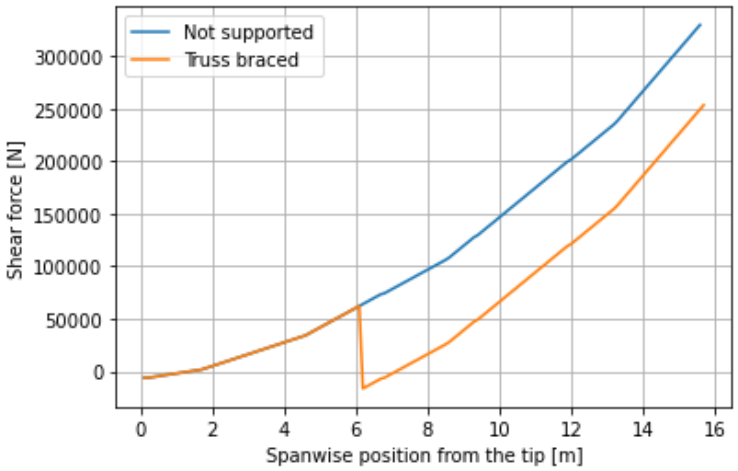

Figure 11.6: Comparison of the shear force over the span of the wing between a truss braced wing and a non-supported wing.

From the diagrams it can be concluded that the assumption of reduction of the wing weight by 30% in Subsection 6.7.2 is correct and validated, as this value is based on empirical data [14]. The total weight decrease due to the truss would likely be lower than 45% as the wing should be locally stiffened to introduce the forces of the truss. In the next step of the design of this aircraft a full wingbox configuration should be selected and analysed to compute a more accurate wing weight, which can be used for the detailed sizing. Also, a material and detailed design of the truss itself should be performed.

12
Performance Analysis

After having designed the systems of the aircraft in more detail, this chapter will analyse the performance of the resulted design. More specifically, it will discuss the mission energy and fuel consumption in Section 12.1, and regenerative performance in Section 12.2. Furthermore, the rate of climb is discussed in Section 12.3, take-off and landing distances in Section 12.4, and reliability in Section 12.5. Finally, Section 12.6 discusses the resource budget that were set up and how the final values compare to that.

12.1. Mission Energy

The first performance aspect that will be analysed is the amount of supplied energy that is required to complete the mission. It is an important parameter as it is not only involved in the sizing process of the aircraft, but also because it directly influences the amount of required fuel, battery energy, emissions, and costs.

The method that will be used to calculate mission energy is a time-stepping approach, where the mission is subdivided into all its individual flight phases. Every flight phase (subscript i) is associated with a certain output power $P_{out,i}$, which is applied over a certain duration t_i. All output powers are associated with a propeller efficiency $\eta_{prop,i}$ and a powertrain efficiency $\eta_{pow,i}$. Both of these efficiencies are different per flight phase, as was shown in Chapter 8 and Chapter 9. Finally, the total supplied mission energy can be calculated, of which the above-described method is summarised in Equation 12.1.

$$E_{sup,mission} = \sum E_i = \sum \frac{1}{\eta_{prop,i}} \cdot \frac{1}{\eta_{pow,i}} \cdot P_{out,i} \cdot t_i \tag{12.1}$$

12.1.1. Taxi

The first flight phase that will be analysed is the taxi phase. Using Equation 12.1, the consumed energy can be calculated if the required power to taxi the aircraft P_{taxi} and the taxi time t_{taxi} are known. P_{taxi} can be calculated with Equation 12.2,

$$P_{taxi} = F_{taxi} \cdot V_{taxi} = \mu_r \cdot (L - W) \cdot V_{taxi}, \tag{12.2}$$

where F_{taxi} is the required traction force to taxi the aircraft at a constant velocity of V_{taxi}. F_{taxi} is proportional the normal force exerted on the aircraft multiplied by a rolling friction coefficient μ_r. V_{taxi} and μ_r are derived from literature and statistics, where the highest reported values for V_{taxi} are chosen, so that the aircraft is able to taxi at high velocities to save mission time when needed. For the taxi velocities, values of 16 to 19 $[kts]$ are typical [3]. Due to these relatively low velocities, aerodynamic lift and drag are neglected, because computations show that drag only makes up 0.46% of the ground drag, and lift only makes up 0.97% of the weight, at a taxi velocity of 19 $[kts]$. Next, the rolling friction coefficient μ_r must be found. Raymer reports values of 0.03 as typical rolling-friction coefficient for surfaced dry runways [11].

Finally, the taxi time t_{taxi} is required. Values for this matter have been derived from literature [67]. However, the values reported there are impeded taxi times, which also include stationary phases of taxi due to interference by traffic, weather and air traffic control [68]. Considering that taxi power is only required during actual

ground motion, the unimpeded taxi times must be found. Based on the acquired data and the simplicity of the method, the P20 method was chosen for analysis [68]. The method can be executed by constructing a cumulative distribution function of taxi time data and subsequently taking the 20th percentile, which will finally result in unimpeded taxi time values. When analysing the acquired taxi time data [67], it was found that the data follows a Poisson distribution $Pois(\lambda)$, where the parameter λ was found to be approximately 16.637. Taking the 20th percentile of the cumulative distribution function results in unimpeded taxi times of 14 and 6 minutes for taxi-out and taxi-in times, respectively, adding up to a total of 20 minutes of unimpeded taxi time.

The total supplied taxi energy can now be calculated by Equation 12.1.1. The propeller efficiency is not incorporated, since taxi is performed using an electric motor that powers the nose wheel (Chapter 16. The efficiency of the electric nose wheel motor η_{nwm} is therefore used instead. For electric motors capable of supplying power in the range of P_{taxi} are reported to have efficiency values of around 90%[1].

$$E_{sup,taxi} = \frac{1}{\eta_{nwm}} \cdot \frac{1}{\eta_{pow,bat}} \cdot P_{taxi} \cdot t_{taxi}$$

The supplied taxi energy for both the taxi-in and taxi-out phases are reported in Table 12.1

12.1.2. Take-off

For the take-off phase, the supplied take-off energy must be found. The take-off power and required take-off ground-run distance are necessary for this computation. The required take-off power is derived from the wing- and power loading diagram (Section 6.2) by finding the intersection between the wing loading line and the take-off performance line. This gives a take-off power of $6650\ [kW]$.

Next, to calculate the supplied take-off energy, the required ground-run time t_g is needed. This value can be determined using the kinematic relation in Equation 12.3.

$$t_g = \int_0^{V_{LOF}} \frac{1}{a}\, dV \tag{12.3}$$

where V_{LOF} is the lift-off speed, which can be computed using the lift formula and taking $C_L = C_{L_{TO}} = 1.735$, which, in turn, was derived using the wing- and power loading diagram (Section 6.2). The acceleration a can be computed using Equation 12.4 [69],

$$a = g_0 \left[\frac{T}{W} - \mu_r - (C_{D,g} - \mu_r C_{L,g}) \frac{\frac{1}{2}\rho V^2}{W/S} \right], \tag{12.4}$$

where $C_{L,g}$ and $C_{D,g}$ are the lift- and drag coefficients affected by the ground effect (index g). The ground effect has not been investigated during aerodynamic analysis of the aircraft, and its effect is therefore omitted. The assumption is then made that $C_{L,g} = C_L$ and $C_{D,g} = C_D$. It is assumed that the ground run is performed zero pitch angle for the aircraft, and therefore at constant angle of attack. The corresponding lift coefficient then has a value of $C_L = 0.616$, giving a $C_D = 0.00888$ (determined in Section 7.5). Lastly, the rotation maneuver is not taken into account and is assumed to occur instantaneously. Hence an immediate transition from C_{L_g} to $C_{L,TO}$ is assumed to occur at the velocity of V_{LOF}. Finally, the ground-run time can be found by numerically integrating $\frac{1}{a}$ with respect to dV, and its value is $t_g = 27.53\ [s]$.

Finally, the supplied take-off energy can be computed using Equation 12.1, where the index i now indicates the take-off phase. Its final value is reported in Table 12.1.

[1] https://www.engineeringtoolbox.com/electrical-motor-efficiency-d_655.html

12.1.3. Climb

For the climb phase, the available climb power $P_{a,climb}$ is assumed to be constant, as the propulsion system is assumed to not suffer from a density lapse because the engines are not air-breathing. The available power is used to generate a power surplus that can be traded for a rate of climb. In turn, a rate of climb is used to reach a certain (cruising) altitude. The rate of climb can be calculated by Equation 12.5 [69].

$$RC_k = \frac{P_a - P_{r,k}}{W} \tag{12.5}$$

where index k indicates a variability with every instance in altitude (dh). As the density decreases, the velocity must be increased to retain force equilibrium. This results in the power required increasing, and consequently reducing the rate of climb with altitude.

As the power- and wing loading diagram has shown in Figure 6.5, the rate of climb requirement at sea-level ($1850\ [ft/min]$) is most constraining. Therefore, the climb power is chosen such that this requirement is met precisely. Climb performance calculations are performed mainly with the purpose to maximise rate of climb. The excess power is maximised, which can be achieved by minimising power required [69]. The aircraft must then fly at an optimal lift coefficient $C_{L_{opt}}$ that can be found by the process shown in Equation 12.6.

$$P_{r,k} = D \cdot V_k = \frac{C_D}{C_L} \cdot W \cdot V_k = \sqrt{\frac{W^3}{S} \frac{2}{\rho} \frac{C_D^2}{C_L^3}} \tag{12.6}$$

It follows that the fraction $\frac{C_D^2}{C_L^3}$ must then be minimised, which occurs for $C_{L_{climb,opt}} = \sqrt{3 \cdot C_{D,0} \cdot \pi \cdot AR \cdot e}$, giving a value of 1.641.

It must be noted, however, that climbing at maximum rate of climb is not necessarily the quickest way to reach the cruising altitude [69] and there is, namely, a time to climb requirement of 12.7 minutes that must be met. Rate of climb data can be still be used for this purpose, however, as this data indicates the time necessary to cover a certain change in altitude. The total time to climb can then be calculated as shown by Equation 12.7, which value is $10.6\ [min]$, which complies with the set requirement of $12.7\ [min]$.

$$t_{climb} = \sum \frac{dh}{RC_k} \tag{12.7}$$

This value can now also be used to calculate the total supplied climb energy. For this, Equation 12.1 can be used again, where the index i now indicates the climb phase. Its final value is reported in Table 12.1.

12.1.4. Cruise

For cruise, two requirements were set. To fly at a cruise Mach number of 0.40 - 0.45 at $FL170$. For the calculations, a Mach number of 0.45 has been used, as in this case more energy is consumed and therefore becomes most critical for sizing the aircraft.

In cruise, altitude is assumed to remain constant. Therefore, no excess power is needed and the power available is assumed equal to the power required. The cruise power can then be calculated as a function of lift-drag ratio and cruise Mach number by use Equation 12.8.

$$P_{a,cr} = P_{r,cr} = D_{cr} \cdot V_{cr} = \frac{1}{\left(\frac{C_L}{C_D}\right)_{cr}} \cdot W \cdot \sqrt{\gamma \cdot R \cdot T_{cr} \cdot M_{cr}^2} \tag{12.8}$$

The cruise time t_{cr} can be determined by dividing the distance spent in the cruise phase by the cruise velocity. The cruise distance is, in turn, calculated by subtracting the horizontally covered distances of the climb and descent phase from the mission range (in this case the harmonic range of $800\ [km]$). The supplied cruise energy can now simply be found by Equation 12.1, where index i now indicates the cruise phase. Its final value is reported in Table 12.1.

12.1.5. Descent

During the descent phase, the descent power consists of several contributions. First, a negative potential energy ΔE_p is overcome, which will be traded for drag in the form a required power $P_{r,desc}$. Optionally, a thrust T_{desc} is applied. The available descent power can now be displayed in the following manner (Equation 12.9). Similarly to the climb phase, The index k indicates variability with altitude, hence the calculations are performed for all altitude instances k (step-size $dh = 1\ [m]$).

$$P_{a,desc,k} = \frac{\Delta E_{pot}}{t_{desc,k}} + D_{desc,k} \cdot V_{desc,k} + T_{desc,k} \cdot V_{desc,k} \tag{12.9}$$

Considering there are no set requirements for the descent phase, any strategy can be chosen for descent. It is chosen to aim for a gliding descent, since that is the most energy-efficient for the mission because, first of all, performing a glide means that no power is applied and therefore the aircraft consumes no energy to propel itself. This also removes the last term of Equation 12.9. Secondly, if the glide angle $\overline{\gamma}$ is minimised, the horizontally covered descent distance is maximised and consequently, the cruise distance is minimised, maximising energy savings. One remark that must be made however, is that a descent cannot be performed fully in gliding conditions, because of airport arrival procedures, restrictions, and air traffic control instructions. This condition is, however, chosen as a baseline to compare other descent strategies to, for example in Section 12.2.

To calculate descent performance, an optimal lift-coefficient $C_{L_{opt}}$ must be found at which the descent phase will be executed. For minimising $\overline{\gamma}$, $C_{L_{opt}}$ can, similarly to the climb phase, be determined by Equation 12.6 [69]. The descent time t_{desc} also be determined according to the same method as for climb, namely by use of Equation 12.7. Finally, the total supplied descent energy can be calculated by use of Equation 12.1, where the index i now indicates the descent phase. Its final value is reported in Table 12.1.

12.1.6. Landing

During landing the aircraft must get rid off its kinetic energy in order to come to a stop. This will be performed by braking the aircraft using wheel brakes, according to CS25 requirements [13]. These requirements also state that reverse thrust may not be incorporated to ensure compliance to landing field requirements. For this reason, no reverse thrust is assumed to be used during landing. It is then concluded that during the landing phase, no supplied mission energy is necessary.

12.1.7. Loiter

During the loiter phase, it is of utmost importance to have the ability to fly for as long as possible. A requirement of 45 minutes of loiter time was specified. Typical loiter altitudes are $1500\ [ft]$ [11]. To achieve the loiter requirement, endurance must be maximised, which can be achieved by minimising energy consumption. For this purpose, the optimal lift coefficient at which loiter will be performed must be found. This process is shown in Equation 12.10.

$$E_{loi} = P \cdot t = D \cdot V \cdot t = \frac{C_D}{C_L} \cdot W \cdot V \cdot t = \sqrt{\frac{W^3}{S} \frac{2}{\rho} \frac{C_D^2}{C_L^3}} \cdot t \tag{12.10}$$

It can be observed that $\left(\frac{C_D^2}{C_L^3}\right)$ must be minimised in order to minimise energy consumption. Differentiating this fraction results in an optimal lift coefficient equal to $\sqrt{3 \cdot C_{D,0} \cdot \pi \cdot AR \cdot e} = 1.641$. Finally, the loiter energy can be computed, which value is reported in Table 12.1.

12.1.8. Diversion

In case of diversion, there exists a requirement to reach a minimum of a $185\ [km]$ diversion distance. A diversion profile will look identical to the baseline mission profile, and consist of normally performed climb and descent phases. Only the cruise phase is different and now performed at a lower altitude for a shorter distance. The diversion cruise altitude is partly dependent on diversion distance, however, typical diversion cruise altitudes are around $6000\ [ft]$ [18].

To achieve the $185\ [km]$ diversion distance requirement, range must be maximised for this phase, which is identical to maximising velocity divided by fuel flow $\frac{V}{F}$. The optimal lift coefficient can be obtained by the process shown in Equation 12.11.

$$\frac{V}{F} = \frac{V}{C_P \cdot \frac{D \cdot V}{\eta_{prop}}} = \frac{\eta_{prop}}{C_P} \cdot \frac{1}{\frac{C_D}{C_L} \cdot W} \tag{12.11}$$

It can be observed that the lift to drag ratio $\frac{C_L}{C_D}$ must be maximised to maximise range. Differentiating this fraction gives an optimal lift coefficient equal to $\sqrt{C_{D,0} \cdot \pi \cdot AR \cdot e} = 0.947$.

Finally, the supplied diversion energy can be computed in the manner as was performed for the baseline mission profile, namely by using the methods for climb, cruise and descent. The final supplied diversion energy is reported in Table 12.1.

12.1.9. Results

This subsection reports the supplied mission energy for all flight phases and different scenarios, as well as the total supplied mission energy. These values are reported in Table 12.1. It must be noted that regeneration is not accounted for in the computations for the total supplied mission energy. How this value is affected by regenerative braking is discussed in detail in Section 12.2.

Table 12.1: Supplied mission energy by flight phase in $[MJ]$.

Flight Phase	$P_{shaft}\ [kW]$	$E_{sup}\ [MJ]$
Taxi-out	89	46
Taxi-in	89	106
Take-off	6650	123
Climb (to $FL170$)	3605	4137
Cruise (DOC)	2033	7998
Cruise (harmonic)	2033	21097
Descent (0% regeneration)	0	0
Landing	0	0
Loiter	3248	6900
Diversion	<3605	6827
Total (DOC)	N/A	12521
Total (harmonic)	N/A	39330

12.2. Regenerative Braking Performance

This section describes and analyses the performance of the regenerative braking system of the aircraft. Analysis are performed for several different regenerative braking strategies, that were described in Section 9.3. The performance of these strategies is analysed as a function of regenerative braking level, which is defined as the percentage of the maximum thrust the propeller can provide in regenerative braking mode. The effects of the various strategies on mission profile, mission energy and mission time are investigated in the following subsections. Limitations on regenerative braking will also be discussed. Conclusions will then be drawn about the preferred regenerative braking strategy for a DOC mission.

12.2.1. Effect on Mission Profile

The first aspect that will be analysed is the effect of regenerative braking on the mission profile. Applying regenerative braking in the descent phase is identical to applying negative thrust. Consequently, the flight path angle must be increased to retain the flight conditions for an optimal descent strategy, as was described in Subsection 12.1.5. The relationship between the applied regenerative braking level and flight path angle is shown in Figure 12.1a. This figure shows a non-linear increase in flight path angle with regenerative braking level, where the regenerative braking strategy for thrust shows the largest increase, namely, from -2.93 to -4.48 $[deg]$ ($+52.9$%). A consequence of this steeper descent path is that the aircraft must now initiate its descent at a later moment, consequently increasing the cruise distance. The effect of the latter is visualised in Figure 12.1b. A proportional relationship can be observed, where the total cruise distance increases by 36.28 $[km]$ ($+14.8$%).

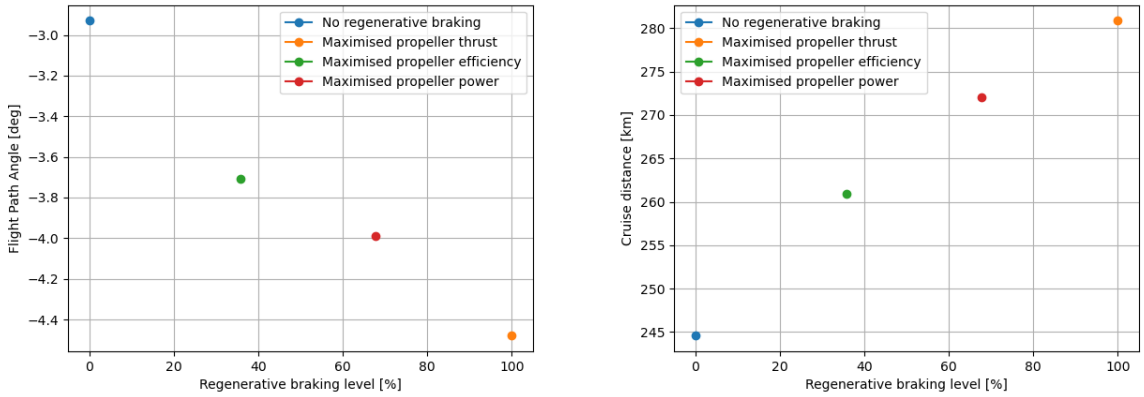

(a) Flight path angle as function of regenerative braking level.

(b) Cruise distance as function of regenerative braking level.

Figure 12.1: Influence of regeneration on flight path angle and cruise distance.

A consequence of the steeper descent path is an extension of the cruise phase, where more energy is required. The effect of this will be discussed in the next subsection.

12.2.2. Effect on Mission Energy

Next, the effect of regenerative braking on the mission energy is analysed. This effect will be investigated for the DOC mission only, as this is the scenario for which the aircraft must be optimised. For this subsection, two aspects will be analysed, namely the regenerated energy in the descent separately, as well as the net supplied mission energy for the DOC case. Investigations will also be performed on the relationship between these two.

When investigating the energy regenerated during descent, it can be obversed that a higher regenerative braking level does not necessarily lead to more energy regeneration. In fact, as the red dot in Figure 12.2a shows, regeneration is maximised when adopting the strategy where the propeller is optimised for propeller power. In that case, a maximum of 178 $[MJ]$ can be regenerated.

Next, when investigating the relationship between regenerative braking level and net DOC mission energy, it can be observed that total mission energy increases with regenerative braking level, as is shown in Figure 12.2b, by an amount of 1080 $[MJ]$ ($+8.6$%) when adopting the maximum thrust strategy. This can be explained by the relatively low efficiency of transferring energy from the flow into the shaft, as was shown in Section 9.3. Secondly, regenerative braking delays the top of descent point due to the higher flight path angle, as is shown in Subsection 12.2.1, consequently increasing the cruise phase distance and increasing its mission energy.

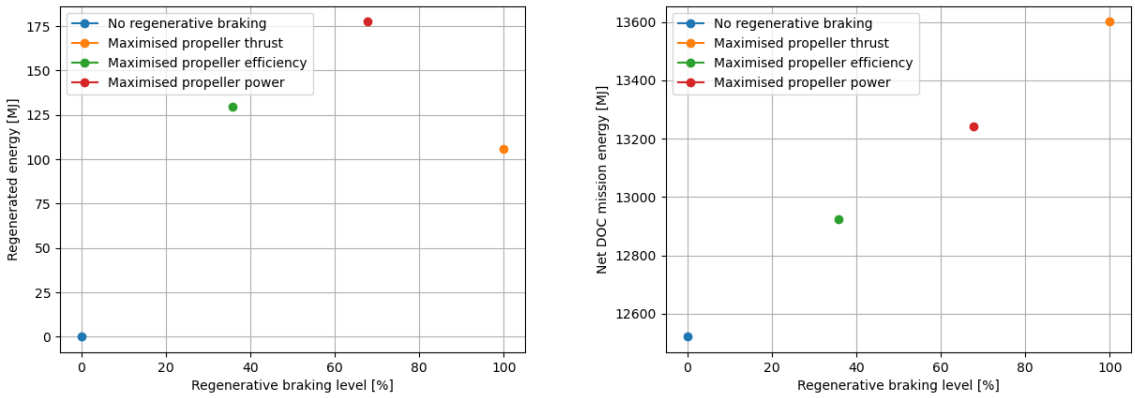

(a) The amount of regenerated energy recuperated in the batteries as a function of regenerative braking level.

(b) The total net DOC mission energy, accounting for recuperated energy, as a function of regenerative braking level.

Figure 12.2: Influence of regeneration on regenerated energy and total supplied mission energy.

It can be concluded from the above analysis that the energy regenerated does not compensate for the extra required energy due to the longer cruise phase.

12.2.3. Effect on Mission Time

As Subsection 12.2.1 shows that the flight path angle increases during regenerative braking. This change in mission profile suggests a possible change in mission time. The total mission time has therefore been investigated for different regenerative braking strategies, whose effects are visualised in Figure 12.3.

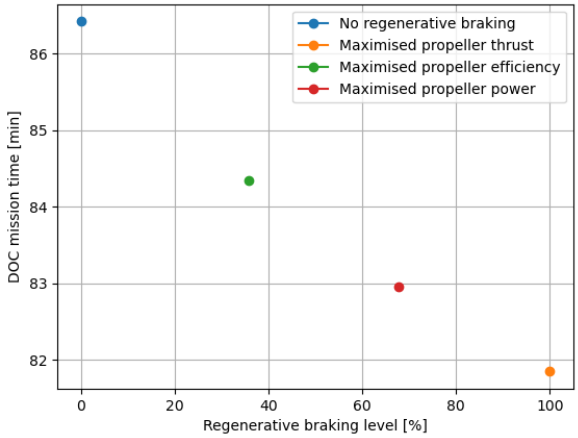

Figure 12.3: Total DOC mission time as a function of regenerative braking level.

The data shows that there is a decrease in mission time when regenerative braking is increased, namely from $86.42\ [min]$ (no regenerative braking) to $81.85\ [min]$ when adopting the maximum thrust strategy. This means a maximum of $4.57\ [min]$ can be saved, which is a 5.3% decrease on the total DOC mission time.

Recuperating energy back into the batteries also reduces the amount energy that must be recharged for the next flight, and can then theoretically save mission time. However, as Figure 16.5 shows, turnaround time is not limited by charging time, and therefore remains unaffected by recuperated energy.

12.2.4. Limitations of Regenerative Braking

Subsection 12.2.2 showed, there is always an increase in net DOC mission energy compared to no regenerative braking. This suggests that problems arise when using the regenerative braking function close the harmonic range. For this purpose, the payload-range diagram of the aircraft must be analysed (Figure 12.4a). After the harmonic range has been reached (the point on the top-right), the pilot must remove payload from the aircraft in order to extend the range, visualised by the line in the diagram having a kink, and subsequently dropping down.

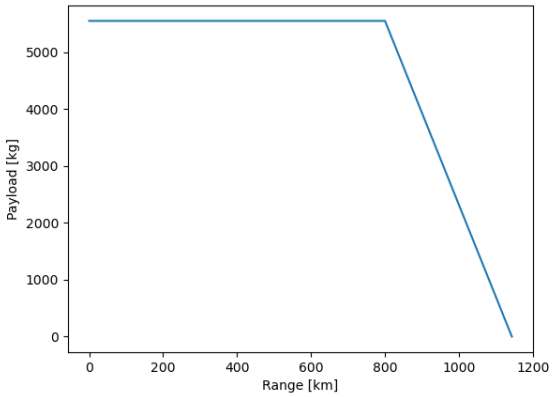

(a) Simplified version of the payload-range diagram for the Hammerhead, where the effect of fuel is neglected.

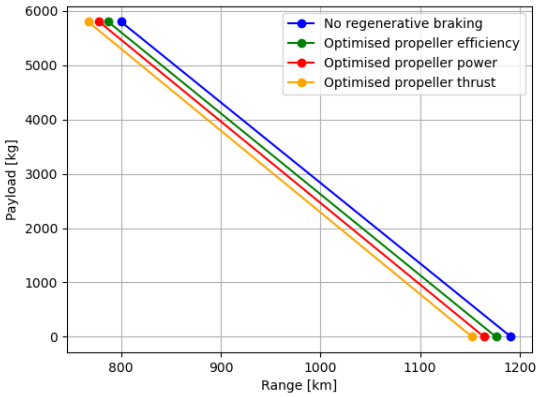

(b) Shift of payload-range line, when regenerative braking is increased.

Figure 12.4: Limitations of regenerative braking when conducting a harmonic range mission.

When zooming in on the line in Figure 12.4b, it can be observed this line shifts to the left when the regenerative braking level is increased, indicating that the regenerative capability of the aircraft reduces when performing missions close to the harmonic range. In fact, in this situation, the pilot must remove more than half a ton of payload in order to retain the harmonic range. If he or she does not, the harmonic range will be reduced by $33\ [km]$.

12.2.5. Conclusions

Now that all regenerative braking strategies have been analysed, conclusions can be drawn on which of these is most optimal in what situation. For this purpose, the results of the analyses performed are gathered in Table 12.2.

Table 12.2: Performance data for different regenerative braking strategies

Strategy	Energy regenerated $[MJ]$	Net DOC mission energy $[MJ]$	DOC mission time $[min]$	Harmonic range $[km]$
Efficiency	130	+404 / +3.2%	-2.08 / -2.4%	-13 / -1.6%
Power	178	+721 / +5.8%	-3.46 / -4.0%	-22 / -2.8%
Thrust	106	+1080 / +8.6%	-4.57 / -5.3%	-33 / -4.1%

When investigating these results, the following conclusions can be drawn:

- The efficient strategy provides the best balance between regenerated energy and net DOC mission energy, but barely saves mission time.
- The power strategy maximises regenerated energy in the descent phase, and provides average performance on the other areas.
- The thrust strategy minimises mission time, but regenerates the least energy.

12.3. Rate of Climb

This section analyses the climb performance of the aircraft for several conditions and tests its compliance with the set requirements [1].

Firstly, the aircraft must be able operate at smaller airports, which may be located in mountainous areas. In order to clear terrain, the aircraft must be able to attain sufficient rates of climb at airport elevation. For this scenario, a requirement of $1850\ [ft/min]$ is set [1]. Furthermore, the aircraft must also attain a $300\ [ft/min]$ climb rate at its cruising altitude of $FL170$ [1]. Also, a sufficient rate of climb must be attainable to reach a maximum operating altitude of $FL250$ [1]. Lastly, for the one engine inoperative case (OEI), an altitude of $4000\ [m]$ must be attainable [1].

Climb performance is computed according to the same method described in Subsection 12.1.3, where the rate of climb is calculated using Equation 12.5. Table 12.3 reports climb performance values for the rate of climb requirements for the aircraft [1].

Table 12.3: Climb performance at sea-level, $FL170$ and $FL250$.

Scenario	**ROC (computed)** $[ft/min]$	**ROC (requirement)** $[ft/min]$
Sea-level	1850	1850
$FL170$	1664	300
$FL250$	1548	attain $FL250$
OEI	1221	attain $4000\ [m]$

Table 12.3 shows that all rate of climb requirements are met. It also shows that the climb rates at $FL250$ and at $4000\ [m]$ for the OEI case are sufficient to reach these respective altitudes.

12.4. Take-off and Landing Field Length

Considering the aircraft must be able to take-off and land on smaller airports, the required field lengths must be computed to assess if the set requirements are met. The take-off and landing field length are defined as the ground run distance s_g added to the distance required to clear a screen height of $50\ [ft]$ s_{scr} [69]. For take-off, the field length is $1000\ [m]$ at maximum take-off weight, and $800\ [m]$ for short take-off and landing operations [1]. The aircraft was given a take-off power derived from the wing- and power loading diagram (Section 6.2), precisely such that the $1000\ [m]$ requirement is met. It must however computed if the designed systems of the aircraft are indeed capable of meeting this requirement. Starting computations with the ground-run distance s_g, which can be calculated by Equation 12.12,

$$s_g = \int_0^{V_{LOF}} \frac{V}{a} dV, \tag{12.12}$$

where a can be calculated using Equation 12.4, and where for all inputs the same values are chosen as were used in Subsection 12.1.2. Next, s_{scr} must be determined. For that, it must first be verified if the screen

height can be cleared by the end of the take-off rotation maneuver. The height cleared by the end of this maneuver can be calculated by Equation 12.13 [69],

$$h_t = \frac{V_{LOF}^2}{g(n_{LOF}-1)}\left(1-\cos\left(\frac{T-D}{W}\right)\right), \tag{12.13}$$

where n_{LOF} is the load-factor during the rotation maneuver, which Ruijgrok reports as approximately equal to 1.15 for propeller aircraft [69].

The horizontal distance covered during this maneuver, s_t, can be calculated by Equation 12.14 [69],

$$s_t = \frac{V_{LOF}^2}{g(n_{LOF}-1)}\frac{T-D}{W} \tag{12.14}$$

From computations it follows that the screen height of $50\ [ft]$ is cleared after a distance of $267.27\ [m]$, which then is the screen distance. Both s_g and s_{scr} can be added to determine the take-off field length, which results in $970\ [m]$.

Next, for the landing phase, it must also be shown that the aircraft complies with the landing field length requirement, which must be smaller than the required take-off field length [1]. Starting with the landing ground-run distance, this value can be determined using Equation 12.15,

$$s_g = \int_{1.15\cdot V_{stall}}^{0}\frac{V}{a}dV = \int_{V_{TD}}^{0}\frac{V}{\mu_{s,max}\cdot\left(1-\frac{L}{W}\right)\cdot g_0}dV \tag{12.15}$$

and where $\mu_{s,max}$ is the maximum static friction force coefficient that the aircraft tires can provide. Typical values are $0.25-0.40$ [70]. The worst case scenario is chosen for analysis ($\mu_{s,max}=0.25$) to ensure the aircraft meets the requirements in all cases. According to Ruijgrok, the touchdown velocity V_{TD} is typically equal to $1.15\cdot V_{stall}$ [69]. V_{stall} is determined from the lift-formula with $C_L = C_{L_{max}} = 3.6$ (determined in Section 7.5), resulting in a $V_{stall} = 41\ [m/s]$. This leads to $V_{TD} = 47.2\ [m/s]$. Furthermore, considering ground spoilers are deployed at touchdown, lift is reduced, and braking force is increased. However, since no research has been conducted on the ground spoiler aerodynamics, no lift reduction will be assumed when calculating braking distance. Lastly, it must be noted that reverse thrust also may not be incorporated in determining the braking distance, as per CS25 requirements [13]. Performing computations results in a landing ground-run distance of $498\ [m]$. Next, the flare distance must be determined. This can be done using the same as was used for the rotation maneuver, using Equation 12.14, where in this case $V = Vapp$ and $n = n_{flare}$. Ruijgrok reports that V_{app} is in general equal to $1.3\cdot Vstall$ [69], resulting in $V_{app} = 53.3\ [m/s]$. Lastly, n_{flare} can be taken as 1.15 [69]. Computations results in a horizontal flare distance of $s_f = 101\ [m]$. Unfortunately, the start of the flare occurs below the screen heigh of $50\ [ft]$. For that reason, the extra horizontal distance required that clears the screen height must be computed. Performing computations and assuming $V = V_{app}$ and an approach path angle $\gamma_{app} = -3.0\ [deg]$ (typical for approaches [69]), the extra required distance equals $240\ [m]$. Combining all values results in a landing field length of $839\ [m]$. Lastly, it follows that the brake force can be reduced to no less than 74% of maximum braking capability to make the landing field requirement.

All computed values for the required take-off and landing field length reported in Table 12.4.

Table 12.4: Take-off and landing field lengths.

Scenario	**Field Length (comp.)** $[m]$	**Field Length (req.)** $[m]$
Take-off (MTOW)	970	1000
Take-off (STOL, no payload)	781	800

Table 12.4: Take-off and landing field lengths.

Scenario	Field Length (comp.) $[m]$	Field Length (req.) $[m]$
Landing (100% brake force)	871	<1000
Landing (>74% brake force)	<1000	1000

12.5. Reliability

The last performance aspect that will be analysed is reliability. This aspect is important not only for passenger safety, but also because component failure must be minimised in order to reach the sustainability goals (Section 15.1). An aircraft consists of a large amount of components with each an individual reliability. This reliability can be determined using an exponential distribution (Equation 12.16[2]).

$$R(t) = e^{-\lambda t} \tag{12.16}$$

Here, λ is the failure rate (number of failures per unit of time) of a component, and t is the time, specified in the same unit of time as the failure rate.

The aircraft's resultant reliability is, however, dependent on the arrangement of these components, namely, if they are arranged in a series or in a parallel configuration. For series arrangements, the reliability of a system can be determined by multiplying the reliabilities of the individual components of that system (Equation 12.17[2]).

$$R_{sys,ser} = R_1 \cdot R_2 \cdot ... \cdot R_n = R^n \tag{12.17}$$

From Equation 12.17 it can be concluded that the reliability of a system in with its components in a series arrangements goes down when the number of components is increased. For systems with their components in parallel arrangement, the opposite holds. Namely, the more components that are added to a system in parallel, the more the reliability of the system increases. This effect can be shown by Equation 12.18[2].

$$R_{sys,par} = 1 - (F_1 \cdot F_2 \cdot ... \cdot F_n) = 1 - F^n = 1 - (1 - R)^n \tag{12.18}$$

The above theory will be applied to calculating the total resultant reliability of the aircraft. For that purpose, the reliability of several systems must be analysed. The systems that are most essential for operating the aircraft safely will be chosen for analysis, namely the batteries, hydrogen fuel cell, and the electric motors. All other systems are not analysed at this stage and considered beyond the scope of this current report.

It must be noted that the reliability analysis that is performed next, is performed for a yearly timeframe. After all, major maintenance must be performed on approximately this time interval, especially for the battery system, as presented in Subsection 15.2.1.

12.5.1. Battery Reliability

The battery system is constructed in the arrangement as is described in Subsection 8.2.4. The battery system contains Li-ion battery cells with an expected life-cycle of 2000 cycles (Subsection 15.2.1). When executing five flights a day for 365 days a year and assuming one flight equals one complete battery cycle, a failure rate of 1.225 failures per year follows for a battery cell. Using Equation 12.16, this results in $R_{bat-cell} = 0.29376$ for a yearly timeframe. Using Equation 12.17 and Equation 12.18, and taking into account the series and parallel arrangements of the batteries, its components and sub-components (described

[2]https://www.intechopen.com/chapters/50094

in Subsection 8.2.4), the reliability of the total battery system results was found to be $R_{bat-sys} = 0.99434$ for the entire battery system.

12.5.2. Hydrogen Fuel-Cell Reliability

Next, the reliability of the hydrogen fuel cell system will be determined. It was found that a stack of hydrogen fuel cells have a life-time of about 20000 cycles[3]. This results in $\lambda_{fuel-cell} = 0.1225\ yr^{-1}$. Its reliability for a yearly timeframe will then be $R = 0.88470$ per cell. For the hydrogen fuel-cell powertrain, two of these stacks are connected in parallel, resulting in $R_{fuel-cell} = 0.98670$.

12.5.3. Propulsion System Reliability

The last system for which the reliability will be analysed is the propulsion system. The propulsion system consists of eight propellers, connected to an electric motor. A failure rate of 5.93 per million flights is reported for electric motors including the gearbox, bearings, winding and housing [71]. Converting this to number of failures per year results in $\lambda_{elec-motor} = 0.014529\ yr^{-1}$, giving $R_{elec-motor} = 0.98558$ for a yearly timeframe. The electric motors are connected in series to an inverter with a failure rate of 4.49 per million flights, or $\lambda_{inv} = 0.11001\ yr^{-1}$, giving a reliability of $R_{inv} = 0.98906$. The two aforementioned reliabilities must be multiplied to obtain the reliability of the motor-inverter sub-assembly. Lastly, the total reliability of the propulsion system can be computed, considering eight of these sub-assemblies are connected in parallel. Computations give a reliability $R_{prop,sys} = 0.\overline{9}$.

12.5.4. Resultant Aircraft Reliability

Finally, the resultant reliability of the aircraft can be computed. Using the systems for which reliability values have been computed, and assuming the battery and hydrogen fuel-cell system function in parallel, which together work in series with the propulsion system, a resultant reliability of $R_{res} = 0.99992$.

12.6. Technical Resource Allocation

In the baseline report [72] the resources were allocated in three different categories, namely technical, sustainable and economic. Table 12.5, Table 12.6, and Table 12.7 show the values that were initially targeted, the associated contingency margins, and the actual value the final design converged to. These tables show that all final values are within the set budgets, apart from the total team time invested. The fly-over noise was not calculated and could therefore not be checked.

Table 12.5: Technical resource target values as stated in the baseline report

Technical	$MTOW\ [kg]$	$W/S[N/m^2]$	Cruise $L/D[-]$	$C_{l_{max}}[-]$
Target value	25000	TBD	20	2.5
Contingency	40%	25%	35%	30%
Actual value	23314	3710	18.5	3.6
Compliance	✓	n.a.	✓	✓

Table 12.6: Sustainability resource target values as stated in the baseline report

Sustainable	CO_2 emiss. $[kg/(pax \cdot 100km)]$	NO_X emiss. $[kg/(pax \cdot 100km)]$	Fly-over noise $[EPNdB]$
Target value	2.25	0.0008	71.6

[3] https://docsend.com/view/t9aw2mk

Table 12.6: Sustainability resource target values as stated in the baseline report

Sustainable	CO_2 emiss. $[kg/(pax \cdot 100km)]$	NO_X emiss. $[kg/(pax \cdot 100km)]$	Fly-over noise $[EPNdB]$
Contingency	20%	20%	5
Actual value	0	0	TBD
Compliance	✓	✓	TBD

Table 12.7: Economic resource target values as stated in the baseline report

Economic	Production cost $[M€]$	Operational cost $[€/hr]$	Total team time invested $[hr]$
Target value	12.7	2088	3680
Contingency	40%	25%	5%
Actual value	8.775	1461	4000
Compliance	✓	✓	✗

13

Requirement Compliance

This chapter presents the compliance matrix, which shows the level of compliance of the designed aircraft to all top level requirements. If compliance to a certain requirement could not be analysed in sufficient detail, the compliance column contains a ”TBD” for this requirement.

Table 13.1: Requirement Compliance Matrix

ID	Requirement	Compliance	Ref.
REQ-TOP-PER-01	The aircraft's design cruise speed shall be at least 450 $[km/h]$	✓	12.1.4
REQ-TOP-PER-02	The aircraft's design cruise speed shall be at most 550 $[km/h]$	✓	12.1.4
REQ-TOP-PER-03	The aircraft's design cruise speed shall be at least Mach 0.4	✓	12.1.4
REQ-TOP-PER-04	The aircraft's design cruise speed shall be at most Mach 0.48	✓	12.1.4
REQ-TOP-PER-05	The aircraft's design cruise altitude shall be FL170	✓	3.1
REQ-TOP-PER-06	The aircraft's design payload shall be at least 5300 $[kg]$	✓	6.7
REQ-TOP-PER-07	The aircraft shall be able to carry 50 passengers (at 95 $[kg]$ per passenger)	✓	6.7 6.4
REQ-TOP-PER-08	The aircraft shall be able to carry at least 500 $[kg]$ of other payload when carrying 50 passengers	✓	6.4
REQ-TOP-PER-09	The aircraft shall be able to carry a payload of at least 5800 $[kg]$	✓	6.4
REQ-TOP-PER-10	The range at which the DOC is evaluated shall be at least 400 $[km]$ at cruise speed with design payload and reserve fuel	✓	17.3
REQ-TOP-PER-11	The aircraft shall have a harmonic range of at least 800 $[km]$ at cruise speed with design payload and reserve fuel	✓	12.1
REQ-TOP-PER-12	The aircraft shall be able to carry the reserve fuel necessary to fly 185 $[km]$ and stay in a 45 $[min]$ holding pattern	✓	12.1
REQ-TOP-PER-13	The aircraft shall have a range of 450 $[km]$ with design payload when taking off from Denver International Airport	✓	12.4

Table 13.1: Requirement Compliance Matrix

ID	Requirement	Compliance	Ref.
REQ-TOP-PER-14	The aircraft shall have a take-off field length of at most 1000 $[m]$ at maximum take-off mass, sea level, from a paved runway, assuming ISA	✓	12.4
REQ-TOP-PER-15	The aircraft shall have a take-off field length of at most 800 $[m]$ at sea level, from a paved runway, assuming international standard atmosphere, for short take-off and landing operation	✓	12.4
REQ-TOP-PER-16	The aircraft's landing field length shall not be longer than the take-off field length	✓	12.4
REQ-TOP-PER-17	The aircraft shall be able to attain a rate of climb of 1850 $[ft/min]$ at maximum take-off mass, sea level, assuming international standard atmosphere	✓	12.3
REQ-TOP-PER-18	The aircraft shall be able to attain a rate of climb of 300 $[ft/min]$ at top of climb	✓	12.3
REQ-TOP-PER-19	The aircraft shall be able to climb to cruise altitude within 12.7 $[min]$	✓	12.3
REQ-TOP-PER-20	The aircraft shall be able to operate up to an altitude of 7620 $[m]$	✓	12.3
REQ-TOP-PER-21	The aircraft shall have a wingspan of at most 36 $[m]$	✓	6.3
REQ-TOP-PER-22	The aircraft shall have at least 1 lavatory	✓	6.4
REQ-TOP-PER-23	The aircraft shall have at least 1 galley	✓	6.4
REQ-TOP-PER-24	The flight shall be comfortable for all passengers and crew during nominal flight operations	✓	6.4.1
REQ-TOP-SAF-01	The aircraft's OEI (or equivalent) service ceiling shall be higher than 4000 $[m]$, at 95% of MTOW and ISA+10 conditions.	✓	12.3
REQ-TOP-SAF-02	The aircraft's cabin altitude shall be lower than 2000 $[m]$.	✓	6.4.1
REQ-TOP-SAF-03	The aircraft's reliability shall be higher than 98%.	✓	12.5
REQ-TOP-SAF-04	The aircraft shall be able to operate in all weather conditions.	✓	12.4
REQ-TOP-SAF-05	The aircraft shall adhere to relevant certification standards and regulations.	TBD	
REQ-TOP-SAF-06	The aircraft shall safely transport all passengers during all phases of flight and ground operations.	✓	12.5
REQ-TOP-SUS-01	The aircraft shall have a reduction in CO_2 emissions during operation of 75% compared to an ATR 42-600 built in 2035.	✓	15.2.2
REQ-TOP-SUS-02	The aircraft shall have a reduction in NO_x emissions during operation of 90 % compared to an ATR 42-600 built in 2035.	✓	15.2.2

Table 13.1: Requirement Compliance Matrix

ID	Requirement	Compliance	Ref.
REQ-TOP-SUS-03	The aircraft shall emit no CO_2 or NO_x during ground operations.	✓	15.2.2
REQ-TOP-SUS-04	The aircraft shall have a sustainable end-of-life solution.	✓	15.2.3
REQ-TOP-FIN-01	The aircraft's DOC shall be competitive with ground transport.	✓	17.3
REQ-TOP-FIN-02	The aircraft's production cost shall be minimised by choosing materials and manufacturing methods appropriate for the annual production rate supported by the aircraft's potential market size	✓	14.3
REQ-TOP-FIN-03	The aircraft shall have have turn-around time of less than 30 $[min]$ after flying DOC range	✓	16.3

Part III

Entering Into Service

14

Further Project Development

Since this conceptual design project had a duration of only ten weeks, there is still abundant room for further progress in the development of this aircraft. In Figure 14.1, the full program timeline and lifetime of the aircraft are shown. After the conceptual design phase, the aircraft will enter the design and certification phase, which is subdivided into the preliminary and detailed component design phase up until the design review. Concurrently, the supply chain needed for the production and assembly of the aircraft will be set up. The design phase ends with ground and flight testing of the aircraft, after which it will be type certified. Shortly after this, the first aircraft will enter into service in 2035, and operate for an estimated 15 years. Production and assembly will continue during this time depending on the demand for the aircraft. This chapter will describe the future design, test, and certification steps, which lay beyond the scope of this project.

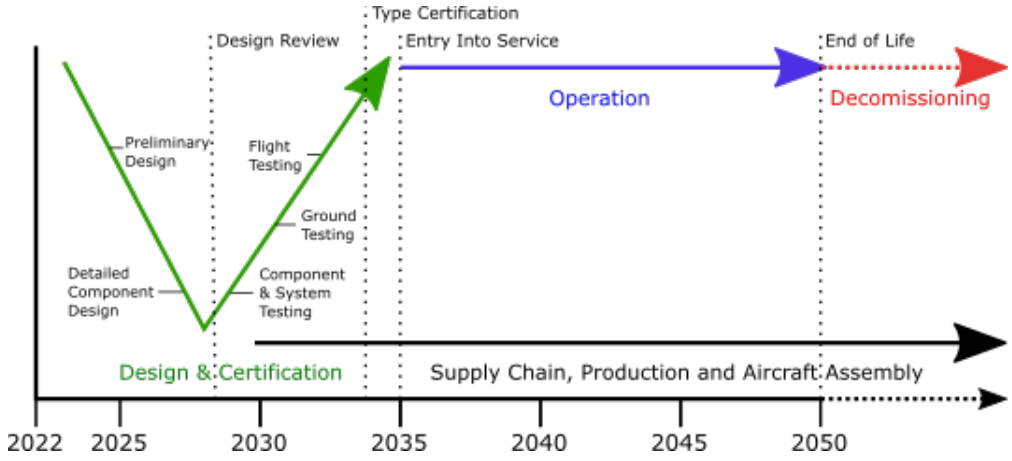

Figure 14.1: The program timeline and aircraft lifetime after the conceptual design phase.

14.1. Post-Project Design Recommendations

During the project, all of the preliminary sizing of the aircraft was performed. Furthermore, a limited conceptual design was performed on specific subsystems of the aircraft due to the constrained time scope of this project. Therefore, quite some aspects of the aircraft have to be worked out in further detail. These include, amongst others:

- Performing a detailed analysis of the structure of the wing box with a finite element method. This gives a proper insight into the loads the wingbox can carry and allows for an accurate evaluation of the wing deflection.
- Performing a detailed sizing and material selection for the truss.
- Performing a detailed design of the fuselage structure.
- Setting up a wiring plan for all the cables and tubes that have to run throughout the aircraft.

- Analysing the controllability of the aircraft in further detail to investigate the possibilities of removing the vertical tail of the design. This would lead to weight saving and allow therefore for a lighter design.
- Writing an advanced control system for the aircraft to assist the pilot in flying the aircraft. The control system should for example automatically shut off the engines in case of an engine failure during cruise to prevent the aircraft from going into a spin. Other safety features should be implemented as well.
- Aerodynamic performance should be evaluated in a CFD model to get a better understanding of the aerodynamic behaviour and more accurate coefficients.
- Validating the simulation software with a scaled wind tunnel test to evaluate the effect of all assumptions.
- Completing the integration of the propulsion system. Preliminary propeller sizing and integration were performed in this report, but should be revisited in later design stages.

A detailed assembly plan should be created to ensure the aircraft's quality. Also, with this, an indication of the production time can be made. Also, all facilities and tools have to be selected or designed to manufacture all the components needed to assemble the aircraft. Both the assembly plan and the manufacturing of components require technical drawings of every element and part. Basic components of the aircraft can be produced by third parties. However, specialised components should be created in-house.

14.2. Test and Certification Process

Before an aircraft is allowed to enter service, it is required to go through an extensive certification process[1]. Failing parts of this certification process may lead to large setbacks in the design process and lead to a delayed entry into service[2]. The certification process should already be started around 2026 due to the fact certifying a completely new aircraft with novel technologies can take up to nine years[3].

In Europe, EASA is responsible for certifying new aircraft. The certification process consists of four steps. The first step is the technical familiarisation and certification basis, in which EASA determines if the project has reached a sufficient degree of maturity. In the second step, the establishment of the certification program, the manufacturer and the EASA define how the compliance with the requirements will be demonstrated. The third step is the compliance demonstration itself and finally, if all requirements are met, an issue of approval is awarded[4]. The production of the aircraft can start after the certification process is finished.

14.3. Production Plan

Where the previous sections touched upon further steps in the design, test, and evaluation process, this section will introduce a first insight into the required development to produce the said aircraft.

Figure 14.2 shows a schematic overview of the global production and assembly order of the aircraft. The grey bar resembles the assembly line, which is a typical method used in aircraft manufacturing. It consists of a physical path in the factory that an aircraft in production follows. This allows the manufacturing groups to stay stationary and perform the same work package over and over again, which increases efficiency and exploits the learning curve that naturally exists for people. The order of assembly is important; the fuselage is the heart of the aircraft, and is assembled first. This serves as a platform for other systems to be mounted to. Externally sourced parts or systems are assembled last, since they require large expenses, which are preferably made later than sooner, following from fundamental economics. Other systems can be sub-assembled in parallel, allowing for decreased manufacturing time and mitigation of risk.

[1] https://www.easa.europa.eu/domains/aircraft-products/aircraft-certification, last consulted June 8, 2022

[2] https://www.seattletimes.com/business/boeing-aerospace/citing-a-serious-flight-test-incident-and-lack-of-design-maturity-faa-slows-boeing-777x-certification/, last consulted June 8, 2022

[3] https://www.faa.gov/aircraft/air_cert/airworthiness_certification/, last consulted June 8th, 2022

[4] https://www.easa.europa.eu/domains/aircraft-products/aircraft-certification, last consulted June 8, 2022

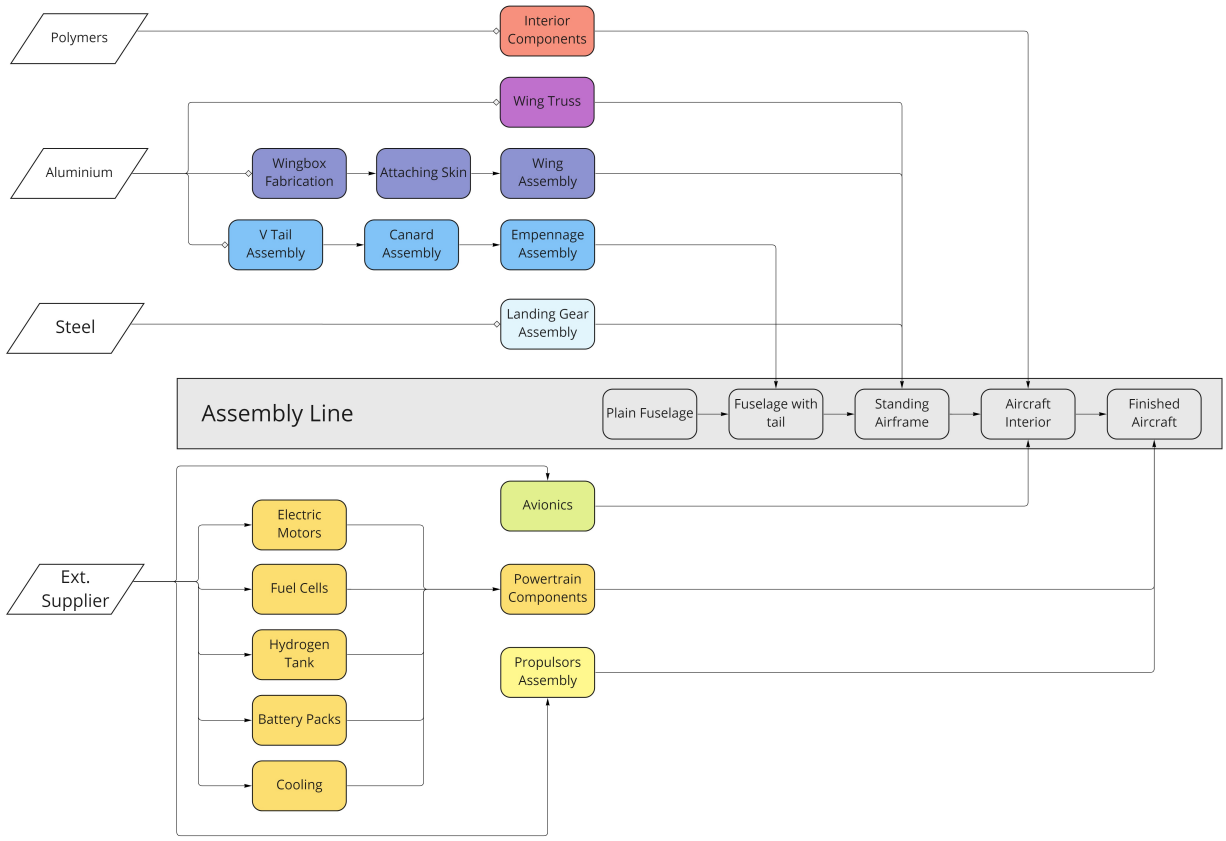

Figure 14.2: Production plan for the aircraft

15

Sustainable Development Strategy

In recent years climate change has become an increasingly important subject. The aviation industry is considered a large contributor to this problem. Even though newly developed aircraft are trying to reduce their emissions, the growth of the aviation market is too large to compensate for this. The Hammerhead will introduce a significant reduction in emissions by having a different energy storage system compared to conventional aircraft, such as the ATR 42-600. In this chapter, this reduction will be quantified. Firstly, the goals related to sustainability are displayed inSection 15.1. Then, a life cycle analysis is performed in Section 15.2 to investigate if these goals are met. Other considerations regarding improvement for sustainability are discussed in Section 15.3.

15.1. Sustainability Goals

Based on the stakeholder requirements certain objectives regarding sustainability were set up. The objectives are summarized here below.

- Limit the production of CO_2 to 2.375 $[kg]$ per passenger per 100 $[km]$ during operation.
- Limit the production of NO_x to 0.001 $[kg]$ per passenger per 100 $[km]$ during operation.
- Ensure a sustainable EOL solution for the aircraft.
- Do not generate CO_2 and NO_x emissions during ground operations.
- Limit additional impact of the environment (use of toxic materials, take-off noise and production methods).
- Attain affordable flights for the general public.

15.2. Life Cycle Analysis

This section quantitatively evaluates the life cycle for the three different phases of the product. These are the production in Subsection 15.2.1, operation phase in Subsection 15.2.2 and the end-of-life in Subsection 15.2.3. In order to visualise what the value of emissions means relative to other aircraft, a comparison is done with the ATR 42-600. The emissions are all translated to CO_2e to make a equitable comparison. Finally, the life cycle analysis is concluded in Subsection 15.2.4.

15.2.1. Production Phase

The production phase evaluates the mass and emissions of certain materials. The materials evaluated are aluminium, composite and lithium-ion batteries. For all of these materials the mass, energy required and emissions are converted into CO_2e and shown in Table 15.1.

Batteries

For lithium-ion batteries, the carbon footprint for the production process would be between 56 and 494 $[kg]$ per $[kWh]$ of battery capacity [73]. A value of 200 $[kg]$ CO_2e is assumed while keeping in mind that the industry of battery production will improve towards 2035 [74]. Considering that the battery capacity is equal to 1335 $[kWh]$ and by assuming a linear behaviour for carbon footprint and battery capacity, the CO_2e can be estimated for an operational lifetime.

Nonetheless, the degradation of the batteries has to be taken into account. Considering an operational lifetime of 15 years 1400 flights per year, and also considering a charge-discharge cycle of the battery between 20% and 90%, the number of cycles before replacement of the battery is assumed to be 2000 cycles. For the current battery cell, the Panasonic 4680 Li-ion, the number of cycles is between 1000 and 2000 cycles depending on the charge discharging nature[1]. Even though the current charge-discharge cycle is not optimal for the life cycle, an enhancement in the life cycle is assumed at the entry of service in 2035 [75]. This would eventually mean that for the operational lifetime of the aircraft, the battery is replaced 11 times.

Composites
For carbon fibre reinforced plastics the amount of energy needed for production would be 380 MJ per kilogram for the whole design process [76]. Knowing that the ATR 42-600 uses 19% composites for its structure and has an OEW of $11700\ [kg]$, the mass of the composites can be determined[2]. For the Hammerhead, it is explained in Section 11.1 that the wingbox is made out of composite. Also, it is assumed that the fuselage, wing, vertical tail and canard are 70% made out of composite leading to an estimation of the mass of 5248 $[kg]$.

Aluminium
The carbon footprint value of the production of aluminium is equal to $23.96\ [t]$ CO_2e per ton of aluminium [77]. For the ATR 42-600 it is assumed that the amount of aluminium that is used would be 81% of the OEW as the 19% is filled with composite materials [2][3]. For the Hammerhead, the remaining 30% from the composite mass estimation is approximated to be the amount of aluminium, which would be $2249\ [kg]$.

Table 15.1: Production phase analysis

Aircraft	Substance	Mass $[t]$	Energy required $[GJ]$	CO_2e $[t]$
Hammerhead	Aluminium	2.25	137.7 [78]	53.91[77]
	Composite	5.25	1840 [76]	101.3 [79]
	Lithium-ion batteries	49.7	2937 [80]	129[81]
ATR 42-600	Aluminium	9.48	580.2 [78]	227.1 [77]
	Composite	2.22	843.6 [76]	42.82 [79]

15.2.2. Operation Phase
The operation phase examines all the (in)direct emissions during operation. This is evaluated for the whole operational lifetime, including the number of missions per year and the design range of the Hammerhead. The ATR 42-600 will be evaluated with the same parameters to make an unbiased comparison. The amount of fuel for the ATR 42-600 is estimated by an interpolation of the block fuel for 200 and $300\ [Nm]$[4]. Further, the emissions for the production of kerosene were also included[5].

For the Hammerhead in operation, one type of greenhouse gas should be considered, as direct emissions of CO_2 and NO_x are eliminated, which is water vapour. Contrails are not likely to form at the cruise altitude at which the Hammerhead operates. Therefore, contrails are not considered [82]. In order to determine the amount of water vapour that is translated to CO_2e some assumptions are made. Firstly, 30% of the gaseous

[1] https://somanytech.com/what-is-tesla-4680-battery-specs-detail-specification
[2] https://www.aerospace-technology.com/projects/atr_42/, last consulted June 14, 2022
[3] https://www.atr-aircraft.com/wp-content/uploads/2020/07/Factsheets_-_ATR_42-600.pdf, last consulted 14 June, 2022
[4] https://www.atr-aircraft.com/wp-content/uploads/2020/07/Factsheets_-_ATR_42-600.pdf, last consulted June 9, 2022
[5] https://www.offsetguide.org/understanding-carbon-offsets/air-travel-climate/climate-impacts-from-aviation/co2-emissions/, last consulted June 19, 2022

water for combustion turns into water vapour for kerosene-driven aircraft [83], [84]. Kerosene consists of different types of hydrocarbons. For example, JP-8 contains mostly paraffins in the range of octane to hexadecane with at maximum decane and dodecane [85]. To simplify the approximation of water vapour, it is assumed that kerosene solely contains dodecane. The chemical reaction formula of dodecane is then as shown below. Based on this the molar mass of H_2O is 13 times higher than for dodecane. In order to determine the mass of kerosene that would be needed for the same mission, the mission energy was translated to mass by using the calorific value of kerosene.

$$2C_{12}H_{26} + 37O_2 \rightarrow 24CO_2 + 26H_2O \tag{15.1}$$

Then, for the hydrogen fuel cell system the amount of water vapour emissions is two and a half times higher compared to kerosene-powered aircraft. The climate impact of water vapour is ten times lower than for CO_2 [82]. Therefore, the assumption was made that the climate impact is equivalent to CO_2e.

Lastly, the CO_2e was determined for the electric energy. The direct emission of CO_2 electric energy is zero. However, it is important how this electric energy has been generated. This would impose an estimation of the retrieval of energy at entry at service in 2035. During the period from 2030 to 2040, it is expected that the share of renewable energy in power generation raises from 57% to 75% [86]. Therefore, a value of 66% share is estimated for 2035. Of course, there would a possibility that all electricity is generated by renewable energy sources for the airports the aircraft would operate. However, it is assumed that the remaining 34% would cause indirect emissions. Further, the greenhouse gas emission intensity in 2030 would be 115 $[g\text{CO}_2\text{e}/kWh]$[6].

Also, it should be considered what the indirect emissions would be for the production of hydrogen. Here, the same value that 34% of the energy sources in 2035 would cause greenhouse gas emissions was taken. Further, the energy consumption of hydrogen is currently between 53 to 70 $[kWh]$ per kilogram of hydrogen and it is estimated that the energy consumption will decrease with 30% by 2030[7] [87]. Based on this a specific energy consumption for hydrogen is assumed at 40 $[kWh]$ per kilogram. Finally, using these values and the greenhouse gas emission intensity in 2030 the emissions caused by the production of hydrogen can be estimated.

Table 15.2: Operational phase analysis

Aircraft	**Substance**	**Mass** $[t]$	**Energy** $[TJ]$	**CO_2e** $[t]$
Hammerhead	LH_2	4141	1167[7,8] [87]	Direct: 464.0 [82]–[84] [9]
				Indirect: 19513 [87][7]
	Electric energy	-	70.65	Indirect: 767.3 [86][6]
ATR 42-600	Kerosene	21659[4]	955.18[9]	Direct: 70015[3]
				Indirect: 10830[10]

[6]https://www.eea.europa.eu/data-and-maps/daviz/co2-emission-intensity-9/#tab-googlechartid_googlechartid_googlechartid_googlechartid_chart_1111 last consulted June 10, 2022

[7]https://www.iea.org/reports/the-future-of-hydrogen, last consulted June 19, 2022

[8]https://chemeng.queensu.ca/courses/CHEE332/files/ethanol_heating-values.pdf, last consulted June 10, 2022

[9]https://www.seai.ie/data-and-insights/seai-statistics/conversion-factors/, last consulted June 10, 2022

[10]https://www.offsetguide.org/understanding-carbon-offsets/air-travel-climate/climate-impacts-from-aviation/co2-emissions/, last consulted June 19, 2022

15.2.3. End-of-Life

In this subsection, a general strategy for treating the aircraft's parts reaching EOL is explained and shown in Figure 15.1. When the entire aircraft will be decommissioned, it will be disassembled, leaving a lot of components to be managed. The goal is to have a standard approach to refer to such that no part is forgotten which would likely cause them to be disposed of in an unsustainable way. For batteries, a more specified EOL solution is discussed and for certain parts including batteries, the sustainability characteristics for EOL will be shown as well in Table 15.3.

General EOL Solution

The preferred EOL solution is re-purposing. In this case, small modifications are applied (if necessary) to convert the object to a new field of application. If this option is unavailable, the components can be recycled by shredding or melting and used for other applications. In case some materials can not separated but possess high calorific values and low pollution potential, they can be used as energy sources for industries as an alternative to fossil fuels[11]. Finally, if none of the aforementioned options is available, the aircraft's waste is used as a land-fill. Such a process may be done in a contained way in case the waste is environmentally hazardous, but the cost and relevance of this option still have to be analysed in more detail.

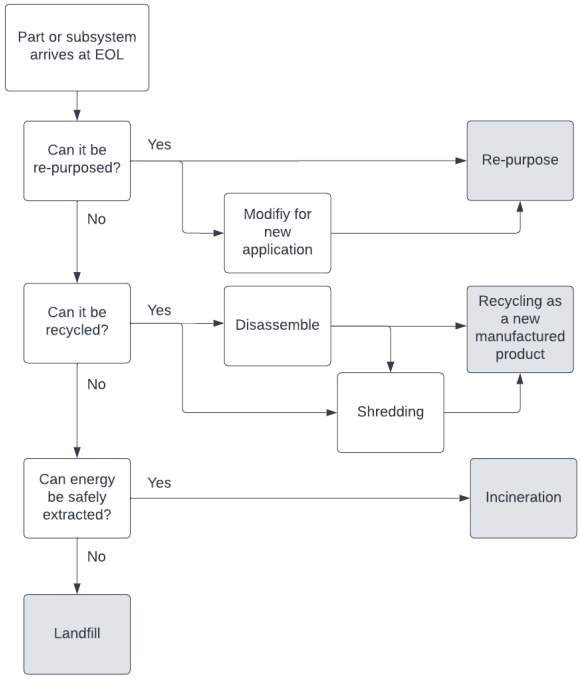

Figure 15.1: EOL strategy for the aircraft's parts and subsystems

EOL Solution Batteries

An example of such an EOL process concerns batteries. These were used as part of the energy storage of the Hammerhead. For lithium-ion batteries at EOL, these would be re-purposed for a stationary application which requires lower specific energy, such as intermittent storage for solar and wind energies [88]. This requires the batteries to be arranged with a different cooling system, but it limits their EOL environmental impact. If the batteries can not be re-purposed or if their performance decays to the point of rendering them useless, they can be partially recycled. Through a pyro-hydrometallurgical process, lithium can be

[11] https://www.bafu.admin.ch/bafu/en/home/topics/waste/info-specialists/waste-disposal-methods.html, last consulted May 12, 2022

separated. Unfortunately, this is not profitable so additional expenses need to be made to ensure proper material recycling. Additionally, copper, cobalt and nickel can be retrieved from the slag but graphite and electrolytes are lost during the process [88]. Thanks to this, up to 80% of lithium-ion batteries' metallic and plastic materials can be recycled [89].

Sustainability Characteristics for EOL

For the end-of-life phase, the energy needed for dismantling and recycling is quantitatively evaluated. Further, the amount of materials that can be recycled is determined. These are shown in Table 15.3.

At the end of life of the battery, the battery has a SOC of 85% of its beginning of life battery capacity, which would be $1135\ [kWh]$. This would be sufficient for other purposes [88] and it is assumed that would be possible for 90% of all battery mass. For the batteries that can not be used for re-purposing, the assumption is made that 80% could be recycled as described in the previous section [89]. Also, the energy required and CO_2e for the pyro-hydrometallurgical process can be estimated as described by Boyden [90]. However, this environmental impact is relatively low in comparison to the energy that is retrieved by re-purposing and recycling itself.

For the carbon fibre reinforced polymer, a decomposition ratio of 97% was found for using peracetic acid as described in Section 11.2 [66]. For the recycling of CFRP with a chemical method, the amount of energy required for each kilogram of CFRP would be 38.4 $[MJ]$ [91].

Aluminium has a recovery rate between 76% and 93% [92]. An optimistic value of 93% was assumed as Gökelma discusses that these values are at the current stage and the production of the aircraft would happen in the near future as described in Chapter 14.

Table 15.3: EOL phase analysis

Aircraft	**Substance**	**Mass recovered** $[t]$	**Energy recovered** $[GJ]$	**CO_2e** $[t]$
Hammerhead	Aluminium	2.09 [92]	128.1 [92]	-50.14 [92]
	Composite	5.09[66]	1589 [66], [91]	-92.01 [91][6]
	Lithium-ion batteries	48.71 [88]	2873 [90]	-122.0 [90]
ATR 42-600	Aluminum	8.82 [92]	539 [92]	-211.6 [92]
	Composite	2.15[66]	735.6 [66], [91]	-38.89[91][6]

15.2.4. Life Cycle Analysis Conclusion

Now every part of the life cycle has been reviewed, the sustainability objectives from Section 15.1 can be examined for their compliance. The first two objectives would be to limit the production of CO_2 and NO_x, as the powertrain system does not emit these greenhouse gases as explained in Section 5.2, these would be met. However, the influence of other emissions translated into CO_2e would have to be evaluated as well. When only taking into account the direct emission during operation as explained in Subsection 15.2.2, it would lead to a value of $0.110\ [kg]$ of CO_2e per passenger per 100 $[km]$ during operation and thus meeting the requirement by much. When considering the indirect emissions, both the emissions of the Hammerhead and ATR 42-600 has to be taking into account to make a equitable comparison, which would change the value of the CO_2 limit in Section 15.1 to 4.39 $[kg]$ per passenger per 100 $[km]$. The value of the Hammerhead would be 4.94 $[kg]$ and therefore would not meet the objective. This can be changed however if the airlines would ensure that more green hydrogen would be produced.

The next goal was to ensure a sustainable EOL solution for the aircraft. A general and a specific solution for batteries was given in Subsection 15.2.3. Further, the life cycle characteristics of the aluminium, batteries

and composites at EOL were given. As this objective can not quantitatively be met further investigation can be performed when a more detailed design is executed.

For ground operations, no CO_2 and NO_x are emitted as explained in Chapter 16. The review on attaining affordable flights is discussed in Chapter 17 and other additional impact on the environment such as production methods will be explained in the following section. Other forms of impact such as noise pollution could be performed in future research.

15.3. Other considerations

Next to the life cycle of the Hammerhead, other considerations to aim for sustainability, which were not qualitatively measured, are addressed here. Firstly, the considerations regarding production are shown in Subsection 15.3.1.

15.3.1. Production

Lithium is an essential component for the batteries used in the selected design concept. Currently, the conventional extraction method which relies on brine evaporation has a high environmental impact. For this project, the use of batteries whose lithium is extracted in a less polluting has been considered. This new extraction method based on ion exchange allows achieving recovery rates twice as high as with the conventional method. This goes along with accelerated process duration and smaller space required[12], which considerably reduces environmental impact.

Batteries are not the only energy source in the selected regional aircraft concept: hydrogen fuel cells are used as the main source of energy. Many types of fuel cells exist, but the most common and efficient types are proton-exchange membrane fuel cells (PEM). Recent developments in air-cooled high-temperature PEM fuel cell technology promise increases in volumetric and gravimetric energy densities, longer lifetimes, lower balance of plant mass fractions and less use of rare metals[13]. This is due to the replacement of the heavy humidifier and liquid cooling module with a lighter compressed air cooling module, potentially making this technology an even better fit for aviation compared to conventional low-temperature PEM fuel cells.

Regarding the origin of the aircraft's energy, hydrogen should be produced by electrolysis because this not only allows to obtain a high level of purity which is compatible with both low-temperature and high-temperature PEM cells but may also lead to zero greenhouse gas emissions if green electricity is used (i.e: coming from solar, wind, hydro or geothermal power sources). Green electricity may also be used for charging the aircraft's batteries to further reduce indirect operational environmental impact, although this option might not be available for all airports.

15.3.2. Materials

To mitigate the high environmental effect of production, it would be an option to consider bio-composites that have a much more sustainable production and end-of-life solution. Overall there are many advantages to choosing natural fibres. The density is lower, the composites are fully biodegradable, cost is much lower, the manufacturing process does not impose any health issues on workers and the material is non-corrosive. However, its drawbacks would be that the compatibility is not good. The thermal stability is low. Natural fibres are able to withstand temperatures only up until 200 $[°C]$. On a macro basis, natural fibres structurally change on a chemical level when subjected to heat [64].

Due to the strict temperature requirements for use of natural fibres, its application is limited. However, there would be solutions where natural fibres would be applicable. As natural fibres are less fire-resistant compared to synthetic fibres, fire retardant coatings can be applied and then could be used in the interior of the cabin [64].

[12] https://lilacsolutions.com/technology/, last consulted May 13, 2022

[13] https://docsend.com/view/t9aw2mk, last consulted May 16th, 2022.

16

Ground Operations

Before the mission is initiated the aircraft needs to be prepared for its next mission. This requires a procedure on ground to meet the requirement of the turnaround time. This chapter explores these operations. In Section 16.1 the infrastructure on ground required for charging and refuelling of hydrogen is explained. Section 16.2 describes the refuelling and charging procedure. Section 16.3 concludes this chapter by discussing the result of the turnaround time based on the operations.

16.1. Airport Infrastructure

In order to facilitate the aircraft at the airport, the infrastructure needs to be discussed for hydrogen refuelling and battery charging as this is different opposed to kerosene refuelling. The infrastructure of hydrogen and battery charging will be explained in Subsection 16.1.1 and Subsection 16.1.2 respectively.

16.1.1. Hydrogen Infrastructure

Firstly, hydrogen would have to be delivered from the production plant to the airport. There are several methods to perform this. These would be via road using tube trailers and cryogenic trucks or via a pipeline [93]. Currently, the most feasible option would be to deliver by a cryogenic truck. However, if the demand of hydrogen increases significantly in the upcoming years this might change.

When liquid hydrogen is delivered at the airport it needs to be stored before refuelling the aircraft. The most critical part of the storage tank at the airport is to accommodate the thermodynamic and pressure requirements for storing liquid hydrogen. This storage tank would have to be decided.

The options for the refuelling system for liquid hydrogen would be either with a bowser or hydrant system. A bowser system would be initially the most logical option because of its low capital cost. A hydrant system may be required when the bowser operation would cause congestion at the refuelling point and internal road network [94]. This eventually would depend on each individual airport. The forecast of FlyZero for this is shown in Figure 16.1. For relatively small airports the choice would be then to choose a bowser system.

Airport Size	2035	2040	2045	2050
Large	Bowser	Consider Hydrant	Hydrant	Hydrant
Medium	Bowser	Bowser	Consider Hydrant	Hydrant
Small	Bowser	Bowser	Bowser	Bowser

Figure 16.1: Hydrogen refuelling system forecast from FlyZero [94]

16.1.2. Recharge Infrastructure

Further, an infrastructure for the batteries would be required. The total battery capacity is equal to a value of 1335 $[kWh]$, which needs to be recharged to a sufficient SOC to be used for the following flight. This needs to be performed rapidly to meet the requirement of having a turnaround time less than thirty minutes. At the current stage, the charging of smaller vehicles such as cars is already implemented on a large scale.

In order to satisfy the industry of aviation high-power chargers would be required. One of these chargers could be the Megawatt Charging System (MCS) from CharIN[1].

The MCS delivers a maximum of $1250\ [V]$ and $3000\ [A]$, which are delivered by a direct current (DC) charging station. Having a DC charging station would require further equipment on ground at the airport, such as transformators [95]. Further, the MCS is combined with the Combined Charging System (CCS) from CharIN as well, which is a standard for charging battery-powered vehicles[2]. These are normally used for commercial vehicles such as cars and trucks. However, for larger battery packs which can withstand a charge rate above $1\ [MW]$ CCS would also be possible[1]. These charging stations are stationary, which would impose that the aircraft would have to be parked at the right position at the gate and the charging station placed at the right longitudinal position where the batteries are placed.

Lastly, as described in Subsection 8.3.1 the fuel cells are turned off at the gate so no cooling of the batteries is present. Therefore, an external battery cooling line is attached to the system as explained in Subsection 8.3.1. Further, during charging the charge rate is much higher than during discharge. This would impose that the temperature of the battery becomes higher. This temperature needs to be regulated to temperatures between 15 and $35\ ^{\circ}C$ [96].

Safety during battery charging

Further to ensure safety during charging some considerations would have to be taken as the high charge rate results in some implications. These would be that the battery would overheat for example. Not only would this be the case on the battery level with all cells combined, but also this would have to be prevented on cell level as this might result in thermal runaway [97].

Thermal runaway is the situation where a cell or a stack of cells would have an undesired elevation of temperature due to failure and this would propagate to other cells potentially causing an increase in temperature and pressure with the result of a fire or even an explosion[3] Thermal runaway is divided into three stages as shown in Figure 16.2 [97].

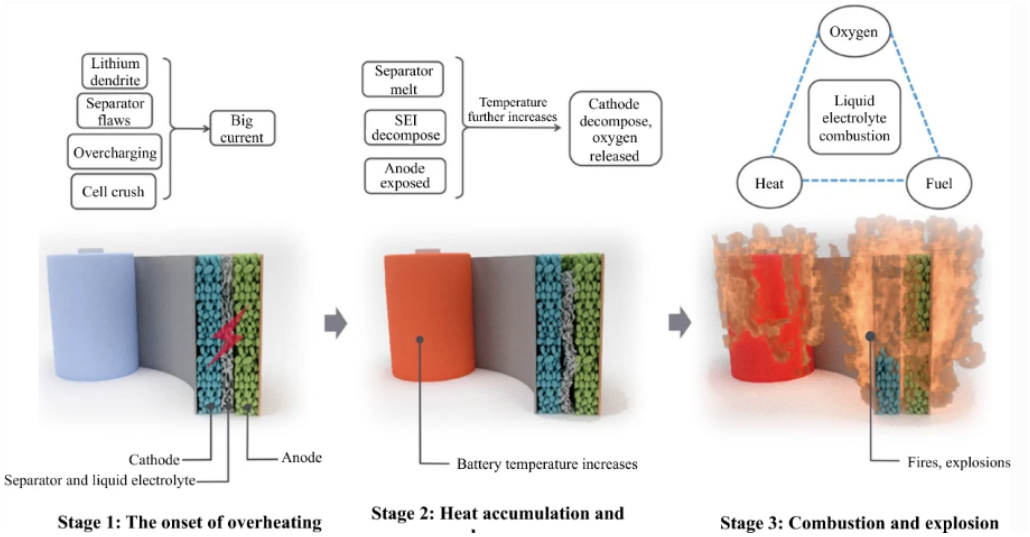

Figure 16.2: Thermal runaway stages [97]

For each stage as shown in Figure 16.2 a mitigation strategy can be set up. Stage 1 is a result of defects in manufacturing and internal shorts. It is of importance that overheating is then avoided as when stage 1 happens safety can not be guaranteed. To avoid stage 1 from taking place a high quality control of the

[1]https://ww w.charin.global/technology/mcs/, last consulted June 3, 2022
[2]https://www.charin.global/technology/dashboard/, last consulted June 3, 2022
[3]https://safetyfirst.airbus.com/lithium-batteries-safe-to-fly/, last consulted June 20, 2022

batteries would be required to circumvent defects. Also, Further, for stage 2 a strategy would be to make of use of cell-venting mechanisms, which would release the gaseous products. Lastly, for stage 3 the liquid electrolyte would then act as the fuel to cause combustion. The strategy for stage 3 would then be to prevent the propagation of fire. This can be mitigated by introducing cell spacing and heat dissipation by having a fire wall between battery cells [97].

16.2. Recharging and Refuelling

This section describes both the procedure of recharging batteries and refuelling of hydrogen in the tank in Subsection 16.2.1 and Subsection 16.2.2 respectively. For refuelling the explosion regulations regarding hydrogen are first reviewed. Then, the whole procedure is explained and finally the managing of leaks and spills is evaluated.

16.2.1. Recharging

As the infrastructure for recharging is known, this procedure can be explained as well. Considering that the MCS has a voltage level of $1250\ [V]$ and that of the powertrain as explained in Section 8.1 can reach up until $1200\ [V]$, the voltage of the MCS would be lowered to the same value. Having a amperage of $3000\ [A]$ the power delivered by the charger would be $3.6\ [MW]$. As the batteries of the powertrain are divided in both sides of the wing, two chargers are used for practicality.

Then, having a total battery capacity of 1335 $[kWh]$ it is assumed that the SOC never exceeds 90% as after the charge rate drops rapidly and its DOD never exceeds a value of 20% [98]. So, a value of capacity that needs to be charged is estimated to be 934.5 $[kWh]$ Having a charging power of $3.6\ [MW]$ and two chargers the charging time would then be $11.5\ [min]$.

16.2.2. Refuelling

First the explosion protection regulations need to be reviewed. These consist of three measures: primary explosion protection, which involves the avoidance of an explosive atmosphere, secondary protection, which describes the avoidance of an ignition source and tertiary protection tries to limit the effects of an explosion. Ensuring that no other substances would be able to penetrate the tank is an example of avoiding an explosive atmosphere. The minimum requirements for explosion protection regulations in the European Union are documented in the ATEX directives [2].

Refuel Procedure

Then, the procedure of refuelling is done in the following manner. Firstly, the docking maneuver is performed. After this the ground vehicle will be connected with the aircraft. Before this happened the tank and fuel system need to be purged. Then, the chill-down is done. Further, to avoid vaporization losses a recovery line is introduced. Finally, the actual refueling can be executed [2].

The docking maneuver is started by positioning the ground vehicle that performs the refuelling. For LH2 the hose and pipe weigh considerably more and can not be operated by one person as would be possible for Jet A-1. Further, the handling of the hoses has certain implications on safety which would require two qualified persons. This can be much more simplified by introducing an (semi-)automated docking system. Currently, a comparable system would be the de-icing vehicle. The (semi-)automated system would be expected to take the same amount of time as for Jet A-1, being approximately equal to $2.5\ [min]$ [2].

Next step would be potentially purging and connecting. For handling liquid hydrogen two options would be available: one option would be Johnston coupling, which is the only vacuum-insulated method, the other would be a clean break disconnect. The clean break disconnect would release a small amount of spillage and the purging procedure wouldn't be required. However, its technical readiness level currently is much lower. For the Johnston method purging is required as an explosive atmosphere is not allowed as described in the explosion protection regulations. Therefore, other gases need to be excluded from the tank and fuel system. One of these requirements would be that the amount of oxygen accessing the system has to be lower than $1\ [ppm]$ and the maximum that can be spilled is $50\ [mL]$. For Johnston coupling vacuum purging is done. This is a process that aims to eliminate all foreign gases from the hose and disconnect which is

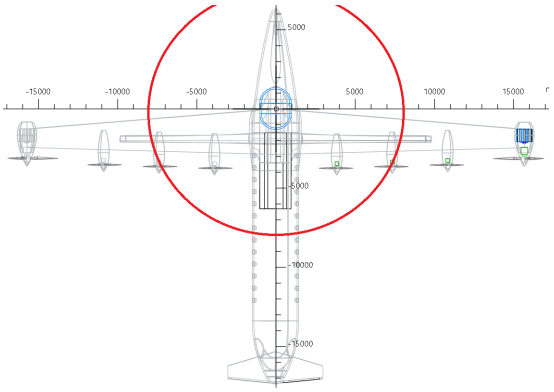

Figure 16.3: Safety zone during fueling

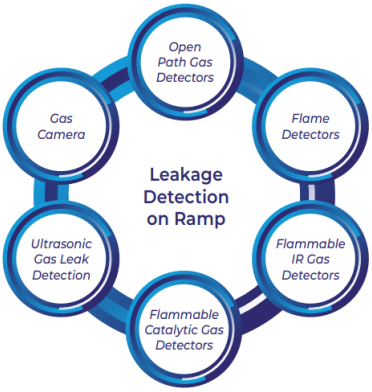

Figure 16.4: Leak detection technologies [94]

performed by alternating in vacuuming and pressurization with an inert gas, which takes $1.5\ [min]$ to perform [2].

The following step would be the chill-down. At ambient pressure, liquid hydrogen is at temperatures below $20.3\ [K]$. This has the consequence that the temperature difference between the tank wall and fluid has a significant effect on the heat transfer. These temperature differences can cause two-phase phenomena, which should be avoided as this negatively influences the mass flow. The purpose of the chill-down is to ensure a vapor-free flow . This step would only take $1\ [min]$ [2].

During refuelling vaporisation losses should be considered. The vaporised hydrogen has to be withdrawn from the tank during refueling as otherwise the pressure within the tank would increase. In order to do this a recovery line is used [2].

After these measures the refuelling itself can be performed. Comparing the refuelling of kerosene to hydrogen, a larger diameter hose for fuelling would be required as density is lower for hydrogen than kerosene. A higher flow rate could be introduced with as a consequence that the handling of the hose will be less flexible and more heavy. This would require a higher level of automation and a robotic arm as assistance. For $1300\ [kg]$ of LH2 in regional aircraft concept the refuelling time for single hose and a flow speed of $2.5\ [m/s]$ for a 4 and $6\ [inch]$ line would be 19 and $9\ [min]$ respectively. Considering that the fuel mass of the aircraft is $301\ [kg]$, the refuelling time would be then approximately $5\ [min]$ for a $4\ [inch]$ hose. However, a problem would be that during refuelling a safety zone is required, imposing that other activities for the turnaround may not be possible. The safety zone for refuelling would require a radius of 8 $[m]$ as shown in Figure 16.3, but for the connecting/disconnecting this value would be $20\ [m]$ which would be even outside of the region of the aircraft. If the turnaround time would become too lengthy other turnaround activities may be automated to run more activities in parallel [94].

After the refueling is performed, the liquid hydrogen that is still in the hose is kept there to limit the loss of liquid hydrogen and evade to have to chill-down the hose again for the following refueling process [2].

Managing Leaks and Spills

When a spill or leak may occur at any stage the procedure would be to first isolate, then allow to evaporate or divert, prevent contact with ignition source and finally use diversions. First would be to consider possible leak points from pipework and the potential impact on other infrastructure. Leak detection instrumentation, sensors and gauges will be needed throughout the transportation, storage and refuelling process to ensure leaks are detected as early as possible to minimise the hazard. The most likely place for a leak to occur is from joints, glands and couplings [94].

There are several types of gas detection technologies that can be used for the detection of hydrogen leaks. A combination of these technologies would detect these leaks earlier resulting in a lower impact. These are shown in Figure 16.4. An example would the ultrasonic gas leak detection technology, which is able to

sensor ultrasound being emitted from gas leaks at high pressure. Alternatively, a leak detection tape can be used which is tape that changes colour when a leak occurs [94].

16.3. Turnaround Time

This section evaluates the time required for all ground operations leading to a turnaround time. The requirement on turnaround time was a maximum of 30 $[min]$, measured from when the aircraft is parked, until it will start its pushback operation. Other operations that are also part of the ground operations that have not yet been discussed are the (dis-)embarking of passengers and crew, cargo (un)loading, pre-flight maintenance check, and cleaning and resupplying of the aircraft cabin.

In Figure 16.5 the work flow diagram for the ground operations is shown. The diagram is divided into five fields of ground operations, which are from top to bottom; cargo, in-fuselage operations, refuelling, recharging, and maintenance check. In general these are performed in parallel, however for one of the activities this is not a possibility. This holds for the (dis-)connecting of the refuelling hose as this requires a large safety zone as described in Subsection 16.2.2. For this activity it is required that some activities are brought to a halt and all other personnel have taken distance to safely (dis)connect the hose. This also implies that no crew, passengers, and cleaning service are in the aircraft before the whole fueling procedure is initiated. In Figure 16.5 for these activities a margin for communication between personnel and to make sure personnel have enough time to leave the area. Further, the cargo would have to be loaded from front to back in the cargo hold as described in Section 6.4. This would have to do that the refuelling safety zone partially reaches the cargo hold area for approximately 1.5 $[m]$ of the 7 $[m]$ length of the cargo hold.

Further, the refuelling itself also has the implication that a safety zone is required. This one is smaller in comparison to the (dis-)connecting safety zone. However, the refuelling is initiated after the aircraft is cleaned and resupplied. The cargo loading can be continued as this is done outside the safety zone. Considering the waiting times before (dis-)connecting and refuelling can be done, the turnaround time has come down to 29.5 $[min]$ and therefore meeting the requirement based on Figure 16.5. If the safety zone would decrease of the refuelling by enhancing the safety regulations in the future the turnaround time can be decreased up to 27 $[min]$ as the cabin can be cleaned and resupplied in parallel.

16.4. Taxiing

One of the top-level requirements was that during ground operations no CO_2 and NO_x was emitted. There many electric taxiing methods. It should be noted upfront that the name of ET systems does not imply that it is driven fully electric. ET methods do have advantages such as reducing greenhouse gas emissions, acoustic noise, fuel consumption and operating costs. ET can further be divided into external (ETS) and internal taxiing systems (ITS). ETS has the advantage of not being invasive to the aircraft design and not add extra weight. The disadvantages are the airport compatibility issues. Furthermore, it might result in longer taxiing times. Most current ITS, however, don't comply with not emitting greenhouse gasses such as the TaxiBot. However, this is mostly the case for conventional aircraft that use kerosene or SAF. If the aircraft has a sustainable propulsion system, ITS could be a viable option. ETS are not an option as these are not able to achieve sufficient speeds (2-6 knots). Therefore, this option is only viable for the pushback operation [4]. Even though Wheeltug would be able to reduce time by performing the pushback operation itself instead of an external tug vehicle, its taxiing speed is currently too low [4]. However, this may improve over the years to conventional taxiing speeds between 16 and 19 $[kts]$ [3]. Therefore, a nose wheel driven taxi system is chosen for the taxi operation.

[4] https://www.ainonline.com/aviation-news/air-transport/2014-02-11/WheelTug-safran-honeywell-and-iai-offer-three-rival-solutions-airline-engine-taxiing

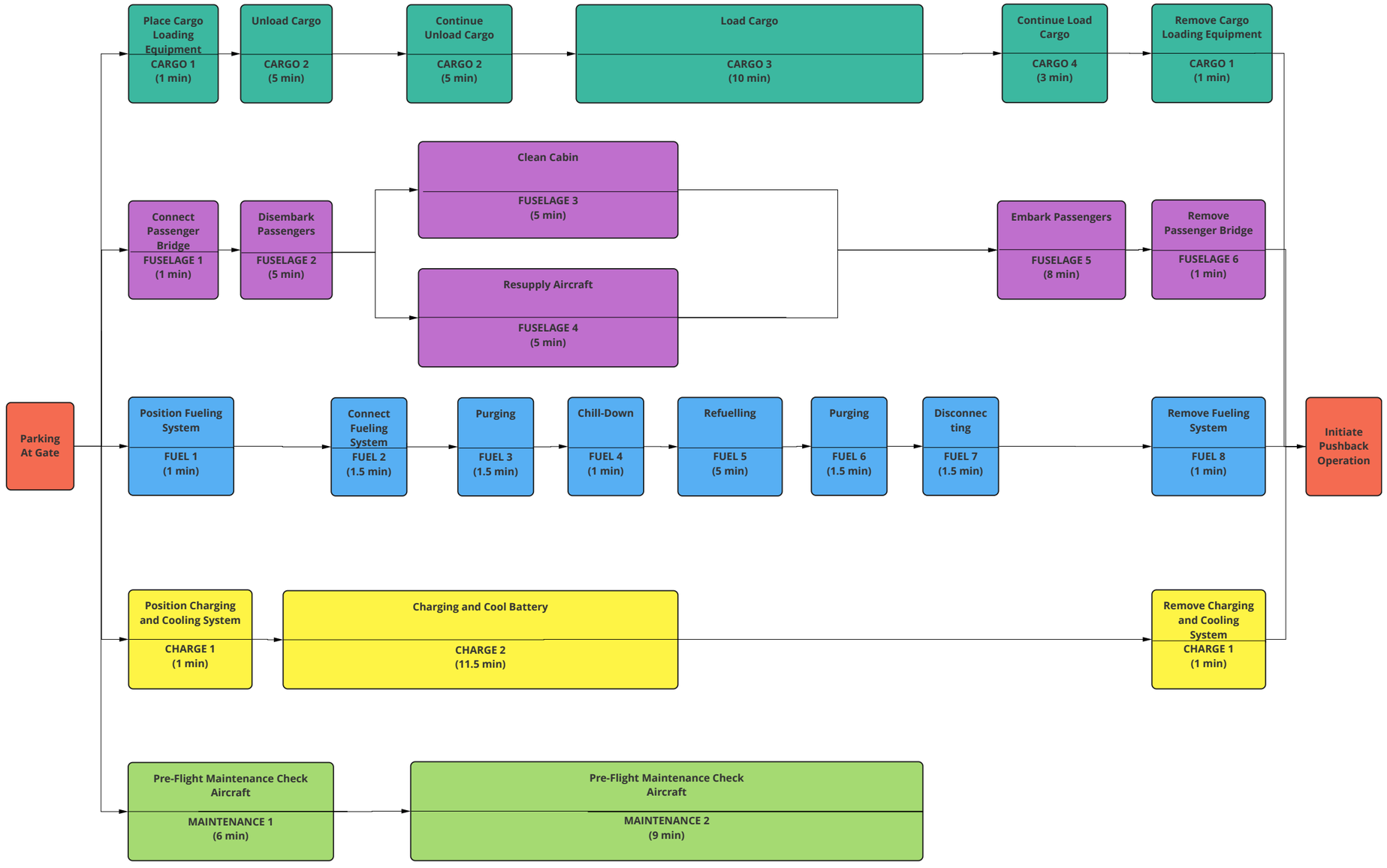

Figure 16.5: Flowchart showing ground operations performed between arrival at the gate and pushback.

17

Financial Overview

This final chapter presents a financial analysis that has been performed to confirm the economic relevance of this project. The cost of the aircraft program will be calculated using Roskam's method, as published in his book "Aircraft Design - Part VIII" [99]. This is presented in Section 17.1. Using the program cost, a selling price and quantities can be assumed to arrive at a break-even point (BEP) for the manufacturer, which is shown in Section 17.2. From the perspective of the buyer, an airline, a DOC and an ROI are calculated and presented in Section 17.3 and Section 17.4. Also, the ticket price per kilometre is given in Section 17.5, and compared to other modes of transport. Finally, a conclusion of this financial analysis is given in Section 17.6.

17.1. Program Cost Breakdown

The total cost of developing and producing the aircraft is paramount to the success of this program. These costs can be divided into two components, which are discussed in Subsection 17.1.1 and Subsection 17.1.2.

17.1.1. Research, Development, Test, and Evaluation Cost

The first component of the program cost for an aircraft consists of the accumulated costs during the design phases, all the way from conceptual planning up to and including certification. Table 17.1 shows these costs, split up into seven categories. The calculation is based on empirical relations compiled by Roskam [99], but the costs are refactored to take evolving technology and inflation into account.

Table 17.1: Research, Development, Test, and Evaluation Costs broken down

Category	**Costs** $[M€]$
Airframe Engineering and Design Cost	39.0
Development Support and Testing Cost	11.1
Flight Test Airplanes Cost	427.0
Flight Test Operations Cost	7.7
Test and Simulation Facilities Cost	31.0
RDTE Profit	51.5
Financing Cost	51.5
Sum	**619.0**

17.1.2. Manufacturing Cost

The second component of the program cost consists of the costs expended during the manufacturing of the aircraft. The main part of this is the actual production cost, and flight test, engineering, and financing cost make up the rest of the costs during this phase. The values are again calculated using [99], where empirical relations are derived and refactored to future prospected values.

Table 17.2: Manufacturing costs broken down.

Category	**Costs** $[M€]$
Airframe Engineering and Design Cost	40.8
Airplane Production Cost	3510.2
Production Flight Test Operations Cost	36.1
Financing Cost	358.7
Sum	**3945.8**

The division of costs over the different categories can be seen in Figure 17.1.

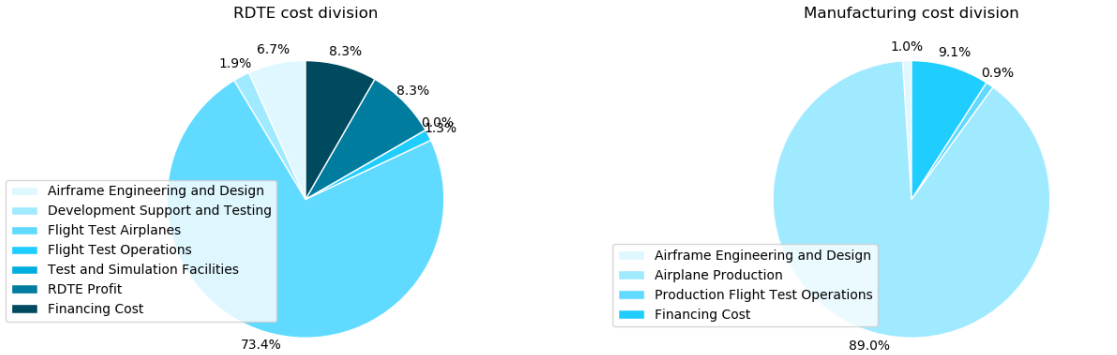

(a) Division of Research, Development, Test, and Evaluation costs

(b) Division of Manufacturing and Acquisition costs

Figure 17.1: Program cost allocation per category

17.2. Manufacturer Break-Even Point

Through analysis of the prospected program costs and sales over time of the aircraft, a break-even point (BEP) can be found. It was found to be in 2042, 20 years after the start of the program in 2022. To arrive at this value several parameters have been assumed. The program costs, as calculated in Section 17.1, were assumed to be spent linearly in time throughout the program. The revenue was calculated based on a total number of sold aircraft of 400, divided over 20 years, starting from 2030 (5 years before entry into service) until 2050. The selling price was estimated to be 14 $[M€]$, based on current competitor prices. The cash flows of the manufacturer for the full aircraft program are plotted in Figure 17.2.

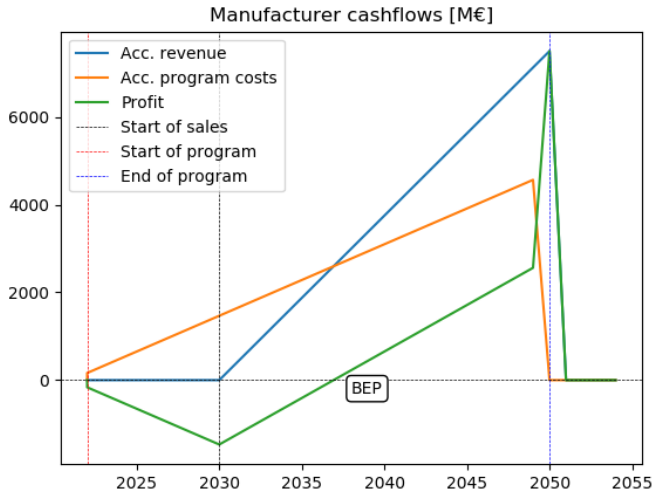

Figure 17.2: Cashflows of the aircraft manufacturer

17.3. Direct Operating Costs

Changing perspective from the manufacturer to the airline, the direct operating costs (DOC) are an important parameter in analysing the competitiveness of an aircraft. The method to calculate these was adapted from [100], and the formula for DOC is presented in Equation 17.1. This calculation is further detailed in the Midterm Report [10].

$$DOC = \frac{1}{R_{mission}}((C_{baggage} + C_{security} + C_{handling} + C_{PRM})N_{pax} + C_{landing} \cdot MTOW \\ +(C_{elec}\Phi + C_{fuel}(1-\Phi))E_{mission} + (C_{maintenance} + (\dot{C}_{pilot} + \dot{C}_{attendant}))t_{mission}) \tag{17.1}$$

In Equation 17.1, the DOC is computed in $[€/km]$, where Φ is the fraction of the aircraft energy supplied by batteries. This results in a DOC of 5.15 $[€/km]$, which is similar to that of a high-speed passenger train [101]. Therefore the requirement to be competitive on DOC to a train is met. The DOC per hour is calculated to be 1461 $[€/hr]$.

The effect of regenerating energy during descent on the DOC was analysed, since it increases the mission energy used, but decreases the mission time. The DOC is slightly more sensitive to mission time than it is to mission energy, and it turns out that the DOC for the DOC mission decreases by 0.3% when using full regeneration. As the mission time is reduced, the DOC per time unit is increased by 5.2% to 1537 $[€/hr]$ by using regeneration. As the DOC range stays constant, the DOC per unit distance is decreased by the same 0.3% from 5.15 $[€/km]$ to 5.13 $[€/km]$. The decrease of 0.3% is well below the estimated accuracy of the program, so the influence of regeneration of DOC is deemed negligible.

17.4. Airline Return on Investment

Another important financial indicator is the return on investment (ROI). It signifies the profit made by operating the aircraft relative to the purchase price, and can be evaluated at a certain amount of years after the purchase. To evaluate the ROI, three parameters were required, namely the aircraft purchase price, operating costs, and operating revenue. The purchase price (P) was taken as 14 $[M€]$, just as in Section 17.2. The operating costs were taken as the sum of indirect operating costs, which were taken as a constant factor, and DOC, which are described in Section 17.3. This can be multiplied by the DOC range, and then multiplied by the number of missions flown per year, to arrive at the operating costs per year (OC_y). The

number of missions flown per year is estimated at 1400, assuming 350 days of operation in a year, operating 4 flights per day. Finally, the yearly operating revenue (R_y) is found by assuming a ticket price of 80 [€], and a seat occupancy factor and capacity of 0.9 and 50 respectively.

$$ROI(N_{years}) = N_{years} \cdot \frac{R_y - OC_y}{P} \cdot 100\% \tag{17.2}$$

Equation 17.1 results in an ROI of 154% after 10 years, and 308% after 20 years of operation.

17.5. End Customer Cost per Kilometer

Again changing perspective, now to that of the end consumer buying a ticket for regional transportation, the cost per travel kilometre on board of this aircraft can be compared to that of competing transport modes. In Section 2.2 the ticket costs per km are tabulated for different modes of transport. With the previously assumed ticket price of 80 [€], and a DOC range of 400 $[km]$, the ticket cost per km is calculated to be 0.2 $[€/km]$. This value is on the high side of the spectrum, being 9% higher than that of train travel, and 26% higher than that of car travel with one passenger. It is lower than the price of boat travel, which is 0.25 $[€/km]$. Although the aircraft is slightly more expensive, the high price is offset by the low travel time. 'Flight shame' is not deemed a problem for this aircraft anymore, as it emits no greenhouse gases during operation.

17.6. Conclusion on Financial Overview

From the financial analysis, some conclusions can be drawn. First of all, the full program cost for the manufacturer is estimated to be 4.565 $[B€]$. With a selling price of 14 $[M€]$ and yearly sales of 20 aircraft, a break-even point is reached by 2042. The most negative profit that is made during the whole program is minus 1500 $[M€]$, which will require an extensive loan structure and induce associated financing costs.

The DOC of the aircraft are calculated to be 5.15 $[€/km]$, which is lower than that of a high-speed train (6.06 $[€/km]$). Using regenerative braking during the mission will increase the DOC per time unit by 5.2%, but the total mission DOC is not affected considerably. The ROI for an airline operating the aircraft is already 154% after 10 years, which is deemed acceptable. After 10 more years of operation, it has grown to 308%.

Finally, from a consumer point of view, the ticket cost per kilometre travelled of $0.2[€/km]$ is lower than that of a boat, and slightly higher than that of a train and a one-person occupied car. As flying is significantly faster than the other modes of transport, this is deemed acceptable.

18
Conclusion

This report aimed to converge on a final conceptual design from the design option chosen in the midterm report [10]. This was done with the focus on the mission need statement and the project objective statement:

Mission Need Statement
"To provide a regional commuter aircraft to transport at least 50 passengers including luggage, which is financially competitive to the ATR 42-600 and comparable to ground transport for direct operating cost. Further, it needs to reduce the CO_2 and NO_X emissions compared to the ATR 42-600 by 75% and 90% respectively, to have a sustainable end-of-life solution, and have a design payload of at least 5300 $[kg]$ and operate at DOC range of at least 400 $[km]$ including reserves."

Project Objective Statement
"To design a regional aircraft leveraging distributed (hybrid)-electric propulsion and regenerative capability, with improved sustainability compared to an ATR 42-600 and driven by requirements from the EU-funded FutPrInt50 project, by ten students in ten weeks."

After evaluating the functions and corresponding requirements of the aircraft, 6 design concepts were set up. These varied in overall aircraft configuration and powertrain concept. After performing a trade-off on both qualitative and quantitative criteria, a concept called CO-15 turned out to be the best option. This concept featured a high truss-braced wing with a canard, leveraging a hybrid hydrogen-electric powertrain system.

A final MTOW of $23314\ [kg]$ was found, with a final OEW of $17867\ [kg]$. This resulted in a wing surface area of $62.2\ [m^2]$, with a wing span of $31.4\ [m]$. The fuselage length is $22.7\ [m]$ and the cabin features a two-by-two seats abreast configuration. The concept was designed to comply with the top-level requirements. For most requirements compliance could be proven, however the requirement on adhering to certification standards could not be analysed well enough at this design stage.

The regenerative braking capabilities of this aircraft can reduce the DOC mission time by 5.2% when regenerating maximally, and increase the mission energy by 8.6% for the same regeneration use. The influence of regeneration on DOC is as low as 0.3%, so this should not be a reason to regenerate during descent. The reduced mission time could be beneficial however if it allows the operator to execute one more flight on a day, for example. It can also be seen as a unique selling point, however, it does come at the cost of a steeper descent, which compromises comfort slightly. Furthermore, when energy is regenerated during descent, the aircraft will land with energy in the battery, which can be used to taxi electrically.

The design presented in this report is viable and competitive at this design stage, but care should be taken in interpreting the findings presented. First of all the project was carried out under a heavy time constraint, and choices had to be made on where to spend resources. This introduced limitations and errors, which are discussed in Chapter 19. Secondly, in general, it is good to be aware that the goal of this project was to arrive at a conceptual design. Further studies should follow up on this project, for which some suggestions are made in Part III of this report, mainly Chapter 14 until Chapter 16.

19

Recommendations For Future Research

While this project was carried out with the best intention and utmost care, throughout the report multiple limitations of the work done have been mentioned. Next to this, towards the end of the project some mistakes were found, for which no time was left to address them properly. This chapter aims to give an overview of these limitations and errors, such that future research can be carried out in a more focused manner.

- For the wingtip propellers, research has shown that a pusher configuration shows potential in reducing power consumption for a given thrust coefficient. This project omitted this because of the more sophisticated design methods this would have required. Future research can benefit from looking into this and potentially changing the tractor propeller into a pusher configuration.
- At a point in the process the weight iteration process output variables were set. Due to mistakes in equations that were found later it needed to be changed, but due to these set output variables for the detailed script being in use it was time wise not possible to adapt these changes. That is why for example the powertrain weight in Section 6.7 does not match the powertrain weight in Section 8.2. However these values do not differ relatively much, thus it was decided to continue working with the output variables in the detailed scripts. T
- In the program the propulsive weight was added two times by accident, explaining the difference between the OEW and the sum of the component weights in Table 6.8.
- As mentioned in Subsection 6.1.1, the detailed design results should fed back into the class-I/class-II iteration. Due to time constraints, this feedback loop from the detailed design to the class-I/class-II iteration was not implemented in this report, but it is recommended to implement in the future.
- Currently, several assumptions are made about the efficiencies, specific powers and weights of the powertrain components. The feasibility of the aircraft depends especially on the development of low TRL powertrain components, such as the fuel cell and LH2. For further development of the aircraft, these accuracy and attainability of these values needs to be reviewed.
- Because hydrogen is such an immature technology for aerospace applications, special attention has to be given to the development of risk mitigation and safety features of the hydrogen systems in the aircraft.
- The current regenerative capabilities are provided by the wingtip propellers only, which enhances the wingtip vortices and increases lift induced drag significantly. This drag increase was not quantified, and might be of unacceptable proportions. This can be looked into in further research.
- The number of panels in the VLM should be increased for detailed design, as only 4 panels in chordwise direction and 10 panels in spanwise direction is fairly low. At least doubling the number of panels in both directions would be recommended. Further verification and validation is also needed.
- Computing lift and drag for more different flight conditions. Currently it is computed only for take-off, climb, cruise, descent, and landing, but analysing more steps, especially in climb and descent, and investigating different thrust settings is recommended.
- An investigation into the installation angle of the canard should be performed, as due to the high stall angle of the canard and low stall angle of the main wing, the aircraft has dangerous stall characteristics.
- The inclusion of rotational effects in the BEM method could be investigated to increase the fidelity of the model.
- Larger ranges of angles of attack including post-stall angles of attack should be considered to improve the accuracy of results in regeneration.

- The influence of using blade sweep and different airfoil sections on the propeller performance may need to be investigated.
- The aeroacoustic effects of the wingtip propellers can be investigated in more detail, especially concerning tonal noise components.
- The tail design and wing positioning should be done with the updated lift coefficient values from the aerodynamic analysis
- The canard stalls after the main wing which could result in dangerous situations. The canard and wing design must be optimized to check if there is a feasible design allowing the canard to stall before the wing. Otherwise a control augmentation system must be designed to alleviate this problem.
- Chapter 11 touched upon the wingbox fitting, truss analysis, and preliminary material choice. Considerably more work can be done on the preliminary and detailed structural design of the aircraft. This concerns several systems, e.g. fuselage stresses, wing skin stresses, control surface loads, and landing gear impact.
- In general, the used software structure for this project was verified and validated throughout the development of it, but more confidence in the methods can still be gained by planning and executing a more meticulous verification and validation campaign.
- The financial analysis performed in Chapter 17 was based on Roskam's method [99], which was first published in 1985. Although it is adjusted to the present day using refactoring values, a more modern method might result in more accurate results.

References

[1] M. Hoogreef, “Project guide: Regional transport aircraft with regenerative propulsion”, Apr. 2022.

[2] J. Mangold, D. Silberhorn, N. Moebs, *et al.*, “Refueling of lh2 aircraft—assessment of turnaround procedures and aircraft design implication”, *Energies*, Mar. 2022.

[3] “A statistical learning approach to the modeling of aircraft taxi-time”, *MIT Lincoln Laboratory, Federal Aviation Administration*, p. 4, Aug. 2010.

[4] M. Lukic, P. Giangrande, A. Hebala, S. Nuzzo, and M. Galea, “Review challenges and future developments of electric taxiing systems”, 2019.

[5] D. S. Lee, D. W. Fahey, P. M. Forster, *et al.*, “Aviation and global climate change in the 21st century”, *Atmospheric Environment*, vol. 43, no. 22, pp. 3520–3537, 2009, ISSN: 1352-2310. DOI: https://doi.org/10.1016/j.atmosenv.2009.04.024.

[6] R. de Vries, “Hybrid-electric aircraft with over-the-wing distributed propulsion: Aerodynamic performance and conceptual design”, English, Ph.D. dissertation, Delft University of Technology, 2022. DOI: 10.4233/uuid:ef87dc11-e7b2-4726-a41f-28588d64c58d.

[7] S. Althuis, A. Boerdijk, E. Emberger, *et al.*, “Dse group 7 - project plan”, Apr. 2022, DSE Deliverable.

[8] T. Stokkermans, N. van Arnhem, T. Sinnige, and L. Veldhuis, “Aerodynamic performance of a wingtip-mounted tractor propeller configuration in windmilling and energy-harvesting conditions”, *AIAA Aviation 2019 Forum*, 2019.

[9] *ITF transport outlook 2021*. OECD Publishing, 2021.

[10] S. Althuis, A. Boerdijk, E. Emberger, *et al.*, “Dse group 7 - midterm report”, May 2022, DSE Deliverable.

[11] D. P. Raymer, “Aircraft design: A conceptual approach”, American Institute of Aeronautics and Astronautics, 1989.

[12] R. Vos, J. Melkert, and B. Zandbergen, *The design of the fuselage*, May 2022.

[13] E. A. S. Agency, “Certification specifications for large aeroplanes cs-25”, Sep. 2007.

[14] E. Torenbeek, “Synthesis of subsonic airplane design”, 1982, ISBN: 90-247-2724-3.

[15] P. C. de Boer, A. d. Wit, and R. C. van Benthem, “Development of a liquid hydrogen-based fuel cell system for the hydra-2 drone”, in *AIAA SCITECH 2022 Forum*, 2022, p. 0443.

[16] Q. Van der Leer and M. Hoogreef, “Aero-propulsive and aero-structural design integration of turboprop aircraft with electric wingtip-mounted propellers”. DOI: https://arc.aiaa.org/doi/pdf/10.2514/6.2022-0167.

[17] F. Oliviero, *Aerospace design and systems engineering elements ii: Aircraft design - aircraft aerodynamic analysis – fundamentals*, 2022.

[18] E. Torenbeek, *Advanced Aircraft Design, Conceptual Design, Analysis and Optimization of Subsonic Civil Airplanes*. John Wiley & Sons, 2013.

[19] B. Bohari, Q. Borlon, M. Bronz, and E. Benard, “Aerodynamic model of propeller–wing interaction for distributed propeller aircraft concept”, *Aerospace Engineering*, vol. 234, no. 10, 2020.

[20] M. Drela, “Flight vehicle aerodynamics”, MIT Press, 2014.

[21] J. D. Anderson, *Fundamentals of aerodynamics*. McGraw-Hill, 2017, ISBN: 9781259129919.

[22] B. Dillner, F. W. May, and J. H. McMasters, “Aerodynamic issues in the design of high-lift systems for transport aircraft”, BOEING MILITARY AIRPLANE CO SEATTLE WA, Tech. Rep., 1984.

[23] F. Oliviero, *Systems engineering & aerospace design: Requirement analysis and design principles for a/c stability and control (part ii)*, 2022.

[24] F. Oliviero, “Aerospace design and systems engineering elements ii: Aircraft design - mobile surfaces on the wing”, 2022.

[25] P. D. Vecchia, D. Malgieri, F. Nicolosi, and A. D. Marco, “Numerical analysis of propeller effects on wing aerodynamic: Tip mounted and distributed propulsion”, *Transportation Research Procedia*, vol. 29, pp. 106–115, 2018, Aerospace Europe CEAS 2017 Conference, ISSN: 2352-1465. DOI: https://doi.org/10.1016/j.trpro.2018.02.010.

[26] F. Oliviero, *Aerospace design and systems engineering elements ii: Aircraft design - aircraft aerodynamic analysis – lift & drag*, 2022.

[27] D. Juschus, “Preliminary propulsion system sizing methods for pem fuel cell aircraft”, 2021.

[28] J. Zhang, Z. Xie, J. Zhang, *et al.*, “High temperature pem fuel cells”, *Journal of power Sources*, vol. 160, no. 2, pp. 872–891, 2006.

[29] K. Ondrejička, V. Ferencey, and M. Stromko, “Modeling of the air-cooled pem fuel cell”, *IFAC-PapersOnLine*, vol. 52, no. 27, pp. 98–105, 2019.

[30] F. Barbir, “Progress in pem fuel cell systems development”, in *Hydrogen Energy System*, Springer, 1995, pp. 203–213.

[31] B. Kienitz, “Optimizing polymer electrolyte membrane thickness to maximize fuel cell vehicle range”, *International Journal of Hydrogen Energy*, vol. 46, no. 19, pp. 11 176–11 182, 2021.

[32] A. G. Rao, F. Yin, and H. G. Werij, “Energy transition in aviation: The role of cryogenic fuels”, *Aerospace*, vol. 7, no. 12, p. 181, 2020.

[33] G. Onorato, “Fuel tank integration for hydrogen airliners”, 2021.

[34] T. Placke, R. Kloepsch, S. Dühnen, and M. Winter, “Lithium ion, lithium metal, and alternative rechargeable battery technologies: The odyssey for high energy density”, *Journal of Solid State Electrochemistry*, vol. 21, no. 7, pp. 1939–1964, 2017.

[35] M. Zwicker, M. Moghadam, W. Zhang, and C. Nielsen, “Automotive battery pack manufacturing–a review of battery to tab joining”, *Journal of Advanced Joining Processes*, vol. 1, p. 100 017, 2020.

[36] N. E. Anderson, S. H. Loewenthal, and J. D. Black, “An analytical method to predict efficiency of aircraft gearboxes”, 1986.

[37] A. D. Anderson, N. J. Renner, Y. Wang, *et al.*, “System weight comparison of electric machine topologies for electric aircraft propulsion”, in *2018 AIAA/IEEE Electric Aircraft Technologies Symposium (EATS)*, IEEE, 2018, pp. 1–16.

[38] M.-S. Wu, K. Liu, Y.-Y. Wang, and C.-C. Wan, “Heat dissipation design for lithium-ion batteries”, *Journal of Power Sources*, vol. 109, no. 1, pp. 160–166, 2002, ISSN: 0378-7753. DOI: https://doi.org/10.1016/S0378-7753(02)00048-4. [Online]. Available: https://www.sciencedirect.com/science/article/pii/S0378775302000484.

[39] Q. Ke, X. Li, J. Guo, W. Cao, Y. Wang, and F. Jiang, “The retarding effect of liquid-cooling thermal management on thermal runaway propagation in lithium-ion batteries”, *Journal of Energy Storage*, vol. 48, p. 104 063, 2022, ISSN: 2352-152X. DOI: https://doi.org/10.1016/j.est.2022.104063. [Online]. Available: https://www.sciencedirect.com/science/article/pii/S2352152X22001001.

[40] B. Zohuri, “Chapter 12 - heat exchangers”, in *Physics of Cryogenics*, B. Zohuri, Ed., Elsevier, 2018, pp. 299–330, ISBN: 978-0-12-814519-7. DOI: https://doi.org/10.1016/B978-0-12-814519-7.00012-4. [Online]. Available: https://www.sciencedirect.com/science/article/pii/B9780128145197000124.

[41] M. D. Moore and B. Fredericks, “Misconceptions of electric propulsion aircraft and their emergent aviation markets”, *AIAA SciTech Forum*, 2014. DOI: 10.2514/6.2014-0535.

[42] N. van Arnhem, G. Eitelberg, T. Sinnige, T. Stokkermans, and L. Veldhuis, “Wingtip-mounted propellers: Aerodynamic analysis of interaction effects and comparison with conventional layout”, *Journal of Aircraft*, 2019.

[43] N. van Arnhem, R. Nederlof, and T. Sinnige, “Aerodynamic performance of wingtip-mounted propellers in tractor and pusher configuration”, *AIAA Aviation 2021 Forum*, 2021.

[44] P. Block, “Pusher propeller noise directivity and trends”, *AIAA 10th Aeroacoustics Conference*, 1986.

[45] Y. Teeuwen, “Propeller design for conceptual turboprop aircraft”, M.S. thesis, Delft University of Technology, 2017.

[46] J. Saltzman and T. G. Ayers, “Pusher propeller noise directivity and trends”, *Journal of Aircraft*, pp. 801–811,

[47] C. F. Wisniewski, A. R. Byerley., W. H. Heiser, K. W. V. Treuren, and W. R. Liller, “The influence of airfoil shape, tip geometry, reynolds number and chord length on small propeller performance and noise”, *AIAA Aviation Forum*, 2015.

[48] P. Sforza, “Commercial airplane design principles”, in P. Sforza, Ed., Boston: Butterworth-Heinemann, 2014, pp. 405–452, ISBN: 978-0-12-419953-8. DOI: https://doi.org/10.1016/B978-0-12-419953-8.00010-3.

[49] M. Haddaoui, “Development of a propeller source noise model”, M.S. thesis, 2019.

[50] A. Olczak, T. Stallard, T. Feng, and P. Stansby, “Comparison of a rans blade element model for tidal turbine arrays with laboratory scale measurements of wake velocity and rotor thrust”, *Journal of Fluids and Structures*, vol. 64, pp. 87–106, Jul. 2016. DOI: 10.1016/j.jfluidstructs.2016.04.001.

[51] S. Raynal, G. Millot, and B. Vasseur, “Vtol propeller performances under realistic aerodynamic loads”, Apr. 2021.

[52] J. Anderson John D., *Fundamentals of aerodynamics*. McGraw-Hill, 2017, p. 754, ISBN: 9781259129919.

[53] J. Dorfling and K. Rokhsaz, “Constrained and unconstrained propeller blade optimization”, *Journal of Aircraft*, pp. 1179–1188, 2014.

[54] C. N. Adkins and R. H. Liebeck, “Design of optimum propellers”, *Journal of Propulsion and Power*, vol. 10, 1994.

[55] M. K. Rwigema, “Propeller blade element momentum theory with vortex wake deflection”, 2010.

[56] Y. Teeuwen, “Propeller design for conceptual turboprop aircraft”, M.S. thesis, Delft University of Technology, 2017, p. 49.

[57] M. Bronz, J.-M. Moschetta, and G. Hattenberger, “Multi-point optimisation of a propulsion set as applied to a multi-tasking mav”, Jul. 2012.

[58] E. Houghton, P. Carpenter, S. H. Collicott, and D. T. Valentine, “Aerodynamics for engineering students (sixth edition)”, in E. Houghton, P. Carpenter, S. H. Collicott, and D. T. Valentine, Eds., Sixth Edition, Boston: Butterworth-Heinemann, 2013, pp. 645–687, ISBN: 978-0-08-096632-8. DOI: https://doi.org/10.1016/B978-0-08-096632-8.00010-2.

[59] J. C. Nash and A. Laplante, “Real-time system to control aircraft propeller pitch”, 2012. DOI: https://doi.org/10.2514/1.4277.

[60] J. Goyal, T. Sinnige, C. Ferreira, and F. Avallone, “Aerodynamic and aeroacoustic characteristics of an isolated propeller at positive and negative thrust”, *AIAA Aviation 2021 Forum*, 2021.

[61] F. Oliviero, *Systems engineering & aerospace design: Requirement analysis and design principles for a/c stability and control (part i)*, 2022.

[62] F. Oliviero, "Systems engineering & aerospace design: A/c sizing for lateral-directional requirements and ground operations", 2022.

[63] N. van Oene, "Landing gear design integration for the tu delft initiator", M.S. thesis, Delft University of Technology, 2019.

[64] N. J. Arockiam, M. Jawaid, and N. Saba, "6 - sustainable bio composites for aircraft components", in *Sustainable Composites for Aerospace Applications*, ser. Woodhead Publishing Series in Composites Science and Engineering, M. Jawaid and M. Thariq, Eds., Woodhead Publishing, 2018, pp. 109–123, ISBN: 978-0-08-102131-6. DOI: https://doi.org/10.1016/B978-0-08-102131-6.00006-2.

[65] G. Moors, C. Kassapoglou, S. Almeida, and C. Ferreira, "Weight trades in the design of a composite wing box: Effect of various design choices", *CEAS Aeronautical Journal*, vol. 10, Jul. 2018. DOI: 10.1007/s13272-018-0321-4.

[66] M. Das, R. Chacko, and S. Varughese, "An efficient method of recycling of cfrp waste using peracetic acid", *ACS Sustainable Chemistry & Engineering*, vol. 6, no. 2, pp. 1564–1571, 2018. DOI: 10.1021/acssuschemeng.7b01456. [Online]. Available: https://doi.org/10.1021/acssuschemeng.7b01456.

[67] I. Deonandan and H. Balakrishnan, "Evaluation of strategies for reducing taxi-out emissions at airports", p. 104 063, 2022, ISSN: 2352-152X. DOI: https://doi.org/10.1016/j.est.2022.104063. [Online]. Available: https://www.sciencedirect.com/science/article/pii/S2352152X22001001.

[68] Y. Zhang and Q. Wang, "Methods for determining unimpeded aircraft taxiing time and evaluating airport taxiing performance", *Chinese Journal of Aeronautics*, vol. 30, no. 2, pp. 523–537, 2017, ISSN: 1000-9361. DOI: https://doi.org/10.1016/j.cja.2017.01.002. [Online]. Available: https://www.sciencedirect.com/science/article/pii/S1000936117300286.

[69] G. Ruijgrok, *Elements of Airplane Performance*. Delft University Press, 1990, ISBN: 9789062756087. [Online]. Available: https://books.google.nl/books?id=TLEZNAAACAAJ.

[70] Y. Niu, S. Zhang, G. Tian, H. Zhu, and W. Zhou, "Estimation for runway friction coefficient based on multi-sensor information fusion and model correlation", *Sensors*, vol. 20, no. 14, 2020, ISSN: 1424-8220. DOI: 10.3390/s20143886.

[71] P.-A. Lambert, D. Alejo, Y. Fefermann, *et al.*, "Long-term hybrid-electric propulsion architecture options for transport aircraft", Oct. 2016.

[72] S. Althuis, A. Boerdijk, E. Emberger, *et al.*, "Dse group 7 - baseline report", Apr. 2022, DSE Deliverable.

[73] "Effects of battery manufacturing on electric vehicle life-cycle greenhouse gas emissions", The International Council of Clean Transportation, Tech. Rep., Feb. 2018.

[74] Y. Liu, R. Zhang, J. Wang, and Y. Wang, "Current and future lithium-ion battery manufacturing", *iScience*, vol. 24, no. 4, p. 102 332, 2021, ISSN: 2589-0042. DOI: https://doi.org/10.1016/j.isci.2021.102332. [Online]. Available: https://www.sciencedirect.com/science/article/pii/S258900422100300X.

[75] B. Scrosati and J. Garche, "Lithium batteries: Status, prospects and future", *Journal of Power Sources*, vol. 195, pp. 2419–2430, May 2010. DOI: 10.1016/j.jpowsour.2009.11.048.

[76] N. A. Shuaib and P. T. Mativenga, "Carbon footprint analysis of fibre reinforced composite recycling processes", *Procedia Manufacturing*, vol. 7, pp. 183–190, 2017, International Conference on Sustainable Materials Processing and Manufacturing, SMPM 2017, 23-25 January 2017, Kruger, ISSN: 2351-9789. DOI: https://doi.org/10.1016/j.promfg.2016.12.046.

[77] M. Gautam, B. Pandey, and M. Agrawal, "Chapter 8 - carbon footprint of aluminum production: Emissions and mitigation", in *Environmental Carbon Footprints*, S. S. Muthu, Ed., Butterworth-Heinemann, 2018, pp. 197–228, ISBN: 978-0-12-812849-7. DOI: https://doi.org/10.1016/B978-0-12-812849-7.00008-8.

[78] P. A. Claisse, "Chapter 32 - alloys and nonferrous metals", in *Civil Engineering Materials*, P. A. Claisse, Ed., Boston: Butterworth-Heinemann, 2016, pp. 361–368, ISBN: 978-0-08-100275-9. DOI: https://doi.org/10.1016/B978-0-08-100275-9.00032-2.

[79] K. Kawajiri and K. Sakamoto, "Environmental impact of carbon fibers fabricated by an innovative manufacturing process on life cycle greenhouse gas emissions", *Sustainable Materials and Technologies*, vol. 31, e00365, 2022, ISSN: 2214-9937. DOI: https://doi.org/10.1016/j.susmat.2021.e00365.

[80] S. Kurland, "Energy use for gwh-scale lithium-ion battery production", *Environmental Research Communications*, vol. 2, no. 1, Dec. 2019.

[81] H. Hao, M. Zhexuan, S. Jiang, Z. Liu, and F. Zhao, "Ghg emissions from the production of lithium-ion batteries for electric vehicles in china", *sustainability*, Apr. 2017.

[82] Clean Sky 2 JU, FCH 2 JU, "Hydrogen-powered aviation: A fact-based study of hydrogen technology, economics, and climate impact by 2050", Tech. Rep., May 2020.

[83] O. J., "The growth in greenhouse gas emissions from commercial aviation part 1 of a series on airlines and climate change", Environmental and Energy Study Institute, Tech. Rep., Oct. 2019.

[84] "Aviation emissions, impacts & mitigation a primer", FAA Office of Environment and Energy, Tech. Rep., Jan. 2015.

[85] M. S. P. Kahandawala, M. J. DeWitt, E. Corporan, and S. S. Sidhu, "Ignition and emission characteristics of surrogate and practical jet fuels", *Energy & Fuels*, vol. 22, no. 6, pp. 3673–3679, 2008. DOI: 10.1021/ef800303a.

[86] "Global renewables outlook: Energy transformation 2050", International Renewable Energy Agency, Tech. Rep., Jan. 2020.

[87] E. Taibi, H. Blanco, R. Miranda, and M. Carmo, “Green hydrogen cost reduction: Scaling up electrolysers to meet the 1.5□c climate goal”, International Renewable Energy Agency, Tech. Rep., Feb. 2020.

[88] S. Dühnen, J. Betz, M. Kolek, R. Schmuch, M. Winter, and T. Placke, “Toward green battery cells: Perspective on materials and technologies”, *Small methods*, vol. 4, 2020. DOI: https://doi.org/10.1002/smtd.202000039.

[89] J. Ribeiro, F. Afonso, I. Ribeiro, *et al.*, “Environmental assessment of hybrid-electric propulsion in conceptual aircraft design”, *Journal of Cleaner Production*, vol. 247, p. 119 477, 2020, ISSN: 0959-6526. DOI: https://doi.org/10.1016/j.jclepro.2019.119477.

[90] “The environmental impacts of recycling portable lithium-ion batteries”, *Procedia CIRP*, vol. 48, pp. 188–193, 2016, The 23rd CIRP Conference on Life Cycle Engineering, ISSN: 2212-8271. DOI: https://doi.org/10.1016/j.procir.2016.03.100.

[91] J. Zhang, V. S. Chevali, H. Wang, and C.-H. Wang, “Current status of carbon fibre and carbon fibre composites recycling”, *Composites Part B: Engineering*, vol. 193, p. 108 053, 2020, ISSN: 1359-8368. DOI: https://doi.org/10.1016/j.compositesb.2020.108053.

[92] M. Gökelma, A. Vallejo-Olivares, and G. Tranell, “Characteristic properties and recyclability of the aluminium fraction of mswi bottom ash”, *Waste Management*, vol. 130, pp. 65–73, 2021, ISSN: 0956-053X. DOI: https://doi.org/10.1016/j.wasman.2021.05.012.

[93] A. Prapotnik Brdnik, R. Kamnik, S. Bo˘zi˘cnik, and M. Marksel, “Ground infrastructure investments for operation of hybrid-electric aircraft”, *IOP Conference Series: Materials Science and Engineering*, 2022.

[94] A. Postma-Kurlanc, H. Leadbetter, and C. Pickard, “Hydrogen infrastructure and operations airports, airlines and airspace”, FlyZero, Tech. Rep., Mar. 2022.

[95] A. M. Kevin Walkowicz and J. Farrell, “R&d insights for extreme fast charging of medium- and heavy-duty vehicles”, National Renewable Energy Laboratory, Tech. Rep., 2019.

[96] N. Mei, X. Xu, and R. Li, “Heat dissipation analysis on the liquid cooling system coupled with a flat heat pipe of a lithium-ion battery”, *ACS Omega*, vol. 5, no. 28, pp. 17 431–17 441, 2020, PMID: 32715228. DOI: 10.1021/acsomega.0c01858.

[97] S. Sripad, A. Bills, and V. Viswanathan, “A review of safety considerations for batteries in aircraft with electric propulsion”, *MRS Bulletin*, vol. 46, no. 5, pp. 435–442, 2021, ISSN: 1938-1425. DOI: 10.1557/s43577-021-00097-1.

[98] M. Mitici, M. Pereira, and F. Oliviero, “Electric flight scheduling with battery-charging and battery-swapping opportunities”, *EURO Journal on Transportation and Logistics*, vol. 11, p. 100 074, 2022, ISSN: 2192-4376. DOI: https://doi.org/10.1016/j.ejtl.2022.100074.

[99] J. Roskam, *Aircraft Design*. Roskam Engineering and Aviation Corporation, 1990, Part 8: Airplane Cost Estimation.

[100] K. Shahwan, “Operating cost analysis of electric aircraft on regional routes”, Ph.D. dissertation, Linköpings Universitet, Dec. 2021.

[101] J. Hudenko, N. Ribakova, and R. Pocs, “Cost that is directly incurred as a result of operating the train service on the 1520 mm rail with primarily freight transportation”, *6th Transport Research Arena 4il 18-21, 2016*, 2016.